Technical Letter Report on Literature Review and Assessment of Potential Seismic Effects on Ongoing Material Degradation

Manuscript Completed: August 2016
Manuscript Published: September 2016

Prepared by Omesh Chopra,[1] Bruce Biwer,[1] Yogen Garud,[1] Dwight Diercks,[2] and David Ma[1]
[1] Environmental Science Division
[2] Nuclear Engineering Division
Argonne National Laboratory, Argonne, IL 60439

Dr. Appajosula Rao, NRC Contracting Officer's Representative

Prepared for
Division of Engineering
Office of Nuclear Regulatory Research
U.S. Nuclear Regulatory Commission
Washington, DC 20555
NRC Job Code V6370

ABSTRACT

All structures, systems, and components (SSCs) in nuclear power plants (NPPs) are subjected to aging degradation during reactor operation because of chemical and mechanical effects and interactions with the service environment. The objective of this program is to evaluate the potential cumulative effects of repeated and sudden, below design basis earthquake loading on progressing degradation of NPP structural materials. Structural damage to NPPs occurs when the cumulative effects of ground acceleration (i.e., seismically induced vibrations) exceed a certain threshold. The American Society of Mechanical Engineers Code Section III design rules and U.S. Nuclear Regulatory Commission regulatory guidance concerning seismic design are summarized, and the postulated and anticipated seismic loads and response spectra for NPP SSCs are discussed. Seismic loading rate effects on the cyclic deformation behavior (including microstructural effects), tensile properties, fracture behavior, and elastic properties of structural alloys used in the primary coolant pressure boundary and other safety-related systems are reviewed in detail. A detailed knowledge of the evolution of material microstructure during service is essential for understanding the fundamental mechanisms of crack initiation and failure. Six specific information gaps related to cumulative seismic damage analysis are identified.

TABLE OF CONTENTS

FIGURES

TABLES

EXECUTIVE SUMMARY

All structures, systems, and components (SSCs) in nuclear power plants (NPPs) are subjected to aging degradation during reactor operation because of chemical and mechanical effects and interactions with the service environment. The objective of this program is to evaluate the potential cumulative effects of repeated and sudden, below safe shutdown earthquake loading on progressing degradation of NPP structural materials. The program addresses knowledge gaps in a fundamental manner, considering the mechanical response of degraded material to establish their basic properties under various stages of degradation and determine whether repeated below design basis earthquake (DBE) events could adversely affect ongoing material and component degradation. Included is a literature review to evaluate the effects of repeated and sudden below-SSE loading on specific degradation mechanisms. This research addresses the U.S. Nuclear Regulatory Commission's (NRC's) long-term research project related to determining the effects of repeated and cumulative below-DBE loading on progressive nuclear reactor material degradation.

The SSCs important to safety are designed to meet consensus codes and standards for NPPs to help ensure that a sufficient design margin is maintained throughout the plant's operating life to ensure that premature failure of such SSCs does not result in unacceptable consequences. In particular, these SSCs are designed to withstand the effects of the DBE, which is also termed as the safe shutdown earthquake (SSE). The SSC design takes into account historical experiences of ground motion at the site and SSE, and this ensures that in the event of an occurrence of an earthquake of concern, the safety systems will function and the plant will shut down in an orderly manner. However, it is not clear if and how this design approach is applicable to reactor coolant pressure boundary (RCPB) components that have ongoing degradation.

A number of analytical and experimental studies have been conducted to better understand the structural response of NPPs considering the presence of cracks in piping components. Many of these studies use seismic hazard analysis in evaluating failure response to SSE conditions, based on the frequency and the size of seismic load and using original material properties, though at elevated operating temperatures. The NRC has also sponsored research on the concept of a "cracked-pipe element" as a "degraded condition" and tested simple and component tests of girth welds. The results of these studies are summarized here.

Seismic Design

Structural damage to NPPs occurs when the cumulative effects of ground acceleration exceed a certain threshold. Design codes typically include an analysis of seismic fatigue degradation based on one SSE and 5 to 20 operating basis earthquakes (OBEs) with 10 to 20 cycles per event, depending on the location. However, seismic events less than the OBE are not considered in the analysis. The fatigue damage from all design transients is evaluated for the period of reactor operation to determine a characteristic-derived property known as the cumulative usage factor (CUF). Strain-rate effects are also an important consideration in seismic damage analysis, and the stress-strain behavior under short-term high strain rate loading may be quite different than that under normal loading conditions.

The present investigation includes a review of NPP design criteria and standards for seismic design, as contained in Title 10, Part 50, of the *Code of Federal Regulations*

(10 CFR Part 50) regulations, the American Society of Mechanical Engineers (ASME) Boiler and Pressure Vessel Code, and NRC Regulatory Guides. In general, designs of NPPs during the 1960s and 1970s used a deterministic approach to seismic design based on site-specific examinations of local and regional seismic, geological, and geotechnical soil conditions to determine the maximum credible earthquake. After 2000, there were attempts to standardize the design of NPPs to include not only a standardized reactor coolant system but also a standardized balance-of-plant. Furthermore, as more data became available on actual recorded earthquake activities, a better understanding developed regarding the shape of the design basis ground response spectra recorded at various sites around the world. However, the analytical techniques and procedures necessary to convert input earthquake motions to resultant seismic forces, moments, or stresses in components need to be examined, considering the current material condition of the components and high-frequency, cyclic elastic straining to evaluate potential impact on component design.

The seismic loads on a structure are inertial loads generated by the deformation of the structure as it vibrates, and the seismic forces depend on the distribution of mass and stiffness throughout the structure. Because structures are typically designed to respond inelastically under vibration, the seismic forces also depend on the manner by which plasticity spreads through the structure, and these forces are typically amplified by resonance effects. In addition, the maximum vibratory accelerations of the SSE must take into account the characteristics of the underlying soil material in transmitting the earthquake-induced motions. Finally, damping effects within the structure must be taken into account.

The information needed for a seismic design includes (a) design ground response spectra, (b) in-structure response spectra, (c) acceleration time history, and (d) seismic anchor movements. The seismic design specifications include (a) the scope and boundaries of components to be seismically designed; (b) the applicable design and construction code; (c) the required seismic function (e.g., operability, leak tightness, and position retention) on the component or piping system; (d) the free-field seismic input for the DBE; (e) the in-structure seismic response spectra; and (f) the operating and design loading conditions concurrent with the seismic load.

The requirements for the acceptability of a component design by analysis are described in ASME Section III, Division 1 Subarticle NB-3210, “Design Criteria.” Alternatively, a design by rule approach as described in Subarticle NB/NC-3600 may be used for piping and piping components. The design methods in Section III Subarticle NB, NC, or NG for ASME Class 1, 2, and CS components also require a fatigue analysis as well as a fracture mechanics evaluation to prevent the likelihood of nonductile failure. The ASME Code fatigue analysis considers all transient loads, and for each load-cycle or load-set pair, an individual fatigue usage factor is determined by the ratio of the number of cycles anticipated during the lifetime of the component to the allowable cycles.

Seismic Loading Rate Effects

The imposed loading rate has been found to be a significant variable in the response of large structures to seismic events. The strain rate imposed during an earthquake is variable, but a range of 0.1 to 10 s^{-1} appears to be typical of strong earthquakes. The effect of loading rate on the corrosion and crack initiation, cyclic deformation behavior, tensile properties, and fracture behavior of NPP structural alloys is reviewed in detail.

Corrosion and Crack Initiation

Seismic loadings can negatively impact the corrosion resistance of NPP structural alloys by straining or cracking the passive oxide film and the underlying metal. In cases where the passive oxide film is ruptured, it would lead to re-passivation of the exposed metal and could promote crack initiation followed by such processes as stress corrosion cracking (SCC) or pitting and crevice corrosion. In addition, any seismic loading that results in passive film rupture could result in the development of micro cracks in the underlying metal that could also lead to SCC or other forms of accelerated corrosion.

The effect of strain without rupture on the passive film is unclear, but corrosion processes could be altered if ion migration in the passive film is altered. Straining of the underlying metal due to a seismic event could cause plastic deformation. The resulting surface tensile residual stresses can enhance general corrosion as well as corrosion fatigue cracking.

Cyclic Deformation Behavior

Existing fatigue strain-versus-life (ε–N) data indicate that in the temperature range of dynamic strain aging (200–370°C) (392–698°F), some heats of carbon and low-alloy steels are sensitive to strain rate even in an inert environment; with decreasing strain rate, the fatigue life may be either unaffected, decrease for some heats, or increase for others. The cyclic stress–strain response of these steels varies with steel type, temperature, and strain rate. In general, they show initial cyclic hardening, followed by cyclic softening or a saturation stage at all strain rates. At high strain amplitudes, a secondary hardening stage is observed prior to fracture.

For wrought austenitic stainless steels (SSs), the fatigue life is generally independent of strain rate at temperatures up to 400°C (752°F). During cyclic straining, austenitic SSs exhibit rapid hardening during the first 50–100 cycles, and the extent of hardening increases with increasing strain amplitude and decreasing temperature and strain rate. The cast austenitic stainless steels (CASS) CF-3, CF-8, and CF-8M generally show behaviors similar to the wrought austenitic SS, though the cyclic-hardening behavior may be influenced by aging in some cases.

For ferritic steels at low constant cyclic strain amplitudes, the dislocation bundles produced during the rapid hardening stage shake down into bundles of fragmented dislocations, whereas a cell structure is developed at higher strain ranges. The saturation cell size generally increases with either a decrease in strain amplitude or an increase in temperature. For the austenitic SSs, initial cyclic hardening is associated with the formation of an increased dislocation density in a uniform planar structure. During subsequent cyclic softening and stabilization, the dislocations eventually evolve into a well-defined cell structure.

Under variable strain fatigue, the dislocation cell structure formed under initial higher strain amplitude can change gradually upon subsequent cycling at lower amplitude, with the cell size increasing by the disintegration of some of the existing cell walls. Depending upon the microstructure that had developed at the high strain amplitude, decreasing the strain amplitude may not lead to the behavior observed for cycling a virgin specimen at the low strain amplitude; some memory of prior strain cycling may remain in the material.

Tensile Properties

Literature data indicate that the yield and ultimate tensile strengths of A508 Cl. 3 and A533 Gr. B steel generally increase with increasing strain rate, while the ductility decreases or shows little effect. However, some data suggest a reversal in the yield and tensile strength behavior with strain rate in the region of the normal light water reactor (LWR) operating temperatures. Dynamic strain aging appears to play a role in this strain rate sensitivity, with serrated flow observed in the temperature range of 140 to 350°C (284 to 662°F), depending upon temperature and strain rate.

For Type 304, 304L, 304N, and 304LN SSs, the yield stress and flow stress are generally found to increase with increasing strain rate, the ultimate tensile strength tends to decrease, and the ductility decreases or shows little change. However, a study on Type 304L SS showed an unexpected decrease in flow stress with increasing strain rate at 427 and 538°C (801 and 1000°F).

For Type 316 SS, the yield and ultimate tensile strengths were found to increase with increasing strain rate at 650°C (1202°F), while the effect on the ductility was relatively small. Subsequent research indicated variable results, with an increase in ductility with increasing strain rate observed at 700°C (1292°F). Most researchers report an increase in flow stress with increasing strain rate for Types 316L and 316LN SSs, but there is some indication of a reversal in the strain rate effect on the ultimate tensile strength at temperatures on the order of 300 to 500°C (572 to 932°F). Elongation and reduction of area also appear to increase somewhat with increasing strain rate, though the opposite effect has been observed for cold-worked material.

The tensile data for Type 304/308 welds and Type 308 SS weld metal show mixed results. Some researchers observe a marked increase in flow stress with increasing strain rate, while others observe only a small effect. The elongation appears to decrease with increasing strain rate for the weld metal and remain roughly constant or increase slightly for the base metal. However, none of these data were obtained in the temperature range of interest for LWRs.

The limited data on the strain-rate effect on the flow stress of Alloy 600 indicate little effect of strain rate on flow stress and ductility at temperatures up to 760°C (1400°F) and marked increase in flow stress with increasing strain rate at higher temperatures. The tensile data for Alloy 690 indicate an increase in flow stress with increasing strain rate over the entire temperature range from −100°C to 1200°C (–148°F to 2192°F), though the magnitude of the effect appears to be temperature-dependent.

Fracture Behavior

The Charpy impact data for A508 Cl. 3 and A533 Gr. B pressure vessel steels indicate either little effect or an increase in the ductile-to-brittle transition temperature (DBTT) with increasing loading rate. An increased loading rate also appears to increase the upper shelf energy somewhat for both steels. Neutron irradiation clearly increases the DBTT, and Type 308 SS weld filler metal appears to be increasingly susceptible to brittle fracture with elevated-temperature aging.

The fracture toughness of A508 Cl. 3 and A533 Gr. B steels generally increases with increasing loading rate, and the fracture toughness-versus-temperature curves shift to higher temperatures. However, a decrease in the crack initiation toughness, J_{Ic}, with increasing strain rate has been observed by some researchers in the temperature range of interest for LWR applications. The J-R curves generally show an increase in cracking resistance with increasing loading rate.

The fracture toughness data for Types 304 and 316 SSs generally suggest a beneficial effect of increasing loading rate on the crack resistance. However, the variability in the data indicates that the loading conditions of interest must be well defined before these results can be reliably applied to a specific loading situation. The limited data in the literature on the effect of loading rate on the fracture toughness properties of the CASS materials are somewhat inconsistent, and as-cast and aged material show different behaviors. Recent work on low-temperature crack propagation for aged CASS CF-8 material in pressurized water reactor (PWR) environments investigated the potential synergy between thermal and hydrogen embrittlement associated with decomposition of the ferrite at reactor temperatures, and a large effect of the coolant environment on fracture toughness was observed.

For Alloy 600, a dramatic degradation in fracture toughness is observed in hydrogenated water at temperatures below 149°C (300°F), an effect attributed to hydrogen-induced intergranular cracking. This behavior is similar to that observed for aged CF-8 material in LWR shutdown water chemistry. At higher temperatures in the same environment, the fracture toughness increases with increasing loading rate. A qualitatively similar behavior occurs for Alloy 690.

Elastic Properties

No strain-rate dependence is observed for the elastic properties of NPP structural alloys.

Information Gaps

Six information gaps were identified in this work, as follows:

1. Low-level seismic events can impose higher loading rates on reactor structural materials than typically experienced during normal operation. These off-normal events have the potential to cause accelerated crack initiation through passive film rupture, micro crack generation, and plastic deformation. The extent of the accelerated crack initiation needs to be investigated.

2. The possible impact of (a) current material condition, (b) loading rates associated with typical seismic events and with low-level seismic fatigue cycles (e.g., magnitudes associated with seismic accelerations between 0.01 g and OBE) on reactor component design needs to be investigated for at least two components, one from reactor core internal components and the other from primary pressure boundary piping.

3. The cumulative effect of elastic strain cycling on material microstructure and the resulting effect on fracture properties of reactor structural materials need to be examined.

4. The reason for the reversed strain rate dependence (i.e., decrease in yield and flow stress with increase in strain rate) at 400°C (752°F) and its potential impact on seismic design of safety-related structures and components need to be determined.

5. The possible decrease in fracture toughness of CASS materials and austenitic SS welds thermally aged at 300 to 370°C (572 to 698°F) and tested under dynamic loading conditions at temperatures between room temperature and 100°C (212°F) needs to be investigated.

6. The potential effect of reduced fracture toughness of Alloys 600 and 690, aged CASS CF-3 and CF-8 materials, and austenitic SS welds in LWR SWC on the seismic design of reactor safety-related components needs to be determined.

ACRONYMS AND ABBREVIATIONS

AEC	Atomic Energy Commission
AMP	aging management program
Argonne	Argonne National Laboratory
ASME	American Society of Mechanical Engineers
ASTM	American Society for Testing and Materials
BPV	boiler and pressure vessel
BWR	boiling water reactor
CASS	cast austenitic stainless steels
CAV	cumulative absolute velocity
CC	concrete containment
CCW	closed cooling water
CEUS	central and eastern United States
CFR	*Code of Federal Regulations*
CGR	crack growth rate
CRD	control rod drive
CRDM	control rod drive mechanism
CT	compact tension
CUF	cumulative usage factor
CW	cold worked
DBE	design basis earthquake
DBTT	ductile-brittle transition temperature
DC	direct current
DO	dissolved oxygen
DH	dissolved hydrogen
DRS	Design Response Spectra
DSA	dynamic strain aging
DSHA	deterministic seismic hazards analysis
EAC	environmentally assisted cracking
ECP	electrochemical corrosion potential
EPR	electrochemical potentiokinetic repassivation
EPRI	Electric Power Research Institute
FAC	flow-accelerated corrosion
FCC	face-centered cubic
FSI	fluid-structure interaction

GALL	Generic Aging Lessons Learned
GDC	general design criteria
GE	General Electric
GMRS	ground motion response spectrum
GTA	gas tungsten arc
HAZ	heat-affected zone
HWC	hydrogen water chemistry
IAEA	International Atomic Energy Agency
IASCC	irradiation-assisted stress corrosion cracking
IG	intergranular
IGSCC	intergranular stress corrosion cracking
ISI	in-service inspection
JAPEIC	Japan Power Engineering and Inspection Corps
J-R	J-integral resistance
JSPS	Japan Society for Promoting Science
LRT	leak rate test
LWR	light water reactor
MC	metal containment
MIC	microbiologically induced corrosion
MMI	Modified Mercalli Intensity
Mn	manganese
Mo	molybdenum
MSC	microstructurally small crack
Nb	niobium
Ni	nickel
NPP	nuclear power plant
NRC	Nuclear Regulatory Commission
NWC	normal water chemistry
OBE	operating basis earthquake
PGA	peak ground acceleration
PLEDGE	Plant Life Extension Diagnosis by GE
PSB	persistent slip band
PSHA	probabilistic seismic hazard analysis

PWR	pressurized water reactor
PWSCC	primary water stress corrosion cracking
RCPB	reactor coolant pressure boundary
RG	regulatory guide
RIS	radiation-induced segregation
RT	room temperature
SA	submerged arc
SAW	submerged arc weld
SCC	stress corrosion cracking
SFE	stacking fault energy
SG	steam generator
SHE	standard hydrogen electrode
SMA	shielded metal arc
SMAW	shielded metal arc weld
SRB	sulfate-reducing bacteria
SRSS	square root of the sum of squares
SS	stainless steel
SSC	structure, system, and component
SSE	safe-shutdown earthquake
SSI	soil-structure interaction
SWC	shutdown water chemistry
TG	transgranular
TGSCC	transgranular stress corrosion cracking
TIG	tungsten inert gas
WUS	western United States

NOMENCLATURE

a	crack length; in some cases it represents acceleration
a_g	maximum rock acceleration
C	coefficient of the power-law J-R curve
C_V	room temperature “normalized” Charpy-impact energy, i.e., Charpy-impact energy per unit fracture area, at any given service and aging time (J/cm^2). The fracture area for a standard Charpy V-notch specimen (ASTM Specification E 23) is 0.8 cm^2. The value of impact energy in J has been divided by 0.8 to obtain “normalized” impact energy in J/cm^2.
da	increment in crack length
dJ	increment in fracture toughness J
e_f	elongation at fracture
e_u	uniform elongation
E	elastic modulus, in some cases it represent Charpy V-notch impact energy in joules
g	acceleration equal to the acceleration of gravity (980.665 cm s^{-2} or 32.2 ft/s)
f_J	J^{th} mode of frequency
f_{Jn}	J^{th} mode of frequency associated with parameter number n
J	J integral, a mathematical expression used to characterize the local stress-strain field at the crack tip region (parameter J represents the driving force for crack propagation)
J_{Ic}	value of J near the onset of crack extension
K	stress intensity factor
K_c	critical stress intensity factor
K_{IA}	critical stress intensity factor for crack arrest
K_{Ic}	critical stress intensity factor for crack extension
K_{ID}	critical stress intensity factor for crack extension under dynamic loading
K_J	J-integral critical stress intensity factor
K_{Jc}	equivalent critical stress intensity factor for crack extension
n	exponent of the power-law J-R curve, and for fatigue usage factor determination it represents number of applied fatigue cycles
N	number of fatigue cycles to failure
P	number of significant parameters considered in structural frequency broadening
R	load ratio
S	spectral acceleration
S_m	maximum value of stress intensity
T	tearing modulus or temperature
U	usage factor
ε	strain
$\dot{\varepsilon}$	strain rate or $d\varepsilon/dt$
ε_a	applied strain
ε_f	fracture strain
ε_t	total strain

ε_u	uniform strain
υ	Poisson ratio
σ	stress
$\bar{\sigma}$	Von Mises effective stress
σ_1 & σ_2	principal stresses in or parallel to the mid plane of the wall of a component
σ_3	principal stress perpendicular to the mid plane of the wall of a component
σ_a	applied stress
σ_f	flow stress, defined as the average of yield and ultimate stress
σ_u	ultimate stress
σ_y	yield stress

SI units of measurements have been used in this report. Conversion factors for measurements in British units are as follows:

To convert from	to	multiply by
in.	mm	25.4
J	Ft-lb	0.7376
kJ/m^2	in.-lb/in.^{2}	5.71015
kJ/mole	kcal/mole	0.239

ACKNOWLEDGMENTS

This work is sponsored by the Office of Nuclear Regulatory Research, U.S. Nuclear Regulatory Commission, under Job Code V6370; Program Manager, Dr. Appajosula Rao.

1 INTRODUCTION

All structures, systems, and components (SSCs) in nuclear power plants (NPPs) are subjected to aging degradation during reactor operation because of chemical and mechanical effects and interactions with the service environment, all of which are influenced by such factors as reactor coolant chemistry, material condition, temperature, neutron irradiation, and mechanical loading.[1–7] The effects of these environmental variables are typically addressed by the plant-specific design and operational technical specifications. Operational experience has shown that depending up on the operating conditions, general corrosion,[8,9] pitting,[10] microbiologically induced corrosion (MIC),[11] flow-accelerated corrosion (FAC),[12–14] and mechanical and thermal fatigue,[1,3,15] are the most commonly observed aging degradation processes for NPPs.

Furthermore, various mechanisms operate, in synergy with temperature, stress state, strain rate, and material condition, resulting in various forms of stress corrosion cracking (SCC), such as intergranular stress corrosion cracking (IGSCC), transgranular stress corrosion cracking (TGSCC), or primary water stress corrosion cracking (PWSCC) in light water reactors (LWRs). In addition, exposure to neutron irradiation for extended periods changes the microstructure (radiation hardening) and microchemistry (radiation-induced segregation, or RIS)[16–18] of reactor core support structures and internal components. Neutron irradiation results in damage at the atomistic and microstructural scales, which is manifested by an increase in the tensile strength and hardness of the material and a decrease in fracture toughness or resistance to brittle fracture,[19–32] commonly known as neutron embrittlement. Neutron irradiation also increases the susceptibility of structures and components to irradiation-assisted stress corrosion cracking (IASCC).[32–37]

In addition, time-dependent material degradation such as fatigue and SCC can lead to formation of micro- and macro-cracks, which can then slowly grow because of chemical and mechanical interactions of the material at the tip of the progressing crack. Metallurgical aspects also control the crack growth rates (CGRs) of such flaws. Dissimilar-metal welds in particular are vulnerable regions in the component because of (a) different microstructure and the redistribution of alloying and interstitial elements compared to base metal and (b) high residual stress resulting from welding. During operation, such cracks can propagate through the component wall, resulting in reactor coolant leakage. Furthermore, for core internal components, neutron irradiation enhances CGRs.

This report addresses the U.S. Nuclear Regulatory Commission's (NRC's) long-term research project related to determining the cumulative effects of repeated low-level seismic loading on progressing nuclear reactor material degradation. The proposed study considers specific aging degradation mechanisms that, from previous operating experience, have been found to be operative for structures and components important to safety and require an aging management program (AMP) to ensure structural and functional integrity. These aging degradation mechanisms include corrosion, FAC, MIC, thermal and neutron embrittlement, and crack growth rates (CGRs) for IGSCC, TGSCC, PWSCC, IASCC, and fatigue loading. The structures and components affected by these aging degradation mechanisms include Class 1 pressure boundary components and those whose functionality is safety-related.

The SSCs important to safety are designed to consensus codes and standards for NPPs such that sufficient design margin is maintained throughout the life of the plant operation to ensure that premature failure of such SSC does not result in unacceptable consequences. The SSCs important to safety are those that are necessary to ensure:

(a) the integrity of the reactor coolant pressure boundary,

(b) the capability to shut down the reactor and maintain it in a safe shutdown condition, or

(c) the capability to prevent or mitigate the consequences of accidents that could result in potential offsite exposures comparable to the guideline exposure of Title 10, Part 50, of the *Code of Federal Regulations* (10 CFR Part 50), "Domestic Licensing of Production and Utilization Facilities,"[38] Section 50.34(a)(1).

General design criteria (GDC)[39] 2, "Design Bases for Protection Against Natural Phenomena," of Appendix A,[40] to 10 CFR Part 50, "Seismic and Geological Siting Criteria for Nuclear Power Plants," requires that all SSCs important to safety be designed to withstand the effects of natural phenomena such as earthquakes, tornados, hurricanes, floods, tsunamis, and seiches without loss of capability to perform their safety function. All SSCs important to safety are designed to withstand the effects of the design basis earthquake (DBE), which is also termed as the safe-shutdown earthquake (SSE). A DBE or SSE is the largest possible earthquake at the site, considering the regional and local geology and seismology and specified characteristics of local and subsurface material. Ground shaking of a DBE might be exceeded, but the probability of this happening is considered small. A NPP is automatically shut down in the event of a SSE. The SSE represents the vibratory ground motion for which SSCs important to safety must be designed to remain functional and within applicable stress, strain, and deformation limits. The SSC design takes into account historical experiences of ground motion at the site and SSE and ensures that in the event of an occurrence of an earthquake of concern, the safety systems will function and the plant will shut down in an orderly manner so that no radionuclides are released to harm the public and the environment.

An operating basis earthquake (OBE) is the largest earthquake that reasonably could be expected to affect the plant site during the operating life of the plant. Its magnitude is typically a third or half of the SSE. All NPPs are designed to withstand the OBE and still operate without undue risk to the health of the public. Nuclear reactors are to be shut down in an event of an earthquake if (a) the site vibratory ground motion exceeds that of an OBE ground motion or (b) there is significant damage. For continued operation, or prior to resuming operation, it is required to determine whether structural and functional damage has occurred to SSCs that are designed in accordance to the American Society of Mechanical Engineers (ASME) Section III Division 1 Code. Examples of such components include tanks, vessels, pumps, valves, piping systems, and their supports.

Furthermore, various NPP structures and components vibrate at different frequencies during a seismic event. Vibrations in the range of 1–10 Hz are of particular concern, because they correspond to damaging response frequencies for most structures and components. Earthquakes below 15 Hz predominate in the western United States (WUS). All NPPs in the WUS are designed to withstand low frequencies. Although NPPs in central and eastern United States (CEUS) are also designed to withstand low frequencies, the typical earthquakes in CEUS are associated with higher frequencies. Higher frequencies are less damaging to large structures, but may adversely affect small components.

For concrete and other building structures, the concept of "cumulative absolute velocity" (CAV) exists as an index for the onset of structural damage from cumulative effects of ground acceleration.[41,42] However, it is not clear if and how such a concept is applicable to reactor coolant pressure boundary (RCPB) components with ongoing degradation. For example, in the NRC Generic Aging Lessons Learned (GALL) report,[2] it is required that the effects of concrete degradation be considered after an earthquake event. However, no such consideration is required for metallic materials degradation in the GALL report.

In the GALL report, the "Detection of Aging Effects" program element of AMP XI S4, 10 CFR Part 50, Appendix J,[43] states that a containment LRT (leak rate test) program is effective in detecting leakage rates of the containment pressure boundary components, including seals and gaskets. While the calculation of leakage rates and satisfactory performance of containment leakage rate testing demonstrates the leak tightness and structural integrity of the containment, it does not by itself provide information that would indicate that aging degradation has begun or that the capacity of the containment may have been reduced for other types of loads, such as seismic loading. This would be achieved with the additional implementation of an acceptable containment in-service inspection program as described in ASME Boiler and Pressure Vessel (BPV) Code, Section XI,[44] Subsections IWE (AMP XI.S1) and IWL (AMP XI.S2).[2] Similar management programs, including any associated inspection requirements, regarding material degradation due to seismic loading effects on the metallic pressure boundary components, have currently not been proposed. All operating nuclear power reactors in the United States are listed in Table 1. The locations of these plants and a few others that have been shut down are shown in Fig. 1.

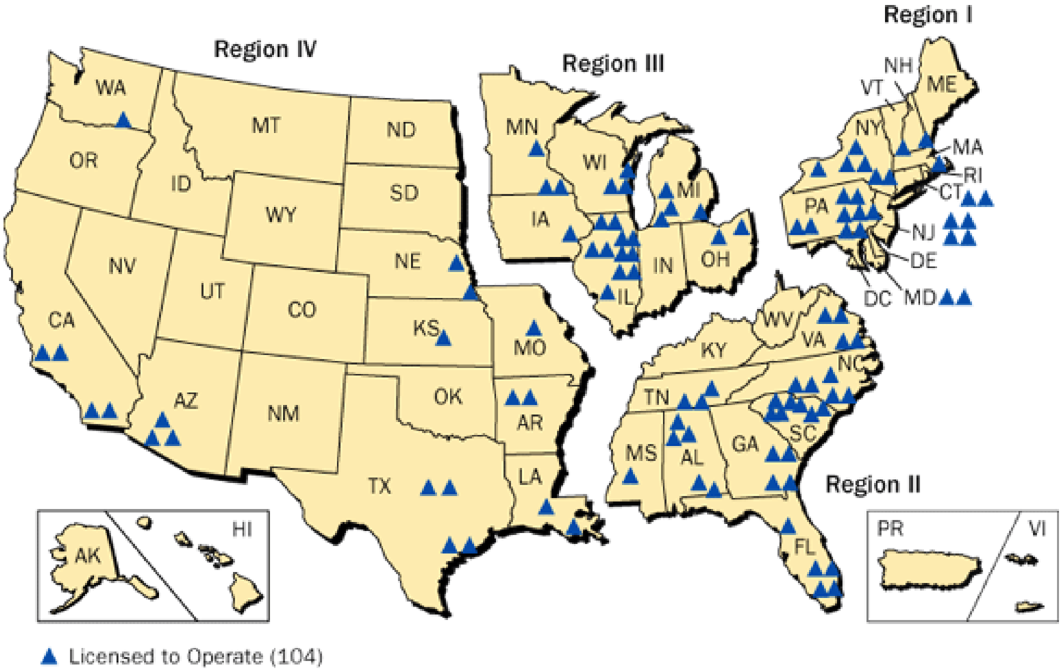

Figure 1. Location of nuclear power reactors in the United States of America. Only 99 plants of these are operating at present.

A number of studies have been conducted recently to better understand the structural response of NPPs to the presence of cracks in piping components, both analytically[45,46] and experimentally. Many of these studies use seismic hazard analysis in evaluating failure response to SSE conditions, based on the frequency and the size of seismic load using the original material properties, though at the elevated operating temperatures. The results of the component and system testing as well as specimen fatigue ratchet tests by GE in 1994[47]

Table 1. List of operating nuclear power reactors in the United States and their type, vendor, location, and date of license.

Unit	Type	MW	Vendor	State	License
Arkansas Nuclear 1	PWR	843	B&WLL	AK	1974
Arkansas Nuclear 2	PWR	995	CE	AK	1974
Beaver Valley 1	PWR	892	W3L	PA	1976
Beaver Valley 2	PWR	846	W3L	PA	1987
Braidwood 1	PWR	1178	W4L	IL	1987
Braidwood 2	PWR	1152	W4L	IL	1988
Browns Ferry 1	BWR	1065	GET4	AL	1973
Browns Ferry 2	BWR	1104	GET4	AL	1974
Browns Ferry 3	BWR	1115	GET4	AL	1976
Brunswick 1	BWR	938	GET4	NC	1976
Brunswick 2	BWR	937	GET4	NC	1974
Byron 1	PWR	1164	W4L	IL	1985
Byron 2	PWR	1136	W4L	IL	1987
Callaway 1	PWR	1236	W4L	MO	1984
Calvert Cliffs 1	PWR	873	CE	MD	1974
Calvert Cliffs 2	PWR	862	CE	MD	1976
Catawba 1	PWR	1129	W4L	SC	1985
Catawba 2	PWR	1129	W4L	SC	1986
Clinton 1	BWR	1065	GET6	IL	1987
Columbia Gen. Station	BWR	1190	GET5	WA	1984
Comanche Peak 1	PWR	1200	W4L	TX	1990
Comanche Peak 2	PWR	1150	W4L	TX	1993
Cooper Station	BWR	830	GET4	NE	1974
Davis-Besse	PWR	893	B&WRL	OH	1977
Diablo Canyon 1	PWR	1151	W4L	CA	1984
Diablo Canyon 2	PWR	1149	W4L	CA	1985
Donald C. Cook 1	PWR	1009	W4L	MI	1974
Donald C. Cook 2	PWR	1060	W4L	MI	1977
Millstone 3	PWR	1227	W4L	CT	1986
Monticello	BWR	579	GET3	MN	1970
Nine Mile Point 1	BWR	621	GET2	NY	1974
Nine Mile Point 2	BWR	1140	GET5	NY	1987
North Anna 1	PWR	981	W3L	VA	1978
North Anna 2	PWR	973	W3L	VA	1980
Oconee 1	PWR	846	B&WLL	SC	1973
Oconee 2	PWR	846	B&WLL	SC	1973
Oconee 3	PWR	846	B&WLL	SC	1974
Oyster Creek	BWR	619	GET2	NJ	1991
Palisades	PWR	778	CE	MI	1971
Palo Verde 1	PWR	1335	CES80	AZ	1985
Palo Verde 2	PWR	1335	CES80	AZ	1986
Palo Verde 3	PWR	1335	CES80	AZ	1987
Peach Bottom 2	BWR	1112	GET4	PA	1973
Peach Bottom 3	BWR	1112	GET4	PA	1974
Perry 1	BWR	1261	GET6	OH	1986
Pilgrim 1	BWR	685	GET3	MA	1972
Point Beach 1	PWR	512	W2L	WI	1970
Point Beach 2	PWR	514	W2L	WI	1973
Prairie Island 1	PWR	551	W2L	MN	1974
Prairie Island 2	PWR	551	W2L	MN	1974
Quad Cities 1	BWR	867	GET3	IL	1972
Quad Cities 2	BWR	869	GET3	IL	1972
R. E. Ginna	PWR	498	W2L	NY	1969
River Bend 1	BWR	989	GET6	LA	1985
Salem 1	PWR	1174	W4L	NJ	1976
Salem 2	PWR	1130	W4L	NJ	1981

Table 1. (Contd.)

Unit	Type	MW	Vendor	State	License	Unit	Type	MW	Vendor	State	License
Dresden 2	BWR	867	GET3	IL	1991	Seabrook 1	PWR	1295	W4L	NH	1990
Dresden 3	BWR	867	GET3	IL	1971	Sequoyah 1	PWR	1148	W4L	TN	1980
Duane Arnold	BWR	640	GET4	IA	1974	Sequoyah 2	PWR	1126	W4L	TN	1981
Fermi 2	BWR	1122	GET4	MI	1985	Shearon Harris 1	PWR	900	W3L	NC	1986
Fitzpatrick	BWR	852	GET4	NY	1974	South Texas 1	PWR	1410	W4L	TX	1988
Fort Calhoun	PWR	500	CE	NE	1973	South Texas 2	PWR	1410	W4L	TX	1989
Grand Gulf 1	BWR	1297	GET4	MS	1984	St. Lucie 1	PWR	839	CE	FL	1976
Hatch 1	BWR	876	GET4	GA	1974	St. Lucie 2	PWR	839	CE	FL	1983
Hatch 2	BWR	883	GET4	GA	1978	Surry 1	PWR	799	W3L	VA	1972
Robinson 2	PWR	710	W3L	SC	1970	Surry 2	PWR	799	W3L	VA	1973
Hope Creek 1	BWR	1061	GET4	NJ	1986	Susquehanna 1	BWR	1149	GET4	PA	1982
Indian Point 2	PWR	1023	W4L	NY	1973	Susquehanna 2	BWR	1140	GET4	PA	1984
Indian Point 3	PWR	1025	W4L	NY	1975	Three Mile Island 1	PWR	786	B&WLL	PA	1974
Joseph M. Farley 1	PWR	851	W3L	AL	1977	Turkey Point 3	PWR	720	W3L	FL	1972
Joseph M. Farley 1	PWR	860	W3L	AL	1981	Turkey Point 4	PWR	720	W3L	FL	1973
LaSalle County 1	BWR	1118	GET5	IL	1982	VC Summer	PWR	966	W3L	SC	1982
LaSalle County 2	BWR	1120	GET5	IL	1983	Vogtle 1	PWR	1109	W4L	GA	1987
Limerick 1	BWR	1134	GET4	PA	1985	Vogtle 2	PWR	1127	W4L	GA	1989
Limerick 2	BWR	1134	GET4	PA	1989	Waterford 3	PWR	1250	CE	LA	1985
McGuire 1	PWR	1100	W4L	NC	1981	Watts Bar 1	PWR	1123	W4L	TN	1996
McGuire 2	PWR	1100	W4L	NC	1983	Wolf Creek 1	PWR	1166	W4L	KS	1985
Millstone 2	PWR	884	CE	CT	1975						

Notes: No commercial NPPs operate in Alaska or Hawaii. B&WLL: Babcock and Wilcox 2-Loop Lower; B&WRL: Babcock and Wilcox 2-Loop Raised; CE: Combustion Engineering; CE80: Combustion Engineering System 80; W2L: Westinghouse 2-Loop; W3L: Westinghouse 3-Loop; W4L: Westinghouse 4-Loop; GET2: General Electric Type 2; GET3: General Electric Type 3; GET4: General Electric Type 4; GET5: General Electric Type 5; GET6: General Electric Type 6.

indicated high structural margins in NPP piping under dynamic loading conditions. In general, the tests showed (a) local yielding in the piping system, (b) redistribution of stresses, and (c) negligible change in the stiffness of the system (hence the natural frequency). The failure mode of the piping was always fatigue, ratcheting, or a combination of the two, and not plastic collapse.

In a more recent study,[48] well-defined cracks of various morphologies and depths were introduced into both experimental coupons and component mockup assemblies, which were then subjected to loads on a shaking table to simulate earthquake loading. The piping component tests included static and dynamic cycling tests of pressurized elbows, tees, nozzles, and reducers. The tests were carried out at high-strain amplitudes, and the results illustrated the accumulation of ratcheting strain.[*] The specimens were cycled until a through-wall crack occurred. The simplified (small) piping system tests were designed to excite the systems to seismic levels well above the typical design earthquake levels in order to induce an elasto-plastic response in the system's components. The results have shown that the cracked components were able to sustain such loading and that premature failure did not occur. The results thus provided added confidence that the component design margin is adequate to prevent catastrophic failure during a simulated SSE loading.

Shao et al.[49] have also documented a study of dynamic response due to seismic loading of degraded NPP structures and components, but not the RCPB material and components. They observed that the degraded structures or components could be more vulnerable to seismic loads because aging or degradation may affect dynamic properties, structural response, resistance or capacity, failure modes, and locations of failure initiation.

This NRC-sponsored research also examined the concept of "cracked-pipe element" as a "degraded condition" and performed simple and component tests of girth welds. [50] These tests were conducted at room temperature, and the results showed that the pipe test failures were due to low-cycle fatigue with small-scale yielding, and that there were large margins on the acceleration needed to cause failure in a single large seismic event compared to the input acceleration in the tests. Based on extrapolated results to full-scale behavior, the authors concluded that a large margin exists for the acceleration to cause failure relative to the typical design peak ground acceleration (PGA) values for U.S. plants.

The PGA values for operating NPPs in the United States are listed in Table 2. The four plants on the West Coast are listed separately at the end of the table. PGA is a measure that has been widely used in developing NPP "fragility estimates." It represents the sensitivity of NPP structures and components to the inertial effects of acceleration during a seismic event. Two PGA values are listed in the table, namely, the value used in the original design and the updated value proposed by the NRC for each NPP in response to the earthquake that occurred near the North Anna NPP on August 23, 2011. The updated PGA value was to be used for the revalidation of the seismic analysis for all operating plants and for the seismic design of new reactors. For some plants, the original analysis was considered overly conservative, and therefore, the proposed PGA value was lower than the original. The August 23 earthquake caused the plant to automatically shut down and resulted in loss of offsite power. This event was followed by a 4.5 magnitude aftershock on August 25. The plant experienced several other aftershocks for several weeks after the main event.

---

[*] Ratcheting represents elastic shakedown behavior in which plastic deformation takes place such that the steady-state is perfectly elastic even though the deformation is due to material strain hardening. It is an open elastic-plastic hysteresis loop in which the material accumulates a net strain during each cycle.

Table 2. PGA values for U.S. NPPs.

NPP Facility	SSE PGA (g units)		NPP Facility	SSE PGA (g units)	
	Original	Updated		Original	Updated
Arkansas Nuclear One (ANO) 1/2	0.200	0.0240	Millstone 2/3	0.170	0.190
Beaver Valley 1/2	0.150	0.167	Monticello 1	0.120	0.153
Belefonte 1/2	0.180	0.344	Nine Mile Point 1/2	0.150	0.200
Braidwood 1/2	0.200	0.208	North Anna 1/2	0.120	0.570
Browns Ferry 1/2/3	0.180	0.378	Oconee 1/2/3	0.100	0.400
Brunswick 1/2	0.160	0.194	Oyster Creek 1	0.180	0.174
Byron 1/2	0.200	0.270	Palo Verde 1/2/3	0.250	0.214
Callaway 1	0.200	0.500	Palisades 1	0.200	0.283
Calvert Cliffs 1/2	0.150	0.112	Peach Bottom 2/3	0.120	0.400
Catawba 1/2	0.150	0.330	Perry 1	0.150	0.188
Clinton 1	0.260	0.260	Pilgrim 1	0.150	0.500
Columbia 1	0.250	0.395	Point Beach 1/2	0.120	0.140
Comanche Peak 1/2	0.120	0.058	Prairie Island 1/2	0.120	0.060
Cooper 1	0.200	0.137	Quad Cities 1/2	0.240	0.160
Davis-Besse 1	0.150	0.167	River Bend 1	0.100	0.105
DC Cook 1/2	0.200	0.137	H B Robinson 2	0.200	0.470
Diablo Canyon 1/2	0.750	0.812	St Lucie 1/2	0.100	0.056
Dresden 2/3	0.200	0.246	Salem 1/2	0.200	0.150
Duane Arnold 1	0.120	0.088	San Onofre 2/3	0.670	a
Joseph M Farley 1/2	0.100	0.068	Seabrook 1	0.250	0.500
Fermi 2	0.150	0.180	Sequoyah 1/2	0.180	0.380
James A FitzPatrick 1	0.150	0.120	South Texas 1/2	0.100	0.056
Fort Calhoun 1	0.170	0.204	Surry 1/2	0.150	0.110
R E Ginna 1	0.150	0.122	Susquehanna 1/2	0.100	0.130
Grand Gulf 1	0.150	0.093	Three Mile Island 1	0.120	0.227
Shearon Harris 1	0.150	0.110	Turkey Point 3/4	0.150	0.040
Edwin I Hatch 1/2	0.150	0.142	Virgil C Summer 1	0.150	0.368
Hope Creek 1	0.200	0.170	Vermont Yankee 1	0.120	0.570
Indian Point 2/3	0.150	0.412	Vogtle 1/2	0.100	0.400
LaSalle County1/2	0.200	0.317	Waterford 3	0.180	0.174
Limerick 1/2	0.150	0.193	Watts Bar 1/2	0.200	0.283
William B MgGuire 1/2	0.150	0.305	Wolf Creek 1	0.120	0.400

[a] Plant has been shut down.

Structural damage to NPPs occurs when the cumulative effects of ground acceleration (i.e., seismically induced vibrations) exceed a certain threshold. The Electric Power Research Institute (EPRI), in 1988, developed the concept of CAV as an index for indicating the onset of structural damage due to the cumulative effect of ground acceleration.[41] The NRC Regulatory Guide (RG) 1.208 states that the threshold between damaging and nondamaging earthquakes (for buildings of good design and construction) conservatively occurs at ground motions with CAVs greater than 0.16 g-seconds.[51]

Fatigue is another major form of degradation that has been considered in design codes. In general, the design transients considered in the fatigue analysis of the RCPB components include, among others, heat-up, cooldown, pressurizer heat-up and cooldown (for pressurized water reactors [PWRs]), reactor trip, turbine trip, leak test, hydrostatic test, and seismic load. The plant start-up and shutdown conditions are considered to impose the major cyclic loads of concern. The seismic loading considered in the fatigue analysis includes one SSE and 5 to 20 OBEs with 10 to 20 cycles per event, depending on the location. Paragraph IV(a)(2)(i) of Appendix S to 10 CFR Part 50 requires that the value of the OBE ground motion must be set to one of the following choices:

(A) One-third or less of the SSE ground motion design response spectra, and the requirements associated with the OBE ground motion in 10 CFR Part 50, Appendix S, Paragraph IV(a)(2)(i)(B)(I), can be satisfied without performing explicit response or design analyses; or

(B) A value greater than one-third of the SSE ground motion design response spectra and analysis and design must be performed to demonstrate that the requirements associated with the OBE ground motion in 10 CFR Part 50, Appendix S, Paragraph IV(a)(2)(i)(B)(I), are satisfied. The design must consider soil-structure interaction effects and the duration of vibratory ground motion.

Paragraph IV(a)(2)(i)(B)(I) of Appendix S[52] to 10 CFR Part 50 states that when subjected to the effects of OBE ground motion in combination with normal operating loads, all SSCs necessary for continued operation without undue risk to the health and safety of the public must remain functional and within applicable stress, strain, and deformation limits. In addition, Paragraph IV(a)(3) of Appendix S to 10 CFR Part 50 requires that if vibratory ground motion exceeds the OBE ground motion or if significant plant damage occurs, the NPP must shut down.

In all fatigue design analyses, any seismic events less than the OBE are not considered in the analysis. The fatigue damage from all transients above OBE, also known as design transients, is evaluated for the period of reactor operation to determine a characteristic derived property known as the cumulative usage factor (CUF).[45] Therefore, this report is focused only on the potential effects of repeated, below-OBE loadings.

The information generated thus far for modeling has generally used the original and as-fabricated material properties and has not considered the potential effects of both the degradation on material properties and the repeated and cumulative effects of repeated below-OBE loadings. The earthquake loading studies conducted thus far have not considered the effects of seismic loading on progressing material degradation with respect to the potential enhancement of such degradation under repeated seismic loading, particularly for below-OBE loading.

Repeated and sudden below-OBE loadings may impose sudden high-strain-rate deformation on reactor materials. The stress-strain behavior under short-term, high-strain-rate loading may be quite different than that under normal loading conditions. Furthermore, it has been postulated[53] that to understand the seismic effects on fatigue better, fatigue tests may need to be performed both under load- and displacement-controlled modes. Since the current ASME Code fatigue design curves for NPP structural materials are based on fatigue data obtained from completely reversed, strain-controlled fatigue tests, the design curves may not be appropriate for high-strain-rate seismic loading.

The objective of this study is to evaluate the potential cumulative effects of repeated and sudden below-OBE loading on progressing degradation of NPP structural materials. The program will address knowledge gaps in a fundamental manner, considering the mechanical response (stress-strain behavior) of degraded material to establish basic properties of degraded materials under various stages of degradation and determine whether such below-OBE events that occur repeatedly during plant operation could adversely affect ongoing material and component degradation and become a safety concern.

A literature review of both domestic and international sources of technical information of generic nature has been conducted to review and evaluate the effects of repeated and sudden below-OBE loading on specific degradation mechanisms. The review considers possible scenarios in which seismic shock loading (severe or lower level/more frequent) could accelerate degradation in passive component materials of construction, thereby reducing the available margin and useful life of RCPB and safety-related components.

This scoping study is expected to provide reactor material degradation fundamental insights, information addressing potential technical issues, and information gaps to support anticipated future NRC needs. The aging degradation mechanisms included in this study are general and pitting corrosion; FAC; MIC; IGSCC; TGSCC; PWSCC; IASCC; thermal and neutron embrittlement; and fatigue crack initiation and growth. The structures and components affected by these aging degradation mechanisms include Class 1 pressure boundary components and those whose functionality is safety-related. Concrete structures, other NPP structures and components of such structures, or spent nuclear fuel pools and structures within the cooling pool, cable, and storage casks are not within the scope of this study.

2 BACKGROUND INFORMATION

GDC 1, “Quality Standards and Records,” in Appendix A, “General Design Criteria of Nuclear Power Plants,”[40] to 10 CFR Part 50, “Domestic Licensing of Production and Utilization Facilities,” requires, in part, that SSCs important to safety be designed, fabricated, erected, and tested to quality standards commensurate with the importance of the safety functions to be performed. Where recognized codes and standards are used, Criterion 1 requires that they be identified and evaluated to determine their applicability, adequacy, and sufficiency and be supplemented or modified as necessary to ensure a quality product in keeping with the required function.

In addition, Criterion 30, “Quality of Reactor Coolant pressure Boundary,” of Appendix A to 10 CFR Part 50 requires, in part, that components that are part of the RCPB be designed, fabricated, erected, and tested to the highest practical standards. Appendix B, “Quality Assurance Criteria for Nuclear Power Plants and Fuel Processing Plants,”[54] to 10 CFR Part 50 requires, in part, that measures be established for the control of special processing of materials and that proper testing be performed. Provisions of ASME BPV Code have been used since 1971 as part of the framework to establish the necessary design, fabrication, construction, testing, and performance requirements for SSCs important to safety. Among other things, ASME standards committees develop improved methods for the construction and in-service inspection (ISI) of ASME Class 1, 2, 3, MC (metal containment), and CC (concrete containment) NPP components.

The regulation in 10 CFR 50.55a, “Codes and Standards,” Subsection 50.55a(c), “Reactor Pressure Boundary,”[55] requires, in part, that components of the RCPB must be designed, fabricated, erected, and tested in accordance with the standards for Class 1 components of Section III, “Rules for Construction of Nuclear Power Plant Components,” of the BPV Code[56] or equivalent quality standards. The regulations in 10 CFR 50.55a(d), “Quality Group B components,” and 50.55a(e), “Quality Group C components,” require that the components classified Quality Group B and C must meet the requirements for Class 2 and 3, respectively, in Section III of ASME BPV Code.[57] The NRC RG 1.26[58] establishes an acceptable method for complying with the applicable 10 CFR Part 50 requirements by classifying fluid systems and components important to safety and applying corresponding quality codes and standards to such systems and components.

The ASME Section III, Division 1 Class 1 components of LWRs are part of the RCPB. Class 2 components are part of the various important-to-safety systems such as emergency core cooling, and Class 3 components are part of the various systems needed for plant operation. These Class 1, 2, and 3 components are designated in RG 1.26 as Quality Groups A, B, and C, respectively. Application of 10 CFR 50.55a and GDC 1 provides assurance that established standard practices of proven or demonstrated effectiveness are used to achieve a high likelihood that these safety functions will be performed and that the codes and standards applied are commensurate with the importance to the safety of these functions.

Nuclear power plant ASME Code Class 1 and 2 components are designed by either ASME Section III, Division 1 “Design by Analysis” (NB-3200 and NC-3200, respectively) or “Design by Rule” (NB-3600 and NC-3600, respectively) to ensure structural integrity of the safety-related RCPB components and core support structures and core internals. ASME Code Class CS (core support structures) components are designed in accordance with Section III Subarticle NG-3200.

ASME publishes a new edition of the BPV Code, which includes Section III, every three years and new addenda every year. ASME BPV Code is incorporated by reference into 10 CFR 50.55a. The latest editions and addenda of Section III that the NRC has approved for use are referred to in 10 CFR 50.55a(a)(1)(i). ASME Code Cases provide alternatives to existing Code requirements that the ASME has developed and approved. The new Code Cases and revisions are incorporated by reference into 10 CFR 50.55a. All Code Cases that have been approved by the NRC are listed in RG 1.84,[59] "Design, Fabrication, and Materials Code Cases Acceptability, ASME Section III." These Code Cases may be used voluntarily by licensees as an alternative to compliance with ASME Code provisions. It is the responsibility of the user to make certain that the provisions of the Code Case do not conflict with licensee commitments or regulatory requirements. Code Cases that the NRC has determined to be unacceptable are listed in NRC RG 1.193.[60] A Code Case may be annulled because (a) its provisions have been incorporated into the Code, (b) the application for which it was developed no longer exists, or (c) experience has shown that the design analysis or construction method is no longer adequate.

2.1 Seismic Design Considerations

2.1.1 Service Conditions

The various components and support structures of a nuclear power system are subjected to plant and system operating and test conditions that are required to be considered in the design basis of the components to satisfy the applicable systems safety criteria. The pressures, temperatures, and mechanical loads to which reactor components and support structures are subjected as a result of plant or system operating or test conditions are referred to as component and support structure design, service, and test loadings. These loadings are established from the anticipated or postulated plant or system operating and test conditions during the intended service life of the component and support structure. The ASME Code defines four levels of service conditions (A, B, C, and D) for various load combinations and stress limits.

- Level A service conditions (normal conditions) include operating pressure during system start-up, normal operation, hot standby, shutdown, and weight loads.

- Level B service conditions (upset conditions, incidents of moderate frequency) consist of fluid transients (e.g., water hammer or relief valve discharge) and OBE seismic loads.

- Level C service conditions (emergency conditions, infrequent conditions, low probability) are those that may necessitate the removal of the components from service for inspection or repair for damages. Therefore, they require reactor shutdown for corrective action and repair of damages.

- Level D service conditions (faulted conditions, extremely low probability of postulated events) permit gross general deformations with some consequent loss of dimensional stability and damages requiring repair, which may require removal of the component. An example of level D loading is a combination of loss of coolant accident and SSE.

Examples of reversing and nonreversing dynamic loads are shown in Fig. 2. Reversing dynamic loads are loads that cycle about a mean value and include building filtered and earthquake loads. Nonreversing dynamic loads are loads that do not cycle about a mean value and include the inertial thrust force due to sudden opening or closing of valves and water

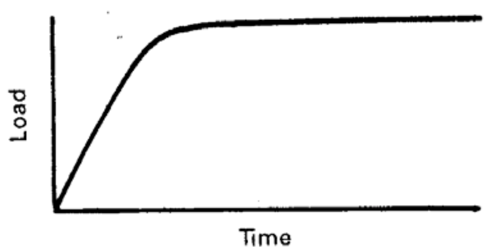

(a) Nonreversing dynamic load (relief/safety valve open-end discharge).

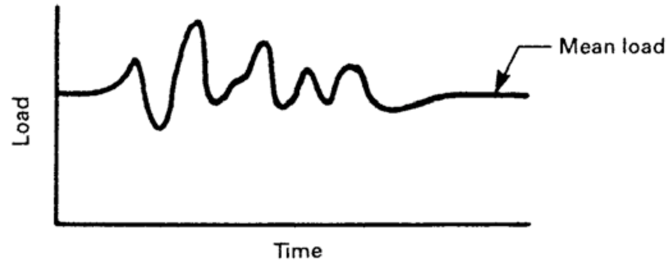

(b) Reversing dynamic load (earthquake load cycling about normal operating conditions).

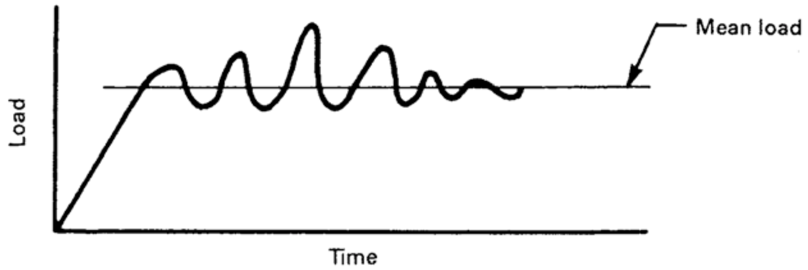

(c) Nonreversing dynamic load (initial water slug followed by reflected waves).

Figure 2. Examples of reversing and nonreversing dynamic loads (ASME Section III, Division 1, Subsection NB-3200, Figure NB-3213-1).

hammer resulting from entrapped water in two-phase flow systems. Reflected waves in a piping system due to flow transients are classified as nonreversing dynamic loads.

The stress levels in the components are calculated for various load combinations from applied internal pressure, dead weight, thermal expansion, earthquake loading, pipe rupture, and plant operational thermal and pressure transients. The basis for the classification of the various stresses is as follows:

(a) Primary stresses are caused by primary loads, and the primary stress limits are intended to prevent plastic deformation.

(b) Secondary stresses are caused by secondary loads, and the primary plus secondary stress limits are intended to prevent excessive plastic deformation leading to incremental collapse.[**]

[**] In limit analysis, collapse load is the maximum load or combinations of loads that a structure made of ideally plastic (non-strain-hardened) material can carry. In such cases, the deformations increase without bound at this load.

(c) Peak stresses are the highest stresses in a local region and are the source for causing fatigue failure. The peak stress limit is intended to prevent failure due to cyclic loading.

In addition, when assurance of operability is required, the following design, service, and test limits are also defined for specific components and support structures:

- Level A service limits must be satisfied for all level A service loadings to which the component or support structure may be subjected in performance of its specific function (ASME Section III, Division 1 NB/NG-3222).

- Level B service limits must be satisfied for all level B service loadings for which these service limits have been designated, and the component or support structure must withstand these loadings without damage requiring repair (ASME Section III, Division 1 NB/NG-3223).

- Level C service limits must be satisfied for all level C service loadings for which these service limits have been designated. These limits permit large deformations in areas of large discontinuity that may necessitate the removal of the component or support structure from service for inspection or repair of damage (ASME Section III, Division 1 NB/NG-3224).

- Level D service limits must be satisfied for all level D service loadings for which these limits have been designated. These limits permit gross general deformations with some consequent loss of dimensional stability and damage requiring repair that may require removal of the component from service (ASME Section III, Division 1 NB/NG-3225).

- Alternating service limits are also defined, which may be more restrictive service limits than defined in the component design specification. Components and support structures may be designed using these more restrictive service limits.

If these service stress limits are too restrictive, ASME Section III, Division 1 NB-3228, provides guidance for using plastic analyses, which allow some relaxation of the basic stress limits (ASME Section III, Division 1 NB/NG-3228). The applied loads are classified as follows:

(a) Primary loads (sustained loads), which include loads caused by internal pressure, dead weight, and the like, and failure due to these loads results in catastrophic failure; and

(b) Secondary loads (expansion loads), which are caused by displacements that arise from thermal expansion, hot- and cold-piping-fluid cyclic loads, seismic anchor movements, and building settlement.

In addition, “alternating stress” is defined as one-half of the calculated peak stress. In fatigue analyses, fatigue failure can be prevented by ensuring that the number of load cycles associated with a specific alternating stress is less than the number of load cycles allowed in the design fatigue curve (S-N curve).

2.1.2 Seismic Design

The seismic design of commercial NPPs has evolved significantly since the 1960s.[61] The initial design of NPPs was based on static analysis in which the seismic loads were applied laterally with an acceleration of 0.05g, 0.10g, and 0.20g in low-, moderate-, and high-seismic-intensity areas, respectively. However, the analytical procedures used to develop the forces and moment, and resultant seismic loadings in structures and components were controlled by computational limitations. In addition, the acceptance criteria were typically limited to one-third increase in normal allowable stresses when seismic stresses were combined with normal dead and live load stresses. The normal allowable stresses were between 0.6 and 0.67 times the specified minimum yield stress.

In 1963, the concepts of dynamic response spectra analysis were introduced in seismic design of NPP structures and components with the publication of the U.S. Atomic Energy Commission report TID-7024.[62] Initially, these concepts were limited to building structures but, by 1971, were gradually extended to include the load definition for mechanical and electrical distribution systems and components. A response spectrum is a plot of the maximum acceleration, velocity, or displacement of a family of oscillations associated with the ground or structures. Each earthquake produces its own unique spectrum of ground motions, which vary in frequency and acceleration and may last several seconds or longer. The record of ground motion recorded on an accelerograph appears as a jagged line that represents the peak values of acceleration/deceleration (Fig. 3). The ground motion response spectrum (GMRS) represents the range of multiple earthquake records shown in Fig. 4; it appears as an irregular graph of peaks and valleys that combines a number of individual response spectra from past earthquakes.[63]

The seismic spectra important to NPP design have PGAs in the range of 5 to 10 Hz. The NRC has developed Design Response Spectra (DRS) statistically from response spectra of past strong-motion earthquakes. In 1973, the former Atomic Energy Commission (AEC), the NRC's predecessor, published RG 1.60, "DRS for Seismic Design of Nuclear Power Plants,"[64] to provide spectral shapes for horizontal and vertical ground movements. It was based on a mean-plus-one standard design basis response based on a normal probability density function, as shown in the horizontal design response spectra in NRC RG 1.60. Furthermore, floor or in-structure response spectra also began to be used in design of structures and components located at other than the free-field surface ground levels of buildings.

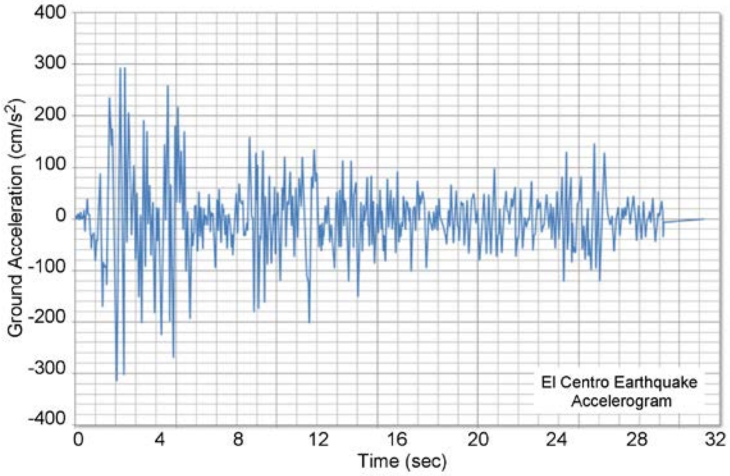

Figure 3. Ground acceleration record of the Imperial Valley Aftershock May 19, 1940, at El Centro, CA.

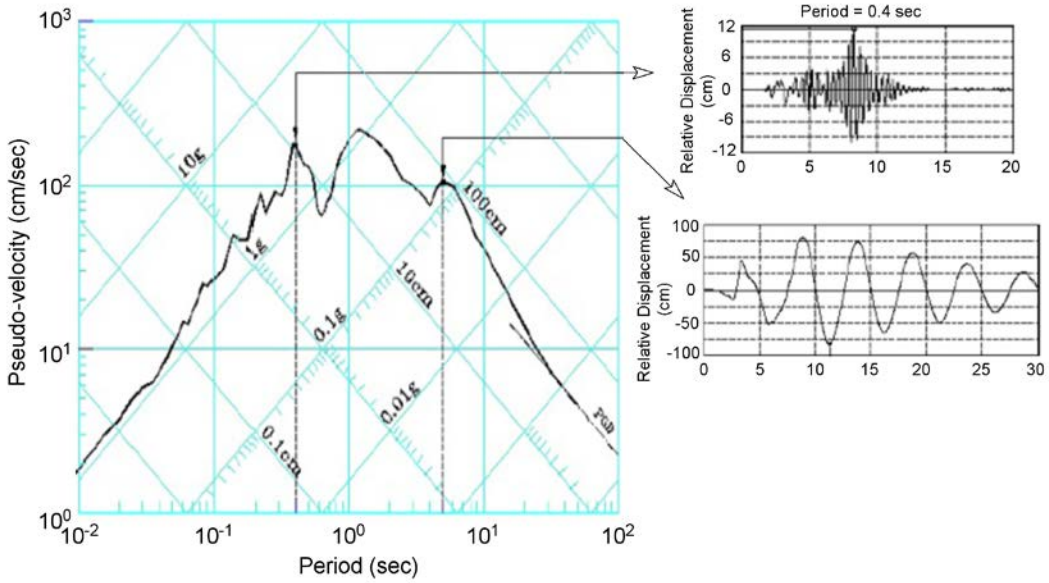

Figure 4. Site-specific ground motion response spectrum (Ref. 63).

In general, designs of NPPs during the 1960s and 1970s used a deterministic approach to seismic design based on site-specific examinations of local and regional seismic, geological, and geotechnical soil conditions to determine the maximum credible earthquake. Deterministic seismic hazard analyses (DSHAs) quantified the effects of a maximum credible earthquake based on known seismic sources sufficiently near the site as well as available historical seismic and geological data to estimate ground motion at the NPP site. Appendix A to 10 CFR Part 100 requires an evaluation of fault and earthquake occurrences to provide the basis for determining an SSE.[40] It describes the limitations for basing seismic design criteria on literature reviews of geographical and geological information and requires supplementing the assessment with studies for vibratory ground motion, evidence of surface faulting, and evidence of seismically induced floods and water waves that could affect the site.

In 10 CFR Part 100, Appendix A, SSE is defined by response spectra corresponding to the maximum vibratory accelerations as outlined in paragraph (a) of Section VI; and where the maximum vibratory accelerations of the SSE at the foundations of the NPP structures are determined to be less than one-tenth the acceleration of gravity (0.1g). The maximum vibratory accelerations of the SSE at these foundations are assumed at least 0.1g.

After 2000, there were attempts to standardize the design of NPPs to include a standardized reactor coolant system as well as balance of plant. This resulted in the development of standardized ground response spectra and floor or in-structure response spectra used in the present day seismic analyses. In the design of new NPPs, the SSE is established on the basis of Probabilistic Seismic Hazard Analysis (PSHA) performed in accordance with 10 CFR 100.23, “Geologic and Seismic Siting Criteria.” Whereas DSHA-based PGA values on a single earthquake source, PSHA utilized recent information on earthquake sources and occurrences and ground motion estimates to establish the probability of exceeding various levels of earthquake-induced ground motion at a specific location during a specific period in the future. The PSHA quantifies the seismic hazard characteristics of a site from seismic hazard curves or “response spectra” developed in part by identifying and characterizing each seismic source in terms of maximum magnitude, magnitude recurrence relationship, and source geometry.

Furthermore, as more data became available on actual recorded earthquake activities, a better understanding developed regarding the shape of the design basis ground response spectra recorded at various sites around the world. For example, data recorded at sites with relatively high seismic activity (e.g., California, Japan, Chile) with a significant amount of faulting and other geographical characteristics indicated that the peak response spectra occurred between 2.5 and 9 Hz. However, earthquake motion recorded at sites with moderate or low seismic activity show that the free-field ground acceleration response spectra peak occurred at much higher frequencies (10–25 Hz). As a result, the standard plant free field ground response spectra have tended to have higher acceleration spectrum amplitudes than the spectra used in the past, particularly on rock sites. In addition, the acceptance criteria have also been updated.

A seismic hazard map of the United States showing 2% probability of exceedance of the design basis PGA in 50 years is presented in Fig. 5. Documented earthquake activity in the United States since 1568 is shown in Fig. 6. Seismic risk is determined from an assessment of historical earthquake activity and a seismic hazard map of a specific region showing the likely PGA values to be experienced during an earthquake with a probability of exceedance.

However, on April 2015, the U.S. Geological Survey released a map of earthquakes thought to be triggered by human activity in the eastern and central United States. All of the areas with increased seismic activity are located near deep fluid injection wells or other industrial activities capable of inducing earthquakes. Oklahoma by far is the worst hit state, it had more earthquakes of magnitude 3 or higher compared to California. Similar increases have been observed in Texas near Dallas-Fort Worth. Earthquakes have been more frequent since 2013 also in Kansa, Colorado, New Mexico, and Ohio. These earthquakes have been occurring at a higher rate than ever before.

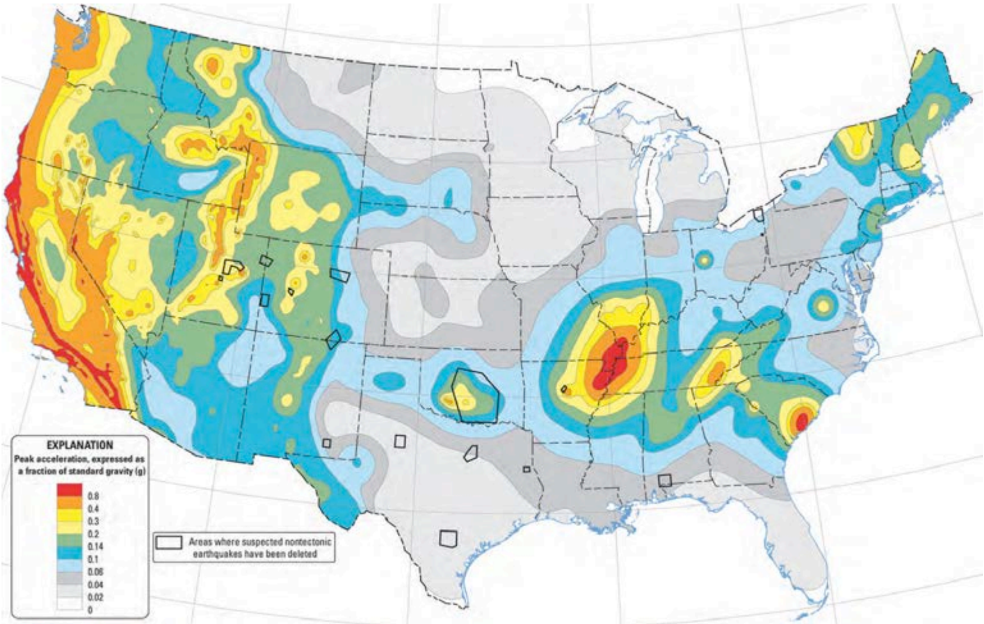

Figure 5. **A seismic hazard map for 2% probability of exceeding design-limit PGA in 50 years.**

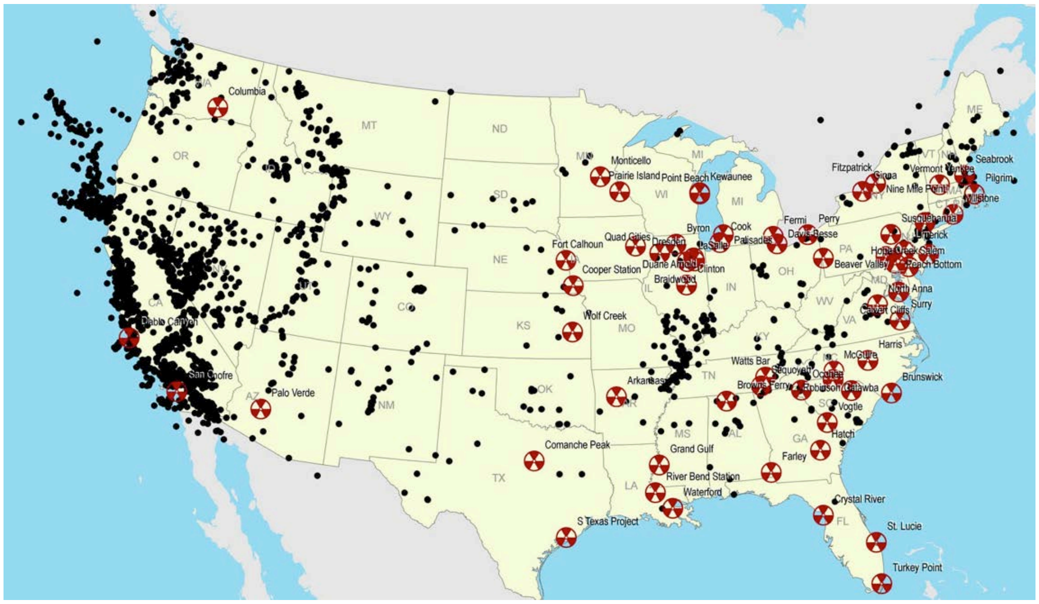

Figure 6. Documented earthquake activity in the United States since 1568.

In general, the seismic design of civil, mechanical, electrical, instrumentation, and control structures and components of NPPs involves three activities:

1. Quantification of seismic load and other concurrent applicable loads and specification of their load combinations;

2. Analysis methods and procedures necessary to convert input earthquake motions normally expressed in the form of acceleration to resultant seismic forces, moments, or stresses in structures and components; and

3. Codes and standards acceptance criteria used to determine the adequacy of the analysis performed in No. 2.

The first and third activities are defined by applicable national codes, standards, and regulatory requirements. The second activity depends on the experience and training of the engineers performing the analysis and their understanding of the analytical techniques.

ASME BPV Code Section III does not require dynamic analysis. The design of NPP structures and components, however, requires consideration of seismic and other dynamic inputs defined in their design specifications. The guidance for seismic analysis of NPP safety-related piping systems are given in ASME Code Non-mandatory Appendices N, “Dynamic Analysis Methods,” and F, “Rules for Evaluation of Service Loading with Level D Service Limits.” The earthquake engineering criteria for NPP construction permits, operating licenses, design certifications, combined licenses, design approvals, or manufacturing licenses are given in Appendix S to 10 CFR Part 50. Special guidance documents such as RG 1.29, “Seismic Design Classification,”[65] RG 1.61, “Damping Values for Seismic Design of Nuclear Power Plants,”[66] and RG 1.92, “Combining Modal Responses and Spatial Components in Seismic Response Analysis,”[67] specify requirements for equipment classification and procedures for combination of loads and describing new analytical techniques.

Component design may be based on the use of static forces resulting from equivalent earthquake acceleration acting at the center of gravity of the extended masses, or a dynamic system analysis may be used to show how seismic loading is transmitted from the defined ground motions to all parts of the buildings and SSCs. Subarticles N-1100 and N-1200 of Non-mandatory Appendix N[68] Article N-1000, “Dynamic Analysis Methods,” describe one or more acceptable steps for seismic analysis. However, because the seismic dynamic analysis involves a series of steps, and some of the steps have acceptable alternative methods, these are not the only acceptable methods. Subarticles N-1300 through N-1700 describe areas of dynamic analysis that are used in the design of NPP components, such as flow-induced vibration and dynamics of coupled fluid-shells.

2.1.3 Selection of Seismic Loads

All NPPs are designed so that earthquakes and other external events will not jeopardize the safety of the plant, particularly the safe shutdown of the reactor. The selection of the intensities of the OBE and DBE (or SSE) depends on the region of the country where the site is located, its geological conditions, and previous seismic experience and records. The information developed from studies of strong-motion earthquakes can be used to obtain estimates of the structural response of NPP components supported by the ground. However, such information is not available for most of the NPP sites. Seismic design of NPP structures and components requires reasonably good estimates for the motion history of the maximum ground acceleration, the maximum ground velocity, and the maximum ground displacement. Furthermore, a high factor of safety may be required for Class 1 components of NPPs, where damage might involve exposure of large numbers of people to excessive radiation hazard.[69]

The methods currently used for the design of NPP structures and components under postulated and anticipated loads during reactor service include techniques for calculating the structural or mechanical response of the structures and components either in terms of a well-defined time history of motion or some probability intensity associated with a general pattern of motion. Unfortunately, the same degree of certainty in the design calculations for earthquake loadings is possible in only a few areas of the world where observations of strong-motion earthquake intensities have been recorded over long periods.[69] The basis and methodology for establishing seismic loads on a structure or component are summarized below.[70]

The seismic loads on a structure are generated by the deformation of the structure as it vibrates, which is different from the gravitational loads and, in most cases, even wind loads. Therefore, the seismic load is part of the dynamics of the structure and is governed by Newton’s second law ($F = ma$). Whereas, the gravitational and effective wind loads are governed by Newton’s third law (action-reaction). The seismic load is the inertial force on the structure and can be expressed in terms of the acceleration of the structure. However, its magnitude and distribution on the structure continually change with time, t, during the vibration created by the seismic event. The first step in seismic design of structures is to determine the maximum seismic force and its distribution on the structure during the seismic event. Particular attention is paid to the use of equivalent static procedures that attempt to capture the principal effects of the essentially dynamic state.

The seismic force depends on the distribution of mass and stiffness throughout the structure. Therefore, the distribution of mass and stiffness of the structure and the manner in which plasticity spreads through the structure are the two key factors critical in determining the maximum magnitude and the distribution of seismic force in the structure. These two factors must be considered in any approach that attempts to quantify the seismic force. The dynamic factor must capture the facts that the seismic force represents an amplification of the vibration of the ground due to resonance effects of the structure and that the maximum amplification depends on the free vibration period of the structure. For an elastic structure, the free vibration period, T, is proportional to √(M/K), where M is the mass and K is the elastic stiffness of the structure. Therefore, for a structure with a uniform or regular mass, the dynamics factor and hence the seismic force depend on the mass and elastic stiffness of the structure.

A response spectrum is simply a plot of the peak or steady-state response, such as displacement, velocity, or acceleration of a series of vibrations of varying natural period (or natural frequency), that are forced into motion by the same base vibration or shock. The resulting plot is used to establish the response of any linear system, given its natural period of vibration. For example, the *acceleration response spectrum*, a graph of the maximum acceleration as a function of the free vibration or natural period, is typically used in assessing the peak response of buildings to earthquakes. The ground response spectrum calculated from recordings of surface ground motion are typically used for correlation with seismic damage.

Figure 7 shows a typical acceleration response spectrum of the averaged and smoothed maximum acceleration of elastic structures founded on rock due to an earthquake; the maximum amplification of the rock acceleration is 2.5. The plot indicates that structures with a small period (i.e., high stiffness or shorter structures) experience higher magnification of the ground acceleration; after the plateau the magnification rapidly decreases for structures with a longer natural period of vibration (i.e. more flexible or taller structures). However, structures are not typically founded on rock; there is soil between the structure and the rock where the earthquake originated. Structures located some distance from the epicenter of the earthquake experience additional acceleration due to the resonance of the soil. However, recent experience indicates that this soil resonance effect was significant for not only structures with higher range of natural period, as initially believed, but it also occurs in the short period range, particularly on soft sites.

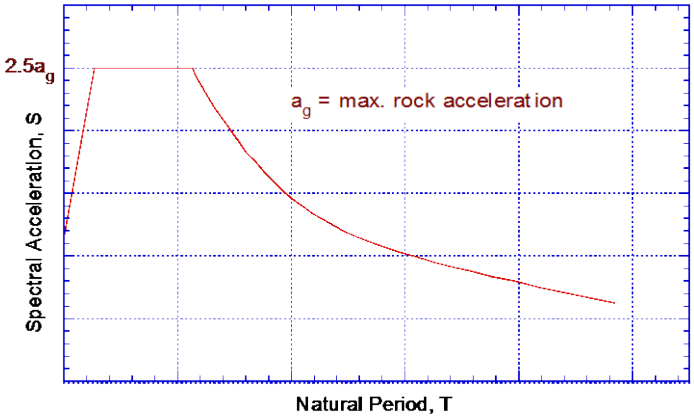

Figure 7. Acceleration response spectrum of elastic structures founded on rock.

2.1.4 Soil Structure Interaction

The maximum vibratory accelerations of the SSE must take into account the characteristics of the underlying soil material in transmitting the earthquake-induced motions at the various locations of the plant's foundation. Depending on the elevation above the foundation, various NPP structures and components vibrate at different frequencies during a seismic event. Vibrations in the range of 1–10 Hz are particularly of concern, because they correspond to damaging resonance frequencies for most structures and components. These accelerations and the corresponding shaking frequencies are parameters that are considered in PSHA, as discussed further in Subsection 2.3.3. The complete seismic spectrum may be characterized by two intervals: PGA and spectral acceleration, averaged between 5 and 10 Hz.

Earthquakes with frequencies below 15 Hz predominate in the WUS. As discussed before, earthquakes below the 10-Hz frequency range pose the greatest hazard; in the WUS, earthquake magnitude is a primary design consideration for NPPs. In CEUS, since recording of seismic events are sparse, NPP designs consider both earthquake magnitude and Modified Mercalli Intensity (MMI). The effect of an earthquake on the earth’s surface is called the intensity. Various intensity scales have been developed during the past several hundred years; the MMI scale is currently used in the United States. The scale, designated by Roman numerals, comprises increasing levels of intensity ranging from imperceptible shaking (designated by number I) to catastrophic destruction (designated by number X). Although NPPs in the CEUS are designed to withstand low-frequency earthquakes, the typical earthquakes in the CEUS are associated with higher frequencies than in the WUS. Higher frequencies are less damaging to large structures but may adversely affect small components.

The response of a structure to earthquake shaking is affected by interactions between three linked systems: the structure, the foundation, and the soil underlying and surrounding the foundation. However, in most analytical methods, the foundation is considered part of the structure. Therefore, the term soil-structure interaction (SSI) is used to describe this effect. The SSI analysis evaluates the collective response of these systems to a specific free-field ground motion. The term “free field” refers to motions not affected by structural vibrations or the scattering of waves at and around the foundation. SSI effects are absent for the theoretical condition of a rigid foundation supported on rigid soil. The SSI effects are categorized as inertial interaction effects, kinematic interaction effects, and soil-foundation flexibility effects.[71] In seismic design analyses, these effects are related to the following:

- *Foundation stiffness and damping*: In a vibrating structure, inertia gives rise to base sheer, moment, and torsion forces, all of which generate displacements and rotations at the soil–foundation interface. These displacements and rotations are possible because of flexibility in the soil–foundation system, and it significantly increases the overall structural flexibility. In addition, these displacements result in energy dissipation due to radiation damping and hysteretic soil damping. These effects are referred to as inertial interaction effects because they are caused by structural inertia.

- *Variation between foundation input motions and free-field ground motions*: The free-field motions and foundation input motions are different for two reasons. First, for stiff foundation elements placed at or below the ground surface, kinematic interactions cause the foundation motions to deviate from the free-field motions because of base slab averaging, wave scattering, and embedment effects, in the absence of both structure and foundation inertia. Second are the relative displacements and rotations between the foundation and free field associated with both structure and foundation inertia.

- *Foundation deformation*: The forces and displacements imposed by the superstructure and the soil medium lead to flexural, axial, and shear deformation of structural foundation elements. These deformations could be significant, particularly for flexible foundations such as rafts and piles. Therefore, foundation components must be designed to account for deformations.

Two methods, a direct analysis and a substructure approach, are used to evaluate the SSI effects. In a direct analysis, the soil and structure are included within the same model and analyzed as a complete system. However, although direct analyses can address all the SSI effects, incorporation of kinematic interaction is challenging. In addition, because direct solution of the SSI problem is difficult from a computational perspective, particularly for a system that is geometrically complex or contains significant nonlinearities on the soil or structural materials, it is rarely used in practice.

In a substructure approach, the SSI analysis is separated into distinct parts that are combined to obtain the complete solution. A proper consideration of SSI effects requires the following:

- An evaluation of free-field soil motions and corresponding soil material properties;
- An evaluation of transfer functions to convert free-field motions to foundation input motions;
- Incorporation of springs and dashpots (or more complex nonlinear elements) to represent the stiffness and damping of the soil–foundation interface; and
- A response analysis of the combined structure-spring/dashpot system with the foundation input motion applied.

2.1.5 Damping Values for Seismic Design

Damping is a measure of the energy dissipation of a material or structural system as it responds to dynamic excitation. The term “damping” is used to assist in mathematical modeling and in solving dynamic equations of motion for a vibratory system in which energy is dissipated. In addition to the energy lost between the structure and its supports on the ground, there are energy losses within the structure itself and at the points of attachment of equipment and components to the structure. One of the ways for damping due to energy losses within a structure, is due to the spread of plasticity or inelasticity throughout the structure.

Structures are typically designed to withstand considerably smaller horizontal forces than those calculated from available earthquake motions that have been recorded. Yet the NPP structures and components do not show any evidence of degradation or damage that one would expect if the design forces reached the levels computed from seismic analysis.[72] For example, the El Centro or Imperial Valley earthquake measuring 7.0 M_W (moment magnitude scale)[***] in the southwest corner of Southern California on May 18, 1940, represented a maximum ground motion acceleration of 0.32g and a maximum ground velocity of 0.36 m/s (14 in./s). The El Centro earthquake ground motion acceleration record is shown in Fig. 3. The horizontal force coefficient for structures with natural periods of 0.5 s was of the order of 0.6 times the weight, even for critical damping values as high as 10%. Yet structures designed for maximum ground motion acceleration of 0.1g performed well under the El Centro earthquake.

Veletsos and Newmark[72] demonstrated that inelastic behavior can effectively reduce the horizontal force coefficient that may be used in seismic design to values of the order of one-fourth or less than those that would be applicable for elastic systems. They recognized that although other factors such as ground coupling also modify the input motion of a specific structure, the process of inelastic energy absorption is a major consideration in seismic design

---

[***] This is equivalent to 6.4 M_L Richter scale.

procedures. Veletsos and Newmark proposed a "ductility factor," defined as the ratio of the maximum deformation and yield point deformation. They concluded that for most materials, including steel and reinforced concrete, plastic deformation on the order of three times the elastic deformation (i.e., corresponding to a ductility factor of 4) does not involve any significant distortions or damage. However, a design based on a ductility factor of 4 would permit the structure to behave elastically or nearly elastically for most earthquakes except those as intense as the SSE. The maximum accelerations in the elasto-plastic systems, and consequently the design load factors of such systems, can be expressed in terms of the corresponding quantities for elastic systems multiplied by a reduction factor related to the degree of plastic deformation, which is permissible.[72]

In an elastic dynamic seismic analysis, the energy that is dissipated is accounted for by specifying the amount of viscous damping (i.e., damping force proportional to the velocity) in the analytical model. The amount of damping in the structural elements and components depends on (a) the intensity of motion, (b) the associated stress levels, and (c) the geometry and energy absorption mechanism within the structural element or component.

The guidance in NRC RG 1.61, "Damping Values for Seismic Design of Nuclear Power Plants,"[73] provides acceptable damping values to be used in the elastic seismic response analysis and design of seismic Category I NPP structures and components in which energy dissipation is approximated by viscous damping unless otherwise specified. Regulatory positions 1 through 5 of Section C of the RG provide the updated damping values for structures; piping; electrical distribution system; heating, ventilation, and air conditioning duct; and mechanical and electrical components, respectively. Damping values higher than those provided in RG 1.61 may be used if documented test data support the higher values. Damping values associated with SSI analysis are not within the scope of RG 1.61.

As noted in regulatory position 1.2 of RG 1.61, "The SSE damping values specified in Table 3 for linear dynamic analysis of structures have been selected based on the examination that the structural response attributed to load combinations that include the SSE will be close to applicable code stress limits, as defined in NUREG-0800[74] Section 3.8." However, there may be cases in which the predicted structural response to load combinations that include the SSE is significantly below the applicable code stress level. Although this is not a concern for structural evaluation, for in-structure response spectra, it is necessary to use the damping-compatible structural response. Consequently, the following additional guidance is provided for analyses used to determine in-structure response spectra:

1. Use of the OBE damping values specified in Table 3, which are acceptable to the staff without further review.

2. Submit a plant-specific technical basis for use of damping values higher than the OBE damping values specified in Table 3, but not greater than the SSE damping values specified in Table 4, subject to staff review on a case-by-case basis.

Table 3. Operating basis earthquake damping values.

Structural Material	Damping (% of Critical Damping)
Reinforced concrete	4
Reinforced masonry	4
Prestressed concrete	3
Welded steel or bolted steel with friction connections	3
Bolted steel with bearing connections	5

Table 4. Safe-shutdown earthquake damping values.

Structural Material	Damping (% of Critical Damping)
Reinforced concrete	7
Reinforced masonry	7
Prestressed concrete	5
Welded steel or bolted steel with friction connections	4
Bolted steel with bearing connections	7

Note: For steel structures with a combination of different connection types, use the lowest specified damping value, or alternatively use a "weighted average" damping value based on the number of each type present in the structure.

2.1.6 Design Response Spectra

The NRC staff has used the 1973 edition (i.e., Rev. 1) of RG 1.60, "DRS for Seismic Design of Nuclear Power Plants,"[64] for numerous siting and licensing activities, and it forms part of the licensing basis for NPPs constructed during the 1970s and 1980s. However, in 1997, the role of PSHA led to the establishment of new requirements for the siting regulation in 10 CFR 100.23, "Geology and Seismic Siting Criteria." The new siting regulation applies to new reactors as well as NPP construction permit or operating licenses on or after January 10, 1997. The new siting requires, in part, the explicit consideration of the uncertainties associated with geological and seismological characteristics through an appropriate analysis, such as PSHA. The role of PSHA also led to the development initially of NRC RG 1.65,[75] which was subsequently replaced in 2007 with NRC RG 1.208, "A Performance-Based Approach to Define the Site-Specific Earthquake Ground Motion."[51] RG 1.208 provides general guidance on methods acceptable to the NRC staff for the following:

1. Conducting geological, geophysical, seismological, and geotechnical investigations;

2. Identifying and characterizing seismic sources;

3. Conducting a PSHA;

4. Determining seismic wave transmission (soil amplification) characteristics of soil and rock sites; and

5. Determining a site-specific, performance-based GMRS satisfying the requirements of paragraphs (c), (d)(1), and (d)(2) of 10 CFR 100.23 and leading to the establishment of a SSE to satisfy the design requirements of Appendix S to 10 CFR Part 50.

According to Appendix S to 10 CFR Part 50, the foundation-level ground motion must be represented by an appropriate response spectrum with a peak ground acceleration of at least 0.1g. The steps necessary to develop the final SSE are described in Chapter 3, "Design of Structures, Components, Equipment, and Systems," of NUREG-0800, and Regulatory Position 5.4 of NRC RG 1.208 provides a detailed description of the development of the final SSE. Although NRC RG 1.60 is no longer used to characterize the hazard for the seismic design of NPPs, the certified seismic design response spectra for several new reactor designs have been derived from RG 1.60 spectra with modified control points to broaden the spectra in the higher frequency range. The RG 1.60 spectral values are based on deterministic values for WUS earthquakes. However, recent observations have shown that higher frequency motions at the CEUS rock sites may be significantly greater than motions recorded at the WUS rock sites.

The recorded ground accelerations and response spectra of past earthquakes provide a basis for the design of structures to resist earthquakes. The response spectra developed for a site are known as the DRS, and are developed statistically from response spectra of past strong-motion earthquakes.[76–79] This procedure was considered acceptable by the NRC staff for defining the DRS on sites underlain by either rock or soil deposits and covering all frequencies of interest. However, for unusually soft sites, modification to this procedure will be required.

The horizontal- and vertical-component DRS that correspond to a maximum horizontal ground acceleration of 1.0g, are shown in Figs. 8 and 9, respectively. For sites with different acceleration values specified for the design earthquake, these DRS without SSI effects should be linearly scaled proportional to the specified maximum horizontal ground acceleration. However, the procedure described above will not apply for sites that (a) are relatively close to the epicenter of an expected earthquake or (b) have physical characteristics that could significantly affect the spectral pattern of input motion, such as being underlain by poor soil deposits. In these cases, the DRS should be developed individually according to the site characteristics.

In Fig. 8, the base diagram consists of three parts: the bottom line on the left part represents the maximum ground displacement; the bottom line on the right part represents the maximum acceleration; and the middle part depends on the maximum velocity. The numerical values of design displacements, velocities, and accelerations for the horizontal component DRS are obtained by multiplying the corresponding values of the maximum ground displacement and acceleration by the factors given in Table 5.

Construction of the spectral shapes in Fig. 9 follow the instructions in Refs. 74 and 75 for the construction of vertical component spectra. Note that the vertical DRS values are two-thirds those of the horizontal DRS for frequencies less than 0.25; for frequencies higher than 3.5, they are the same, while the ratio varies between two-thirds and 1 for frequencies between 0.25 and 3.5. The numerical values of design displacements, velocities, and accelerations in these spectra are obtained by multiplying the corresponding values of the maximum horizontal ground motion (acceleration = 1.0g and displacement = 0.914 m [36 in.]) by the factors in Table 6.

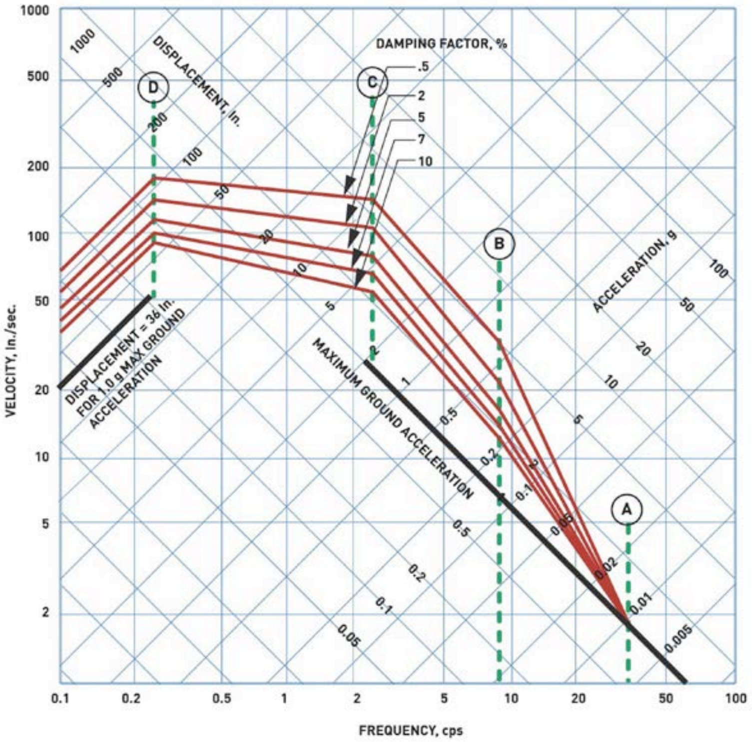

Figure 8. Horizontal design response spectra scaled to 1g horizontal ground acceleration (NRC RG-1.60 Figure 1).

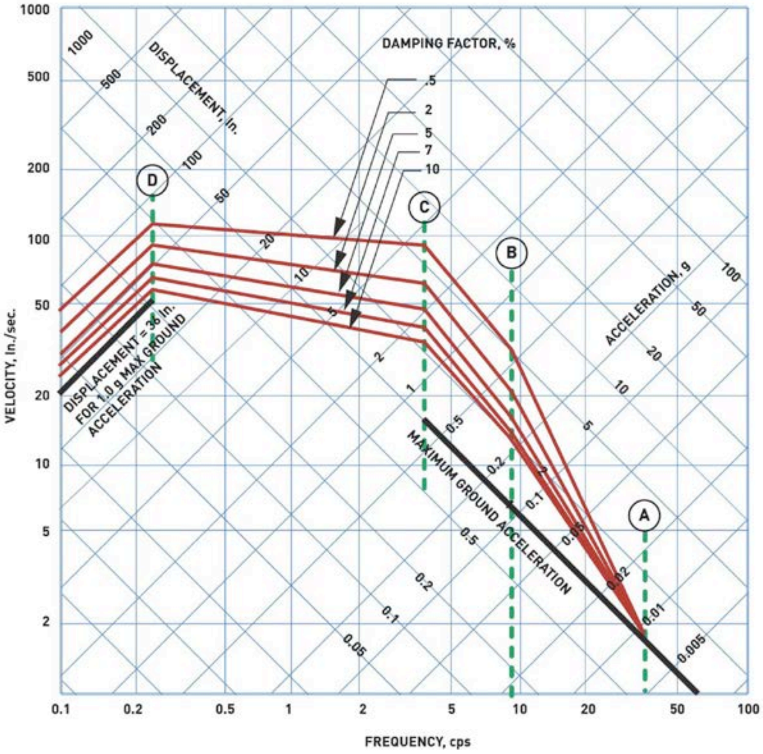

Figure 9. Vertical design response spectra scaled to 1g horizontal ground acceleration (NRC RG-1.60 Figure 2).

Table 5. Horizontal design response spectra: relative values of spectrum amplification factors for control points (NRC RG 1.60 Table 1).

Percent of Critical Damping	Amplification Factors for Control Points			
	Acceleration[a,b]			Displacement[a,b]
	A (22 cps)	B (9 cps)	C (3.5 cps)	D (0.25 cps)
0.5	1.0	4.96	5.95	3.20
2.0	1.0	3.54	4.25	2.50
5.0	1.0	2.61	3.13	2.05
7.0	1.0	2.27	2.72	1.88
10.0	1.0	1.90	2.28	1.70

[a] Maximum ground displacement is taken proportional to maximum ground acceleration and is 0.914 m (36 in.) for ground acceleration of 1.0 gravity.

[b] Acceleration and displacement amplification factor are taken from recommendations given in Ref. 76.

Table 6. Vertical design response spectra: relative values of spectrum amplification factors for control points (NRC RG 1.60, Table 2).

Percent of Critical Damping	Amplification Factors for Control Points			
	Acceleration[a,b]			Displacement[a,b]
	A (22 cps)	B (9 cps)	C (3.5 cps)	D (0.25 cps)
0.5	1.0	4.96	5.67[c]	2.13
2.0	1.0	3.54	4.05	1.67
5.0	1.0	2.61	2.98	1.37
7.0	1.0	2.27	2.59	1.25
10.0	1.0	1.90	2.17	1.13

[a] Maximum ground displacement is taken proportional to maximum ground acceleration and is 0.914 m (36 in.) for ground acceleration of 1.0 gravity.

[b] Acceleration amplification factors for the vertical design response spectra are equal to those for horizontal design response spectra at a given frequency, whereas displacement amplification factors are 2/3 those for horizontal design response spectra. These ratios, between the amplification factors for the two design response spectra are in agreement with those recommended in Ref. 76.

[c] These values were changed to make this table consistent with the discussions of vertical components in the discussion section of NRC RG 1.60, Rev. 2.

An example of horizontal SSE response spectra with 5% critical damping is shown in Fig. 10. It is anchored in the high frequency range at a specific value of acceleration; in this case, 0.28g. The response spectrum is scaled up or down (or remain unchanged) depending on the PGA of the actual NPP site. The PGA values at various NPP sites in the United States are listed in Table 2.

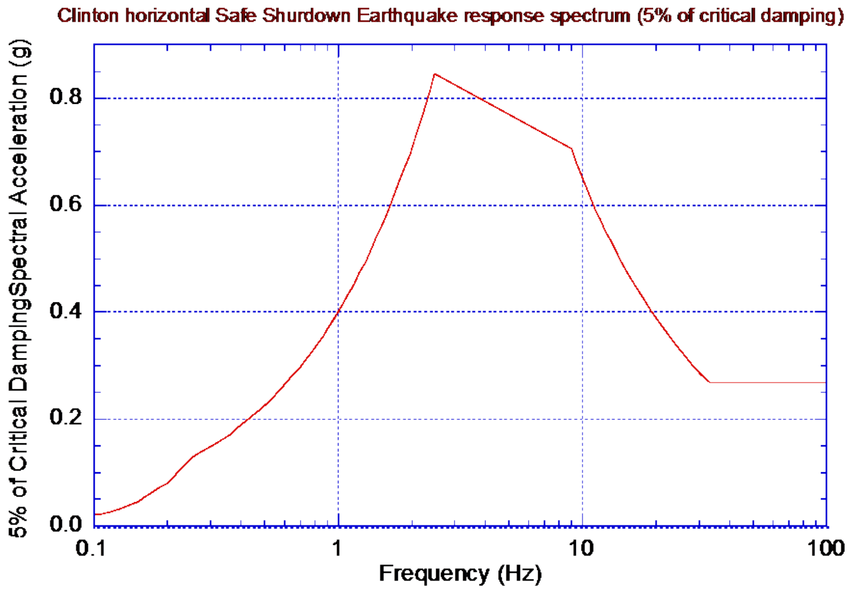

Figure 10. **Horizontal SSE response spectrum with 5% critical damping.**

Establishing the seismic loads for RCPB components and reactor core support structures and core internals typically involves the following steps:

1. Develop the SSE response spectra that define the PGA and an acceleration response spectrum that is representative of the specific site.

2. Generate two horizontal and one vertical ground acceleration time histories. A single set of three mutually orthogonal, statistically independent, synthetic acceleration time histories is used as the input in the dynamic analysis of seismic Category I structures. The synthetic time histories are generated by modifying a set of actual recorded earthquake time histories and the following NRC guidelines:
   - The response spectra of the time histories must envelop the design response spectra.
   - The time histories must last at least 20 seconds.
   - The time histories must contain at least 6 seconds of strong motion.

3. Develop acceleration time histories and in-structure response spectra (also called floor response spectra) at various locations (such as supports of piping, reactor vessel) of the reactor building, incorporating a SSI analysis.

The third step provides seismic loads in the form of in-structure response spectra or time-histories for RCPB components and reactor core internals or any other components within the reactor building. A time-history analysis is required if the system has small clearances (gaps) between the components (e.g., reactor internals).

An example of design horizontal time histories, H2 acceleration, velocity, and displacement is shown in Fig. 11. Design horizontal time history, H1, is applied in the north south (global X or 1) direction; design horizontal time history, H2, is applied in the east-west (global Y or 2) direction; and design vertical time history is applied in the vertical (global Z or 3) direction.

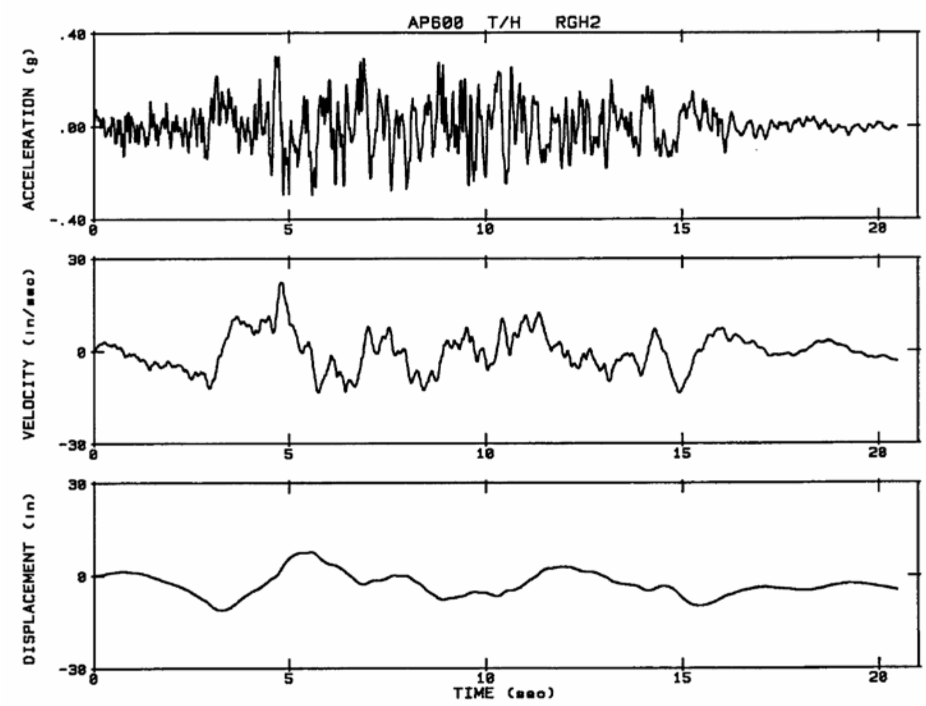

Figure 11. **An example of design horizontal time histories for H2 acceleration, velocity, and displacement.**

2.1.7 In-Structure Response Spectra

NRC RG 1.122, "Development of Floor DRS for Seismic Design of Floor-Supported Equipment or Components,"[80] describes methods that are acceptable to NRC staff for developing the two horizontal and one vertical in-structure response spectra (e.g., floor response spectra) from the time history motions resulting from the dynamic analysis of the supporting structure. Because a large number of degrees of freedom would be necessary if the complete plant was treated in a single mathematical model, the plant is usually divided into several separate systems. Thus, usually there are one or more mathematical models of supporting structures. Each supporting structure normally supports one or more systems or pieces of equipment. Because most equipment that has a small mass relative to the supporting structure, it would also have negligible interaction effects on the support structure. Therefore, such equipment needs to be included only in the mass distribution of the mathematical model for that structure. However, for other major equipment systems such as the reactor coolant system, its stiffness, mass, and resulting frequency range should be included in the model for the supporting structure to account for potential dynamic interaction effects.

The two horizontal and the vertical in-structure response spectra can be calculated from the time history motions of the supporting structure at the various floors or other equipment-support locations of interest. It is important that the spectrum ordinates are calculated at the natural frequencies of the supporting structure and at frequencies sufficiently close to produce accurate response spectra.

In seismic analyses performed separately for each of the three directions, the ordinates of the floor design response spectrum for a given direction, at the location of interest, are obtained by combining the ordinates of the three floor response spectra for that direction, according to the SRSS criterion. The same procedure is used for seismic analysis for un-symmetric structures.

The resulting response spectrum is smoothed with peaks broadened. In the case of symmetric structures, the floor design response spectrum for a given direction will be the smoothed floor response spectrum for that direction.

In addition, uncertainties in the structural frequencies can arise because of uncertainties in parameters such as the material properties of the structure and soil, damping values, soil-structure interaction techniques, and the approximations in the modeling techniques used in seismic analysis. To account for these uncertainties, the computed floor response spectra from the floor time history motions is smoothed, and peaks associated with each of the structural frequencies are broadened (see Fig. 12) by a frequency, Δf_J, expressed as

$$\Delta f_J = \left[\left(0.05 f_J\right)^2 + \sum_{n=1}^{P} \left(\Delta f_{Jn}\right)^2 \right]^{1/2} \quad \text{(not less than } 0.1f_J\text{),} \qquad (1)$$

where Δf_{Jn} denotes the variation in the J-th mode frequency, f_J, due to variation in parameter number n, and P is the number of significant parameters considered. A value of $0.1f_J$ is used if the actual computed value of Δf_J is less than $0.1f_J$. If the above procedure is not used, Δf_J is taken as $0.1f_J$.

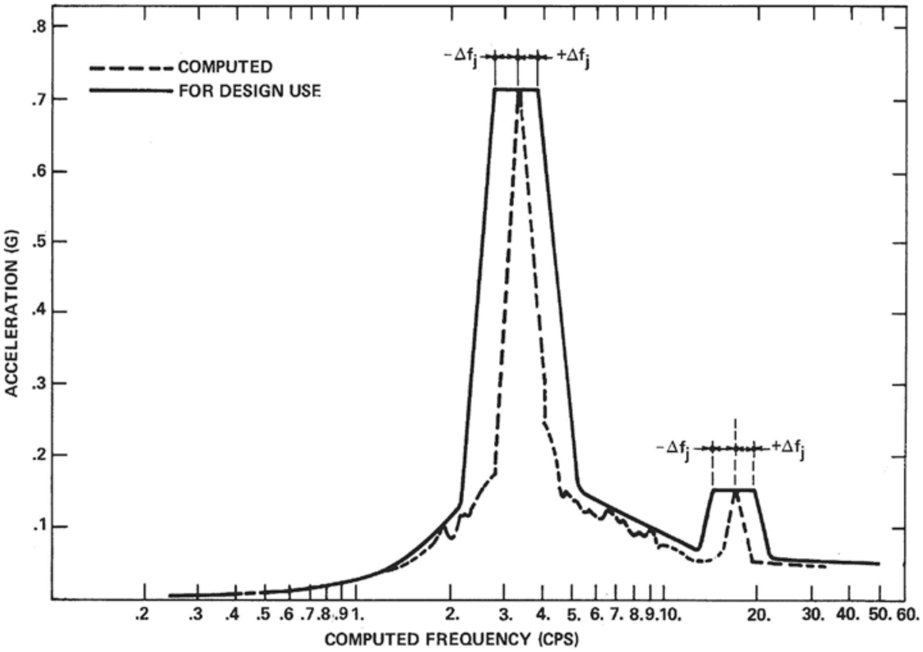

Figure 12. **Vertical design response spectra scaled to 1g horizontal ground acceleration.**

When the mathematical model of the supporting structure is subjected simultaneously to the action of three spatial components of an earthquake, the calculated response spectrum in a given direction with peaks broadened and smoothed is considered the floor design response spectrum in that direction.

2.1.8 Seismic Design and Qualification

The information needed for a seismic design includes:

(i) design ground response spectra,

(ii) in-structure response spectra,

(iii) acceleration time history, and

(iv) seismic anchor movements.

The seismic design specifications include:

(a) the scope and boundaries of components to be seismically designed,

(b) the applicable design and construction code,

(c) the required seismic function (e.g., operability, leak tightness, and position retention) of the component or piping system,

(d) the free-field seismic input for the design basis earthquake,

(e) the in-structure seismic response spectra, and

(f) the operating and design loading conditions concurrent with the seismic load.

Operability is the ability of the component to deliver, control, or shut off flow during or after the SSE. The seismic qualification of the components that must remain operable during the SSE must be established by static or dynamic analysis or by testing. Leak tightness is the ability of the component to prevent leakage to the environment during or following SSE. The requirements for seismic qualification of components such as piping systems depend on the pipe size and the magnitude of the seismic input. The requirements for pipe larger than 50.8 mm (2 in.) nominal pipe size and for an earthquake with a PGA value larger than 0.3g are the same as the operability requirements. For smaller size pipes or when PGA values are less than 0.3g, the position retention rules apply for leak tightness, with additional requirements that the loads imposed on nonwelded and nonflanged pipe joints are within specified limits. Position retention is the ability of the component not to fall or collapse in case of an earthquake. The seismic qualification of systems and components that must retain position but need not perform a function or be leak-tight may be established by installing bracing using the standard support and restraint spacing criteria. The adequacy of the component supports and their attachment to the building should be established. Seismic design analysis should be used to establish the seismic load on each component support, and the adequacy of the supports and anchorage for position retention should be demonstrated against failure modes that could cause loss of position.

Seismic qualification of existing components should consider the current material condition of the component. Maintenance records of the equipment or components should be examined to assess their adequacy, operability, and structural integrity. The quality of the construction and the maintenance condition of the components should be established by inspection. If corrosion or environmentally assisted cracking is postulated, the component should be examined by nondestructive volumetric techniques such as radiographic, ultrasonic, or eddy current examinations to indicate the presence of discontinuities/flaws in the material or wall thinning.

The seismic design of a system or component should also consider interaction of seismic-induced failure of a SSC that affects the function of the system or component being qualified. These interactions are of four types:

1. A falling interaction involves an overhead or adjacent structure or component falling on a critical component.

2. A sway or swing interaction occurs when an adjacent or suspended structure or component swings or rocks during a seismic event and affects a critical component.

3. A spray interaction involves spraying or flooding of a critical component due to leakage or rupture of an overhead or adjacent system or component.

4. A system interaction is an accidental signal resulting in unanticipated operating conditions, such as an unintended closure of a valve or start-up of a pump. A significant interaction results in damage of the component or equipment being targeted.

However, because the original design of reactor structures and components is based on the original material properties, does not consider the current condition of the material, and does not consider loading rate effects, and also because fatigue cycles below OBE are excluded from the fatigue analyses, their possible impacts on reactor component design need to be evaluated. Such evaluations should be performed in the next phase of this program for two components, one from the reactor core support structure and core internal components and the other from the primary pressure boundary piping.

2.1.9 Component Design

2.1.9.1 ASME Section III, Division 1 NB/NC/NG-3200 Design by Analysis

In accordance with Section III Subarticle NB-3210 “Design Criteria,” the requirements for the acceptability of a design by analysis are as follows:

(a) The design shall be such that stress intensities will not exceed the limits described in Subarticle NB-3211 and Subarticle NB-3100 tabulated in Section II, Part D, Subpart 1, Tables 2A, 2B, and 4.

(b) The design details shall conform to the rules given in NB-3100 and those given in the subarticle applicable to the specific component.

(c) For configurations where compressive stresses occur, in addition to the requirements of (a) and (b) above, the critical buckling stress shall be taken into account. For the special case of external pressure, NB-3133 applies.

(d) Protection against nonductile fracture shall be provided by satisfying one of the following provisions:
    (1) performing an evaluation of service and test conditions by method similar to those contained in Appendix G; or
    (2) for piping, pump, and valve material thickness greater than 64 mm (2.5 in.), establishing a lowest service temperature that is not lower than RT_{NDT} (NB-2331) + 56°C (100°F); or

(3) for piping, pump, and valve material thickness equal to or less than 64 mm (2.5 in.), the requirements of NB-2332(a) shall be met at or below the lowest service temperature as established in the design specifications.

The NB/NG/NC-3200 design is based on the maximum shear theory (NB-3212). The maximum shear stress at a given location is equal to one-half the difference between the algebraically largest and the algebraically smallest of the three principal stresses at that location. Failure or gross distortion of a component occurs when the normal stress or shear stress developed due to the imposed loading exceeds the yield strength of the material. The design loading conditions are typically evaluated by linear elastic methods, rules for stress categorization, and appropriate design limits. However, the NB/NC-3200 method also allows plastic analysis, elastic-plastic analysis, and experimental stress analysis. The basis for the classification of the various stresses was discussed in Section 2.1.1.

In the linear elastic method, the design stresses are considered as stress intensities, S_m, rather than longitudinal or hoop stresses or σ_1, σ_2, or σ_3 principal stresses. The stress intensity is defined as twice the maximum shear stress defined above. Thus, for Class 1 components and piping, the stress intensity is determined by using the Tresca criteria as the maximum value of the following:

$$\mathbf{S_m} = \mathbf{max} \quad \begin{matrix} |\sigma_1 - \sigma_2| \\ |\sigma_2 - \sigma_3| \\ |\sigma_3 - \sigma_1| \end{matrix}$$

where σ_1 and σ_2 are the principal stresses in or parallel to the mid-plane of the wall of the component and σ_3 is the principal stress perpendicular to the mid-plane of the component wall. The principal stresses are taken to be positive when tensile and negative when compressive. In the latter case, the stress intensity increases. The allowable stress, S_m, is taken as the lesser of the material ultimate tensile stress at temperatures determined from the tables in ASME Code Section II Part D divided by 3, or 2/3 times the yield stress at temperatures also determined from ASME Division 1 Section II Part D.

The stress limits that must be satisfied for design loadings under Service Levels A, B, C, and D; test loads; and special stresses are described in ASME BPV Code Section III Subarticles 3222 through 3227. Guidance for the applications of plastic analysis is discussed in Section III Subarticle NB-3228.

2.1.9.2 ASME Section III, Division 1 NB/NC-3600 Design by Rule

ASME BPV Code Section III, Division 1 Subarticle NB/NC-3600 design is based on a set of simple formulas to determine either the maximum thickness or the maximum allowable working pressure for pressure load conditions. It applies only to piping and piping components. The expressions provided in ASME Section III Code are based on maximum stress theory. The NB/NC-3600 method provides a quick, simple, and acceptable method for the design and construction of piping and vessel for high-pressure systems. The NB/NC-3200 method requires a higher degree of stress analysis than the NB/NC-3600 method, because in NB-3200 all aspects of loading are considered and evaluated. In the NB-3600 approach, piping components are represented by a beam element in the model, and the calculated stresses are multiplied by a stress index factor to account for the actual component geometry. ASME Section III, Division 1 Subarticle NB-3656(b)(4) specifies the stress limits for stresses due to seismic anchor motion caused by SSE and other reversing dynamic loading in level D service loads. Seismic anchor motion is the differential motion between two piping supports (e.g., support at a higher elevation would be subjected to larger motion than those at a lower elevation) or the differential motion between an equipment nozzle and a piping support. The seismic anchor motion loads are deformation-based and, like thermal expansion, are considered as secondary stress and should satisfy the primary plus secondary stress limits. Other special requirements for piping support design and strength analysis are contained in Subarticle NF-3600, “Design Rules for Piping Supports.”

For Class 1 nuclear piping, detailed modeling is required to calculate primary stresses, primary plus secondary stresses, and peak stress, which include effects of local stress concentrations and discontinuities to meet the ASME Code stress intensity limits at the service temperature for various service conditions. However, the size, number, and complexity in a typical NPP make such detailed modeling of all piping components (e.g., elbow, tee, reducer, nozzle, and so on) impractical. Instead, the overall piping stresses are calculated at discrete points (of maximum stress) using simple beam-type finite element models. Local stress concentrations due to nonuniformity in the piping cross sections are accounted for through use of stress intensity factors (stress indices) for specific piping components.

By developing a set of stress indices, the stress in NPP piping can be calculated easily and conservatively. In the NB-3600 methodologies, the stress orientations are ignored and only the resultant moment is used in the stress calculation. For those pipe components that do not satisfy the simplified analysis approach, Section III Subarticle NB-3600 allows detailed stress analysis as specified in Subarticle NB-3200, “Design by Analysis.” In the NB-3200 analysis, a detailed finite element model is developed and all the stress orientations are considered; the resulting stress values are based on actual component dimensions. In general, the nuclear industry has found that it is more economical to replace or modify a piping component that does not meet the simplified design-by-rule approach than it is to perform the detailed analysis.

The stress intensity limits in ASME Section III, Division 1 Subarticle NB-3600 piping analysis by design by rule approach are Subarticle NB-3652 for primary stress, NB-3653.1 for primary plus secondary stress, and NB-3653.2 for peak stress (fatigue analysis). Three main stress indices are used in these analyses: B-indices for primary stress evaluation, C-indices for primary plus secondary stress evaluation, and K-indices for peak stress fatigue evaluation. The B1 and B2 stress indices are intended to protect the piping without gross plastic deformation and against catastrophic failure. The stress indices are used to modify nominal stress equations for straight pipes so that the behavior of piping components such as elbows can be controlled using the same basic stress limits as for straight pipe. Values for the B, C, and K stress indices are given in Table NB-3681(a)-1 for a variety of piping components. The methods for determining flexibility factors for some commonly used piping products are given in Subarticle NB-3686.

Piping stress due to seismic loads includes seismic inertia effects and anchor movements. Both should be considered in the NB-3600 piping design analysis. Anchor motion due to earthquake and other reversing-type dynamic loading is the differential motion between (a) two pipe supports (e.g., piping support at higher elevation would have a larger support motion than supports at lower elevation) or (b) an equipment nozzle and a pipe support. Earthquake anchor motion loads are deformation-based and, like the thermal expansion load, are considered as secondary stress and should satisfy the primary plus secondary stress intensity limit when combined with other loads. Earthquake anchor movements are generally input as relative displacements at piping supports in performing a static analysis, and the resulting stresses are combined with the piping stresses due to inertia effect. ASME BPV Code Section III Subarticle

NB-3656(b)(4) specifies the following stress limits for stresses due to earthquake anchor motions and other reversing type dynamic loading in level D service loads. Note that service level D loads involve SSE only; OBE is considered as a service level B load.

NB-3600 does not contain any equations for deflection limits. NB-3654.2(b) specifies that any deflection limits prescribed by the design specification must be satisfied for level B service loads. NB-3655.5 specifies that any deformation or deflection limits prescribed by the design specifications must be considered with respect to level C service limits.

2.1.9.3 ASME Section III, Division 1 Subarticle NB/NC/NG Fatigue Analysis

The design methods in ASME Code Section III, Division 1 Subarticle NB, NC, or NG for ASME Class 1, 2, and CS components require a fatigue analysis as well as a fracture mechanics evaluation to prevent the likelihood of nonductile failure. The ASME Code fatigue analysis considers all transient loads based on the anticipated number of thermal and pressure transients, and for each load-cycle or load-set pair, an individual fatigue usage factor is determined by the ratio of the number of cycles anticipated during the lifetime of the component to the allowable cycles. Figs. I-9.1 through I-9.6 of ASME BPV Code Section III Mandatory Appendix I specify fatigue design curves for various materials that define the allowable number of cycles as a function of applied stress amplitude. The CUF is the sum of the individual usage factors for all load-set pairs. ASME Code Section III requires that at each location, the CUF, calculated based on Miner's rule, must not exceed unity for acceptable fatigue design. Thus,

$$\mathrm{CUF} = \Sigma U_i = \Sigma(n_i/N_i) \qquad (2)$$

where U_i is the usage factor; n_i is the number of operating cycles at stress level i; and N_i is the number of cycles to failure at stress level i determined from the ASME Code Section III, Division 1 fatigue design curve.

Although ASME Code Section III rules apply to Class 1 components, those fatigue design rules are sometimes applied to other classes of components to provide a robust fatigue design in situations in which known fatigue issues exist or fatigue duty is high (e.g., Class 2 PWR feedwater nozzles). In addition, an environmental correction factor, F_{en}, is also applied to these components if they are exposed to an LWR coolant environment. The methodology for estimating F_{en} is described in detail in NUREG/CR-6909 Rev. 1.[15] The fatigue analyses for U.S. NPPs typically consider 5 OBEs and 1 SSE with 10 cycles for each event. However, some analyses consider 20 cycles for each event.

2.2 Common Forms of Corrosion

The present review is confined to the potential effects associated with below DBEs on the corrosion processes of nickel and steel alloys used in NPP applications such as reactor operation including steam generation and cooling. A refresher on the basic corrosion processes found in a LWR environment is presented followed by an investigation into the interactions between seismic loadings and corrosion behavior in Section 4.

2.2.1 General Corrosion – Passive Films

The ability of metals to resist corrosion in a LWR environment depends on their ability to form a protective outer oxide layer, generally referred to as a passive film. The film serves to help mitigate the dissolution of the metal into solution through a number of potential mechanisms as discussed in the following sections.

2.2.1.1 Film Formation

A metal in an aqueous solution is subject to electrochemical reactions dependent on the metal and the chemical species in solution. Electrochemical reactions occur in pairs, referred to as the “half-cell” reactions, where oxidation occurs at the anode (location which supplies electrons) and reduction occurs at the cathode (location which consumes electrons). Thus, the anodic and cathodic reactions can occur next to each other or be at an extended distance from each other so long as they are in electrical contact (i.e., electrons must be exchanged).

As an example, in a solution with dissolved oxygen, two metal atoms at the metal surface could react to form cations in solution, giving up four electrons (Eq. 3), while an oxygen molecule on the metal surface simultaneously reacts with two water molecules and the four electrons to produce four hydroxyl ions in solution (Eq. 4).

$$2M \rightarrow 2M_{aq}^{2+} + 4e^{-} \qquad \text{oxidation} \qquad (3)$$

$$O_2 + 2H_2O + 4e^{-} \rightarrow 4OH^{-} \qquad \text{reduction} \qquad (4)$$

If conditions remain favorable, such as in an acidic environment, reactions in Eqs. 3 and 4 could continue, resulting in dissolution of the metal. However, other reactions are also possible, such as the precipitation of the metal as an oxide back onto the metal surface (Eq. 5). In this case, precipitation back on the metal surface would begin to impede reactions in Eqs. 3 and 4, as the precipitate starts to block diffusion of the metal ion away from the surface and oxygen toward the surface.

$$M_{aq}^{2+} + H_2O \rightarrow MO + 2H^{+} \qquad \text{precipitation} \qquad (5)$$

Under other conditions, such as in an alkaline environment, the metal can oxidize to form either a metal anion in solution (Eq. 6) or a surface oxide (Eq. 7).

$$M + nH_2O \rightarrow MO_n^{n-} + 2nH^{+} + ne^{-} \qquad \text{oxidation} \qquad (6)$$

$$M + H_2O \rightarrow MO + 2H^{+} + 2e^{-} \qquad \text{oxidation} \qquad (7)$$

As mentioned previously, the oxidation reactions (Eqs. 3, 6, and 7) are balanced by a range of potential reduction reactions (Eqs. 4, 8, and 9) in aqueous systems in order to main electrical neutrality within the system. Other common reduction reactions include the reduction of hydrogen cations (Eq. 8) in acidic environments or the reduction of water in neutral or alkaline environments (Eq. 9).

$$2H^{+} + 2e^{-} \rightarrow H_2 \qquad \text{reduction} \qquad (8)$$

$$2H_2O + 2e^{+} \rightarrow H_2 + 2OH^{-} \qquad \text{reduction} \qquad (9)$$

These equations provide a simple description of the basic general corrosion processes in LWRs.[1,3] At any given time, a variety of oxidation/reduction reactions are occurring throughout the system involving a number of different metal alloys. The stability of the reactants versus the potential reaction products provides the thermodynamic driving force behind the processes that eventually take place. In LWR systems, general corrosion is minimized by adjusting operating conditions in a range that favors the formation of stable oxide compounds on the metal alloys involved. This goal is partially offset by the need, depending on the reactor type, to control the radiation field and avoid fuel performance issues. In general, water chemistries are kept to a near neutral pH (controlled by Li injection), maintained at low dissolved oxygen levels, and often include controlled hydrogen concentrations to mitigate water hydrolysis.

Precipitation and oxidation reactions, such as those in Eq. 5 and Eq. 7, respectively, contribute to the growth of an oxide film on a structural alloy. The extent to which they occur depends, in part, on the reaction kinetics. The reaction kinetics are controlled by the availability of the reactants at the metal surface. For example, the reaction in Eq. 7 depends on the mobility and concentration of water molecules, hydrogen ions, and electrons in the oxide layer because of their need to travel between the metal surface and the water.

As the passive oxide film grows thicker, reactants and products of the corrosion processes become less mobile in the film, and, at some point, a steady state or equilibrium is attained. The overall thermodynamic driving force behind the corrosion processes is balanced by the resistance of the passive oxide film to passage of reactants and products between the underlying metal and the surrounding aqueous environment.

2.2.1.2 Layer Structure

The water chemistry in current LWR environments is carefully controlled to minimize the metal corrosion rate in the system.[81–83] This control results in passive films typically characterized by a two-layer structure with an inner transition zone in the case of steels and nickel alloys.

Carbon Steel and Low Alloy Steels

The exposure of carbon and low alloy steels to de-oxygenated neutral and alkaline aqueous environments at high temperatures (~300^{o}C) invariably leads to a double-layer corrosion film at its surface.[84–86] Both layers are composed of magnetite (Fe_3O_4). The inner layer is fine grained and more protective,[86,87] growing in place at the metal surface with the concomitant dissolution of some iron ions into solution. The outer layer is the result of the precipitation of iron ions from solution to form larger crystallites on the surface once solution saturation is obtained.[87] A similar duplex layer structure of magnetite is formed in high-temperature steam environments as well.[86,87] At intermediate temperatures, such as those experienced during reactor start-up and shutdown, different iron oxide products, less protective than an adherent Fe_3O_4 film, are formed, leading to accelerated corrosion.[88]

Stainless Steels

Similar to carbon steel, a two-layer oxide structure has been observed to form on austenitic stainless steels (SSs) at temperatures of about 300°C (572°F) in an aqueous environment. Early work had concluded that a double layer of Fe_3O_4, which has a spinel structure, formed the passive film, which is similar to that on carbon steels.[84] Diffraction experiments had shown the presence of spinel compounds on the surface of SS after exposure in water at 300°C (572°F).[89,90] Detailed x-ray powder diffraction work showed that SS samples had a passive film composed of two layers with an inner layer having a spinel structure, postulated to be of the type $FeO \cdot Cr_2O_3$.[91] This finding is consistent with later work that showed the structure of the inner layer to correspond to that of a spinel with the general formula $(Ni,Fe)(Fe,Cr)_2O_4$.[92–99] The inner layer appears to form a fine-grained[95,98,100,101] compact, continuous film strongly bonded to the metal substrate because of its epitaxial solid-state growth within the small crystalline regions on the metal substrate.[102,103] This conclusion is further supported by the observation of nano-crystalized grains in a recrystallized zone of the substrate metal at the oxide interface.[99] This inner oxide layer has been often characterized as having an increased Cr concentration relative to the base metal[91–94,99,104,105] and a reduced Ni concentration.[91] The elevated Cr concentration is not attributed to migration of Cr ions, but rather it is the result of a depleted Fe concentration due to preferential dissolution of the Fe[105,106] and migration of Fe^{2+} from the oxide/metal interface through any oxide layer(s) to the solution interface due to oxidation of the metal with the concomitant migration of oxygen in some form in the opposite direction.

The outer layer of the passive film on SS generally exhibits a spinel structure[92,97–100] and is composed of iron-rich precipitation products.[94, 96,98,107] The nature of the precipitation products depends on the water chemistry. Magnetite, which has the spinel structure noted above, is the predominant precipitation product in pressure water reactor/hydrogen water chemistry (PWR/HWC) water (low dissolved oxygen [DO])[93,96,98,99,107] with nickel ferrite also present.[95,97,107] Under normal water chemistry (NWC) conditions (higher DO), hematite (Fe_2O_3) is the predominant iron precipitation product in both α-Fe_2O_3 and γ-Fe_2O_3 forms.[95,96,107] The α-Fe_2O_3 phase has a rhombohedral (corundum) structure, and γ-Fe_2O_3 has a cubic (spinel) structure, is metastable, and occurs naturally as maghemite. In addition, the precipitation products (“crud”) found in operating nuclear reactors have been identified as a nickel ferrite,[108] and the overall passive film is composed of spinels.[109]

Whereas the inner layer of the passive film is enriched in Cr and slightly depleted in Ni, the underlying base metal has been observed to exhibit slightly enriched Ni concentrations in both 304 and 316 SS[92,98,99,101,110,111] and depletion in Cr in 304 SS.[92,99] Hydrogen enrichment has also been observed in the metal just below the passive film on Type 316 SS[111] in conjunction with the enriched Ni.

Additives to LWR cooling water, such as boron and lithium, could find their way into passive films and impact their structure and properties. Lozano-Perez et al.[110] observed small amounts (~200 ppm) of lithium distributed throughout the passive film, while boron was not detected.

Surface preparation of the metal has an effect on the thickness of the passive film layer.[99,106] In general, electropolished surfaces tend to have a thinner more stable passive film than those that were mechanically polished. The electropolishing removes the residual stress in the surface layer, which promotes oxidation. Any cold work on the surface introduces a deformed microstructure that facilitates oxygen advancement into the metal.[110] The passive oxide film thickness also tends to increase with O_2 concentration in the aqueous environment and decreases with the concentration of H_2O_2.[107]

Nickel Alloys

The passive film on nickel-based alloys (A600, A690, and A800) in PWR water (low oxygen with hydrogen added) is composed of two, possibly three, oxide layers. Similar to the passive film on SS, the inner layer on Alloy 690 is continuous, Cr-rich (Fe- and Ni-depleted), and composed of fine crystallites with a spinel structure.[112,113] This layer has been identified as a mixed iron and nickel chromite (such as $Ni_{(1-x)}Fe_xCr_2O_4$ or $(Ni,Fe,Cr)_3O_4$.[112–115] However, dispersed Cr_2O_3

nodules were observed at the interface between the base metal and the inner oxide layer by Sennour et al.,[112] and Wang et al.[113] observed Cr_2O_3 as part of the inner layer, primarily at low oxygen concentrations (<0.01 ppm). Carrette et al. observed either a very thin continuous Cr-enriched oxide layer on the metal or a heterogeneous, less-continuous Cr-rich layer on the metal dependent on differences in water chemistry attributed to two different experimental autoclave setups.[116] On Alloy 600, Panter et al. also observed a very thin chromium oxide layer, considered the barrier layer, between the base metal and the rest of the film.[114]

The outer passive film layer is composed of larger, precipitated crystallites of nickel ferrite, rich in iron ($Ni_{(1-z)}Fe_{(2+z)}O_4$).[112,114] The outer layer crystallites appear to be growing epitaxially on the inner layer, and the presence of nickel hydroxide has been observed.[112]

At higher dissolved oxygen concentrations (e.g., 2 ppm dissolved oxygen), the formation of NiO was observed in both the inner and outer layers, but was not protective as far as limiting the conduction of anions and cations through the layers.[113] At 3 ppm dissolved oxygen, a porous inner layer of NiO was formed and the outer layer was sparsely packed spinel particles.[117]

No chromium depletion in the metal at the base of the chromium-rich inner layer was observed by Sennour et al.[112] on Alloy 690, but chromium depletion was observed by Panter et al.[114] on Alloy 600.

2.2.1.3 Ion Mobility in Passive Films

The formation of the passive films on SS and nickel alloys can be explained, in part, by the mobility of the metal ions in the surface oxides. The relative ion mobility of the metal ions in a spinel-type structure has been shown to be[106,118]

$$Fe^{3+} \text{ and } Mn^{2+} > Fe^{2+} > Co^{2+} > Ni^{2+} >> Cr^{3+}.$$

This order is consistent with the relative thermodynamic stability of the ions in the metal locations in the oxide lattice.[118] As discussed earlier, the higher mobility of the iron ions enhances its dissolution, leading to inner passive layer compounds richer in nickel and chromium and an outer precipitated layer rich in iron.[106] Co-60 was observed uniformly throughout the passive layer in steam generator tubes taken from PWRs, with the conclusion that its source was from the reactor coolant, having dissolved from cobalt-containing alloys elsewhere in the reactor.[109]

The passive film growth rate is controlled by the inner layer,[106] with the inner layer thickness reaching a steady-state thickness determined by the electrochemical potential difference between the base metal and the surrounding aqueous solution needed for ion migration through the oxide.

The diffusion of hydrogen and oxygen in the passive oxide film is another key parameter in the oxide composition and growth. In SS passive films, oxygen and hydrogen appear to diffuse independently of each other.[111] However, the diffusion of hydrogen in nickel alloy passive films is likely tied to the transport of hydroxide ions.[119]

2.2.1.4 Stress and Strain

The formation of and protection afforded by a passive film on a metal substrate is affected by the inherent stability of the metal surface itself and any externally applied stresses. The stability of the metal surface depends on its chemical composition, metal manufacturing processes, and applied surface finish treatment, which can lead to residual stresses at and below the metal surface. Externally applied stresses include tensile and compressive loads encountered in the metal component's environment. A review of the types of impacts experienced in these situations can help in the understanding of low impact seismic events.

Residual Stress Effects

The surface treatment of a metal plays a role in the thickness of the surface oxide layer. For example, physical machining and polishing of a metal surface results in more physical surface and sub-surface damage than electropolishing,[94,97,103–106] which results in a thinner oxide layer (slower corrosion rate) for the electropolished surface under the same set of environmental conditions. The faster corrosion rate for non-electropolished surfaces can be attributed to the removal of localized stress effects at the metal surface by electropolishing.[106] However, the slower corrosion rate on an electropolished nickel Alloy 600 sample, after 25 h of exposure to a simulated PWR primary water environment at 320°C, was attributed to the formation of a more stable oxide layer with a higher chromium content than was formed on a mechanically polished sample.[120]

As a further example, Souier and Chiesa[121] used conductive atomic force microscopy to determine the electrical and electrochemical properties of the passive layer formed on Type 304L SS in chloride-containing solutions after various mechanical and/or electropolishing surface treatments. They found that the high conductivity regions in the surface film corresponded to the presence of strain-hardened zones in the underlying metal produced by surface preparation, and that these regions were favorable sites for pitting corrosion. Another example of increased pitting susceptibility due to stress is discussed in Section 3.2.2.

External Tensile and Compressive Loads

The composition and structure of the oxide layer play a role in its protective nature. An increased compressive load was required to rupture the oxide layer on SS in acid solutions when the Cr content of the steel was increased.[122] The increased Cr content of the steel results in a more extensive Cr_2O_3 layer on the metal surface, and Cr_2O_3 is stronger than films with incorporated iron or nickel. The oxide layers were found to fracture under a load on the order of 50 μN at a temperature of 40°C on SS in acid.[122] Additional work showed that oxide films with a lower amorphous content (higher crystalline content) require higher compressive loads to fracture, with the highest loads needed to fracture the film with the highest degree of crystalline structure grown epitaxially on the metal substrate.[107]

In tensile tests with 304 SS at 288°C in aerated and deaerated high-purity water, the rupture strain of the surface oxide increased as the concentration of Zn or the exposure time to Zn-containing solutions increased.[108] The rupture strain of the oxide layer was observed to double when the Zn concentration was increased to 60 parts per billion (ppb) or the exposure time to a solution of 20 ppb Zn exceeded 300 h.[108] On the other hand, a decrease in a compressive load was required to rupture the oxide layer on 304 SS in a 0.1M sulfuric acid solution with an increase in NaCl concentration.[109] The exact mechanism of how the Zn or Cl increases or decreases, respectively, the passive film's ability to handle stress is not known, but it is correlated with its chemical composition and structure. Conversely, Navai[123] showed that elastic and plastic tensile and compressive stresses on 302 SS could influence the thickness and composition of the passive layer. Takeda et al.[124] also showed that the composition of the oxide film on 316 SS in a simulated BWR environment is modified by a change in applied stress. Navai and Debbouz[125] also demonstrated that the oxide layer thickness on a 316 SS sample was different under unstrained, tensile stress, or compressive stress conditions.

Cracking of the passive film on Type 304L SS under externally imposed tensile loads has been investigated by Darowicki et al.[126] using dynamic electrochemical impedance spectroscopy. The specimens were loaded under static tensile stress of 380 MPa in a 0.5M NaCl solution at room temperature, and the resulting impedance spectra were analyzed. Not surprisingly, they found that the presence of a static tensile stress, an aggressive environment, and anodic polarization strongly influenced the cracking behavior of the passive film. Cracking was observed at imposed potentials of $E = -0.150$ and 0.0 V, but not at potentials of −0.200 and −0.300 V. In a follow-on study,[127] they tested cold-worked Type 304L specimens pulled to failure at strain rates ranging from 10^{-5} s^{-1} to 16×10^{-5} s^{-1}. They found passive film cracking occurred at lower elongation values for lower strain rates and at longer elongation values for higher strain rates.

Not only rupture of the passive film, but also elastic and plastic strain can cause enhanced corrosion. The primary focus in this area is more on changes to the underlying metal rather than the passive film. Pan[128] investigated the room temperature corrosion behavior of AISI 2205 duplex SS (22% Cr, 5.5% Ni, 3% Mo) under cyclic loading at 1 Hz between 0 and 0.1% (elastic cycling) and between 0 and 1% (plastic cycling) tensile strains in a 0.5M NaCl solution. Based on measurements of surface corrosion potential, he found that corrosion was significantly accelerated by plastic cycling of the metal. He also observed that slip bands were the preferred sites for localized corrosion due to the higher potential gradient that could facilitate electron transfer at such locations. However, no correlation with the state of the passive film was attempted.

Xu and Cheng[129,130] studied the corrosion of X100 pipeline steel under both elastic and plastic monotonic strains in a near-neutral pH bicarbonate solution. They found that the imposition of a static elastic tensile stress produced no detectable effect on the electrochemical corrosion potential of the steel, as the resulting strain on the specimen was incapable of fracturing the corrosion scale formed on the steel surface. A dynamically applied elastic load weakened the scale by expanding its pores, and thus somewhat increased the steel corrosion. On the other hand, plastic pre-strains of the metal of up to 3.9% produced a significant effect on corrosion behavior. Both anodic and cathodic reactions were enhanced by plastic pre-strain, with the effect on the anodic reaction being more significant. The authors concluded that a non-uniform distribution of plastic stress and plastic strain on pipelines could be expected to result in localized corrosion and the initiation of corrosion pits and even cracks. Deformation has also been observed to accelerate the corrosion of X80 pipeline steel.[131]

2.2.2 Pitting and Crevice Corrosion

Pitting corrosion is a form of localized corrosive attack in which cavities or pits are formed on the material surface. Pitting corrosion can be difficult to detect, since the resulting pits are often concealed by corrosion products. This is of a particular concern because a small pit can develop in a localized region and grow undetected to a sufficient depth to threaten the integrity of a large component. Corrosion pits may also act as stress risers that can lead to crack initiation. Pitting is often related to some form of local breakdown in the protective surface or oxide layer. The breakdown could be due to mechanical, chemical, or electrochemical factors. Other factors that can contribute to pitting attack are localized damage of an applied protective coating or the presence of foreign particles or other non-uniformities (e.g., non-metallic inclusions) at the surface.

Mechanistically, pitting is caused by the formation of an electrochemical cell in which the susceptible localized region where the pit is formed becomes locally anodic with respect to the larger surrounding surface, which becomes cathodic. As an example, at the site of the pit, the metal is dissolved according to the chemical reaction given in Eq. 3. The charge-balancing reaction in the cathodic region away from the pit is given by Eq. 4. The net result of these reactions is that metal is dissolved from the growing pit and transformed into a hydrolyzed corrosion product. The process appears to be autocatalytic in that once the pit starts to grow, the resulting localized chemical conditions are such that further pit growth is promoted. Pits typically initiate at some chemical or physical heterogeneity on the original or newly created surface, such as inclusions, second-phase particles, grain boundaries, dislocations, and mechanical flaws or damage.

Pitting due to corrosion has been observed in many industrial and NPP systems (mostly pertaining to the balance of plant systems utilizing service water and cooling water).[132,133] Bowman and Guthrie[134] reported on several multi-year investigations of the iron corrosion involving pitting under tubercles found in the service water systems of many operating power plants, confirming that the iron deposits were not from soluble iron in the water but from the piping material. They also noted that the deepest pitting was associated with the largest tubercles and that differential aeration cells set up by the tubercles together with MIC were responsible for the severe pitting in these systems in which both the iron- and sulfur (sulfate)-reducing (naturally occurring) bacteria played a role.

A recent case study[135] reported the occurrence of SCC with pitting in the heat affected zone of welded SS pipe; although the piping was from the petrochemical industry, the application was for carrying utility water in an underground soil environment. The main environmental factors in this case were attributed to the presence of chlorides and reducing conditions, causing (local) degradation of passive films and weld residual stresses with localized deformation of the low stacking-fault energy material.

Crevice corrosion is a form of localized corrosion associated with the presence of small volumes of stagnant solution in tight gaps, or crevices, such as are present under gaskets, fasteners, insulating material, surface deposits, at incomplete weld penetrations, and in other regions of limited fluid accessibility including cracks initiated by fatigue. Crevice corrosion is initiated by changes in the local chemistry of the solution within the crevice. With respect to the bulk solution, these changes can include (1) the depletion of the oxygen or corrosion inhibitor, (2) the buildup of corrosive species (e.g., chlorides) within the crevice, and (3) a change in the pH of the solution in the crevice. The chemistry behind crevice corrosion is an important influence on environmentally assisted cracking such as SCC.[136]

The mechanism of crevice corrosion involves the depletion of dissolved oxygen or other oxidant in the solution trapped in the stagnant crevice (consumption rate in the crevice is faster than the rate of transport into it), resulting in a differential aeration electrochemical cell in which the metal surface inside the crevice becomes anodic with respect to the bulk material outside the crevice (anions are driven into the crack and cations out of it). This results in a shift in electrochemical potential and pH that can favor metal dissolution rather than a stable passive layer favored in bulk solution, similar to that which occurs in pitting corrosion.[137] For more information, Turnbull has reviewed a number of the processes that can potentially occur in cracks.[136]

A buildup in the concentrations of other corrosive species within the crevice can further contribute to the corrosion process. In nuclear steam generators, for example, the continued boil-off of coolant in crevices on the secondary side of the steam generator leaves behind nonvolatile impurity species such as chlorides and sulfates, and these impurities can achieve concentration factors as high as 10^8 in the crevice.[139] Such impurity concentrations, in conjunction with the depletion of oxygen in the crevice, promote the breakdown of the protective passive film on the steam generator components, resulting in severe corrosive attack.

2.2.3 Microbiologically Induced Corrosion

The corrosion induced or enhanced by microbial agents is commonly known as microbiologically (or microbially) induced (or influenced) corrosion (MIC). It is considered to be a form of environmentally assisted degradation in the presence of microbes (including bacteria) and the associated biofilms produced by the microbes. In this regard, the biofilms play a critical role, just as the oxide films do in the case of non-microbial corrosion. However, a key difference is the presence of living organisms, with more than 90% of the biofilm consisting of water. Biofilm, typically, is what provides the protection to colonies of microorganisms, not to the substrata, and allows for the transport of nutrients to the microorganisms. The microorganisms generate and sustain a local chemistry environment – at their interface with the metal or metal-oxide (or corrosion product) – that is dynamic and active. This local environment often leads to or influences the sustained corrosion, referred to as the MIC, via direct or enhanced dissolution of alloy constituents, or via degradation of passivity or corrosion films of the alloy, or both.

As such, the underlying mechanism(s) and several key factors involved in the MIC are quite different from those of abiotic corrosion (although the basic principles of corrosion are common). MIC itself has been extensively investigated and several comprehensive reviews exist, for example, covering bio-mechanisms and analytical techniques,[140–142] phenomenology and influence factors,[143,144] and operational guidelines.[145–147] These references may be consulted for details on the various aspects of MIC.

MIC is the form of corrosive attack observed most commonly in aqueous environments that is associated with the presence of microorganisms that either cause corrosive attack directly (e.g., iron oxide bacteria) or produce corrosive species as a part of their metabolic cycle (e.g., sulfate-reducing and sulfur-oxidizing bacteria). The exceptional diversity of the microbiological world includes a great variety of potentially harmful microorganisms that results in a similar diversity of associated corrosive species, including H_2S, SO_2, SO_4^{2-}, NO^{2-}, and $C_2H_3O_2^{1-}$, as well as a number of other organic and inorganic acids. These microorganisms typically form as thin adherent biofilms on component surfaces and are found at temperatures as high as 120ºC (248ºF), pH values ranging from 0 to 13, salinity levels up to near saturation, and in NPP radiation fields. Preventive treatments to address MIC typically include regular surface cleanings to remove biofilms, the use of biocides, and draining and dry storage.

MIC has been noted to occur in (ferrous and non-ferrous) metallic and non-metallic (e.g., concrete) materials; thus it is also in reinforced concrete structures. It is also known to occur in aerobic (oxygen bearing) and anaerobic conditions; these conditions can be present at the same general location, with the latter near the interface of biofilm with the substrata, where the steep gradients in chemical conditions are supported by the action of microbes within the biofilms. It is also important to note that the “film” in biofilm is not a continuous or homogeneous structure. Understanding the structure and role of biofilms in local corrosion and the response of their interface with the component surface under loading is of critical importance. In addition, the response of prevailing microbial species, especially their metabolic activity, under environmental stressors during seismic events, is likely to influence the MIC.

It is the ecosystem of the biogens or bacteria, not so much the bacteria themselves, which protects the microorganisms, supports their metabolism, and seems to be the major participant influencing the MIC – the ecosystem has many parts to it, generally described as the biofilm. Representative ways for well-defined microbial involvement of biofilms in the corrosion of metals include metabolic reactions in the biofilm (1) consuming oxygen, the cathodic reactant; (2) controlling the mass transport of the corrosion reactants and products, therefore changing the kinetics of the corrosion process; (3) generating corrosive substances; and (4) generating substances that serve as auxiliary cathodic reactants.[148]

Biofilms associated with MIC are microbiologically diverse and structurally complex, making it difficult to identify or ascertain the active microorganisms (at the interface between the biofilm and metal surface) most likely responsible for the ecosystem supporting the MIC. The formation of biofilms incorporates and supports many different types of bacteria at a given location. These films and microbial activities create and maintain significant variations (with steep gradients) in chemical and electrochemical conditions. As a result, while the nominal water and its contact with the top layer of a biofilm may be an aerobic (oxygenated) environment, the bottom/lower layers (adjacent to component surfaces) environment often is anaerobic. In addition to being discontinuous and unevenly spread, biofilm formation (resulting local environment) can lead to local breakdown and/or re-establishment of otherwise protective oxide films. These characteristics of biofilms are critical in initiating and maintaining the MIC. The growth, metabolic activity (rate), and interaction of microbes via biofilms are primary factors governing MIC kinetics, in addition to the commonly known factors that affect the abiotic corrosion.

Figure 13 illustrates typical disposition of the biofilm interface and electrochemical/physical processes involved in MIC; the case of MIC in mild steel involving sulfur species is considered where sulfate-reducing bacteria (SRB) are the primary microbes. While other microbes also can lead to MIC,[140] SRB are considered one of the main culprits in industrial MIC contexts in which much of the corrosion damage done by biofilms is in the anaerobic area at their base where the SRB thrive and produce corrosive acids and form sulfur products.[140,149–151]

The presence of iron sulfide quantities as a by-product, in excess of sulfur either in the corroded metal or in the environment in contact with the metal, has been noted in associating metallic

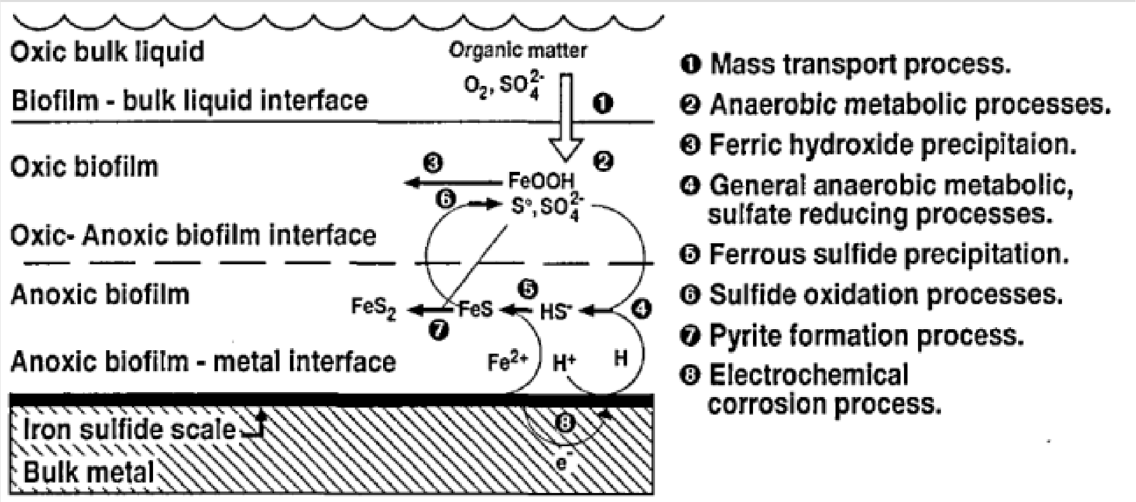

Figure 13. **Schematic diagram of transport and transformation processes in MIC in the case of mild steel involving sulfur species in aerobic/anaerobic biofilms (Ref. 151).**

corrosion with bacterial activity under anaerobic conditions, since as early as 1940,[152] with pitting as the form of corrosion in steels. This is the classic manifestation of the role of SRB. The microbial distribution and activities lead to promoting and maintaining the separation of anodic and cathodic areas on the component surface, which also exacerbates the localized corrosion due to pitting. Pitting is often autocatalytic and typically results in wall perforations.

Although pitting is the more prevalent manifestation of MIC, other forms affected by microbial corrosion include: SCC,[153,154] enhanced galvanic corrosion,[132,155] enhanced erosion-corrosion and hydrogen embrittlement,[132,153,156–158] and de-alloying.[132,153,159,160] A recent article by Gu et al.[143] provides an overview of the basic considerations in the process of microbiological corrosion of metallic materials.

MIC has been noted in nuclear power generation systems,[150,154,161–163] among other industrial systems,[132] and has been investigated for decades.[140,143,149,164] Of particular interest is the MIC of metallic components, often associated with bacterial microorganisms, in water environments commonly used in LWR systems. Systems utilizing open sources of water (e.g., brackish water, lake or river water, seawater) are typically subject to MIC. These systems include, for example, condensers or heat-exchange units, makeup water units, and service water systems. Buried pipes and concrete structures subject to wet environments are other examples of systems subject to MIC. Safety-related concrete structures include foundation, support, and biological shielding, and containment and cooling water system structures such as intake wells intake pipes, pump house wells, and cooling towers.[133]

Functionality of some of the safety-related equipment is supported by the closed cooling water (CCW) system mostly made of carbon steel components, with heat-exchanger tubing typically made of copper alloys or SS. In the case of CCW, system leakages and makeup water additions generally add to the propensity for MIC. In addition, MIC in service water systems[165–167] has resulted in regulatory actions in the past. At one nuclear plant, continued issues with pinhole leaks, pitting, and other localized forms of degradation due to MIC resulted in the replacement of the entire buried carbon steel piping of the safety-related Essential Service Water systems, with high density polyethylene that has exceptional resistance to MIC.[168]

The wide range of operating conditions, materials, and environments leading to or accelerating various forms of aging-related degradation due to MIC is indicative of its significance. The interaction of these conditions and microbial activity with the component surface and microstructural and microchemical characteristics is dynamically driven by energy considerations localized on a micro-scale, all of which are likely candidates for some impact of seismic activity.

2.2.4 Flow-Accelerated Corrosion

Flow-accelerated corrosion (FAC), also known as flow-assisted corrosion, is that form of corrosion in which the loss of material involves metal oxidation and oxide dissolution such that the kinetics of both processes are significantly enhanced by the flow of liquid over the oxide layer. The result is a progressive thinning of the steel component, and a number of serious piping failures have occurred in fossil-fuel plants and NPPs due to this process. The underlying mechanism and several key factors causing the FAC are quite different from those of direct mechanical erosion, cavitation, or particle impingement. The SSCs of interest are made of carbon steels and low-alloy steels with low chromium content, and the conditions include either single-phase water or steam-water (wet steam) environments.

FAC itself has been extensively investigated, and several comprehensive reviews exist, for example, covering theoretical and experimental work,[169–171] empirical prediction models BRT-CICERO™ (Refs. 172, 173) and CHECWORKS™ (Ref. 174), phenomenology and influence factors,[175] and operational management programs.[176] These references may be consulted for details on the various aspects of FAC.

In general, FAC occurs under specific conditions with respect to flow rate, pH, dissolved oxygen content in the water, and temperature. The process is enhanced by increasing flow rate and is most commonly seen at locations subject to turbulent or accelerated flow, such as piping elbows, valves, and orifices. In addition, increasing the pH of the water increases the corrosion rate, since the solubility of Fe in water increases with increasing pH. On the other hand, increasing the dissolved oxygen content in the water tends to stabilize the oxide film on steel surfaces, thereby reducing the susceptibility to FAC. Components appear to be most susceptible to FAC in the approximate temperature range of 120 to 230ºC (250–450ºF), though failures have been seen at higher temperatures. Finally, increasing the Cr content in low-alloy steels reduces the susceptibility to FAC, and SSs, with their more adherent and stable protective oxide films due to a higher Cr content (see Sections 2.2.1.2 and 2.2.1.4), are not subject to this corrosion process.

As a significant degradation mechanism, FAC is both time-dependent and cumulative in its effect. The effect of main concern to the structural integrity is the continued loss of load-bearing wall thickness. This wall thinning is local or localized, but over a sizeable surface area. The thinning is spatially and temporally non-uniform; the thinning rate is neither uniform nor fixed, contrary to the commonly used assumption in many prediction methods (even though some approximations or judgments may be involved in generating and implementing correction factors, after the fact, that only reflect the past response). Under certain conditions, the degradation rate can be relatively high, leading to significant wall loss even if the conditions last only for a short term.

The primary factors that influence the FAC rate include: temperature, local fluid pH, water chemistry (e.g., oxygen content, additives like amines, etc.), steam quality and void fraction, component geometry and system layout, material composition, flow velocity, and turbulence. These factors interact to produce FAC damage via key processes, which are summarized schematically in Fig. 14 as a reference point. In the wetted locations susceptible to FAC, the overall process typically consists of convective diffusion (of soluble species through the oxide and boundary layer) with reductive dissolution of the oxidation product. As such, both the solubility and stability of the oxide are the governing factors. Furthermore, the FAC rate is directly affected by the mass transport, which depends on the solubility and concentration of the soluble iron in the solution next to the diffusion layer, as well as the local flow velocity, turbulence, and eddies that are all affected by the prevailing flow pattern.

The service failures due to FAC have been discussed in several reviews to date.[177,178] One common observation of note from this pool of operating experience is that failures have tended to occur in areas of locally disturbed flow regions that exhibit an enhanced FAC rate. In particular, the critical assessment of case studies on recent major FAC events[179] showed that despite the nominally same water chemistry and piping material, the FAC damage was confined only to where the flow patterns were locally disturbed with high flow-rate, turbulence, and flow-attachment (i.e., disturbed turbulence). In addition, it was noted that the apparent bias in under-predicting the FAC rate occurred at the regions of turbulence in these failure cases.[179] Analytical (computational fluid dynamics) work and simulations,[180–184] as well as experimental

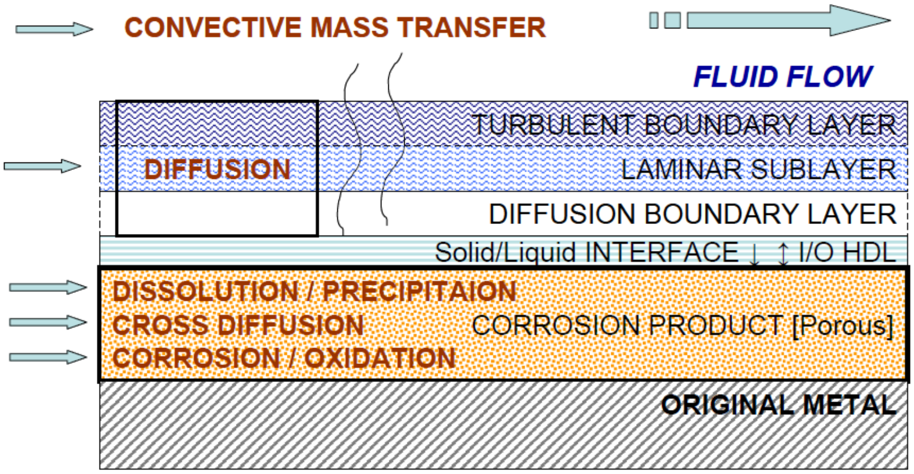

Figure 14. Schematic summary of key processes underlying the FAC phenomenon (Ref. 179).

investigations,[169,170,185] also confirm the critical role of locally disturbed flow conditions (of turbulence and swirling).

Therefore, in a given FAC-susceptible system (i.e., material and nominal environment), the main factor determining the FAC rate is the local fluid flow characteristics, including the turbulence, eddies, and the integrity/stability of the boundary layer (next to the component surface).

2.3 Stress Corrosion Cracking

Stress corrosion cracking (SCC) is one of the major aging degradation processes for reactor coolant pressure boundary components and reactor safety-related system components in both boiling water reactors (BWRs) and pressurized water reactors (PWRs).[186–191] The main difference between a BWR and PWR is that in the former, water is boiled directly by the nuclear fuel and steam is separated and dried before passing through the turbine. In the latter, sub-cooled primary coolant cools the fuel and exchanges its heat via a steam generator to produce steam to drive a turbine and an alternator in the secondary system. Operating temperatures range between 280 and 320°C (536 and 608°F) except for the PWR pressurizer, which operates at 343°C (649°F).

The term SCC represents crack initiation and sub-critical crack growth of susceptible alloys under the influence of a “corrosive” environment and tensile stress. It is a complex process controlled by the synergistic interaction between metallurgical, environment, and mechanical parameters. These three conditions are necessary and must occur simultaneously for SCC to occur. The absence of any one of these conditions or the reduction of one of these below a threshold value can prevent SCC. The three necessary conditions for SCC are illustrated in Fig. 15.

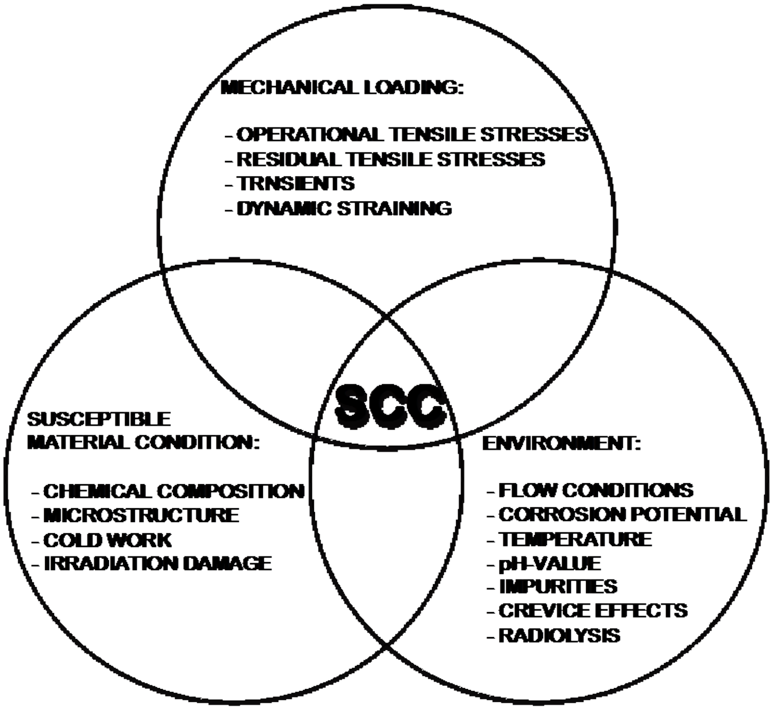

Figure 15. Critical conditions for stress corrosion cracking.

SCC can occur in both BWR and PWR components, and it can be across the grain (i.e., transgranular [TG]) or along the grain boundaries (i.e., intergranular [IG]). Note that SCC does not occur in all environments and that an environment that causes SCC in one alloy does not necessarily cause SCC in another alloy.[190] However, most alloys are susceptible to SCC in at least one environment. In general, SCC propagates perpendicular to principal tensile stress with little or no macroscopic plastic deformation. The SCC fracture surface has a brittle-like appearance. Both IGSCC and TGSCC can occur in the same alloy depending on the material microstructure, the environment, and its stress/strain state.[190] However, the degree of crack branching can vary based on the three necessary conditions.

Aging degradation due to IGSCC has occurred in several BWR components made of austenitic SSs and nickel alloys. [1,4,187,188,191] Examples include the recirculation piping, reactor internal components, and some parts of the reactor pressure vessel such as the in-core monitor housing and control rod stub tubes. The primary reason is that aging degradation by SCC had not been considered in the original design of BWRs. During the past 50 years, the mechanism of IGSCC of BWR components has been investigated in detail, and various methods for prevention, mitigation, and repair, have been developed. Nevertheless, the IGSCC issue has not been fully resolved and is still a concern for BWR components.

Regarding PWRs, Alloy 600 components and associated welds have experienced PWSCC during the past 40 years.[192–196] For examples, PWSCC has occurred in control rod drive mechanism (CRDM) nozzles, pressurizer instrumentations and heater sleeves, steam generator tubes, and hot-leg penetrations. Research and development effort has defined the key parameters that control PWSCC. However, a mechanistic understanding of PWSCC has not yet been established. An empirical relationship based on experimental results and field experience has been developed. Recent experience at the Davis-Besse NPP has shown that PWSCC of the CRDM nozzles can lead to boric-acid corrosion of the reactor pressure vessel head because of primary water leaks, which could have a significant effect on plant safety.[196,197]

Another SCC mechanism that is common to both BWRs and PWRs is TGSCC of austenitic SSs. It is typically caused by chloride contamination although other halide anions such as fluorides can also cause TGSCC.[198–200] Typically, it initiates on the outside surfaces of components where contaminants can accumulate from periodic wetting due to condensation or primary water leaks. The stress required for chloride TGSCC is relatively low, close to the proportional limit of solution annealed austenitic SSs.[190] Implementation of known procedures that ensure adequate surface cleanliness is being recommended. The choice and specification of acceptable insulation materials is an important consideration. These three SCC processes and their characteristics and operating experience are discussed further in the next sections. The critical parameters important for these processes are also identified.

2.3.1 Intergranular Stress Corrosion Cracking

2.3.1.1 Characteristics of IGSCC

Under "normal" conditions of stress and environment, several structural alloys have shown susceptibility to IGSCC in BWRs because of the alloy itself or its fabrication history. In BWRs, IGSCC has occurred in austenitic SS and nickel alloys. The initiation of IGSCC occurs when the following three necessary conditions are simultaneously present[191] (Fig. 15):

1. A microstructure that is "sensitized" due to thermal sensitization during welding and/or stress relief heat treatment to produce a chromium-depleted region (i.e., the heat-affected zone [HAZ]) at the grain boundary. The depletion of chromium is due to the precipitation of $M_{23}C_6$ carbides.[201] A reduction in chromium concentration of as little as 2% compared to the bulk concentration reduces the passivity of the region relative to the grains, thereby increasing the susceptibility to IGSCC.[190]

2. Tensile stress, associated primarily with weld residual stresses. The thermal stresses created during welding exceed the yield stress of the material, thereby causing deformation and resulting residual stresses. The material yield stress is about 140 MPa at 288°C (550°F) for Type 304 SS.

3. An oxidizing environment caused by excess oxygen or hydrogen peroxide species in water due to radiolysis. The corrosion potential or the electrochemical corrosion potential (ECP) of the environment is typically about –230 mV with respect to standard hydrogen electrode (SHE) for stainless steel in high-temperature water (i.e., greater than 90°C [194°F]).[202]

The occurrences of IGSCC in BWR environments has been attributed to either slip oxidation/dissolution[203] or hydrogen-induced cracking mechanisms.[204] The slip dissolution model requires that the surface oxide film is thermodynamically stable to ensure that a crack will propagate with a high aspect ratio without degrading into a blunt pit. A strain increment ruptures that film, thereby exposing the underlying matrix to the environment. Once the passive oxide film is ruptured, crack extension is controlled by dissolution of freshly exposed surfaces and by the oxidation characteristics.

Hydrogen-induced cracking is explained as follows. Hydrogen produced by the oxidation reaction at or near the crack tip is partly absorbed into the metal. The absorbed hydrogen diffuses ahead of the crack tip, interacts with inclusions, and leads to the formation of cleavage cracks at the inclusion/matrix interface. Linkage of the cleavage cracks leads to discontinuous crack extension in addition to extension caused by mechanical fatigue. Other hydrogen-induced fracture processes may also enhance CGRs in LWR environments. For example, hydrogen can cause localized crack tip plasticity by reducing the stress required for dislocation motion.

Both slip oxidation/dissolution and hydrogen-induced cracking mechanisms depend on the rates of oxide rupture, passivation, and liquid diffusion. Therefore, it is difficult to differentiate between the two processes or to establish their relative contribution to environmental enhancement of CGRs. However, for BWRs, the slip oxidation/dissolution model has been successfully used to address IGSCC concerns under the range of environments, stress conditions, and materials relevant for BWR operations.[205] The model uses Faraday's relationship and equates crack propagation to the oxidation charge density at the crack tip that is associated with the transformation of the metal to the oxidized states (i.e., MO or M_{aq}^{+}). A schematic representation of (a) the physical processes at the crack tip and (b) the relevant phenomena in the crack enclave, associated with the slip-dissolution mechanism of crack advance, are shown in Figs. 16a and b, respectively.

The two significant processes involved in IGSCC of structural alloys in BWRs are as follows:

1. The creation of a crack tip environment that is noticeably different from the bulk environment due to mass transport of solvent cations (controlled by potential drop, convection, etc.), water, and anions within the crack enclave. The main factor that drives this process is the potential drop along the length of the crack,[205] created by the highly oxidizing conditions at the crack mouth.

2. The oxidation rate at the crack tip of the material whose composition may be significantly different from the bulk material (e.g., sensitization), and is being strained by the applied loads and residual stresses.

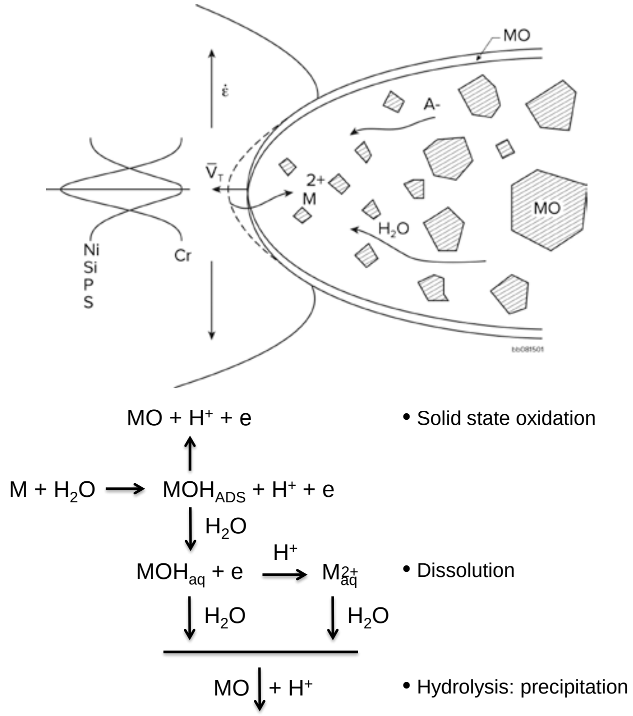

Figure 16a. **Schematic of the physical process at the crack tip, illustrating the large amount of precipitated oxide in the crack enclave (Ref. 205).**

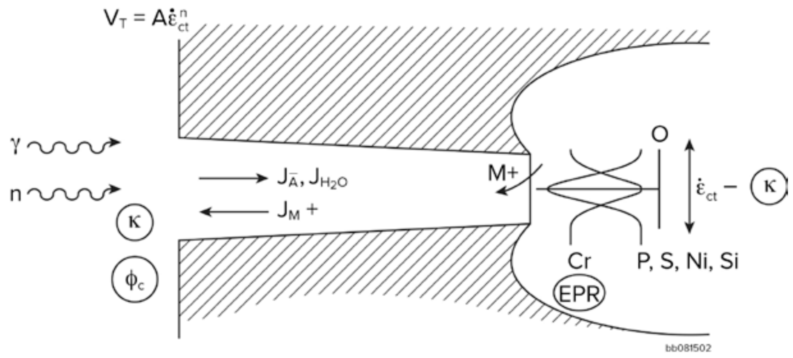

$$V_T = 7.8 \times 10^{-3} n^{3.6} \left[6 \times 10^{-14} K^4 \right]^n$$

$$n \left\{ \frac{e^{f(\kappa)}}{e^{f(\kappa)} + e^{f(\phi)_c}} \right\}^{f(EPR)}$$

Figure 16b. Schematic of the crack enclave and the relevant phenomena associated with the slip-oxidation mechanism of crack advance (Ref. 205).

Two basic approaches have been used to quantify the IGSCC process. Macdonald and coworkers directly coupled the total oxidation current emanating from the strained crack tip with the reduction rate at the crack mouth (involving oxygen and hydrogen peroxide).[206,207] A detailed description of the other approach by General Electric (GE) is presented in their Plant Life Extension Diagnosis by GE (PLEDGE) model for IGSCC evaluations in BWRs. The GE model equates the crack propagation rate to the oxidation kinetics in the localized crack tip environment of the strained crack tip material (Fig. 16a).[205,208] In this model, the corrosion potential at the crack mouth is considered an important component in creating a mechanism for anion and acidity concentration at the crack tip (Fig. 16b). The coupled environmental fracture model of Macdonald et al.[206,207] and the PLEDGE model by GE identify the same important parameters that control SCC of austenitic SSs in BWRs. These parameters include ECP, water conductivity, material sensitization, and stress intensity factor K, although there are some significant differences in the predicted cracking behavior at the extreme range of these parameters. However, the PLEDGE model is currently being used for GE BWRs in the United States; further details of the GE approach are described below.

The PLEDGE model considers that after the protective oxide film at the crack tip is ruptured, the oxidation rate and, therefore, the crack propagation rate will be rapid and controlled by the activation or diffusion kinetics of dissolution of the exposed metal surface. Furthermore, for most BWR systems where cracking would be of interest, a protective oxide is thermodynamically stable. It would reform via solid-state oxidation and/or precipitation from solution on the bare surface. As a result, the oxidation/dissolution rate will fall from the bare surface value, i_o, following a time period, t_o, according to:

$$i_i = i_o \, (t/t_o)^{-n}, \qquad (10)$$

where n is the repassivation rate parameter. As a result, the rate of total oxidation charge density and, therefore, crack tip advance will slow with time after the crack tip oxide is initially ruptured. Crack propagation can be maintained only if the oxide film rupture reoccurs. Thus, for a given crack tip environment, corrosion potential, and material condition, the crack propagation rate would be controlled by the change in oxidation charge density with time as well as the frequency of film rupture at the strained crack tip. The change in oxidation current density with time (and hence oxidation charge density) following the rupture of a protective film at the crack tip, is shown schematically in Fig. 17.[205] The frequency of film rupture will be determined by the fracture strain of the film, ε_f, and the strain rate at the crack tip, $(d\varepsilon/dt)_{ct}$.

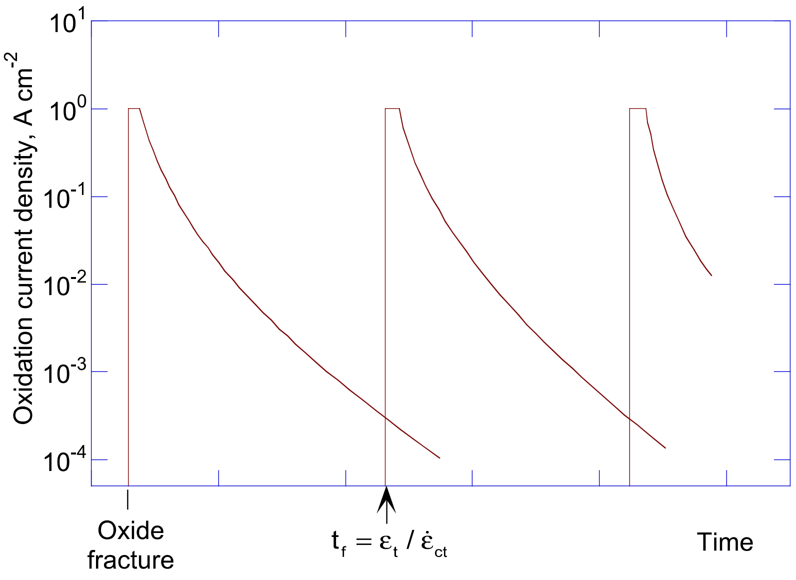

$$V = \frac{da}{dt};\ \bar{V}_{av} = \frac{M}{zpF} \cdot \frac{O_f}{t_f}$$

Figure 17. Schematic oxidation current density vs. time relationship for a strained crack tip (Ref. 205).

Hence, by invoking Faraday's law, the average environmentally controlled crack propagation rate, da/dt, is related to the strain rate at the crack tip, $(d\varepsilon/dt)_{ct}$, the oxidation rate at the bared crack tip (i_o), and the repassivation rate parameter (n), via:

$$da/dt = (M/zpF)\left[i_o t_o^n/(1-n)\varepsilon f^n\right](d\varepsilon/dt)_{ct}^n, \tag{11}$$

where M and p are atomic weight and density of the crack tip metal, respectively, F is Faraday's constant, and z is the number of electrons involved in the overall oxidation of an atom of metal.

The slip-oxidation mechanism may be applied to not only SCC, but also strain-induced cracking and environmentally assisted fatigue. Under constant load or displacement conditions for SCC, the crack tip strain rate will be related to the creep processes at a moving crack tip.[205] Under monotonic or cyclic bulk strain conditions for strain-induced cracking and corrosion fatigue, the crack tip strain rate is related to the applied strain rate.

However, to apply the PLEDGE model to address SCC concerns in BWR pressure boundary systems, it is necessary to redefine Eq. 11 for environmentally controlled crack propagation rate in terms of measurable engineering or operational parameters (Fig. 16b) as follows:

(a) Define the crack tip alloy composition in terms of the bulk alloy composition and heat treatment, and the crack tip environment composition in terms of the anionic concentration or conductivity, DO, hydrogen and hydrogen peroxide contents, or corrosion potential at the crack mouth, etc.

(b) Measure the reaction rates for the crack tip alloy/environment system that corresponds to the actual BWR system.

(c) Define the crack tip strain rate in terms of continuum parameters such as stress, stress intensity, loading frequency, etc.

The relevant fundamental reactions pertinent to crack tip systems have been extensively investigated. Based on the extensive work conducted in these areas for austenitic and ferritic alloys in BWR system, the basic parameters in Eq. 11 have been quantified. For austenitic SSs, Eq. 11 may be written as:

$$\mathbf{da/dt = 7.8 \times 10^{-3} n^{3.6} \left(d\varepsilon/dt\right)_{ct}^{n}}, \tag{12}$$

where da/dt is in units of cm/s, the crack tip strain rate is in units of per second, and the passivation rate parameter, n ,varies between 0.33 and 1.0. It is controlled by the crack tip environmental (e.g., pH, potential, anionic activity) and material conditions (e.g., percentage chromium depletion in grain boundary). The parameter n has been redefined in terms of measurable bulk system parameters such as water conductivity (K), corrosion potential (ϕ_c), and the electrochemical potentiokinetic repassivation (EPR) parameter. The corrosion potential is a function of the DO and hydrogen peroxide content, and EPR is related to the chromium depletion at the grain boundary. Thus,

$$\mathbf{n\left\{\frac{e^{f(k)}}{e^{f(k)}+e^{g(\phi)}c}\right\}^{h(EPR)}}. \tag{13}$$

In Eq. 12, the crack tip strain rate $(d\varepsilon/dt)_{ct}$ has been related to the engineering stress or stress intensity parameters. Under constant load, the crack tip strain rate is expressed in terms of the stress intensity factor, K, as

$$\mathbf{da/dt = 8.8 \times 10^{-14} K^{4}}, \tag{14}$$

where the strain rate is in units of per second (s^{-1}) and K is in MPa$\sqrt{m}$.

Later, the crack tip strain rate was modified to include the effects of crack advance. The changes in the associated stress field would activate further dislocation sources that would increase the crack tip strain rate proportional to CGR and the strain field in front of the crack tip. Therefore, the resulting crack tip strain rate would depend on a dynamic equilibrium between the CGR-dependent strain rate and the contribution due to exhaustion creep, which decreases with time at BWR operating temperatures. Thus,

$$\mathbf{\left(da/dt\right)_{ct} = \left(da/dt\right)_{creep} + \left(d\varepsilon/da\right)\left(da/dt\right)}, \tag{15}$$

where a is the distance in front of the original crack.

2.3.1.2 IGSCC Operating Experience

IGSCC has been observed in various BWR structural components during the past 50 years. These occurrences have been described in Volume 13C of the ASM Handbook.[209] The earliest incidents of IGSCC occurred in the BWR Type 304 SS fuel cladding. It was caused by the tensile hoop stress developed due to fuel swelling and the highly oxidizing water chemistry.[191] The problem was mitigated by replacing the SS cladding with zirconium alloys. In addition, there were several incidents of IGSCC in BWR subsystems. In late 1965, cracking was observed in weld HAZ of a 150-mm (6-in.) Type 304 SS recirculation bypass piping after the less than 6-y service. The cracking was attributed to compositional heterogeneity in the grain boundaries caused by the thermo-mechanical fabrication procedures.[191] By 1974, the phenomenon of SCC was recognized as a generic issue for Type 304 SS in BWRs.

During the mid-1970s, several incidents of IGSCC occurred in welded small-diameter (<250-mm [10-in.]) Type 304 SS piping. In 1978, IGSCC in a large-diameter 650 mm (26-in.) pipe was first observed in a foreign BWR. In the early 1980s, several cases of IGSCC were found in 710 mm (28-in.) diameter recirculation piping in domestic BWRs.[191] In 1992, IGSCC was observed in the HAZ of Ti-stabilized Type 321 SS pipe welds in German reactors. Several incidents of cracking were observed in systems containing reactor coolant at temperatures above 200°C (392°F), particularly in the reactor coolant cleanup and pressurized bearing water systems.[190] A few cases of IGSCC were also found in stabilized Type 347 SS. Failure analyses indicated that the root cause was welding-related thermal sensitization of the materials that contained relatively high C and a low stabilization ratio (Ti/C).

In the late 1990s, SCC was detected in the HAZ of a low-C Type 316NG pipe, in a Swedish reactor. Root cause evaluations indicated that cracking was due to very high residual strains in the HAZ caused by weld shrinkage.[210] From 2002, SCC cracks have also been observed in Type 316NG piping in several reactors in Japan. The root cause for cracking was surface cold work introduced in the material during the fabrication process and high residual strains caused by welding.

In addition to the piping, SCC cracking has also been observed in reactor vessel nozzles and penetrations. For example, several BWRs in the United States have experienced SCC cracking of the Type 304 SS control rod drive (CRD) stub tubes. High residual stresses in the sensitized weld material were attributed as the root cause for cracking.[211] In the late 1980s and 1990s, cracking of Type 304 SS in-core monitoring housing was found in several BWRs in Japan. In one case, cracking was through-wall and due to IGSCC in the HAZ of the housing attachment weld to the reactor pressure vessel, leading to leakage.

SCC in nickel-base Alloy 600 was first observed in the recirculation inlet nozzle safe ends of the Duane Arnold plant in 1978. Cracking had occurred in the HAZ of the thermal sleeve to safe end welds of all eight nozzles, and one of these was through wall. The cause of cracking was high residual stresses and crevice conditions due to thermal sleeve weld design.[212] Interdendritic SCC in Alloy 182 was first observed in the weld butters in the inlet/outlet nozzle safe ends at Pilgrim in 1984. Similar Alloy 182 cracking in nozzle safe end welds has been observed in several plants. IGSCC has also been observed in access hole covers and shroud head bolts. In 2001, leakage from a CRD stub tube due to SCC of Alloy 182 weld metal was found in a reactor in Japan. However, no other cracking of Alloy 182 at CDR stub tubes has been reported.

These incidences of IGSCC indicate the importance of water purity control and other preventive measures such as the use of low-C grades of SSs to avoid sensitization and weld overlays to reduce residual stresses caused by the welding process.

2.3.1.3 IGSCC Fracture Morphology

In IGSCC, cracks advance along crystal grain boundaries. Typically, the grain boundary facets are smooth. However, in some instances, the fracture morphology may appear IG at low magnification, while at high magnification the boundary facets reveal fan-shaped lines typical of a TG crack.[213] Solomon has termed such fracture as granulated fracture morphology. This morphology is produced by TG cracking in the Cr-depleted zone near the grain boundary. For austenitic SSs in LWR environments, fracture morphology is often a combination of IG and granulated fracture.

2.3.1.4 Critical Factors for IGSCC

Susceptible Material

In general, the susceptibility of a specific alloy to IGSCC strongly depends on the alloy microstructure and its metallurgical condition.[191] Examples of these alloys include weld-sensitized, furnace-sensitized, or cold-worked Types 304 and 316 SS and mill-annealed nickel-base Alloy 600 and as-welded Alloy 182 weld metal. Two major material factors contribute to IGSCC of structural alloys in BWR primary coolant systems: thermal sensitization and cold work. In BWRs, IGSCC of austenitic SSs and nickel base alloys occurred first in thermally sensitized materials, which were then replaced with low-C grades or stabilized grades. However, IGSCC subsequently occurred in these materials due to cold work introduced in the material during fabrication. Typically, the hardness of the material has been above 300 H_v. In most cases, the initial cracking was TG, which later changed to IG mode. The initial TG cracking was associated with a surface layer of cold work introduced by grinding or other severe surface machining techniques.

Thermal sensitization of non-stabilized austenitic SS containing greater than 0.030 wt.% carbon can make them susceptible to IGSCC, provided sufficient tensile stress is applied and the environment can maintain the corrosion reaction. When these SSs are furnace-treated or welded in a temperature range of approximately 550–580°C (1022–1076°F) for a sufficient time, $M_{23}C_6$ carbide precipitates at the grain boundaries because of the insolubility of carbon in the alloy. Since chromium provides corrosion resistance to austenitic SSs, the chromium is the predominant element in $M_{23}C_6$; carbide precipitation creates a chromium-depleted region at the grain boundary that is much less resistant to aqueous corrosion. In fact, the depleted region is no longer SS but a small area of low-alloy steel anode galvanically coupled to the large area of SS base metal cathode.[191] These thermally sensitized SSs are susceptible to IGSCC under the influence of a corrosive environment and sufficient tensile stress. A similar sensitization mechanism occurs in austenitic nickel-base alloys such as Alloys 600 and 182, which makes them susceptible to IGSCC.

Furthermore, cold work also increases the susceptibility for all forms of corrosion, including IGSCC or TGSCC in the BWR environment. [191] Cold work generally refers to plastic deformation that occurs in a specific temperature regime and for a time such that the strain hardening created by the deformation is not recovered. Examples of fabrication processes that produce cold work include turning, grinding, drilling, milling, cutting, shearing, stamping, hammering, and bending. The mechanism by which cold work affects the susceptibility of austenitic alloys to IGSCC is not well understood. An unfavorable interaction among deformation-induced martensite, high residual stress, and localized deformation is possible.[190] Studies on the effect of cold work and other associated metallurgical parameters on the susceptibility to IGSCC indicate the following.[191]

(i) Cold-worked Type 304 SS has the highest susceptibility to IGSCC in the BWR environment. Type 304 SSs with hardness greater than RB = 100 are susceptible to cold work-induced SCC in the BWR environment.

(ii) Cold work synergistically augments the kinetics of sensitization. The presence of cold work-induced martensite further exacerbates the effect on sensitization kinetics.

(iii) Although cold work and martensite do not produce sensitization, typical fabrication processes produce sensitization because of the high temperatures and stresses generated by the processes. Even low-carbon SSs can become highly susceptible to IGSCC because of the synergistic effects of cold work and sensitization.

Environment

The two parameters that help create an aggressive environment for IGSCC of BWR structural alloys are ECP and reactor coolant conductivity. The ECP is a measure of the tendency of an alloy for a corrosion reaction. It varies with the alloy's condition and its purity, metal and other ions in the solution, temperature, fluid velocity, current flow, etc. In a high-purity BWR coolant environment, the ECP of all structural alloys is primarily controlled by the level of DO in the coolant.[191] As mentioned earlier, IGSCC initiation of thermally sensitized SS is possible in highest purity water when the ECP is greater than –230 mV (SHE).[202] The ECP is primarily influenced by oxidizing radiolysis products, O_2 and H_2O_2, dissolved in the high-temperature water.[190] The main oxidant is H_2O_2, which exists transiently in direct cycle BWR systems. It decomposes quite rapidly to oxygen on out-of-core surfaces away from the radiation field.

The other parameter is reactor coolant conductivity, or the coolant's ability to conduct electricity. Typically, high-purity water has low conductivity; it conducts electricity because of the presence of hydrogen (H^+) and hydroxide (OH^-) ions produced by the ionization of water molecules.[191] The presence of other ions in the solution increases its conductivity, thereby increasing its ability to conduct electricity and thus, depending on the nature of the ions, increasing the kinetics of corrosion.

Another factor that can influence the environmental conditions is a creviced geometry, which can create water chemistries orders of magnitude worse than that indicated by the bulk coolant environment, as discussed in Section 3. The presence of crevices creates a large ECP difference between the crack mouth and the crack tip, lowers the pH, and increases the concentration of typical corrosive anions inside the crevice, all of which increase the susceptibility of even most materials that are resistant to IGSCC. This process is particularly true for Alloy 600, where cracking has typically occurred under creviced conditions.[191]

Mechanical Loading

As discussed in Section 3, applied stress is an important parameter for damaging or rupturing the protective oxide film during both initiation and propagation of cracks caused by SCC. Increasing the applied stress decreases the time for IGSCC initiation. In BWRs, most of the cracks occur near welds where the magnitude of residual stresses due to weld shrinkage is an important factor for both initiation of IGSCC and growth of these cracks. IGSCC cracks propagate primarily through the HAZ of the weld. For dissimilar welds, cracking occurs mainly in the Alloy 182 weld metal and, in some cases, propagates a short distance into the base metal.[190]

There are three types of mechanical loading in LWRs: (a) primary stresses from reactor operation including mechanical and pressure load stresses, (b) secondary stresses due to thermal gradients and transients, and (c) fabrication stresses that are introduced during machining or forming operations (e.g., surface grinding, bending, straightening, etc.) and more importantly welding.[191] Fabrication stresses can be quite high; there are numerous examples of IGSCC in reactor components with no externally applied stress. Unfortunately, the magnitude of fabrication stresses, particularly produced by welding or surface grinding, is not known. In addition, flaws and surface imperfections can act as stress raisers, increasing the local stress near the surface. Consequently, it is difficult to define a threshold stress for initiation of IGSCC in reactor components.

A threshold stress for IGSCC can be defined for some materials;[201] the stress dependence of IGSCC for furnace-sensitized Type 304 SS is shown in Fig. 18. However, this threshold is for normal reactor operating conditions. The threshold stress may change with variations in the environmental conditions. For example, if chloride or sulfate intrusions occur, the threshold stress for IGSCC would decrease, and cracks can initiate under “off normal” conditions.

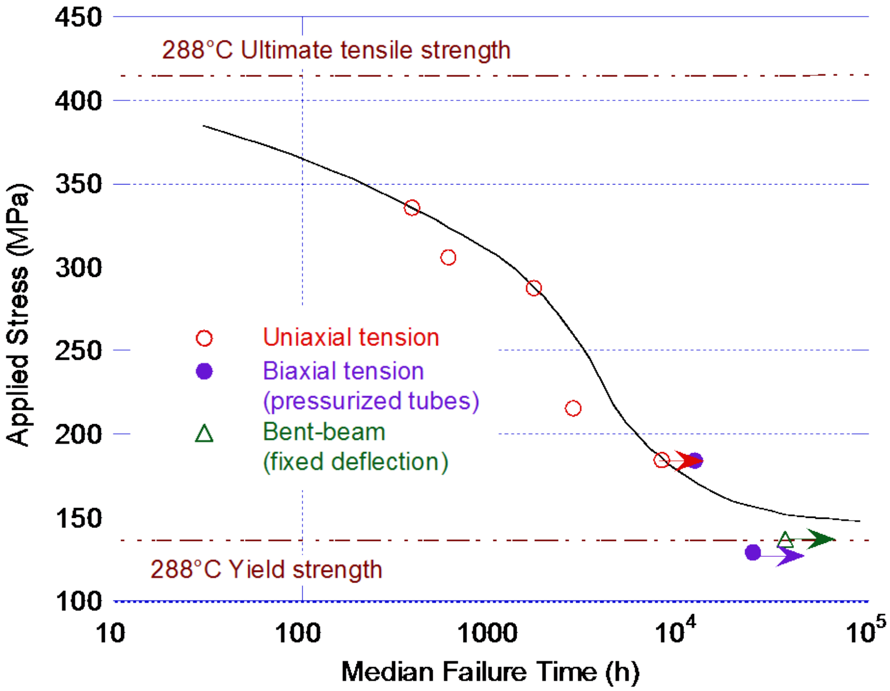

Figure 18. **Stress dependence of IGSCC of a furnace-sensitized Type 304 SS in 288°C (550°F) water with 0.2 ppm DO (Ref. 201).**

In contrast to crack initiation, the stress dependence of crack growth can be better defined. The SCC growth rates in base metal or HAZ can be correlated to the local stress intensity factor, K. Such calculations are more complex for welds because of the anisotropy of the weld metal microstructure.

Significant Parameters for IGSCC

The PLEDGE model for IGSCC evaluation in BWRs identifies and evaluates the interacting effects of mass transport within the crack enclave, oxidation or reduction rates at the crack tip and crack mouth, and the crack tip strain rate. The results have been used to identify the generic system changes that would reduce the extent of environmentally assisted cracking in LWRs.[214] For example, the relevant fundamental reactions pertinent to crack tip systems have been used to express the average environmentally controlled crack propagation rate in terms of the passivation rate and crack tip strain rate. Thus, since the passivation rate depends on the crack tip environment and the material condition, the crack propagation rate can be decreased by modifying the service environment and material conditions. Such information has been successfully used to predict the effects of Zn on oxide fracture strain and passivation rate, and the effects of chloride and sulfate on passivation rate.[205]

2.3.1.5 Preventive Measures

The preventive measures for IGSCC include improving all three critical conditions – a sensitized material, high tensile stress, and an aggressive environment – that lead to SCC of austenitic SSs and Ni alloys used in LWRs as structural materials. The comprehensive programs outlined in NUREG-0313, Rev. 2,[215] and NRC Generic Letter GL 88-01[216] describe improvements that would reduce the susceptibility to IGSCC.[2] A combination of both low C content and high stabilization ratio (e.g., Nb/C>13) can improve the resistance of the material to IGSCC in BWR environments.[190] However, although a high Nb/C ratio for Type 347 SS or a high Ti/C ratio for Type 321 SS improves the resistance to IGSCC, Nb/C>12 or Ti/C>8 promotes the formation of the ferrite phase, which can transform to the brittle sigma phase during a solution heat treatment process. Therefore, recent versions of specifications for Types 347 and 321 have limited the Nb/C or Ti/C ratios, respectively, below these values.[217]

Similarly, Alloys 600 and 182 have been modified with Nb additions to prevent thermal sensitization. In addition, Alloy X-750 has been used for high-strength applications in BWRs. Typically, Alloy X-750 is given an equalized and aged heat treatment, which is susceptible to IGSCC under BWR conditions. Therefore, another single heat treatment is used for Alloy X-750 in which the material is solution-annealed at 1093°C (1999°F) for one to two hours followed by aging at 704°C (1299°F) for about 20 h.[190] This treatment precipitates the strengthening gamma prime phase, $NiAl_3$ together with a fine, dense $M_{23}C_6$ carbide distribution at the grain boundaries; this microstructure is more resistant to IGSCC.

Proper material heat treatment, heat sink welding, and stress improvement using either induction heating stress improvement or mechanical stress improvement techniques decrease the residual stresses in the material, thereby reducing the susceptibility of the material to IGSCC.[216] Reinforcement of cracked welds with weld overlay is also acceptable for short-term operation. In addition, adequate measures should be taken to avoid introducing excessive surface cold work during fabrication machining processes. Furthermore, the use of EPRI water chemistry guidelines (e.g., EPRI 1016579 or BWRVIP-190 for BWRs and EPRI 1014986 for primary coolant in PWRs), stringent control of conductivity, and measures to prevent chloride contaminations can significantly reduce susceptibility to IGSCC.[2]

2.3.2 Transgranular Stress Corrosion Cracking

Another form of SCC that has been observed in both BWRs and PWRs is TGSCC of austenitic SSs. It can occur even in solution-annealed austenitic SSs, in the absence of material sensitization, if it is subjected to high stress and an oxygenated water environment contaminated with chlorides. Other halide anions such as fluoride can also cause TGSCC. It can also occur in sensitized SSs, subjected to a high-stress, corrosive environment, and when the component surfaces have been abused by grinding or other machining or fabrication process. The sources of chloride contamination are component insulation and ambient air. Marine environments are commonly chloride-contaminated, and a large industrial complex can emit chloride in the form of chlorine-contaminated air. For external surfaces, the temperature range of concern is from about 50°C to 100°C (122°F to 212°F); the upper temperature depends on the dew point of the environment for condensation to occur.[1]

Typically, the surface must be wet at least part of the time for SCC to occur. Wetting due to condensation or nearby water leaks results in the formation of an aqueous environment, which in the presence of contaminants can cause TGSCC. Furthermore, TGSCC is usually accompanied by pitting or crevice corrosion.[190] The stress required for chloride-induced TGSCC is relatively modest, the threshold being close to the proportional limit of solution-annealed austenitic SSs.[190] TGSCC cracks are crystallographic in nature with well-defined slip steps that are generally along crystallographic planes.[218] The cracks always propagate perpendicular to the applied stress. Under relatively high tensile stresses, many microcracks associated with slip bands are created, all propagating perpendicular to the applied stress. These cracks eventually coalesce into a larger crack.

It is, therefore, apparent that TGSCC would not be expected to occur under normal operating water chemistry conditions for BWRs and PWRs. However, TGSCC can occur on internal surfaces of reactor components. A common occurrence of such TGSCC is in the dead legs and stagnant systems where chloride contamination and oxygen concentration can build up with time, leading to SCC of both solution-annealed and sensitized SSs.[1] TGSCC is of particular concern if the material surface is highly cold-worked. Typically, depending on the material composition and degree of sensitization, both IGSCC and TGSCC can occur in the same material; IGSCC may transition to TGSCC morphology or TGSCC may transition to IGSCC morphology. The mechanism for TGSCC is not well established. Depending on the nature of the material deformation behavior ahead of the crack tip, several mechanisms have been proposed. A brief description of these mechanisms is presented below.

2.3.2.1 Proposed Mechanism of TGSCC

Dissolution Mechanism

The GE slip oxidation/dissolution model[203,205] is the earliest model proposed for IGSCC in BWRs, in which crack advance occurs primarily by dissolution. The model considers that a strain increment occurs to rupture that film, thereby exposing the underlying matrix to the environment. Once the passive oxide film is ruptured, crack extension is controlled by dissolution of freshly exposed surfaces and by the oxidation characteristics. However, the typical fracture morphology observed in TGSCC is not consistent with a simple dissolution process.

Lichter et al.[219] have recently proposed a stress-assisted directed-dissolution model, which considers that high elastic stresses stretch the interatomic bonds such that rates of dissolution are increased by an order of magnitude. Dissolution is directed along low-index crystallographic planes to minimize the energy for bond breaking, as atoms are removed from the lattice. However, some dislocation emission from a crack tip is necessary to open cracks and allow solution access and diffusion of ions away from the crack tip. Qiao and Mao[220] have suggested that in material/environment combinations where hydrogen is generated, the dissolution rate may be increased because interstitial hydrogen would weaken the bonds.

Corrosion-Enhanced Localized Plasticity

The corrosion-enhanced plasticity model for SCC in ductile face-centered cubic (FCC) alloys such as Type 316L SS has been proposed by Magnin et al.[221–223] The model is based on a corrosion-deformation interaction at the crack tip. It emphasizes that both localized anodic dissolution and localized hydrogen entry into the alloy can enhance the local plasticity. A schematic diagram of the different stages of the corrosion-enhanced plasticity model is shown in Fig. 19. The model considers the following events at the crack tip:

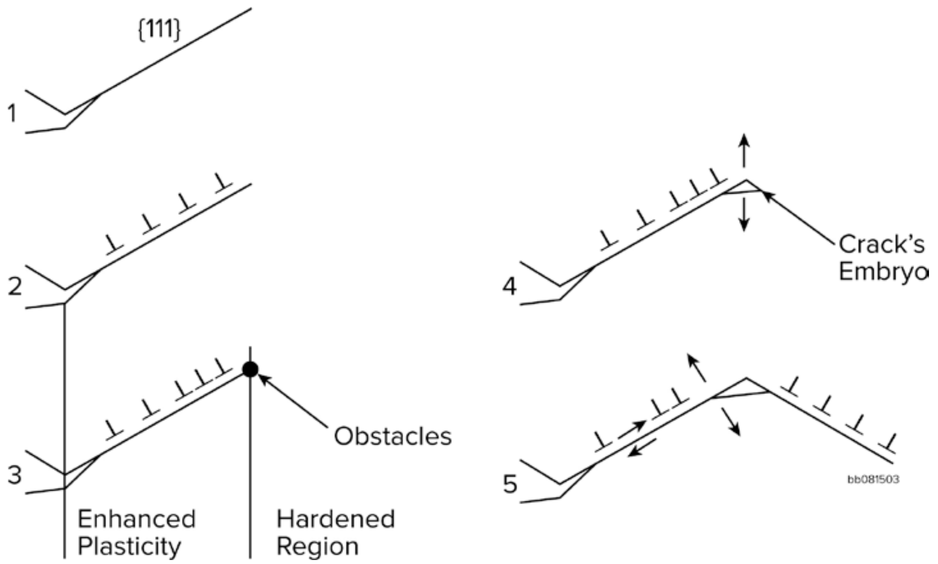

Figure 19. Schematic diagram of the different stages of the corrosion-enhanced plasticity model (Ref. 223).

(1) After depassivation, localized anodic dissolution takes place on the {111} slip planes at the crack tip. This induces a slip step formation. This is a necessary first step that leads to corrosion-deformation interactions in smooth specimens. An enhanced localized plasticity then occurs because of the localized corrosion on {111} slip planes. The localized shearing on these planes is favored by dissolution and adsorption. More mobile-dislocations can be injected because of stress concentration and vacancy production due to localized dissolution, and because of adsorption and absorption of hydrogen, which can lower the critical shear stress. Crack blunting is reduced. Thus, the role of corrosion (dissolution and adsorption) is essential but indirect; it enhances the local plasticity at the crack tip.

(2) The enhanced plasticity is localized near the surface. Dislocations that are emitted would then interact with obstacles such as precipitates, grain boundaries, or previously formed dislocation configurations (e.g., bundles and Lomer locks). Two zones are considered: an enhanced plasticity zone blocked by a previously hardened zone. This will lead to the formation of dislocation pile-ups and an increase in local stress.

(3) If the obstacles are strong enough, the local critical stress intensity factor, $K_{Ic,}$ will be reached, particularly if it is lowered by the absorption of hydrogen. Thus, a crack

embryo will form by a Stroh-like mechanism[****] for nucleation of a crack, at the obstacle.[221,222]

(4) The energy of decohesion of the {111} microfacets can decrease because of absorption of hydrogen. The normal stress on these facets can be sufficient to open the crack along the {111} plane. Dislocations are then emitted on a symmetrical plane relative to the general crack plane, shielding the new crack tip. Depending on the crystallographic orientation, this cracking can occur mainly on {111} or sometimes on {100} and {110} facets.

(5) This process is expected to lead to regular changes of crack planes, resulting in a zig-zag microcracking on {111} and/or {100} facets.

The model assumes that once blunting is decreased and the crack is sharp, dislocations are nucleated on a preferential slip plane, depending on the local loading mode versus the orientation of the grain. Thus, the approach is similar to the classical problem of cleavage due to pile-ups produced by Frank-Read sources.

Corrosion-Assisted Cleavage

The proposed corrosion-assisted cleavage mechanism is similar to the previous mechanism and considers that dissolution is occurring along a {111} slip plane to produce a “dog-leg” (similar to events 1–3 above), which along with a dislocation pile-up, increases the stress on a Lomer-Cottrell lock at the head of the pile-up such that a cleavage crack nucleates at the lock.[198] However, the cleavage crack is proposed to propagate along the {111} plane, with further dissolution along the {111} plane. A schematic drawing of the process is shown in Fig. 20.

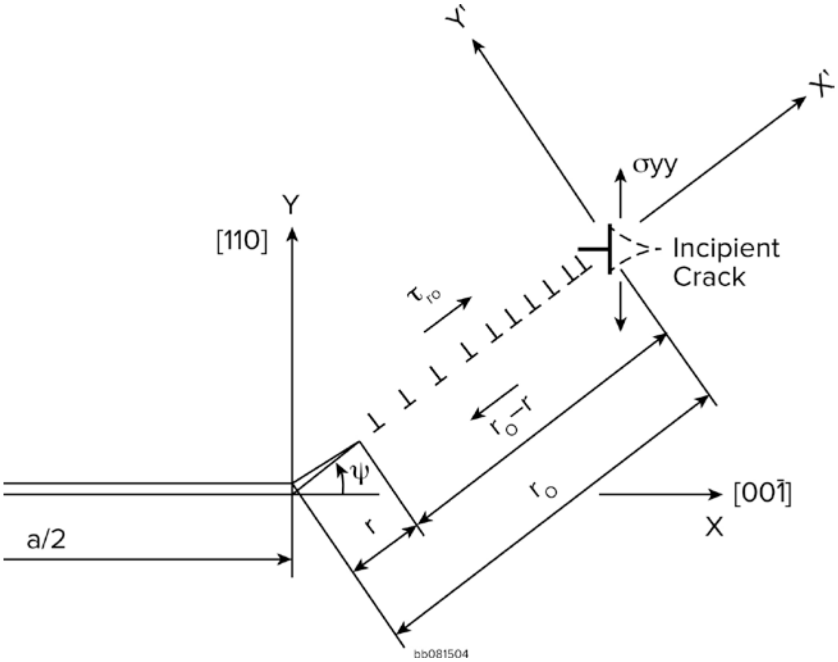

Figure 20. Schematic diagram of the different stages of the corrosion-enhanced plasticity model (Ref. 198).

[****] The mechanism by which a piled-up group of dislocations generates a crack at the head of the pile-up.

Thus, the model considers that the re-initiation of cracking results from dissolution-assisted failure of Lomer-Cottrell locks, and that the ensuing microfacets form because of the stress-enhanced dissolution of atoms from the resulting sharp crack tip. This microfacet growth is temporarily stopped by dislocation emission from the crack tip when the diffusion rate of the complex ions away from the tip is inadequate.[198] This slows down its growth, allowing activation of slip to occur. The microfacets are delineated by slip on the secondary planes, which shears the ligaments. Because the ligaments form on different planes, these ligaments have the effect of restraining the crack opening displacement (COD), which, in turn, controls the effective stress intensity factor acting upon the crack. However, continued shearing of the ligaments, enhanced by dissolution, continually raises the stress intensity factor, causing further growth. The microfacet growth is determined by the change in local COD, thereby allowing the electrolyte to reach the crack tip.

Selective Corrosion Vacancy Creep

According to this model,[224] a high concentration of vacancies is produced by selective corrosion or dissolution of iron. These vacancies diffuse ahead of the cracks and promote dislocation climb and cross slip, thereby localizing deformation or creep near the crack tip. In addition, vacancies could cluster to form nano-voids along low-index crystallographic planes. A combination of vacancy-enhanced creep and vacancy clustering is considered to result in cleavage-like cracking.

Adsorption-Induced Dislocation Emission

The adsorption-induced dislocation emission model[225–227] considers that the interatomic bonds at the crack tip are weakened because of adsorption of environmental hydrogen atoms within several atomic layers of the crack tip surface, as well as hydrogen at the surface, thereby facilitating dislocation emission.[228] A schematic diagram of the adsorption-induced dislocation emission is shown in Fig. 21. Unlike ductile materials where void formation occurs around particles or other sites in the plastic zone ahead of the crack tip, crack growth in some FCC materials, such as austenitic SSs, occurs by slip from the crack tip as well as void formation ahead of the crack tip. According to this model, diffusion or dislocation transport of hydrogen, although not required, may also occur, resulting in hydrogen adsorption and dislocation emission from the tips of voids. Thus, the macroscopic fracture planes bisect the angle between the active slip planes, and the crack front lies along the line of intersection of crack planes and slip planes.[228] For example, {111} fracture planes and <110> directions of cracking can be produced when alternate slip occurs on {111} planes. Small dimples would be observed on the fracture surface at high magnification.

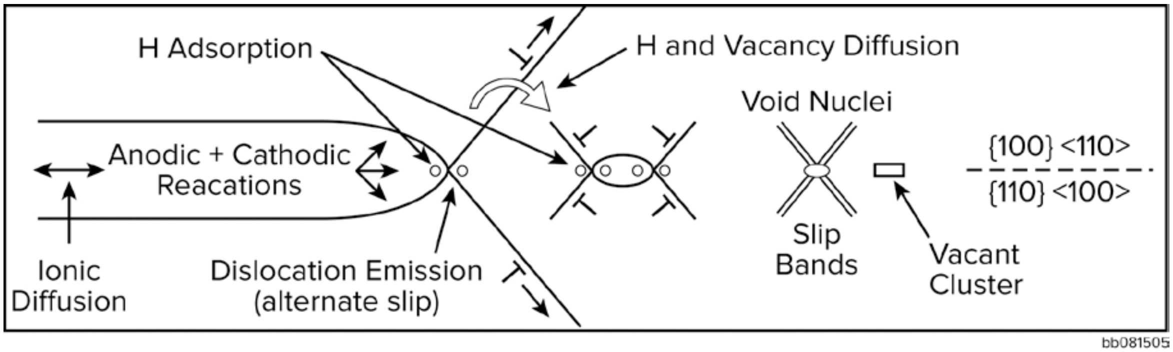

Figure 21. **Schematic diagram illustrating adsorption-induced dislocation emission mechanism (Ref. 228).**

Hydrogen-Enhanced Decohesion

Decohesion is the oldest and most commonly considered mechanism for hydrogen embrittlement. It is associated with embrittlement because of the decrease in the atomic bond strength due to the local concentration of hydrogen. The main issue in determining the applicability of this mechanism in hydrogen embrittlement depends on whether hydrogen causes a sufficient decrease in the separation energy or the cohesive stress under conditions that lead to fracture.[229] However, there is no definitive evidence to support a significant decrease in either the separation energy or the cohesive stress. The decohesion mechanism remains a possible failure mechanism.

Hydrogen-Enhanced Localized Plasticity

This mechanism has been supported by the work of Lynch[227] and Birnbaum et al.[229–231] on several structural alloys, including austenitic SSs and Ni alloys. In recent years, it has become evident that, unlike the common belief that hydrogen-related “brittle” fracture is based on loss of macroscopic ductility, it may in fact be associated with locally enhanced plasticity at the crack tip. Because the distribution of hydrogen can be non-uniform under an applied stress, locally the flow stress can be greatly reduced leading to localized deformation and failure by ductile processes. The overall macroscopic deformation remains small. The macroscopic fracture by such a process would appear brittle because of the highly localized nature of the ductile failure. Both investigations agree that addition of hydrogen can decrease the flow stress and lead to strain localization. However, Lynch views the process as a surface effect, whereas Birnbaum et al. consider it to occur in the volume of the material as well as at the surface.

The most likely location for entry of hydrogen into the material from external sources is the crack tip because that is where plastic deformation occurs and where surface barriers to hydrogen ingress are minimized. The presence of hydrogen in solid solution decreases the resistance to dislocation motion due to obstacles, and therefore decreases the stress for plastic deformation.[229] Thus, the flow stress is decreased in regions of high hydrogen concentrations at the crack tip and other elastic singularities. Dislocation slip occurs in these regions at stress levels well below those required for deformation in other parts of the material (i.e., slip localization), which leads to fracture.

2.3.2.2 TGSCC Operating Experience

The most common occurrence of TGSCC of austenitic SSs (e.g., Types 304 and 316 SS) in nuclear power plants is the external surfaces of components under wet insulation or pipes exposed to chloride-contaminated marine environments or large industrial complexes that emit chloride or chlorine-contaminated air.[1] Insulation can get wet from reactor coolant leakage from adjacent components or by getting soaked from fire sprinkler action. Chlorides leaching out from the insulation deposit on the component surface, eventually reaching a concentration that can cause TGSCC in highly stressed areas near welds or bends.

In addition, as mentioned earlier, there are several incidences of TGSCC from internal surfaces of components in dead legs and stagnant systems where chloride contamination and oxygen concentration can build up with time.[1] One location that has been frequently affected by TGSCC in PWRs is in canopy seals that assure the pressure boundary of threaded connections in the CRDM housings that are located above the reactor pressure vessel head. The CRDM penetration attached to the reactor vessel closure head consists of a Ni-alloy tube section welded to the head adapter flange, which has three threaded joints and seal welds at three different levels. The top canopy seal weld is the third weld between the rod travel housing and the canopy lip. Because the DO content inside the canopy seal weld can increase during plant start-ups, SCC of the seal weld is a potential concern. Furthermore, since the canopy seal welds are dead-end cavities, the welds are susceptible to TGSCC because of potential contamination of chlorides from lubricants used for threads. Such leaks have also caused boric acid corrosion of the reactor pressure vessel head low-alloy steel. Other locations include instrumentation lines and other small-diameter lines.

2.3.2.3 TGSCC Fracture Morphology

For austenitic SSs in LWR environments, TGSCC fracture has a discontinuous cleavage-like fracture morphology with crack arrest markings.[224,228] Typically, the fracture surface contains several secondary cracks that extend away but in the direction of the macroscopic crack propagation direction (MPD), giving it a fan-like appearance (also referred as a river pattern). The crack propagation direction changes at twin boundaries or grain boundaries, and crack growth is intermittent.

Zhu et al.[232] have characterized the TGSCC fracture morphology in Type 316L SS. A river-like fractograph in a Type 316L SS single crystal tested in boiling 45 wt.% $MgCl_2$ solution under a nominal stress of 20 MPa is shown in Fig. 22. The MPD, marked by dotted lines, is smooth and continuous, and approximately from several to more than ten microns in width. A number of secondary cracks and steps, marked by arrows, emanate from the MPD and extend toward both sides of MPD at an angle. In this example, the mid-width of the crack acted as the nucleation site of numerous secondary cracks and steps. The angled extension of a few secondary cracks and steps resulted in the formation of the discontinuous surface morphology.

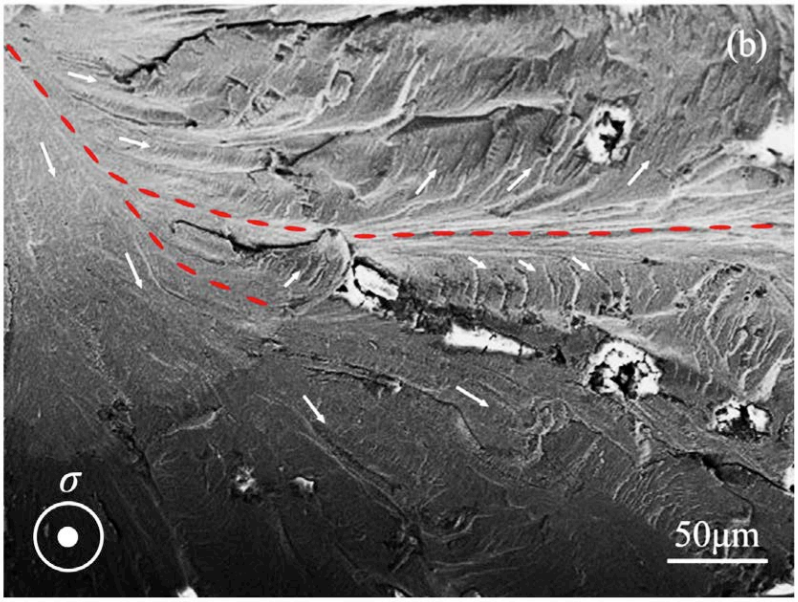

Figure 22. **Typical river-like fractograph of microcracks in a Type 316L SS single crystal tested in boiling 45 wt.% $MgCl_2$ solution under a nominal stress of 20 MPa. The dotted lines mark the propagation direction and arrows mark the discontinuous secondary cracks and steps emanating from the propagation direction (Ref. 228).**

2.3.2.4 Critical Factors for TGSCC

Similar to the significant parameters identified for IGSCC, increasing the passivation rate at the crack tip by controlling the corrosion potential/anionic activity combinations or by changes in material composition increase the resistance for TGSCC. The crack tip strain rate can be decreased by modifying the service environment and material condition, thereby improving the cracking resistance. The overall rupture frequency for the protective oxide film controls the CGR for TGSCC.

In addition, buildup of the oxygen concentration or the chloride contamination in the reactor coolant or the introduction of residual stress/strain from surface cold work, such as grinding or other machining or fabrication process, increase susceptibility to TGSCC. Furthermore, for TGSCC, external surfaces have to be wetted at least part of the time. Therefore, the temperature has to be in the range 50 to 100°C (122 to 212°F), depending on the dew point. For internal surfaces, the likely locations for TGSCC are dead legs or stagnant systems where chloride contamination and oxygen concentration can build up leading to TGSCC.

2.3.2.5 Preventive Measures

The preventive measures discussed for IGSCC are also applicable for preventing TGSCC. In addition, preventing chloride contaminants from accumulating on external surfaces by periodic washing or on internal surfaces in dead legs or stagnant systems by periodic flushing can decrease the likelihood of buildup of chloride contamination. Furthermore, implementing adequate measures to prevent introduction of surface cold work, due to grinding or other severe fabrication process, also decreases the susceptibility of TGSCC.

2.3.3 Primary Water Stress Corrosion Cracking

Primary water stress corrosion cracking has been a significant aging degradation mechanism for PWRs. Unlike IGSCC, which occurs in oxygenated water (i.e., at high corrosion potentials), PWSCC occurs in a PWR primary coolant environment with low DO content (i.e., low corrosion potentials). Primarily, it affects Ni alloys such as Alloy 600 and associated weld metals such as Alloys 132/182/82. It also affects high-strength Ni-alloy fasteners and springs fabricated from precipitation-hardened Alloys X750 and 718. Only a few cases of PWSCC of sensitized or cold-worked austenitic SSs have been reported.[233–235] The fracture morphology of PWSCC can be either IG or TG in Ni-alloys; typically, it is IG. Studies in 1959 at the French atomic research center showed that IGSCC could occur in Alloy 600 exposed to nominal high-temperature water.[236] The results indicated that the corrosion potential is a critical parameter for PWSCC in PWRs, which, unfortunately, was an uncontrolled parameter in earlier studies. In PWRs, the hydrogen partial pressure is maintained at a level that prevents the decomposition of water by radiolysis. However, it is in the exact range for PWSCC susceptibility of Ni alloys.[237]

The conditions for SCC or general corrosion under LWR operating environments are shown on a Pourbaix diagram for nickel and iron in Fig. 23. In PWRs, the water in primary and secondary coolant systems is alkali treated and free of oxygen to minimize general corrosion as well as corrosion product release rates of structural materials.[234] The use of lithium hydroxide and boric acid in the primary coolant system fixes the pH at operating temperature to about 6.8 and 7.4; typically, it is above 7. In addition, the primary water contains 20–30 ml (STP) per liter (or 1.8-4.5 ppm) dissolved hydrogen (DH). As a result, the primary system corrosion potential is close to the H_2/H^+ redox potential (or reduction potential) for nearly all structural materials.

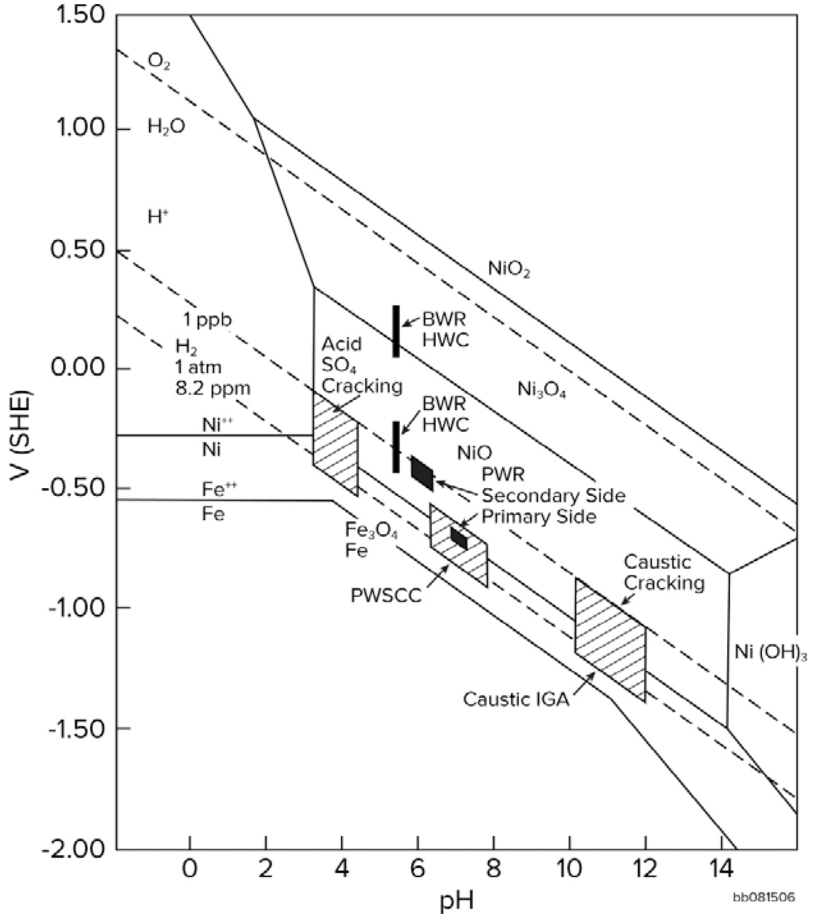

Figure 23. Pourbaix diagram for nickel and iron at 300°C (572°F) showing the principal pH vs. potential combination for PWR primary and secondary water and BWR normal and hydrogen water chemistries and the modes of SCC for Alloy 600 (Ref. 234).

In contrast, the reactor coolant system in BWRs contains high purity water to ensure low corrosion rates. In NWC BWR plants, radiolytic decomposition of water as well as removal of non-condensable gases at the turbine condenser establish a significant amount of DO and hydrogen peroxide in the coolant. Therefore, the corrosion potential is 500 mV more than in a PWR coolant environment. In HWC BWR plants, to prevent IGSCC of sensitized and cold-worked SSs, hydrogen is added to the coolant to decrease corrosion potentials to values between those of NWC BWR and PWR primary systems. The pH-potential combinations for SCC in primary and secondary coolant environments and NWC and HWC BWR environments are identified in Fig. 23.

2.3.3.1 Proposed Mechanism of PWSCC

Although extensive studies have been conducted during the past 40 years on cracking of structural materials in PWR environments, there is no consensus regarding the nature of the cracking mechanism. Both estimations of component life and preventive measures for PWSCC are based on empirical, phenomenological correlations. It is well known that the critical parameters that control PWSCC include the presence of high residual stress, cold work, temperature, and carbide morphology in the material. In addition, the partial pressure of hydrogen has a significant effect on cracking. The susceptibility to PWSCC is the greatest when the hydrogen corrosion potential is near the Ni/NiO equilibrium (Fig. 23).[238] It decreases at both higher and lower potentials within a narrow range of ±80 mV. This is a classical sign of an oxidation/dissolution-controlled mechanism of SCC.[239] The existing data also indicate that the mechanism of cracking does not apparently change between 300°C (572°F) sub-cooled water and 400°C (752°F) superheated steam.[234]

Most of the proposed mechanisms for PWSCC fall into two categories: (a) evolution of hydrogen at the cathode within a crack and (b) oxidation/dissolution of metal at the crack tip. The significant models for PWSCC are described below.

Hydrogen Embrittlement Mechanism

Several models based on hydrogen embrittlement have been proposed for PWSCC of structural materials in PWRs. The models involve (i) diffusion of hydrogen to a small zone of metal at the crack tip and (ii) the concentration of hydrogen within this zone. The presence of hydrogen leads to atomic-scale decohesion or hydrogen-induced fracture of the metal. However, none of these hydrogen embrittlement models explains the observed decrease in PWSCC susceptibility with increasing DH after a maximum susceptibility observed at the Ni/NiO transition.

Oxidation/Dissolution Mechanism

This model involves metal oxidation at the crack tip. The mechanism may involve metal dissolution as in the slip dissolution/oxidation model or other features of in-situ metal oxidation. The model is also known as the slip-oxidation, de-alloying, or vacancy injection and surface diffusion model. A common observation in PWSCC failures of Alloy 600 and its associated weld metals is the presence of very high residual stresses exceeding the nominal yield strength, often combined with a roughly machined or heavily ground surface finish.[234] The other major factors influencing SCC cracking are material microstructure and temperature. For example, Cr carbide precipitates at the grain boundaries improve the resistance to cracking, whereas intragranular carbides have the opposite effect. Even sensitized materials, with grain boundary carbides and an adjacent narrow zone of Cr depletion, have improved resistance to SCC cracking in PWR water, which is in sharp contrast to their poor resistance in oxygenated BWR NWC.

The existing data suggests that the oxidation process is more likely to explain the major experimental observations of PWSCC. The cracking rate is controlled by solid-state ion diffusion. Although the slip/dissolution and solid-state diffusion models for PWSCC are related, they differ in terms of the mechanisms that control CGRs.

Internal Oxidation Mechanism

The conventional mechanisms, based on anodic slip dissolution or hydrogen embrittlement discussed above, have not been able to explain adequately the process of PWSCC. An alternative mechanism has been proposed for PWSCC based on internal oxidation.[240] This model adequately explains the high activation energy and stress exponent observed for PWSCC crack growth, as well as the influence of hydrogen overpressure, grain boundary carbide morphology, and cold work on PWSCC.

In internal oxidation, the minor element in an alloy is preferentially oxidized while the solvent metal remains largely unattacked. Consequently, a necessary condition for internal oxidation is that the redox or reduction potential of the environment has to be close to the equilibrium oxidation potential on the solvent metal to prevent it from forming a protective surface oxide film.[241] Therefore, the minor element should not exceed a critical concentration where it can develop a protective surface film independently. In Ni-Cr alloys, the critical concentration of Cr for passivation at the Ni/NiO equilibrium increases with decreasing temperature.[241]

This model considers that for PWSCC initiation, oxidation causes damage to the metal surface leading to grain boundary oxidation and embrittlement, which leads to IG microcracks under applied stress. A schematic diagram of the internal oxidation PWSCC mechanism is shown in Fig. 24. In addition, the crack propagates by alternating grain boundary oxidation/embrittlement and crack advance in the oxidized and embrittled grain boundary.

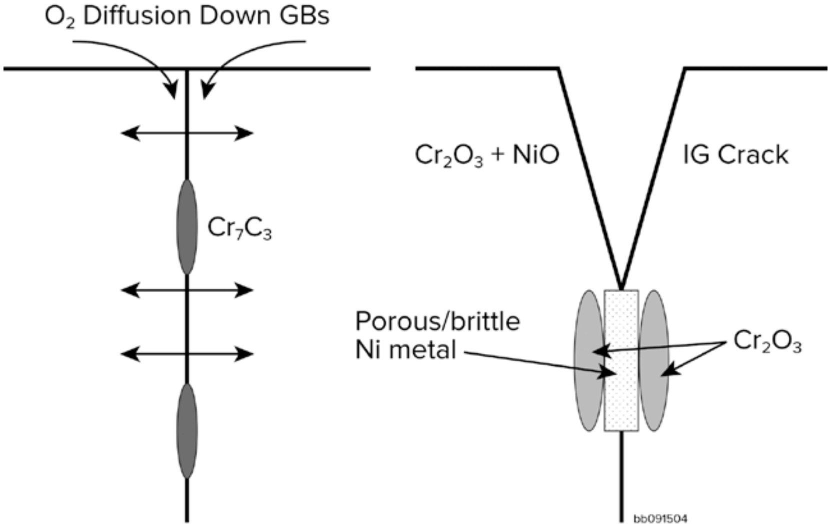

Figure 24. Schematic diagram of internal oxidation mechanism for PWSCC of Ni-Cr alloys (Ref. 242).

2.3.3.2 PWSCC Operating Experience

Nickel Base Alloys

Stress corrosion cracks have been detected in mill-annealed Alloy 600 steam generator (SG) tubes since the 1970s. These failures led to several experimental investigations and an extensive in-service inspection and maintenance program related to PWSCC.[243–246] By 2014, all SGs with tubes fabricated from mill-annealed Alloy 600 were replaced with tubes made from a more SCC resistant Ni alloy. Similar SG replacements have also occurred in the United States. To improve the SCC resistance, the mill-annealed Alloy 600 product was given a heat treatment at 715°C (1319°F) for 5–12 h (known as the thermally treated Alloy 600TT). Although the heat treatment was designed to reduce residual stresses due to fabrication processes, it proved beneficial for IGSCC resistance because of a semi-continuous precipitation of a network of $M_{23}C_6$ carbides at the grain boundaries. The nature and the grain boundary coverage of the carbides play an important role in improving resistance to PWSCC. However, although the resistance of Alloy 600TT to both PWSCC initiation and propagation is greatly improved, the alloy is not completely immune to PWSCC. Many tubes of Alloy 600TT have cracked in service in the roll transition zone.[244] The probability of PWSCC decreases when the grain boundary coverage is greater than 35% throughout the material.[243] The higher the yield stress, the lower the initiation time. It is believed that preferential oxidation of the carbide delays grain boundary oxidation, the primary mechanism of PWSCC; oxidation of Cr in the carbides is thermodynamically favored compared to that in the surrounding Alloy 600 matrix.[237]

Furthermore, such a boundary provides a more torturous diffusion path for grain boundary oxidation.

In addition, several incidences of PWSCC have occurred since 1989 in wrought Alloy 600 components such as CRDM nozzles,[247–252] pressurizer instrument nozzles[247] and heater sleeves,[235] SG drain nozzles,[248,253] bottom-mounted instrumentation nozzles,[254] and safe-end nozzle welds.[255–258] Other examples of Ni-alloy PWSCC are cracking of SG divider plates and divider stubs[259] and guide tube support pins.[260,261] The safety concerns related to PWSCC of the latter are damage to the fuel- or safety-related components due to loose parts, whereas, collapse of the divider plates is considered unrealistic.

In 1989, a primary water leak was detected in a pressurizer nozzle during a hydrostatic test in France. Another leaking nozzle was found during a hydrostatic test a month later in another plant. In all French PWRs, the pressurizer nozzles were made from wrought Alloy 600. Detailed metallography of the failed components indicated that these leaks were caused by PWSCC. By 1992, the Alloy 600 components were replaced with austenitic SS components.[237]

Similarly, in September 1991, during a hydrostatic test, a minor leak was detected in one of the CRDM penetrations on the reactor vessel head of Bugey 3 reactor in France. A detailed examination of the defective penetration revealed a dozen axial cracks up to 8 mm (0.3 in.) long. The cracks had IG fracture morphology and were grouped at the 0° and 180° locations along the circumference of the tube. No circumferential cracks were detected. During the early 1990s, similar inspections of other plants revealed several other CRDM penetrations with PWSCC cracks (2.8% of the penetrations).[237] In 1994, Electricité de France (EdF) decided to replace all Alloy 600 CRDM penetrations with Alloy 690, welded with Alloy 152.

The first evidence of PWSCC of CRDM nozzles in the U.S. PWRs occurred in 2000. However, unlike the French PWRs where the cracks were always axial, some circumferential cracking occurred in a few U.S. plants. The NRC issued Bulletin 2001-01, “Circumferential Cracking of Reactor Pressure Vessel Head Penetration Nozzles,” after the discovery of cracked nozzles in 2000 and 2001 at Oconee Units 2 and 3.[262] At Oconee Unit 3, two CRDM nozzles had through-wall-circumferential cracks above the J-groove attachment weld. The cracks had initiated from the outside diameter of the CRDM nozzle under the vessel head. The presence of circumferential cracks raised safety concerns because of possible nozzle ejection and risk of a loss of coolant accident.

Austenitic Stainless Steels

The NPP primary pressure boundary components are fabricated from austenitic SSs. Their operating experience in PWRs during the past 40 years has been generally good. Based on appropriate design, fabrication processes, and primary water chemistry, unsensitized austenitic SSs have not suffered from PWSCC.[195,263,264] The few exceptions are severely cold-worked materials by processes such as grinding or other machining or fabrication processes[265–268] or in the presence of chlorides or sulfates in oxygenated water.[269,270] Cracking due to SCC has been observed in austenitic SS components in the (a) dead legs of auxiliary systems connected to the primary loop, (b) canopy seal welds between the vessel head penetrations and the CRDM, and (c) leak-off connections to the packing box of valves.[263]

Metallurgical studies, conducted on austenitic SS components withdrawn from French PWRs,[263] showed TG branches in the dead-leg components were always associated with chloride contamination. The initiation of SCC was often at pitting sites, which indicated that the environment was near neutral or weakly acidic. The chloride-induced SCC was enhanced by relatively high DO content; oxygen was suspected to be present in the dead legs because of insufficient venting before pressurization of the primary system. In Type 316L SS, SCC degradation was typically detected after 30,000 to 70,000 h operation at about 200°C (392°F).

In French PWRs, SCC in canopy seal welds has been observed since 1992, after 8,000 to 80,000 h operation.[263] SCC in canopy seal welds was first observed in the United States at the end of the 1980s.[271] Metallurgical studies on leaking canopy seal welds removed from French PWRs also showed TG cracks that had initiated on the inner surface exposed to the reactor coolant environment at about 195°C (383°F). These cracks propagated through the base metal of the CRDM or the vessel head penetration flange and/or the weld metal, to the outer surface. Similar TG cracks oriented at 70°C (158°F) to the pipe axis have also been observed in leak-off connections to the packing box of valves in French PWRs since the early 1990s. The inner surface of these connections were exposed to water at 150–328°C (302–622°F) and contained high concentrations of chlorine and sulfur because of leaching from the packing.

During the 2004 refueling outage at the Ringhals 4 reactor, leakage was observed through the middle canopy seal welds of four CRDMs.[195] The weld connects the latch housing and the rod travel housing, and has no structural significance. The cause of the leakage was determined to be IGSCC. A detailed metallographic and fractographic analysis indicated that the root cause of the leakage was (a) extensive sensitization in the rod travel housing caused by large heat input for an oversized tungsten inert gas (TIG) seal weld, (b) a local oxidizing environment due to trapped air at the startup of the operating cycle and which gets dissolved into the reactor water after 2 to 3 weeks, and (c) thermal stresses appearing in the region when the control rod is shifted in its position.

Carbide precipitation was observed in the material more than 25 mm (1 in.) from the weld. Multiple initiation sites were found where shallow cracks had developed. The depth of cracks varied from a few grains up to about 5 mm. The concentration of oxygen necessary for SCC decreases with increasing chloride concentration. In near-neutral water, initiation of SCC is extremely low at temperatures below 100°C (212°F). In weakly acidic water (pH ~3–4), SCC can be initiated at temperatures as low as 40–70°C (104–158°F).[263]

Studies on cold-worked austenitic SSs indicate that these materials become susceptible to SCC in high-temperature aerated water when their hardness is greater than ~300 Hv. A similar trend is expected in a PWR primary coolant environment. The hardness thresholds for crack initiation and propagation are respectively 240 $Hv_{0.1}$ and 310 $Hv_{0.1}$.[266]

2.3.3.3 PWSCC Fracture Morphology

In the 1970s, the fracture morphology of the SCC cracks observed in the mill-annealed Alloy 600 tubes was primarily IG. The cracks were usually axial and were located on the secondary side in the region of the tube support plate and on the primary side in the roll transition zone and the small radius U-bends.

The fracture morphology of the SCC cracks found in the Ringhals 4 canopy seal welds in the austenitic SS control rod travel housing during the 2004 refueling outage was predominantly the IG, although there were regions of TG cracks particularly in the initiation stages.[195] The region closest to the weld fusion zone was almost entirely IG cracking. The breakthrough region on the outer surface appeared to be caused by ductile tearing. Most likely, it occurred due to sudden transients caused by a dropped control rod or reactor trip and shutdown.

However, the fracture morphology of cracks caused by SCC in austenitic SS components in PWRs in the presence of chlorides is primarily TG, except for the case of sensitized material. The fracture surface appears brittle with the presence of crystallographic facets and has a fan shape pattern and ligaments of coalescence. Typically, the two fracture surfaces show good geometrical agreement, indicating little or no plastic deformation at the crack tip or anodic dissolution for crack advance.

2.3.3.4 Critical Factors for PWSCC

Materials Aspects

As discussed earlier, unlike the high susceptibility of austenitic SS components to IGSCC in a NWC BWR environment, SS components have suffered from relatively few incidences of IGSCC in PWR environments. These few occurrences have been attributed to a combination of a highly oxidizing environment caused by trapped oxygen in stagnant systems and severely cold-worked material due to processes such as grinding or other machining or fabrication processes.[272,273] However, Ni alloys such as Alloy 600 and its associated Alloys 132 and 182 weld metals are susceptible to PWSCC in a primary coolant environment. The high-strength Ni alloys such as Alloy X750, and to a lesser extent Alloy 718, are also susceptible to PWSCC.

The existing data indicate that the susceptibility of Alloy 600 to PWSCC strongly depends on the metallurgical structure of the material, particularly the carbide morphology, and the amount of cold work in the material. In general, Alloy 600 with a large number of carbide precipitates at the grain boundaries shows greater resistance to PWSCC, whereas Alloy 600 with a large number of intragranular carbides is most susceptible to PWSCC. The most resistant microstructure consists of a semi-continuous decoration of carbides at the grain boundaries. A high mill anneal temperature favors the precipitation of IG carbides to produce a desired microstructure.

A possible explanation for improved resistance to PWSCC is selective oxidation of carbides at the grain boundaries. The carbides act as a sink for oxygen and present a more difficult diffusion path for oxygen. Another explanation is that IG cracks are blunted by carbides. According to this mechanism, dislocations are preferentially emitted from carbides at the crack tip, thereby reducing the stress concentration around the carbides.[274]

Environmental Aspects

For austenitic SSs, the main environmental parameter for PWSCC is the presence of chlorides or sulfates in oxygenated water. Chloride-induced SCC is enhanced by high DO content, which is typically present in stagnant sections because of insufficient venting before pressurization of the system.

The two environmental parameters that influence PWSCC of Ni alloys are temperature and the hydrogen concentration in the water. The effect of DH on the CGRs in Alloy 600 and its welds has been investigated extensively during the past 25 years. The results indicate that, for Ni alloys, the CGR has a maximum at a hydrogen concentration approximately corresponding to the Ni/NiO equilibrium potential.[275] The effect of DH is larger for Alloys 132 and 182 weld metals than for Alloy 600. Furthermore, the PWR coolant temperature varies significantly in the primary coolant system; it is lowest in the cold-leg pipe (286°C [547°F]) and the highest in the pressurizer (343°C [649°F]). The reason for this maximum at the Ni/NiO equilibrium potential is not well understood. The existing data indicate that the CGRs increase with increasing temperature.[275]

Investigations on the effect of hydrogen on PWSCC initiation in Ni alloys indicate that the resistance to cracking continuously increases with decreasing hydrogen content.[276] However, the typical concentration of hydrogen in PWRs is 25–50 cc H_2/kg H_2O. At this range, the influence of hydrogen is relatively small. For significant benefits of reduced hydrogen concentrations, the hydrogen content has to be in the range of 7–8 cc H_2/kg H_2O; such low hydrogen contents are not used in any operating PWRs.[190]

The available data on the influence of Li content and the presence of Zn indicate little or no effect on PWSCC initiation or CGRs. Zn is added to some PWR primary loops to reduce the activity buildup.

Stress Aspects

Experimental data obtained from constant-load PWSCC tests on several Ni alloys and associated weld metals indicate that Alloy 600 and its weld metals Alloy 132/82 have an identifiable threshold stress, whereas no threshold stress has been measured for high-Cr Alloy 690 and its weld metals Alloy 152/52.[190] For austenitic SS components, the surface residual stress due to grinding or other finishing processes plays an important role in PWSCC.

Significant Parameters for PWSCC

The material parameters that have a significant effect on PWSCC are the amount of cold work in the material and, for Ni alloys, the metallurgical structure, particularly the carbide morphology. The most resistant structure consists of semi-continuous decoration of carbides at the grain boundaries. The main environmental parameter for PWSCC is the presence of chlorides or sulfates in oxygenated water. In addition, for Ni-alloys, the CGRs are maximum at a hydrogen concentration approximately corresponding to the Ni/NiO equilibrium potential. Regarding the effects of applied stress, Alloy 600 exhibits an identifiable threshold stress for PWSCC, whereas, for austenitic SS components, the surface residual stress due to grinding or other finishing processes play an important role.

2.3.3.5 Modeling

During the past 40 years, considerable effort has been spent to estimate the potential occurrence and evolution of PWSCC in Ni-base alloys in PWRs. Typically, the reactor vessel head CRDM nozzles and steam generator tubes are the components of particular concern regarding PWSCC. In PWRs, the time to initiate PWSCC dominates the life of a component. For Ni alloys, it involves a significant incubation period that depends on temperature, fabrication-related residual stress, and material susceptibility.[237] For the CRDM nozzles and associated J-groove welds, a risk-based approach has been developed in the United States for classifying the occurrence of PWSCC as a function of service time and temperature.

The procedure is described in ASME Code Case CC N-729-1, “Alternative Examination Requirements for PWR Reactor Vessel Upper Heads with Nozzles Having Pressure Retaining Partial-Penetration Nozzles, Section XI, Division 1,” June 28, 2005. The effective degradation years, which represents the susceptibility to PWSCC crack initiation, is calculated as an effective operating time at a reference temperature of 315°C (599°F), using an activation energy for PWSCC initiation of 209 kJ/mol (50 kcal/mol).[237] In addition, an accurate estimation of the

CGR associated with PWSCC is used to define the inspection interval based on the minimum reliable measurable defect size and minimum allowable flaw size. The re-inspection years are calculated using an activation energy of 130 kJ/mol (31 kcal/mol), which is typical for PWSCC propagation rate in Alloy 600.[237]

In the United States, it is possible to operate a nuclear plant with a known initiated PWSCC flaw, provided an aging management program is in place, which includes a set of criteria and a procedure for crack detection during periodic inspection and an acceptable flaw tolerance evaluation that includes crack initiation and/or growth, for establishing the inspection interval. Some countries, however, use a deterministic approach, and SCC defects have to be removed/repaired before plant operation. Empirical correlations based on laboratory tests on archive materials are used to rank the PWSCC susceptibility of Alloy 600 components. A Monte Carlo methodology is applied to account for the intrinsic variability of the input parameters in the model.

In the various forms of SCC, the crack tip is at low potential (i.e., deaerated) in all cases. Furthermore, in LWRs, the environmental conditions for crack growth are similar. Thus, the main difference between BWRs and PWRs is the additives that shift the reactor coolant pH at reactor temperatures of 274–288°C (525–550°F) in BWRs and 290–338°C (554–640°F) in PWRs, from 5.6 to 7.2, and H_2 fugacity ~50 vs. 3,000 ppb H_2. Out of these, temperature is the most significant parameter for SSs. For Ni alloys, both temperature and H_2 fugacity are important.

Predictive equations for PWSCC were first developed for steam generator tubes and later extended to pressurizer nozzles and vessel head CRDM nozzles. The expressions for the life of Alloy 600 components are usually based on the empirical relation:

$$t_f = C\frac{\sigma^{-4}}{I_m}\exp\left(\frac{E}{RT}\right), \tag{16}$$

where t_f is the failure time (hours), C is a constant, σ is the applied stress (MPa), I_m is a material susceptibility index, E is the apparent activation energy (44 kcal/mole), R is the universal gas constant, and T is the absolute temperature (K).

The component stress is established based on finite element stress analyses or experimental data applied to system mock-ups. The material variability regarding susceptibility to PWSCC is established based on the material indices, I_m.[277] Table 1.1 of Ref. 234 provides guidance for establishing the material index. The information is based on either minimum time to failure of plant components or laboratory data on accelerated tests on representative plant materials. The constant C is adjusted such that an index of unity corresponds to a minimum failure time of 10,000 h at 325°C (617°F) and an applied stress of 450 MPa. In addition, temperature and stress indices are defined relative to the reference condition of 325°C (617°F) and 450 MPa, as follows:

$$I_\theta = \exp\left[\left(\frac{-E}{R}\right)\left(\frac{1}{T}-\frac{1}{598}\right)\right] \quad I_\sigma = \left(\frac{\sigma}{450}\right)^4. \tag{17}$$

Thus, $t_f = \dfrac{10{,}000}{I_m \cdot I_\theta \cdot I_\sigma}$. (18)

The variability of the susceptibility of Alloy 600 to IGSCC has been quantified to assess cracking in the vessel upper head CRDM nozzles of French PWRs, and extended to other Alloy 600 primary coolant system components.[278] The model considers three types of microstructure related to C content, thermal treatment, particularly the temperature at the end of the forging or rolling operation, and yield strength after hot-working:

- Class A with primarily intergranular carbide precipitates;
- Class B recrystallized with carbides on a prior grain boundary network;
- Class C recrystallized with randomized intragranular carbides as well as carbides on prior grain boundaries.

These classes are then linked to their IGSCC resistance (i.e., material susceptibility index).[234] The results yield significant scatter in the material susceptibility to IGSCC in PWRs. This variability combined with the variability in the stress values of various components yield a distribution of failures with time that is fitted to a Weibull distribution.[278,279] Monte Carlo methodology has also been used to estimate the percentage of cracked penetrations as a function of time and material susceptibility.[278]

A more pragmatic approach for predicting CGRs in Alloy 600 components in PWRs is based on empirical measurements of CGRs as a function of crack tip stress intensity, K_I, expressed as,

$$\frac{da}{dt} = C \cdot \left(K_I - 9\right)^n \qquad (K_I \text{ in MPa}\sqrt{\text{m}}) \tag{19}$$

The temperature dependence of constant C is estimated using an activation energy of 130 kJ/mol (31 kcal/mole).

2.3.3.6 Preventive Measures

Mitigation measures for PWSCC are based on control and improvement of plant water chemistry to delay the onset of various corrosion processes.[237] In addition, a pH of the primary coolant system helps to reduce radiation fields. Optimizing the hydrogen content in the primary coolant may help mitigate initiation of PWSCC and/or crack propagation in Ni alloys.[237] Existing data indicate that in PWR primary water and superheated steam, the initiation time decreases with increasing hydrogen content in the range used in PWR primary water.[280–282] In superheated hydrogenated steam, a minimum is observed at corrosion potentials near the Ni/NiO redox reaction.[280,281] However, in high-temperature water, a clear minimum in initiation time is not observed; initiation times may reach a low plateau or continue to decrease at hydrogen concentration greater than about 15–20 cm^3 H_2/kg of water at 325°C (617°F).[281,283]

Some plants use Zn injection in the PWR primary coolant system to reduce radiation fields. Adding Zn to the coolant changes the nature of the oxide layers. Zn slowly replaces Ni and Co in spinel ferrite oxides because of a higher stability of Zn ferrite spinel.[284,285] The main effect of the presence of Zn in the oxide layer is to form a more protective thin layer that reduces the corrosion and cation release rate, thereby reducing the radiation fields. Zn additions may also be effective in mitigation of PWSCC initiation in Ni alloys.[286] However, a clear effect on crack propagation is not obvious.

For steam generator application, initially, mitigation of PWSCC in mill-annealed Alloy 600 was achieved by the use of thermally treated Alloy 600TT. However, it did not provide complete immunity of the alloy to PWSCC. In the mid to late-1980s, to mitigate PWSCC in the mechanically rolled transition zone, some utilities applied shot peening to Alloy 600 tube bundles, thereby introducing compressive stresses in the inner tube surface. However, operating experience with shot-peened tubes indicates that when shot peening is performed after a few fuel cycles of plant operation, it did not completely prevent PWSCC, but when applied before the first operation of SG, no PWSCC has been detected even after 20 years of operation.[287]

Furthermore, Alloy 690 is used instead of Alloy 600 for new and replacement components. The associated weld metals for Alloy 690 are Alloys 52 and 152. These alloys are characterized by significantly higher Cr content (~30%). The performance of these alloys is much better than Alloy 600 and its weld metals. Several investigations have confirmed the superior resistance of Alloys 690, 152, and 52 to PWSCC initiation at temperatures up to 360°C (680°F). Nonetheless, laboratory data indicate that PWSCC propagation can occur in materials with at least 10% of unidirectional cold work or with a degraded microstructure.

By the end of the 1980s, hydraulic expansion of tubes into the tube sheet was universally adopted, which resulted in much reduced residual stresses in the transition zone. The potential of PWSCC in the tight U-bends of the first two rows of the SG has been resolved by the use of thermally treated alloy, provided cracks had not already initiated.[237] At present, PWSCC has not occurred in Alloy 600TT and Alloy 800 tubes after more than 21 years of operation.[237]

For strain-hardened austenitic SS components, the U.S. NPP industry has recommended ASME Code Case N60-2 to 5 described in NRC Regulatory Guide, RG 1.84, Rev. 35, “Design, Fabrication, and Materials Code Case Acceptability,” ASME Section III, October 2010. The regulatory guide notes that the ASME Code Cases may be accepted with the additional condition that the maximum yield strength of austenitic SSs should not exceed 90 ksi (~630 MPa), to prevent the susceptibility of these materials to environmental cracking.

2.3.4 Irradiation-Assisted Stress Corrosion Cracking

A major concern regarding the structural and functional integrity of LWR core support structure and internals materials (i.e., primarily austenitic SSs) is IASCC. Several incidents of IASCC have occurred since the mid-1970s in control blade handles and instrumentation tubes of BWRs, and since the 1990s, in BWR core shroud and PWR baffle bolts. As the name implies, IASCC is literally the irradiation-assisted enhancement of SCC susceptibility of materials. The factors that influence IASCC of austenitic SSs include neutron irradiation conditions such as neutron fluence, flux, and energy spectrum; cold work; material composition; corrosion potential; water purity; temperature; and loading conditions. The susceptibility of austenitic SSs to IASCC increases with neutron fluence, corrosion potential, and water conductivity.

It is well known that SCC of materials in high-temperature, high-pressure water depends on three factors: a susceptible material, relatively high stress, and an aggressive environment. In the film rupture/slip oxidation model, the fundamental elements of SCC have been described in terms of the processes that occur at the crack tip[33,187,288] and are considered to include: dynamic strain at the crack tip that disrupts the passive film, thereby exposing fresh metal surface, followed by rapid metal oxidation and the subsequent repassivation, a process that can be quantitatively linked to crack advance.[289] The kinetics of repassivation are primarily a function of the local chemistry and material composition, as well as the mass transport processes that establish the local crack tip chemistry.[288] The effect of water chemistry is particularly important because it can change the corrosion reactions at the crack tip. Metallurgical and microstructural parameters are also important because sensitization of the material by thermal treatment or irradiation hardening due to radiation damage can alter the localized deformation and creep processes at the crack tip, thereby changing the film rupture frequency.

A review of the existing data on IASCC susceptibility has identified the following key material and environmental parameters that influence the susceptibility of LWR core internals to IASCC.

Crack growth rate data have been obtained on irradiated wrought and cast austenitic SSs as well as SS weld metal and weld HAZ materials in LWR environments. The specimens were either machined from materials from LWR core internal components (mostly BWR components) or irradiated, after machining, under LWR irradiation conditions. However, some of the high neutron dose data have been obtained on materials irradiated in fast reactors, and the applicability of the data for estimating irradiation effects under LWR operating conditions needs to be evaluated.

Stress corrosion cracking is a complex phenomenon that depends on several parameters, such as material composition and processing, irradiation effects, water chemistry, loading condition, and temperature. As a result of these complexities and uncertainties in experimental measurements, the CGR vs. K data in LWR environments show significant variability (up to 1,000×), and it is not yet possible to determine specific effects of these parameters on SCC growth rates with high confidence under all conditions of interest.

The quality of experimental CGR data and potential sources of uncertainty in experimental measurements and data scatter are discussed further in the following sections.

2.3.4.1 Test Procedures

Nearly all of the recent CGR data on irradiated materials in simulated BWR and PWR environments have been obtained on compact tension (CT) specimens (1/4-T or 1/2-T) or four-point bend specimens. The tests are performed in accordance with American Society for Testing and Materials (ASTM) methods. The specimens are fatigue precracked (typically in air) to create a starter crack and (a) actively loaded in the environment to determine the SCC growth rates and (b) under cyclic loading to measure fatigue CGRs. The fatigue CGR tests are conducted with a triangular or slow/fast saw-tooth waveform with rise times up to 10,000 s and load ratio, R, between 0.2 and 0.9. The SCC growth rate tests are conducted under constant K with or without periodic partial unloading. The stress intensity factor for SCC tests (and maximum stress intensity factor K_{max} for fatigue tests) is in the range 3–40 MPa $m^{1/2}$.

In addition, the reversing direct current (DC) potential difference method is used to monitor crack extension. The crack extensions determined from the DC potential drop method are corrected to match the final optically measured crack length. In most studies, crack lengths obtained from the DC potential drop method have shown good agreement with post-test fractographic measurements; typically, the potential drop measurements are 5–20% smaller. The CGRs are determined from the slope of the corrected crack length vs. time plots. For cyclic loading, the CGR can be expressed in terms of a time-based growth rate (da/dt) or a growth rate per cycle (da/dN).

The major source for variability in measured SCC growth rates is crack morphology. Typically, SCC of austenitic SSs in high-temperature water is IG, whereas the starter crack for SCC tests is produced by fatigue cycling in air, which creates a TG crack. Depending on the susceptibility of the material to SCC, the TG crack may not transition to an IG crack during the test, or may transition only along a portion of the specimen width. Even if precracking is carried out in simulated LWR environments, an IG crack is not guaranteed. Under the more rapid cyclic loading, the crack growth is dominated by mechanical fatigue, which nearly always creates a TG crack. In some studies, the specimens are subsequently subjected to gentle cycling at relatively low frequency and high load ratio (to reduce the contribution of mechanical fatigue) and facilitate the transition of a TG crack to an IG crack.[32,290] The data scatter is significantly reduced in studies that follow such a test procedure.

2.3.4.2 Specimen K/Size Criterion

The proposed K/size criterion for irradiated materials can also introduce inaccurate screening of the measured CGR data. Fracture mechanics is a correlative technology that does not attempt to describe the mechanisms that are occurring at the crack tip. It correlates the behavior of components with that of specimens using the K parameter. If two cracks have the same K, then they have the same strains and stresses in a region near the crack tip. Mathematically, it can be shown that K characterizes the stresses and strains at the crack tip if the plastic zone size is "small enough." The ASTM specifications for specimen K/size criterion are intended to ensure that the plastic zone is small and K is controlling. For constant load tests, ASTM E 1681 requires that

$$B_{eff} \text{ and } (W - a) \geq 2.5\,(K/\sigma_y)^2, \tag{20}$$

where W is the specimen width, σ_y is the yield stress of the material, a is crack length, and the B_{eff} is the specimen effective thickness, which is defined in terms of specimen thickness B and specimen net thickness B_N as $(B\,B_N)^{0.5}$. For high strain-hardening materials (i.e., ratio of ultimate stress to yield stress $[\sigma_u/(\sigma_y] \geq 1.3)$, Eq. 20 allows the use of the flow stress defined as $\sigma_f = (\sigma_y + \sigma_u)/2$ rather than the yield stress.

This K/size criterion was developed for materials that show work hardening and, therefore, may not be applicable for materials irradiated to fluence levels where, on a local level, they do not strain harden and exhibit strain softening. An alternative K/size criterion based on an "effective yield stress" has been proposed for which the irradiation-induced increase in yield stress is discounted by a factor of 2 for moderately irradiated materials,[291] and by a factor of 3 for highly irradiated materials.[292] Thus, the effective yield stress is defined as $\sigma_{eff} = (\sigma_{yirr} + \sigma_{ynonirr})/2$ or $\sigma_{eff} = (\sigma_{yirr} + \sigma_{ynonirr})/3$. These proposed criteria were not developed based on analyses of crack tip plastic strain or experimental comparisons of specimens with different degrees of constraint. Rather, they were proposed to explain some unusual IASCC growth rate results that did not show the benefit of decreased corrosion potential on growth rates in austenitic SSs irradiated to moderate irradiation levels (i.e., 3–4 dpa). The proposed criteria seem to be based on an implicit assumption that if the benefit of reduced corrosion potential on CGRs is effective at one K level and is not effective at a higher K level, then it must be due to a violation of the K/size criterion, the argument being that since austenitic SSs irradiated above approximately 3 dpa exhibit strain softening, the K/size criterion based on the measured yield strength of the irradiated material is inadequate for such materials. It is not clear whether due consideration has been given to the possibility of other effects. Tensile property data for irradiated SSs indicate that strain softening in highly irradiated austenitic SSs is rarely more than 10–15%.

Recent investigations have evaluated the validity of the K/size criterion for irradiated materials by comparing the plastic strain distribution in a ½-T CT specimen estimated from finite element method calculations with experimentally observed plastic deformation area.[293,294] The plastic zone size has been estimated to be 0.2–0.4 mm (0.008–0.016 in.) at K = 30 MPa $m^{1/2}$.[294] The results indicate that for an austenitic SS irradiated to 3×10^{25} n/ m^2, the appropriate K range for SCC growth rate tests is at least 30 MPa $m^{1/2}$ for a (5.8-mm [0.23-in.] thick) ½-T CT specimen. This is higher than that predicted by using the effective yield stress instead of the measured value. Detailed metallographic evaluation of the fracture surface also does not show any indication of a loss in constraint in these specimens (i.e., the fracture morphology does not change, and the fracture plane is straight and normal to the stress axis).[32] In view of these studies, caution should be exercised to not use a K/size criterion that may screen out key experimental data.

2.3.4.3 Rising K or dK/da Effects

In LWR components, K can increase as the crack depth, a, increases with crack advance, and it can increase and then decrease due to the through-wall weld residual stress profile, which is usually U-shaped. Consequently, as the crack advances through the wall, K can increase, remain relatively constant, or decrease, depending on the residual stress profile. Initially, when the crack depth is small, K could increase very rapidly because it is proportional to the square root of crack depth ($K \alpha \sigma\sqrt{a}$). Studies on austenitic SSs and Ni alloys in high-purity water with 2000 ppb O_2 at 288°C (550°F) have shown that rising K (+dK/da) at K values that are relevant for LWR components can increase the CGRs significantly, whereas decreasing K (–dK/da) has little or no effect.[107] Under rising K conditions, growth rates can be more than two orders of magnitude higher than those under constant K conditions.

As discussed by Andresen and Morra,[295] dynamic strain at the crack tip is an important element of crack advance under SCC conditions. As the crack advances, the process of stress and strain redistribution sustains crack growth. It leads to slip offset, which ruptures the surface oxide film, and the crack advances due to oxidation/dissolution of the metal. Thus, there is an inherent synergy between crack advance and growth rate itself (or dK/da as the crack advances). The data presented by Andresen and Morra[295] indicate that when changes in K are controlled by dK/da, very different responses can be seen for rising versus falling K conditions. For example, rising K results in an increased growth rate, which causes a faster increase in K, which is a positive feedback. Decreasing K, on the other hand, yields negative feedback. These results indicate that CGR data obtained from tests where K was allowed to increase during the test or was decreased too fast may give erroneous results for the K dependence of SCC growth rates. Caution should be exercised while interpreting such results.

2.3.4.4 Reloading Effects

For some irradiated austenitic SS materials, small increases in the stress intensity factor K due to either load perturbations or the reloading portion of the partial unload/reload cycle during a SCC growth rate test result in a rapid or step-like crack extension.[296] The growth rates during such periods are as high as 10^{-7} m/s (4×10^{-6} in./s). Such reloading effects produce a classic staircase appearance in the crack length vs. time plots. Similar behavior has been observed in nonirradiated CW SSs with high yield strength.[33] This behavior has often been attributed to the breaking of uncracked ligaments in the material and is believed to occur in materials with an uneven crack front. The significance and cause for this behavior should be investigated.

2.3.4.5 Estimation of Crack Growth Rates

The effects of various material and environmental conditions on the SCC growth rates in austenitic SS materials irradiated in BWRs and PWRs are discussed next.

BWR Environments

Dependence of stress intensity factor: The SCC growth rates for various grades and heats of austenitic SSs irradiated from 5×10^{24} to 2.5×10^{26} n/m^2 (0.75 to 37.5 dpa) in NWC BWR and HWC BWR environments are shown in Figs. 25a-c and Figs. 26a-c, respectively. These figures include data obtained for the CGRs of HAZ materials, both submerged arc weld (SAW) and shielded metal arc weld (SMAW), and for sensitized SSs. Also included are the K vs. CGR disposition curves proposed in the NRC report NUREG-0313 for nonirradiated sensitized austenitic SSs in high-purity water[215] and the curve proposed by EPRI for austenitic SS BWR core internal components.[297] The NUREG-0313 disposition curve is expressed as

$$da/dt\ (m/s) = A_1\ (K)^{2.161}, \tag{21}$$

where K is in MPa m$^{1/2}$ and the magnitude of A_1 depends on the water chemistry. The value of A_1 is 2.1×10^{-13} in water with 8 ppm DO and 7.0×10^{-14} in water with 0.2 ppm DO. It is smaller in low-potential HWC BWR and PWR primary water environments.

The EPRI disposition curve for use in BWR core environments is expressed as

$$da/dt\ (m/s) = A_2\ (K)^{2.5}, \tag{22}$$

where the constant A_2 is 4.564×10^{-13} in NWC BWR and 1.512×10^{-13} in HWC BWR environments. The EPRI correlations are based on two datasets; GE and Japan Power Engineering and Inspection Corp. (JAPEIC) data for SSs irradiated to 4.0–4.5 dpa,[297] and the Halden reactor data (IFA 639 test series) for Type 304, 347, and 316NG SSs that were irradiated to 13.5, 2.25, and 1.35 dpa.[298] The significant results in NWC and HWC BWR environments are summarized as follows.

In the NWC BWR environment, the SCC growth rates of austenitic SSs irradiated to 5 dpa could be a factor of 10 higher than the NUREG-0313 disposition curve for nonirradiated SSs in 8 ppm water, while austenitic SSs irradiated to 10–12 dpa could be a factor of 25 higher than the NUREG-0313 curve. For the end-of-60-year-life fluence level (3×10^{25} n/m^2 or 4.5 dpa), the CGRs of some SS materials could be significantly higher than the CGR disposition curve proposed by EPRI.[297] A CGR disposition curve that is a factor of 10 higher than the NUREG-0313 curve bounds nearly 80% of the data obtained in the NWC BWR environment for SSs irradiated up to 4.25 dpa. The results also indicate that the SCC growth rates for SSs irradiated in a PWR to 18 or 37.5 dpa (square and triangle symbols in Fig. 25c) are below the NUREG-0313 disposition curve for nonirradiated SSs. The reasons for the low CGRs observed for these highly irradiated materials are not clear. However, both materials came from the same reactor. It is possible that this behavior is unique to the material microstructure and microchemistry.

In general, CGR data obtained using test procedures in which the specimen was precracked in air and then transferred to the autoclave for the SCC test in the environment show much more variability at K values of 8–15 MPa m$^{1/2}$ (Halden data in Fig. 25) than data obtained using test procedures in which the specimen was precracked in the environment and the TG fatigue crack was transitioned to an IG crack by using slow fatigue cycling in the environment before starting

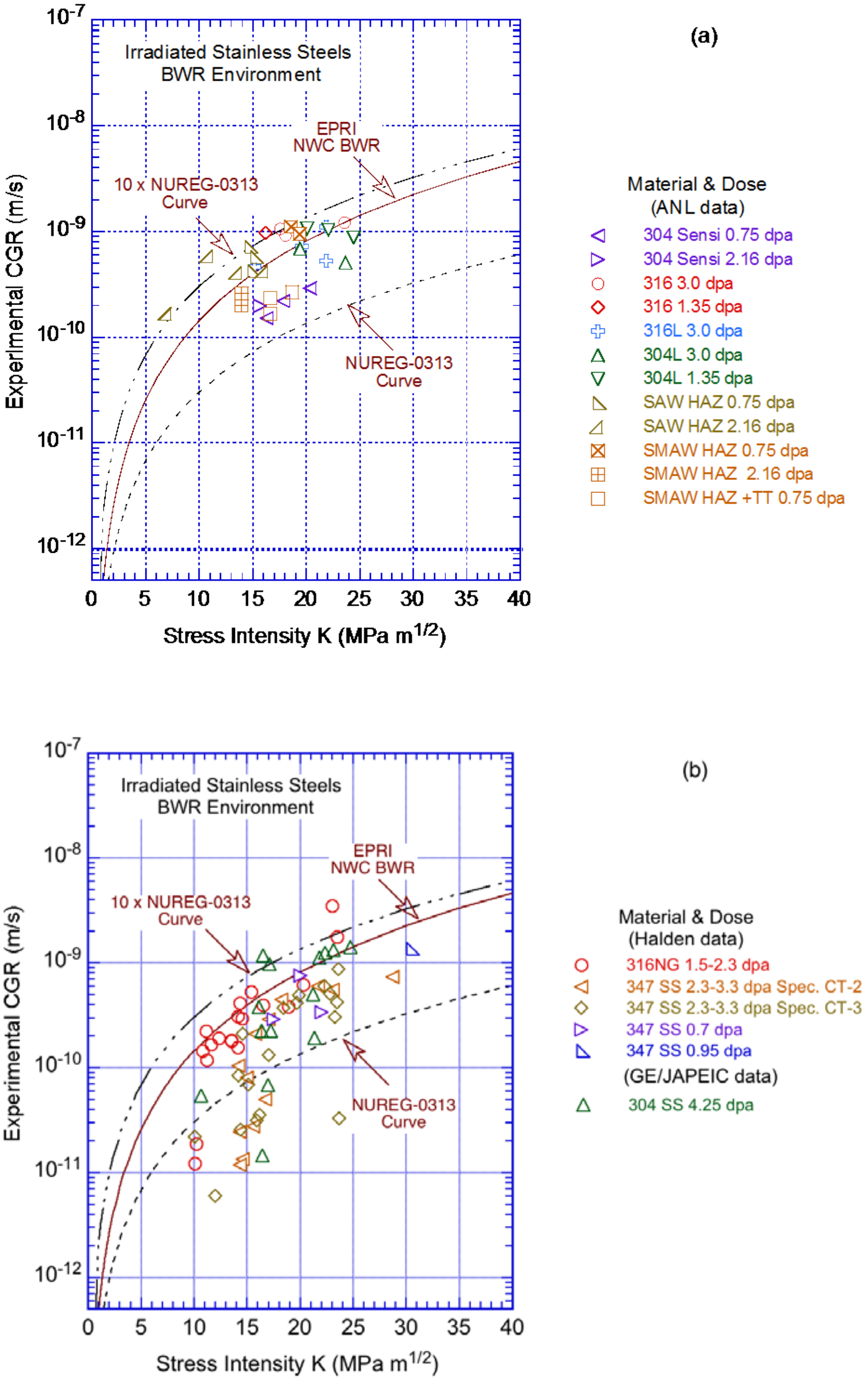

Figure 25. SCC growth rates in NWC BWR environment on austenitic SSs irradiated to (a) 0.75–3.0 dpa (Refs. 32,290,301,302), (b) 0.7–4.25 dpa (Refs. 297–300), and (c) 5.5–37.5 dpa (Refs. 36,292,298–300).

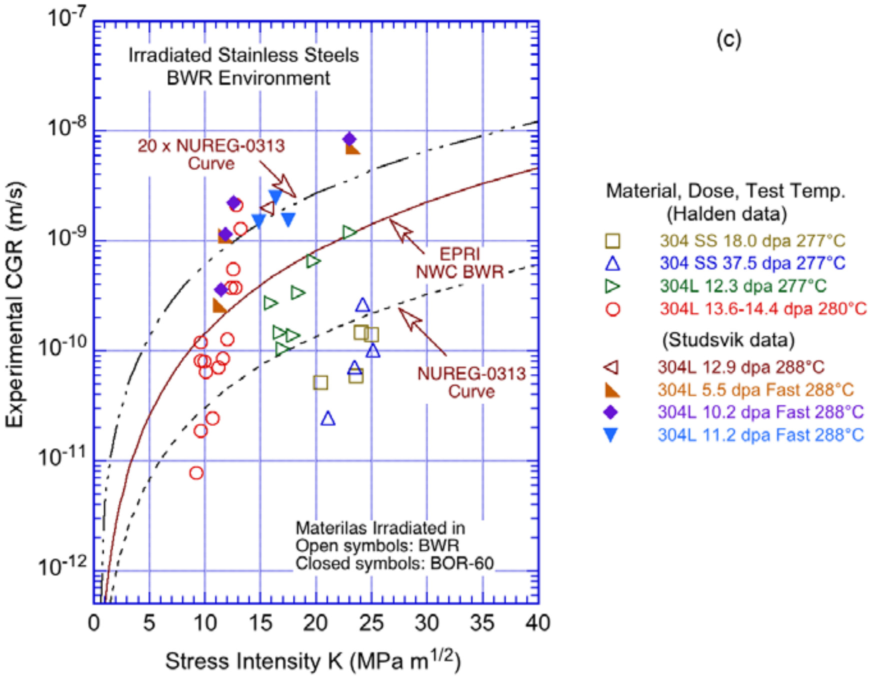

Figure 25. **(Contd.)**

the SCC test (see Argonne National Laboratory [Argonne] and Studsvik data in Fig. 25). This difference does not appear to be due to differences in material or irradiation conditions because data obtained at Halden and Studsvik on the same heat of Type 304L SS BWR control-rod blade material irradiated to comparable neutron dose (e.g., the two horizontal triangles [▷ and ◁] in Fig. 25c for Type 304L irradiated to 12.3 and 12.9 dpa, respectively) show more than a factor 10 higher growth rates for the material tested at Studsvik than for the material tested at Halden. Although there is only one data point for the Studsvik data, the factor of 10 difference in the CGR is not due to experimental data scatter because data obtained by the test procedure used in the Studsvik study do not exhibit such large data scatter.[36,292]

For the tests at Argonne and Studsvik, the CGRs at 3–11 MPa m$^{1/2}$ were obtained by decreasing K from 14–20 MPa m$^{1/2}$ to the low values. As a result, the cracks were growing at a rate ≥8 × 10^{-10} m/s (3.15 × 10^{-8} in./s) before K was decreased, whereas in the Halden data, tests were started at low K and the CGRs were <1 × 10^{-10} m/s (4 × 10^{-9} in./s).

The exponent for K in Eq. 21 is typically between 1.7 and 2.7 for SSs irradiated up to about 5 dpa. For the Halden data, the exponent was about 2 for the IFA-639 test series and about 2.5 for the IFA-658 test series. Exponents are between 1.5 and 2.0 for the Argonne data sets. For SSs irradiated to higher dose levels, this exponent could be as high as 7 for some data sets. However, for the SSs irradiated to 18.0 or 37.5 dpa, stable CGRs were observed only with periodic unloading, and the rates were relatively insensitive to changes in K.

The CGRs for the various grades and heats of SSs irradiated to the same dose seem to be the same. The CGRs obtained at Halden on Type 316NG and 347 SSs irradiated to 2.0–3.5 dpa are similar.[298] Similarly, the CGRs obtained at Argonne on Type 304L, 316L, or 316 SSs irradiated to 1.35–3.0 dpa are comparable.[32] However, the rates for weld HAZ are slightly higher than those for solution-annealed materials (Fig. 25a). The higher rates most likely are due to weld residual strains, which could be as high as 30% of the room-temperature tensile strain.[288]

Effect of corrosion potential: The data shown in Fig. 26 for SCC growth rates in the HWC BWR environment show a significant decrease in growth rates relative to those in the NWC BWR environment for SSs irradiated to less than 3 dpa; little or no reduction for some heats of SSs irradiated to 3–4 dpa; and no decrease for all SSs irradiated to 12–14.5 dpa. Furthermore, the materials irradiated to 18 or 37.5 dpa did not show any benefit of decreased corrosion potential on CGRs, but they did not show a sustained crack advance under constant K. In these high-dose materials, growth rates were established with periodic unloading, and the rates even in an NWC BWR environment were below the NUREG-0313 curve for nonirradiated SSs. However, as discussed above, the reason for these anomalous results is not known. Another significant feature of the cracking behavior of high dose materials was the “staircase” or reloading effect. In the HWC BWR environment, each unloading/reloading cycle was accompanied by a step or “jump” in crack length, creating a staircase or stepped crack growth. Although this behavior is often attributed to breaking of uncracked ligaments or straightening of the crack front, it is not clear why it should occur only in the HWC environment. Additional data in HWC BWR or PWR environments are needed on high-dose materials to better understand the IASCC behavior of austenitic SSs.

The results in Fig. 26 clearly indicate that the benefit of low-potential environments on SCC growth rates may be lost for some heats of SSs irradiated to fluence levels as low as 3 dpa, although there is variability in the data. Some of the data for the 3–4 dpa materials (e.g., circles and triangle in Fig. 26a and diamonds and horizontal triangles in Fig. 26b) are often considered invalid because of the high K values that exceeded the proposed K/size criterion for irradiated materials (i.e., irradiation-induced increase in yield stress is discounted by a factor of 2). However, the arguments against the validity of the data do not seem to have a well-developed

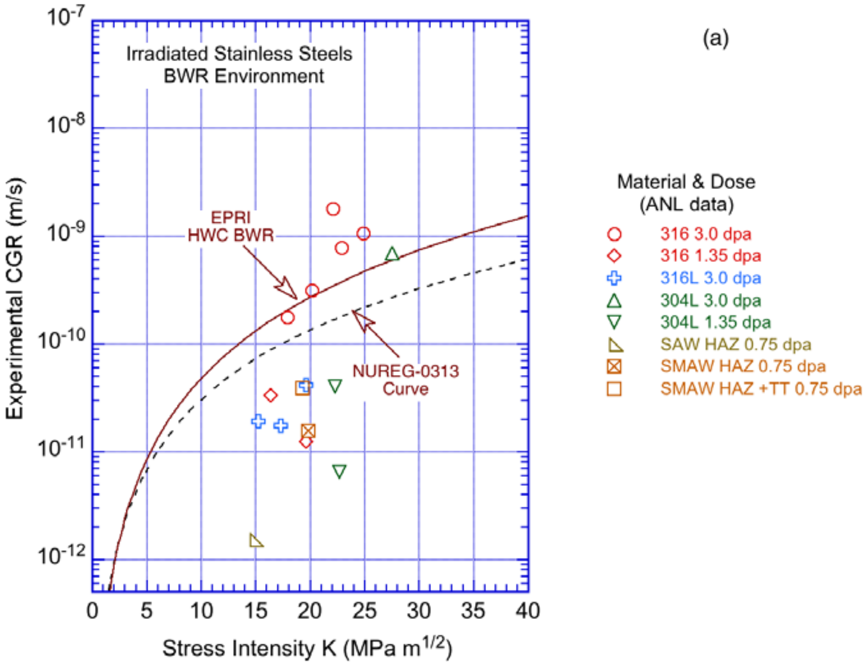

Figure 26. **SCC growth rates in HWC BWR environment on austenitic SSs irradiated to (a) 0.75–3.0 dpa (Refs. 32,290,301,302), (b) 0.7–4.25 dpa (Refs. 297–300), and (c) 5.5–37.5 dpa (Refs. 36,292,298–300).**

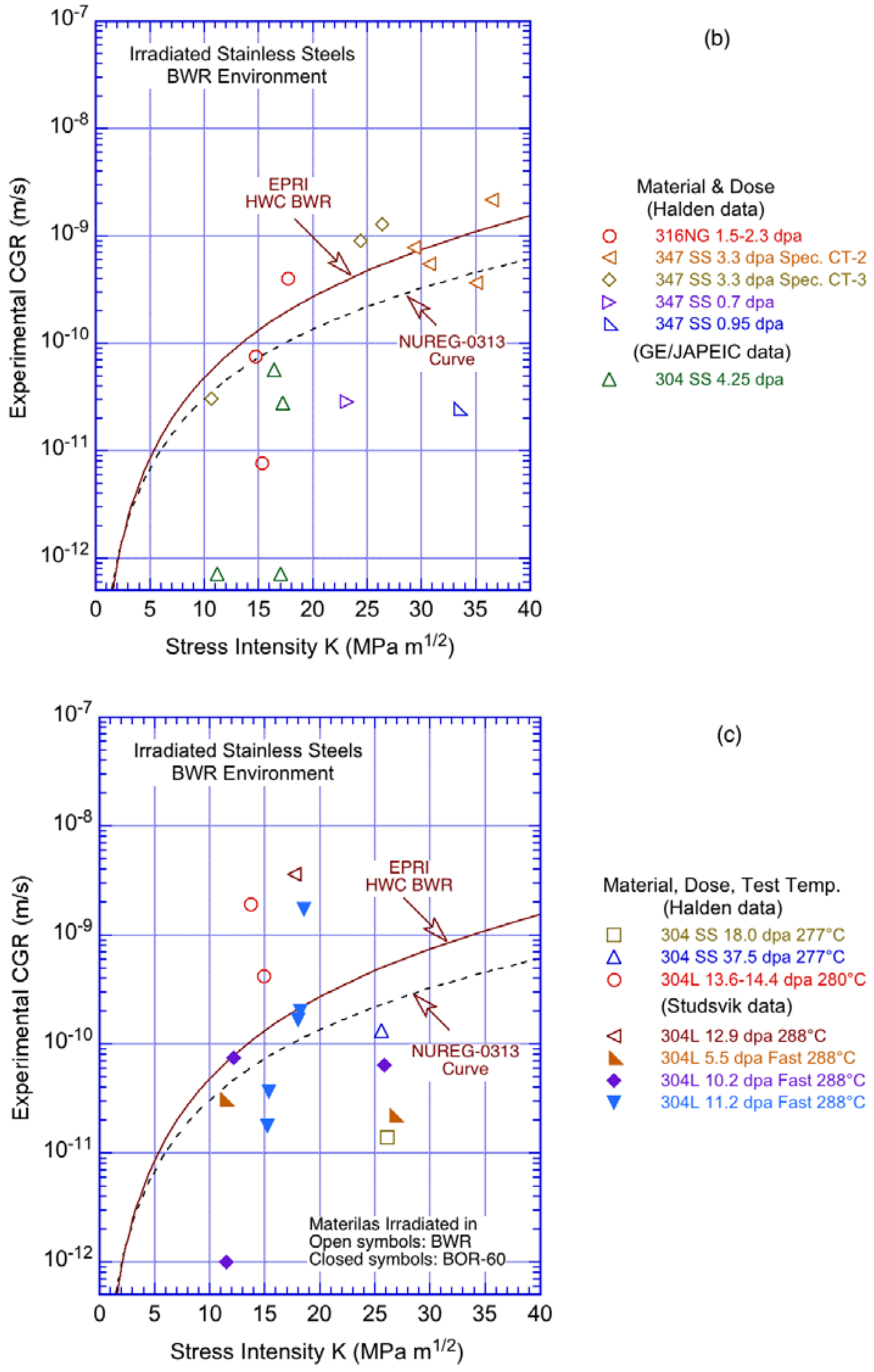

Figure 26. (Contd.)

technical basis. Some internal consistency checks can be used to demonstrate the validity of the Halden data for Type 347 SS irradiated to 2.3–3.3 dpa (diamonds in Figs. 25b and 26b).

The growth rates observed during the test time from 720 to 840 h, for two identical specimens (CT-2 and CT-3) of this material tested in the HWC BWR environment, were 7.32×10^{-10} m/s (2.88×10^{-8} in./s) at 28.7 MPa $m^{1/2}$ and 8.75×10^{-10} m/s (3.44×10^{-8} in./s) at 23.6 MPa $m^{1/2}$, respectively.[298] The environment was then changed to HWC, and the rates for the two specimens during test time 840 to 950 h were 7.77×10^{-10} m/s (3.06×10^{-8} in./s) at 29.3 MPa $m^{1/2}$ and 8.9×10^{-10} m/s (3.5×10^{-8} in./s) at 24.4 MPa $m^{1/2}$, respectively. The growth rates for both specimens did not decrease after the corrosion potential was decreased. Also, note that the applied K for specimen CT-2 in NWC was higher than that for specimen CT-3 in HWC. If the measured CGR for specimen CT-3 is invalid in HWC, it should also be invalid for specimen CT-2 in NWC. The experimental data or the post-test fractography of these samples do not show any indication that the specimen constraints were exceeded for these specimens.

As discussed earlier, such results should not be screened out simply because they do not agree with the current understanding of the IASCC behavior of austenitic SSs. The feature that is common between specimens CT-2 and CT-3 is that although the K values are different, the growth rates for the specimens were comparable and may represent a threshold rate above which CGRs are relatively insensitive to changes in stress intensity factor K or corrosion potential. Additional data on SSs irradiated to 3–8 dpa are needed to accurately establish the threshold for IASCC susceptibility in low-potential PWR environments.

Effect of Neutron Fluence: The SCC growth rates for various grades and heats of austenitic SSs, irradiated from 5×10^{24} n/m^2 to 2.5×10^{26} n/m^2 (0.75 to 37.5 dpa) in NWC BWR and HWC BWR environments at 288°C (550°F) and K = 20 MPa $m^{1/2}$ as a function of neutron dose, are shown in Figs. 27a and b, respectively. All materials, except those irradiated in a fast reactor, were irradiated in BWRs at temperatures of 280–300°C (536–572°F); the fast reactor irradiations were at 320°C (572°F). In the NWC BWR environment, the CGR increases above the NUREG-0313 level for doses >0.5 dpa, and the CGR also increases with dose out to about 10 dpa, although there is variability in the data. In the HWC BWR environment, the CGRs do not exceed the NUREG-0313 levels until the fluence is ≥3.0 dpa. The CGRs in the HWC environment for materials irradiated to 12–15 dpa are comparable to those observed in the

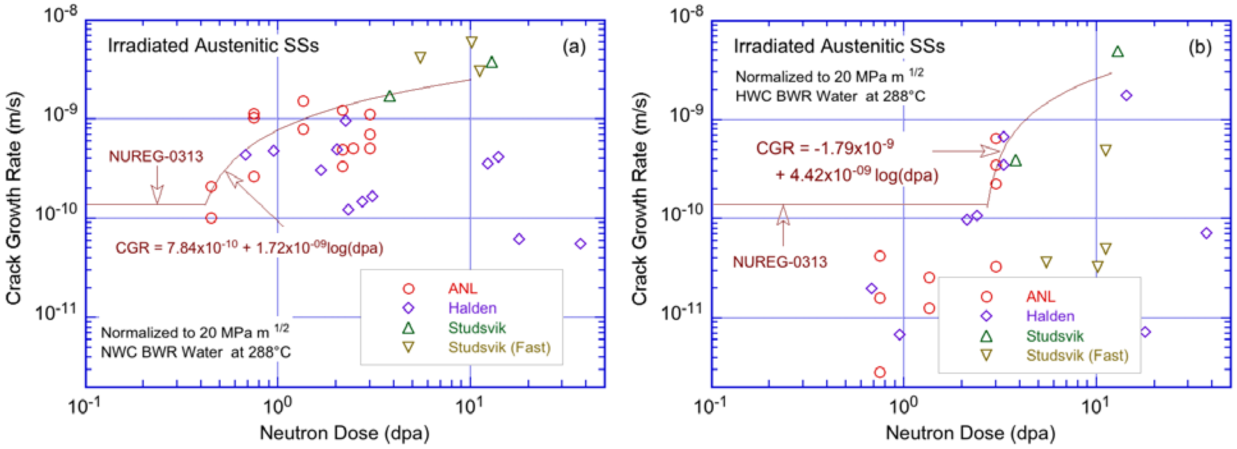

Figure 27. **SCC growth rates of irradiated austenitic SSs in (a) NWC and (b) HWC BWR environments at 288°C (550°F) and a K of 20 MPa $m^{1/2}$ plotted as a function of neutron dose.**

NWC BWR environment. However, as noted previously, there are some anomalous data with very low growth rates; the CGRs of SSs irradiated to about 19 and 38 dpa are below the NUREG-0313 curve for nonirradiated sensitized SSs in high DO water. The curves in Fig. 27 bound approximately 75th percentile of the data in the NWC environment and even more of the data for the HWC environment. The curves assume a threshold dose of 0.45 dpa and 2.7 dpa (or 3 × 10^{24} and 1.8 × 10^{25} n/m^2) in the NWC and HWC environments, respectively. The curves assume that the constant A_1 in the NUREG-0313 disposition curve (Eq. 21) varies with neutron dose. In the NWC environment, A_1 is taken as

$$A_1 = 1.21 \times 10^{-12} + 2.65 \times 10^{-12} \log(\text{dpa}), \tag{23}$$

and in the HWC environment as

$$A_1 = 2.76 \times 10^{-12} + 6.82 \times 10^{-12} \log(\text{dpa}). \tag{24}$$

Note that because Eqs. 23 and 24 define the constant A_1 in Eq. 21, these values must be multiplied by $(20)^{2.161}$ to obtain the expression for the CGR curves shown in Fig. 27.

PWR Environments

The SCC growth rate for irradiated austenitic SSs in the PWR environment have been investigated at Halden[296,303] on BWR irradiated materials; at Studsvik[36] on BOR-60 irradiated materials; and in several EPRI-sponsored studies on BWR and PWR irradiated materials. The total irradiation dose for these materials was in the range of 3.0–37.5 dpa with test temperatures of 288–340°C (550–644°F). The measured growth rates in various grades and heats of austenitic SSs in the PWR environment are shown in Fig. 28. There is a great deal of variability

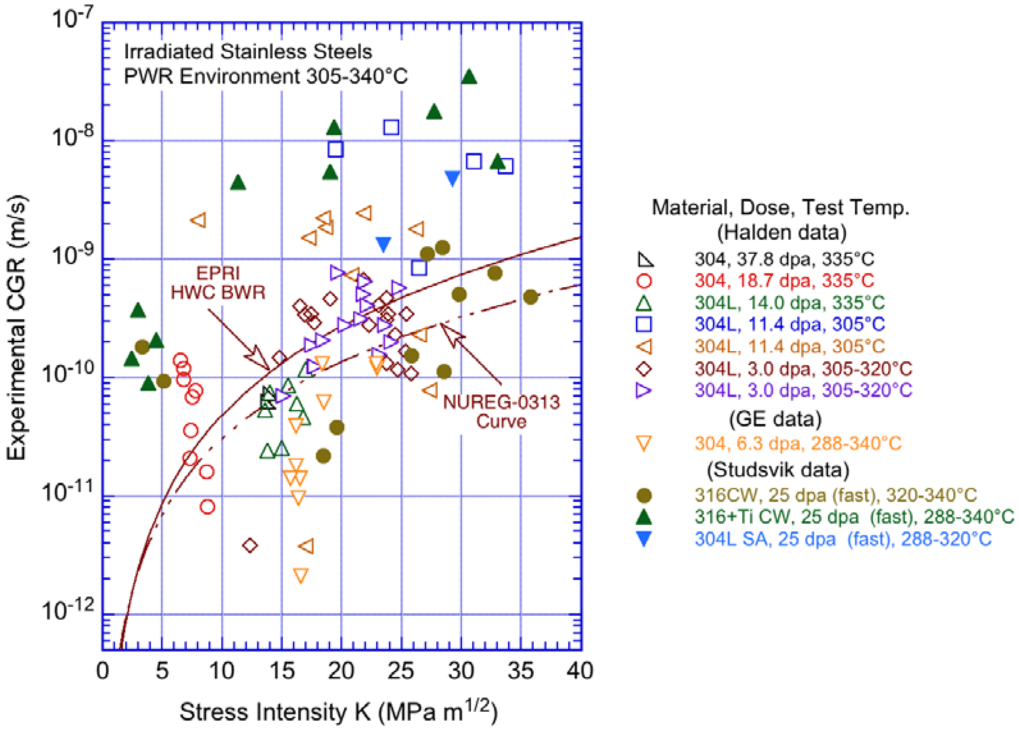

Figure 28. **SCC growth rates of austenitic SSs irradiated to 3.0–37.8 dpa in a PWR environment (Refs. 36,296,303,304).**

in the reported data. For a given material and irradiation condition, the variability is on the order of 10. The variability in CGR due to differing materials and irradiation conditions is on the order of 1,000.

Available data for a specific material indicate that the CGRs increase with temperature. The temperature dependence of the SCC growth rates in irradiated and nonirradiated austenitic SSs yields activation energies between 60 and 150 kJ/mol (14 and 36 kcal/mol). The CGRs of irradiated CW Type 316+Ti SS in the PWR environment at temperatures between 288 and 340°C (550 and 644°F) yield an activation energy of 105 kJ/mol.[36] An activation energy of 100 kJ/mol was used to normalize the data shown in Fig. 28 to a temperature of 320°C (608°F); the normalized CGRs are shown in Fig. 29 for materials irradiated to (a) 3 dpa and (b) 11–25 dpa. The significant results are as follows.

In general, in the PWR environment at 320°C (608°F), the SCC growth rates of materials irradiated up to 12 dpa are above the EPRI disposition curve for the HWC BWR environment at 288°C (550°F). More than half the data points for Type 304L SS irradiated to 3 dpa are above the EPRI curve (Fig. 29a). The CGRs for Type 304L SS irradiated to 11.4 dpa and for fast-reactor-irradiated materials (except cold worked [CW] Type 316 SS) irradiated to 25 dpa are about two orders of magnitude higher than the NUREG-0313 curve (Fig 29b).

The high growth rates in the 11.4 dpa material have been explained based on possible effects of short test duration, high K values, and a high grain-boundary Si concentration. As seen in Fig. 28 and observed earlier for the NWC BWR environment, CGRs in non-CW SSs irradiated to 14 dpa or higher are mostly below the NUREG-0313 curve for nonirradiated SSs, and are not plotted in Fig. 29.

Figure 30 shows the SCC growth rates as a function of neutron dose for various grades and heats of austenitic SSs that had been irradiated to 0.7–37.5 dpa in HWC BWR water at 288°C (550°F) or the PWR environment at 320°C (608°F), with K = 20 MPa $m^{1/2}$. All materials except those irradiated in a fast reactor were irradiated in BWRs at temperatures of 280–300°C (536–572°F); the fast reactor irradiations were at 320°C (608°F). The data for the HWC BWR or PWR environments may be represented by the bounding curves shown in the figure. The curve represents a variation of A_1 in the NUREG-0313 disposition curve (Eq. 21) with neutron dose that is expressed by Eq. 24.

The available SCC growth rate data for irradiated austenitic SSs in PWR environments show significant variability. The reasons for the high CGRs for some heats irradiated to 11.4 dpa and the unusually low growth rates in SSs irradiated above 18 dpa are not known. In addition, most of the data in the PWR environment were obtained on materials irradiated in either BWRs or the BOR-60 fast reactor. The possible effects of differences in neutron spectrum and flux (fast vs. LWR) or irradiation temperature (288°C [550°F] for BWRs vs. >320°C [608°F] for PWRs) cannot be determined from the existing data. Additional data on PWR-irradiated materials and materials irradiated at different temperatures (e.g., between 300 and 350°C [572 and 662°F]) are needed to better understand the IASCC susceptibility of austenitic SSs in PWR environments.

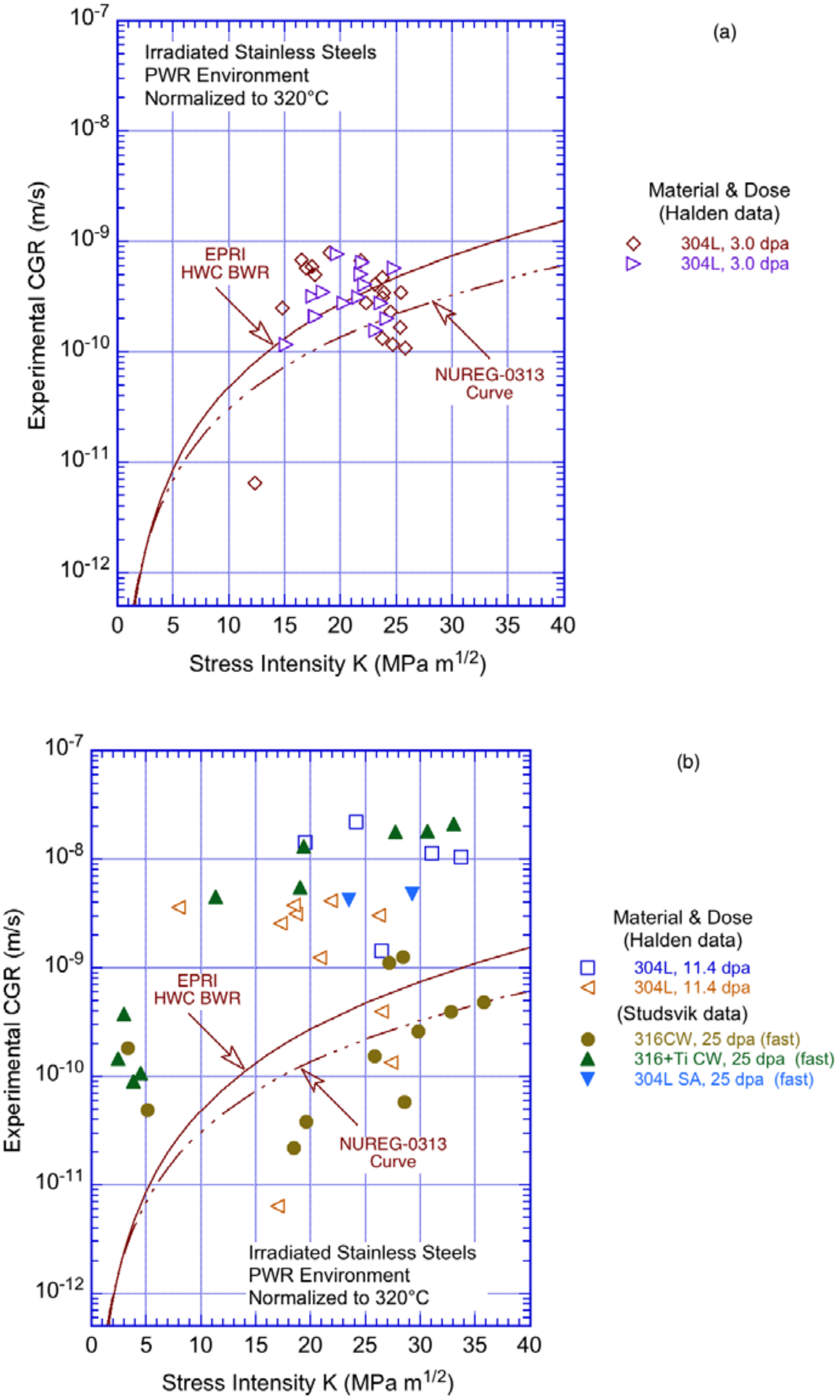

Figure 29. Normalized SCC growth rates in PWR environment for austenitic SSs irradiated to (a) 3 dpa and (b) 11–25 dpa (Refs. 36,296,303,304).

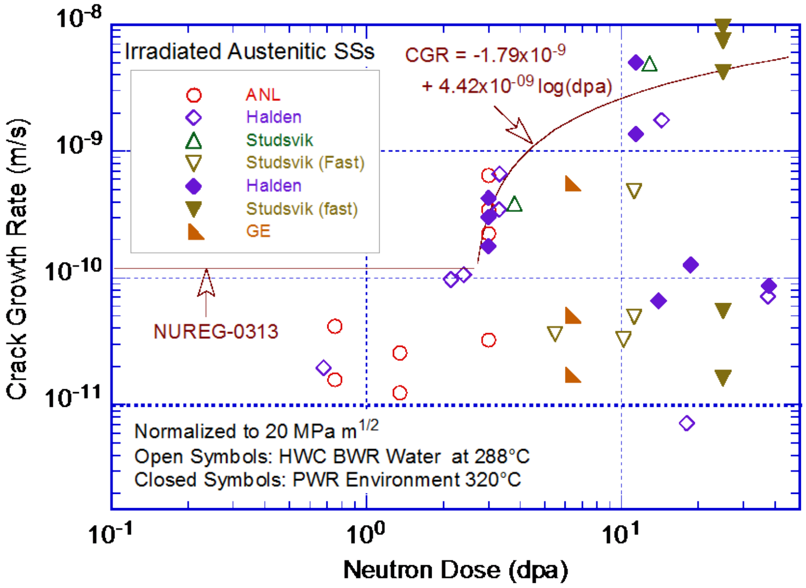

Figure 30. **Crack growth rates for irradiated austenitic SSs in HWC BWR water at 288°C (550°F) or PWR environment at 320°C (608°F) plotted as a function of neutron dose.**

2.4 Material Embrittlement and Fatigue Cracking

The fracture toughness of austenitic SSs has been divided into three broad categories.[21] Category III corresponds to materials with high toughness and J_{Ic} that is above 150 kJ/m^2 (857 in.-lb/in.^{2}), and fracture occurs after stable crack extension at stresses well above the yield strength. Category II corresponds to intermediate toughness materials with J_{Ic} in a range of 30–150 kJ/m^2 (171–857 in.-lb/in.^{2}), and fracture occurs by stable or unstable crack extension at stress levels close to the yield strength. Category I corresponds to materials with low toughness and J_{Ic} of <30 kJ/m^2 (<171 in.-lb/in.^{2}), and fracture occurs below the yield strength with little or no controlled crack extension.

Nonirradiated and unaged wrought and cast austenitic stainless steels fall in Category III. The fracture toughness J_{Ic} values for Type 304 and 316 SS at temperatures up to 125°C (257°F) vary between 169 and 1,660 kJ/m^2 (965 and 9479 in.-lb/in.^{2}).[21] The J_{Ic} values at 400–550°C (752–1022°F) are approximately 35% lower. Fracture in such high-toughness materials is by the nucleation and coalescence of microvoids and is characterized by a dimpled fracture morphology. Cast austenitic stainless steel (CASS) materials typically exhibit ductile fracture at temperatures up to 550°C (1022°F). The overall fracture toughness of CASS material is affected by the density and morphology of second-phase inclusions in the material, and it varies with the casting method. For example, static cast products have slightly lower fracture toughness than the centrifugally cast pipes.

Austenitic SSs and CASS materials are used extensively as structural alloys in LWR systems, including reactor core internal components, because of their excellent ductility, high notch toughness, corrosion resistance, and good formability. CASS materials are used in components such as valve bodies, pump casings, primary coolant piping, and some reactor core internal components. At LWR operating temperature, thermal aging effects are not observed in wrought austenitic SSs because they consist of primarily the austenite phase. However, austenitic SS welds and CASS materials have a duplex structure consisting of both austenite and ferrite phases. The ferrite phase provides additional benefits; it increases tensile strength and improves resistance to SCC. The ferrite phase in CASS materials is susceptible to thermal embrittlement after extended operation at reactor operating temperatures,[21,305–332] typically 282°C (540°F) for boiling water reactors (BWRs), 288–327°C (550–621°F) for pressurized water reactor (PWR) primary coolant piping, and 343°C (650°F) for PWR pressurizers.

In addition, thermal aging embrittlement of materials other than CASS used in reactor components includes (1) temper embrittlement and (2) strain aging embrittlement.[1] Ferritic and low alloy steels are subject to both of these degradation mechanisms but wrought austenitic SSs are not affected by either mechanism. Temper embrittlement of low alloy steels is caused by the diffusion and segregation of impurity elements, such as phosphorous, tin, antimony, and arsenic, into the grain boundaries after prolonged exposure to temperatures in the range of 350–575°C (662–1067°F). At temperatures above this range, the impurities tend toward solution in the ferrite matrix. For example, little or no grain boundary segregation is observed at temperatures above 625°C (1157°F). At temperatures below this range, very long exposure times are necessary for the impurities to diffuse to, and segregate in, the grain boundaries. The presence of carbon tends to accelerate the embrittlement process, due to preferential segregation of the impurities at the interface between grain boundary carbides and ferrite grains. The role of other alloying elements, such as chromium, nickel, magnesium, and molybdenum, in the acceleration or retardation of the temper embrittlement process has been studied extensively. The principal manifestation of temper embrittlement in low alloy steels is an increase in ductile-to-brittle transition temperature, due to the change from predominantly cleavage fracture (before temper embrittlement) to predominantly intergranular fracture along impurity segregation paths (after temper embrittlement).

Strain aging embrittlement occurs in CW ferritic steels when they are subjected to temperatures in the range of 260–371°C (500–700°F) and is caused by the pinning of dislocations by interstitial impurities (nitrogen, carbon, etc.). Post-weld heat treatment of reactor vessel components following cold working during fabrication mitigates, but does not eliminate, the effects of strain aging embrittlement. However, following post-weld beat treatment, residual strain aging embrittlement has only a slight effect on the ductility and fracture toughness of LWR vessel component materials under the environmental and loading conditions of interest.

In addition, for wrought and cast austenitic SSs used in the reactor core internal components, exposure to neutron irradiation for extended periods changes their microstructure (radiation hardening) and microchemistry (radiation-induced segregation) and degrades their fracture properties.[16–37] In such instances, a fracture mechanics methodology, such as linear-elastic fracture mechanics (LEFM) or elastic-plastic fracture mechanics (EPFM) is needed for analyzing structural integrity and developing inspection guidelines. The fracture toughness of such materials is represented by fracture mechanics parameters such as J_{Ic}, the J value near the onset of crack extension, and T, the tearing modulus, which characterizes the slope of the J-R curve:

$$T = (dJ/da)(E/\sigma_f^2), \tag{25}$$

where E is the elastic modulus, a is the crack length, and σ_f is the flow stress defined as the average of the yield strength (σ_y) and ultimate strength (σ_u). The LEFM methodology is used where failure involves negligible plastic deformation, and the fracture toughness is represented by the parameter K_{Ic}, which characterizes the resistance of the material to unstable crack extension. For small-scale yielding (such as deep cracks in bending in sufficiently large specimens), the fracture toughness can be characterized by J_{Ic}. Since J_{Ic} and K_{Ic} have different units, it is often convenient to represent J_{Ic} in terms of a parameter K_{Jc}, which has the unit of the stress intensity factor and is determined from the J_{Ic} value by using the relationship

$$K_{Jc} = (E' J_{Ic})^{1/2}, \tag{26}$$

where the normalized elastic modulus is given by $E' = E/(1 - \upsilon^2)$, E is the elastic modulus, and υ is the Poisson ratio. Only in cases in which LEFM is applicable is K_{Jc} equal to the critical stress intensity. In ASTM Specification E 1820-06, J_{Ic} is determined from the intersection of the best-fit power-law J-R curve with the 0.2-offset line parallel to the blunting line. The blunting line is defined as

$$J = M\sigma_f\Delta a, \tag{27}$$

where σ_f is the flow stress, Δa is crack extension, and the constraint factor M is 2 or a value determined from the best fit of the experimental data. However, the analysis procedures described in the ASTM specifications for J_{Ic} determination are not applicable to austenitic SSs because of their extremely high toughness, ductility, and strain-hardening ability. The main difference concerns the expression for the crack-tip blunting line. For austenitic SSs, a value of 2 for M significantly over-predicts the crack extension; therefore, it yields a non-conservative value of J_{Ic}.[21,312] For austenitic SSs, a value of 4 for M better defines the blunting line. The constraint factor m, which relates J to the crack tip opening displacement (CTOD), is given by

$$J = m\sigma_y(\text{CTOD}). \tag{28}$$

The use of a higher value for m in Eq. 27 is consistent with the expected variation of m and σ_f with strain hardening. The factor m is 1 for materials with an intermediate to a high strength and low strain hardening, and it is 2 for materials with a low strength and high strain hardening, such as austenitic SSs. For the latter, the yield strength is approximately two-thirds of the flow stress, and the crack extension associated with blunting is approximately one-third of CTOD.[21] Thus, for such materials, the crack tip blunting line is given by

$$J = m\sigma_y(\text{CTOD}) \approx 2(2\sigma_f/3)(3\Delta a) = 4\sigma_f\Delta a; \tag{29}$$

i.e., Eq. 27 with M = 4. This relationship has been used to determine J_{Ic} in most investigations on neutron embrittlement, including this study.[23,32] However, a value of 2 for M has also been used by some investigators.[27] The use of a value of 2 for M in Eq. 27 typically yields a higher value of J_{Ic} for Category III materials (i.e., with J_{Ic} above 150 kJ/cm²). However, the difference in J_{Ic} values determined by using values of M of 2 or 4 is insignificant for Category II materials (i.e., J_{Ic} of <100 kJ/cm²). Since, for embrittlement evaluations of irradiated and/or thermally aged austenitic SSs, only the fracture toughness that has been reduced to Category II levels are of interest, the effect of differences in the procedure to determine J_{Ic} is likely to be small.

Extensive studies on the thermal embrittlement of CASS materials have been conducted at Georg Fischer Co.,[305] Westinghouse,[306] The Welding Institute,[308] EPRI,[309] Framatome,[310–313] Central Electricity Generating Board,[†,314] EdF,[315–320] Mitsubishi Heavy Industries,[328–331] Japan Nuclear Energy Safety Organization,[332] and Argonne,[324–327] In the Argonne study, a procedure and correlations were developed for estimating the Charpy-impact energy and fracture toughness J-R curve of CASS components under LWR operating conditions from material

---

[†] The British electricity industry from 1957 to 1990 when it was privatized.

information readily available in certified material test records. The methodology was initially described in NRC topical report NUREG/CR-4513, Rev.1,[326] and has recently been updated in Rev. 2[‡] of the report.

The Argonne methodology is applicable to Grades CF-3, CF-3A, CF-3M, CF-8, CF-8A, and CF-8M of CASS materials within the ASTM Specification A351 for austenitic castings for pressure-retaining parts and Specification A451 for centrifugally cast austenitic SS pipes for high-temperature service. The methodology was applicable only to CASS materials containing up to 40% ferrite, and provides guidance for evaluating the combined effects of thermal and neutron embrittlement for materials used in the reactor core internals.

2.4.1 Thermal Embrittlement

2.4.1.1 Mechanism of Thermal Embrittlement

Cast Austenitic Stainless Steel

It has been known that binary Fe-Cr alloys are susceptible to severe embrittlement when exposed to temperatures in the range of 300 to 500°C (572 to 932°F).[333–335] The potential for significant embrittlement of CASS materials has been confirmed by studies at Argonne.[324–327] The results indicate that thermal aging increases their hardness and tensile strength; decreases ductility, impact strength, and fracture toughness; and shifts the Charpy transition curve to higher temperatures. Various grades and heats of CASS exhibit varying degrees of thermal embrittlement. The low-carbon (low-C) CF-3 materials are the most resistant to thermal embrittlement, and the Mo-bearing, high-C, CF-8M materials are the least resistant. Ferrite morphology has a strong effect on the degree or extent of embrittlement, and the material composition has a significant effect on the kinetics of embrittlement. In addition, as the results of studies on the kinetics of thermal aging demonstrate, thermal embrittlement of CASS materials can occur during the initial 40-y license period for power reactor operation.[324]

The fracture of the 300 series austenitic SSs occurs essentially as a result of the nucleation, growth, and coalescence of microvoids, which results in a dimpled fracture morphology, irrespective of the test temperature.[21] The heat-to-heat variability is due to the differences in the density and morphology of carbides and inclusions, which serve as nucleation sites for void formation. A similar fracture behavior is observed in CASS materials. Voids nucleate preferentially within the ferrite phase or at inclusions and phase boundaries.[21,316,321] However, the overall fracture toughness is controlled by the volume fraction of ferrite. In the unaged condition, CASS materials exhibit a ductile dimpled fracture, and their ductile-to-brittle transition temperature is much lower than room temperature. The high-carbon CF-8 or CF-8M materials have a higher transition temperature compared to the CF-3 materials. The carbides weaken the boundaries and lead to phase boundary separation with little or no strain hardening.[324] In addition, the fracture toughness of wrought austenitic SSs is lower in the longitudinal direction (T-L orientation)[§] than in the L-T orientation.[27] The same effects of material orientation are possible in CASS materials, depending on the morphology of the ferrite phase and distribution of second-phase particles.

[‡] Sent for publication.

[§] The first letter represents the direction perpendicular to the plane of the crack, and the second letter represents the direction of crack advance. For plates, L = longitudinal or rolling direction and T = transverse direction (i.e., across the thickness). For pipes, L = longitudinal or axial direction and C = circumferential direction (across the wall).

The time-temperature curves for the formation of various phases in thermally aged CASS materials[307] are shown in Fig. 31. At reactor operating temperatures of 280–370°C (535–698°F), the thermal aging of CASS materials leads to: (a) spinodal decomposition of the ferrite into high-Cr α’ and low-Cr α regions; (b) nucleation and growth of the high-Cr α’ phase; (c) precipitation of an Ni- and Si-rich G phase, $M_{23}C_6$ carbide, and γ_2 (austenite); and (d) additional precipitation and growth of existing carbides at ferrite/austenite phase boundaries.[336–343] At temperatures above 550°C (1020°F), embrittlement is largely due to the formation of the sigma phase, and the formation of chi phase influences mechanical properties. Furthermore, microstructural studies indicate that the microstructural changes during thermal aging at temperature above 400°C (752°F) are significantly different from those at reactor operating temperatures. At high temperatures, there is significant precipitation of carbides and nitrides and/or growth of existing carbides. In addition, the precipitation of Cr-rich carbides is always accompanied by a decrease in the ferrite content.[307] Therefore, extrapolation of the results of thermal aging studies at 425–500°C (797–930°F) may yield non-conservative estimates.

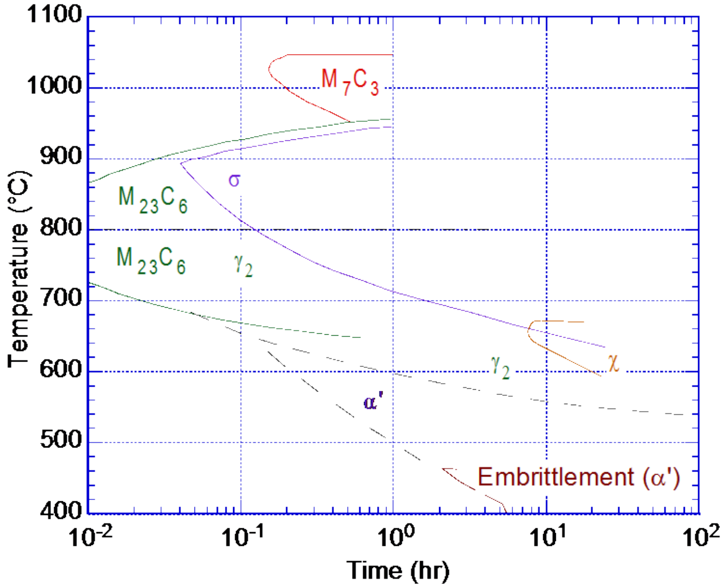

Figure 31. Time-temperature curve for the formation of various phases in CASS materials (Ref. 307).

Austenitic Stainless Steel Welds

In austenitic SS welds, the ferrite phase is desired for controlling the weld solidification behavior and inhibiting the formation of low-melting-point compounds such as sulfides and phosphides, which promote microfissuring.[21] Because the ferrite phase is brittle at low temperatures, austenitic SS welds also exhibit a ductile-brittle transition temperature (DBTT) phenomenon. However, at ambient and elevated temperatures, the ferrite phase shows a ductile deformation behavior. The fracture toughness of Type 304/308 and 316/16-8-2 welds depends on the weld process, but not composition.[21] For a given weld process, both these weld metals exhibit similar fracture toughness.[25] In general, gas tungsten arc (GTA) welds exhibit the highest toughness and submerged arc (SA) welds the lowest. The J_{Ic} values for the SA welds are about one-third those for the GTA welds.

Although austenitic SS welds have a duplex structure and their chemical compositions are similar to those of CASS materials, their fracture toughness is lower than that of the wrought SSs and most CASS materials. Typically, austenitic SS welds exhibit ductile dimpled fracture morphology at temperatures up to 550°C (1022°F).[344] Because of a high density of inclusions in the weld, the dimples are relatively small and shallow, and are often associated with inclusions. The overall fracture toughness of SS welds is controlled by the density and morphology of second-phase inclusions in the material, and it varies with the weld process. For example, GTA/metal inert gas (MIG)/TIG welds exhibit the highest toughness; shielded metal arc (SMA)/ manual metal arc (MMA) welds and GTA welds have intermediate toughness; and SA welds have the lowest toughness.[21] The median value of J_{Ic} is 492 kJ/m^2 (2809 in.-lb/in.^{2}) for GTA welds and 147 kJ/m^2 (839 in.-lb/in.^{2}) for SA welds at temperatures up to 125°C (257°F). The fracture toughness of the (HAZ material is typically superior to that of the weld metal.

Because the microstructure and fracture behavior of austenitic SS welds are significantly different from that of CASS materials, the Argonne fracture toughness estimation methodology for CASS materials is not applicable to austenitic SS welds. The NUREG/CR-4513, Rev. 1, correlations account for mechanical-property degradation of typical heats of CASS but do not consider the effects of compositional or structural differences that may arise from various welding processes, all of which have a strong effect on the failure mechanism of weld materials. Consequently, the approach used to evaluate thermal and neutron embrittlement of austenitic SS welds relies on establishing a lower-bound fracture toughness J-R curve for unaged and aged, and non-irradiated and irradiated SS welds.

Austenitic SS welds generally contain 5–15% ferrite, but their mechanical properties typically differ from those of CASS materials. Earlier studies conducted at Argonne[344] indicated that, for a given ferrite content, the tensile strength of austenitic SS welds is higher and fracture toughness is lower than those of CASS materials. Experimental data[344] indicate that CASS materials with very poor fracture toughness are relatively insensitive to thermal aging. In these steels, failure is controlled by void formation near inclusions or other flaws in the material (i.e., by processes that are not sensitive to thermal aging). These results suggest that austenitic SS welds with poor fracture toughness (e.g., SA and SMA welds) should be relatively less sensitive to thermal aging than GTA welds.

2.4.1.2 Fracture Behavior of Aged Materials

Cast Austenitic Stainless Steel

A study at EdF on the evolution of mechanical properties of thermally aged CASS materials and metallurgical and aging parameters indicated that at room temperature (RT), the brittle transgranular fracture of ferrite takes place primarily by cleavage; some twinning has also been observed in embrittled material.[316,345] Multiple cleavage of ferrite is observed throughout the material. At higher temperatures, cleavage of the ferrite is reduced and twinning plays an important role in brittle failure. Both Charpy-impact and compact tension (CT) specimens exhibit similar fracture behavior. However, a greater degree of embrittlement is needed for cleavage to occur in CT specimens. In Charpy-impact specimens tested at RT, the ferrite/austenite phase boundary exhibits a jagged appearance with very fine lines and straight deformation bands within the ferrite islands (i.e., slip bands and twins), as seen in Fig. 32.[324] The fracture behavior of the austenite also changes from a dimple fracture to shear fracture. The presence of a completely embrittled ferrite skeleton promotes the low energy failure mode of ductile shearing or tearing of the austenite ligaments between the islands of ferrite.[346]

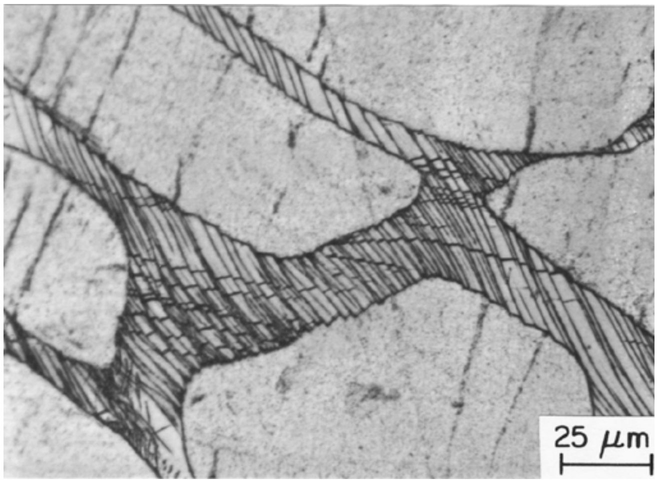

**Figure 32.
Deformation twins in a Charpy-impact specimen of CF-8 material aged for 30,000 h at 350°C (662°F) and tested at 290°C (554° F) (Ref. 324).**

Severely embrittled CASS materials exhibit large areas of brittle transgranular fracture of ferrite, linked by ductile shearing or tearing of the austenite ligaments. The degree of embrittlement and thus the toughness of the material are controlled by the amount of brittle fracture. A predominantly brittle failure occurs when either the ferrite phase is continuous (e.g., in cast material with a large ferrite content) or the ferrite/austenite phase boundary provides an easy path for crack propagation (e.g., in high-C grades of cast material with large phase-boundary carbides). Ferrite contents of about 10% or more can provide a continuous fracture path.

Austenitic Stainless Steel Welds

In austenitic SS welds, the overall fracture toughness is controlled by the density and morphology of the second-phase particles and to some extent by the ferrite content of the weld. The fracture toughness of SS welds is generally lower than that of cast or wrought austenitic SSs because of the higher density of inclusions. Among austenitic SS welds, SA and SMA welds have poor fracture toughness relative to GTA welds; they have a high density of manganese- and silicon-rich silicates and silicides. High silicon contents are generic to the SA and SMA welds because of silicon pickup from the flux. Typically, SA welds have 0.6–1.0% Si, SMA welds have 0.5–0.8% Si, and GTA welds have <0.5% Si.[21]

Furthermore, in materials with a duplex structure (e.g., austenitic SS welds), the ferrite phase exhibits a ductile-to-brittle-transition temperature. Its plastic straining capacity is substantially decreased at low temperatures. However, the ferrite phase is ductile at room temperature and higher temperatures. Therefore, in the unaged condition, austenitic SS welds exhibit a ductile dimpled fracture. The transition temperatures of unaged materials are relatively low. The differences in the transition temperature for the various unaged heats and grades of CASS materials are due to the amount of ferrite and the differences in the mechanism of brittle fracture. The high-carbon CF-8 or CF-8M steels have a higher transition temperature than CF-3 steels because of the presence of phase boundary carbides. The carbides weaken the boundaries and lead to premature phase boundary separation with little or no strain hardening.

The thermal aging of austenitic SS welds at 300–450°C (572–842°F) results in thermal embrittlement of the ferrite and, depending on the amount, morphology, and distribution of ferrite and second-phase particles, the ductile-to-brittle-transition temperature shifts to higher temperatures.[21,324–327] Thermal aging of austenitic SS welds leads to spinodal decomposition of the ferrite to form the α' phase, formation of Ni- and titanium (Ti)-rich silicides (the G phase, $Ti_6Ni_{16}Si_7$) in the ferrite, precipitation of $M_{23}C_6$ carbides on the phase boundaries, and limited

M_6C carbides in the matrix.[21] However, because SS welds typically contain less than 15% ferrite, the ferrite content has little effect on the overall fracture toughness. The degradation of fracture toughness of SS welds primarily occurs due to the presence of grain boundary or phase boundary carbides, which initiate localized intergranular cracking. Fracture occurs along the delta ferrite regions where the second-phase particles initiate voids/cracks either by decohesion of the ferrite/austenite interphase or particle cracking.[347] The dominant failure process is transgranular dimple fracture; intergranular cracking is limited to a few isolated regions.[21] However, the fracture toughness of welds is influenced by material orientation.

2.4.1.3 Distribution and Morphology of Ferrite

Cast Austenitic Stainless Steel

The degree and kinetics of thermal embrittlement of CASS materials are controlled essentially by the amount, size, and distribution of the ferrite and to some extent by the presence of carbides or nitrides at the phase boundaries. These parameters, in turn, depend on the chemical composition of the material and the manufacturing process. The pseudo binary diagram for a Fe-Ni-19%Cr system is shown in Fig. 33. Duplex SSs that solidify in the δ+γ (ferrite and austenite) regime exhibit vermicular and interdendritic lacy ferrite morphology. Materials with high Cr contents solidify into a primary δ ferrite phase and have lathy ferrite morphology. During further cooling of the solidified material, if the concentrations of the γ-forming elements (e.g., C, N, Mn, and Ni) are sufficient, a fraction of the δ ferrite transforms to γ austenite. If the cooling rate between 900 and 600°C (1652 and 1112°F) is slow, δ ferrite can transform to the brittle sigma (σ) phase and $M_{23}C_6$ carbides can precipitate at the phase boundaries. Both lead to degradation of the mechanical properties.

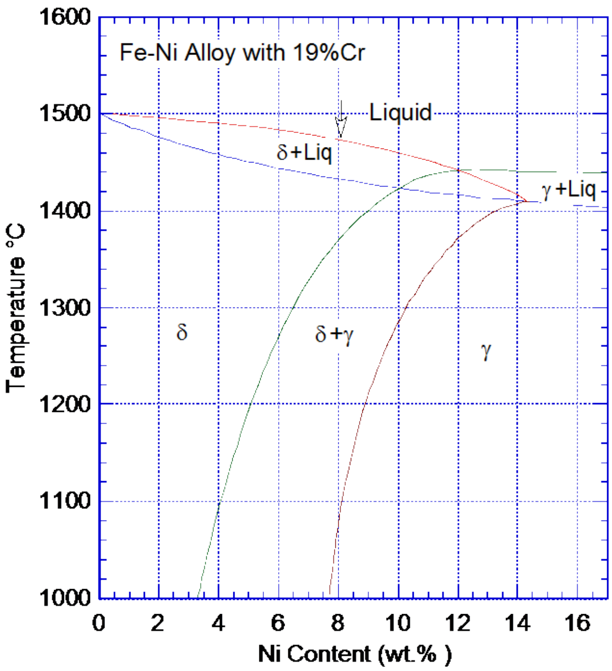

Figure 33.
Pseudo binary diagram for Fe-Ni-19%Cr alloy (Ref. 348).

In the Argonne study on thermal embrittlement of CASS materials,[326] a value of 10% Ni was used to differentiate whether primary γ (austenite) forms during solidification of the CF-8M castings from the liquid. For compositions containing <10% Ni, the solidification sequence is as follows: Liq. $\rightarrow$ Liq. + $\delta \rightarrow \delta$, with $\delta \rightarrow \gamma$ in the solid.[348] Austenite nucleates predominantly at ferrite grain boundaries and to a lesser extent at interdendritic locations within the ferrite. For compositions containing ≥10% Ni, the solidification sequence is likely to be as follows: Liq. → Liq. + δ → Liq. + δ + γ → δ + γ, with δ → γ continuing in the solid.[348] The austenite forms first in the liquid as a secondary phase enveloping the primary ferrite. Upon further cooling, it grows in the remaining liquid as well as into the ferrite. The latter growth continues below the solidus line. The actual microstructure of the casting depends on the Cr/Ni ratio for the specific composition. Because of significant differences in the composition and microstructure of the ferrite in CF-8M materials with <10 or ≥10% Ni, the thermal aging behavior is significantly different for these two materials. Studies by Massoud et al.[318] have identified several differences in the thermal aging behavior of CASS materials produced by different foundries. The significant results are as follows:

- The microstructure produced by spinodal decomposition is very sensitive to the initial state of the ferrite in the as-quenched condition. Any manufacturing parameter that improves the homogeneity of the ferrite (e.g., rapid quench and long homogenizing heat treatments) results in a more aging-resistant material, but the beginning of the decomposition is delayed.

- The homogenizing treatment holding time and the quenching rate affect the beginning of the decomposition of the ferrite and, therefore, the overall kinetics of aging.

- An increase in the temperature for homogenizing treatment increases the ferrite content and alters the chemical composition of each phase. Consequently, it affects the aging behavior. Spinodal decomposition is sooner in these materials. However, materials treated at high temperatures are less sensitive to embrittlement because their Cr content is lower.

- The solidification rate affects the ferrite morphology and the toughness transition curve, but it does not affect the aging behavior of the material.

Austenitic Stainless Steel Welds

For commercial AISI 300 series austenitic SSs, the weld ferrite content varies from 0 to about 20 volume percent (%), depending primarily on the material composition, and to a lesser extent on weld cooling rate.[349–358] However, the solidification behavior and subsequent solid-state transformation within the weld metal during cooling (shown in Fig. 34) control the microstructural characteristics of the weld. Therefore, establishing the formation and distribution of different ferrite morphologies in the weld is rather difficult.[355]

In Fig. 34, the structure of the equilibrium phase of composition C_o with Fe-20 wt.% Cr and 10 wt.% Ni (i.e., typical for Type 304 SS welded with Type 308 electrode) is ferritic at temperatures in the range of 1380–1420°C (2516–2588°F) and austenitic below 1120°C (2048°F). Upon cooling, this composition passes through a two-phase regime (δ + γ). The resulting microstructures have been related to the weld material phase diagram[353] and to the ratio of the Cr and Ni equivalents (Cr_{eq}/Ni_{eq}).[350] However, they are also affected by the cooling rate.[353,354] For CASS materials with <10% Ni, primary ferrite is first formed followed by solid-state transformation of δ to γ. The residual δ is observed at the dendrite core.[355] In materials

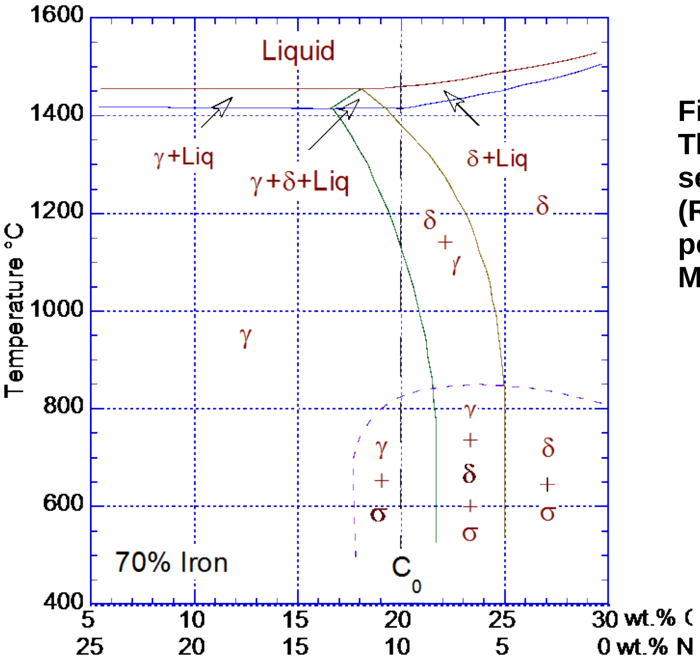

Figure 34.
The 70% constant Fe vertical section of the Fe-Ni-Cr system (Ref. 355). Reprinted with permission of The Minerals, Metals & Materials Society.

with ≥10% Ni, the residual δ is observed at the dendrite boundaries. The solidification mode of SSs can be predicted based on the Cr_{eq}/Ni_{eq} ratio using the Schaeffler equation:[352,359]

Austenite mode: $Cr_{eq}/Ni_{eq} \le 1.48,$ (30)

Ferrite/austenite mode: $1.48 \le Cr_{eq}/Ni_{eq} \le 1.95,$ (31)

Ferrite mode: $1.95 \le Cr_{eq}/Ni_{eq},$ (32)

where Cr_{eq} and Ni_{eq} are determined from the material composition in wt.%,

$$Cr_{eq} = Cr + 1.5Si + Mo + 0.5Nb + 2Ti, \text{ and} \quad (33)$$

$$Ni_{eq} = Ni + 0.5Mn + 30C + 30(N - 0.06). \quad (34)$$

Because of the differences in the solidification behavior because of changes in the Cr and Ni content of the weld, both the morphology and composition of the δ-ferrite can vary significantly between the different modes of solidification. Furthermore, due to differences in the Cr_{eq}/Ni_{eq} ratio of the base metal and weld compositions and solute segregation during solidification, the composition of welds of nominal composition C_o can vary significantly prior to any solid-state transformation.

Davies[360] has summarized the composition profiles predicted by different models (shown in Fig. 35) in a bar solidified from liquid of composition C_o. The figure shows a case in which equilibrium distribution coefficient $k < 1$. The fraction of the melt of initial composition C_o that has solidified is plotted along the *x*-axis. In Fig. 35, line (a) represents the uniform composition profile C_o for equilibrium solidification. The other three cases are for no diffusion in the solid and equilibrium at the liquid-solid interface. Complete mixing in the liquid is typically assumed in the solidification of welds shown as curve (c) in the figure. The final liquid solidifies as a eutectic;

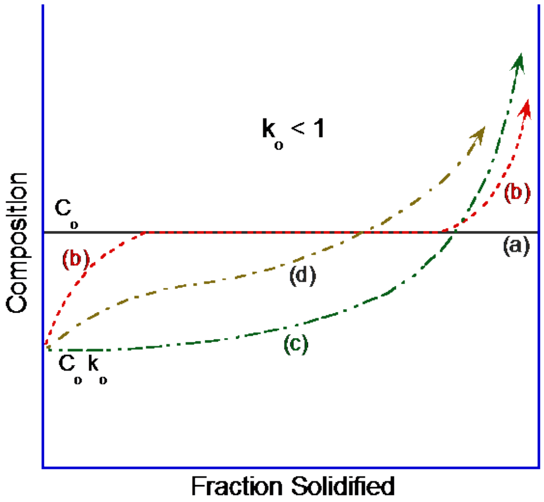

Figure 35.
Solute distributions predicted by different models in a frozen bar from liquid of composition C_o: (a) equilibrium cooling, (b) solute mixing in the liquid by diffusion only, (c) complete mixing in the liquid, and (d) partial solute mixing in the liquid (Ref. 360 as reproduced in Ref. 355. Reprinted with permission of The Minerals, Metals & Materials Society).

this occurs within the interdendritic regions. Case (b) represents mixing in the liquid by diffusion only. This results in the formation of a solute-rich boundary layer at the liquid-solid interface, which depends on the solute distribution k, the diffusion coefficient in the liquid, and the solidification velocity. Case (d) represents some mixing in the liquid by convection in addition to diffusion. Note that in all cases, the initial solid to form at dendrite or cell core is composed of $C_o k_o$, where k_o corresponds to the initial C_o. Examples of typical ferrite morphology of two welds in Type 304 pipes of different sizes are shown in Fig. 36. Material designated PWWO is a weld overlay and PWMS weld was treated by the Mechanical Stress Improvement Process.

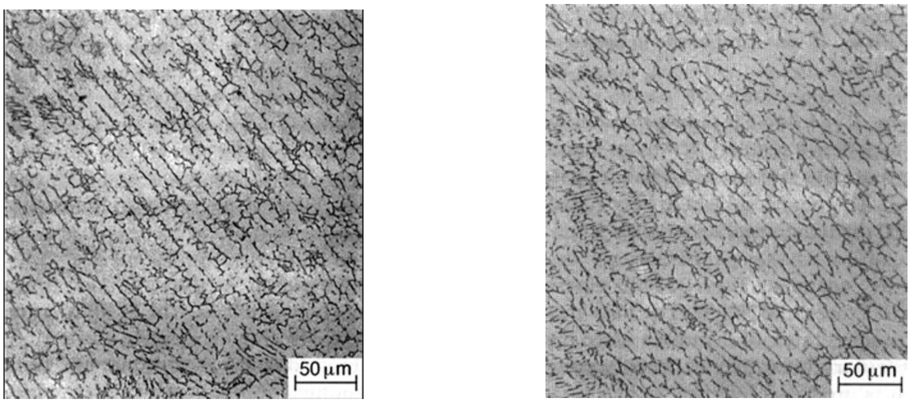

PWWO PWMS

Figure 36. Typical ferrite morphology in two different welds (Ref. 344).

David[354] studied the ferrite morphology and variations in ferrite content in two Type 308 SS multipass welds and identified four distinct ferrite morphologies: vermicular, lacy, acicular, and globular. The welds were prepared by the GTA process with a Type 304L SS plate. Ferrite number (FN) was measured using a Magne-gage in accordance with American Welding Society (AWS) A4.2-74[361] procedure. The average FNs of the root pass deposited in the buttered and not buttered weld were 13 and 8, respectively. The lower ferrite content of the weld prepared without buttering was attributed to weld-metal dilution with the base metal. The ferrite content of the root pass decreased further because of the dilution due to thermal effects during the other weld passes. Variations in ferrite content were also observed within the weld. The FN values[††]

[††] FN values determined from the modified Schaeffler diagram.

at various weld locations varied from 9 to 13 and from 5 to 14 for the buttered and not buttered welds, respectively. Based on the composition of the weld metal, the calculated ferrite content, without dilution, is 8.1% from Hull's equivalent factor,[351] 5.9% from the ASTM A800/A800M methodology (based on the Schoefer diagram),[362,363] and about 13.8% from the modified Schaeffler diagram.[364,365] The variations in ferrite content are due in part to differences in the N pickup during welding.[354]

The results[354] indicate that the solidification sequences in Type 308 SS welds include primary crystallization of δ-ferrite with subsequent envelopment by austenite, followed by further transformations from liquid $\rightarrow \gamma$ and $\delta \rightarrow \gamma$.[354] As the sample cools below the solidus temperature, the transformation at the liquid/γ interface is completed, leaving behind a skeletal network of untransformed δ-ferrite along the cores of the primary and secondary dendrite arms. This residual ferrite is rich in Cr, which makes it very stable. However, primary ferrite, with lower average Cr content (24–25 wt.%), may transform into Widmanstätten austenite and ferrite during rapid cooling. These two transformations involve extensive solute redistribution by diffusion; the results could be used to explain the various ferrite morphologies observed in austenitic SS welds.[354]

Similar results were observed by Abe and Watanabe[359] in Type 316L SS welds that were prepared using two different filler metals containing 11.27 and 13.72 wt.% Ni. One weld solidified in primary ferrite mode and the other in primary austenite mode. The ferrite contents of the welds were 12.7% and 2.5%. The low-Ni, high-ferrite weld showed predominantly a vermicular morphology with small amounts of lathy and acicular ferrite, while the high-Ni, low-ferrite weld showed islands of δ-ferrite at the dendrite boundaries. Note that these ferrite morphologies may appear continuous or discontinuous depending on the section of the weld viewed. Therefore, caution must be exercised in characterization of the ferrite.

2.4.2 Neutron Embrittlement

2.4.2.1 Low-Alloy Steels

As discussed earlier, long-term exposure to neutron irradiation of LWR structural materials changes their microstructure (radiation hardening) and microchemistry (radiation-induced segregation, or RIS),[16–18] which results in an increase in the tensile strength and hardness of the material and a decrease in fracture toughness or resistance to brittle fracture, commonly known as neutron embrittlement.[19–32] In ferritic steels, neutron embrittlement is typically quantified by an increase in the reference temperature, nil-ductility transition (RT_{NDT}), and a drop in the Charpy upper shelf energy. It is primarily caused by the formation of copper-rich precipitates that harden the matrix and reduce fracture toughness. The formation of these precipitates is enhanced by neutron irradiation.

During the past 50 years, extensive databases have been compiled on neutron embrittlement of pressure vessel steels, including the surveillance capsule data from LWRs as well as test reactors. These results are used for evaluating and predicting embrittlement of reactor vessel steels. Embrittlement trend curve models have been developed for predicting the shift in RT_{NDT} and drop in upper shelf energy as a function of copper, nickel, and fluence. These curves are given in NRC Regulatory Guide RG-1.99, Rev. 2.[366]

The extent of neutron embrittlement varies significantly between different types of ferritic steel (e.g., carbon or low-alloy steels) and even between different heats of the same steel. These differences are due to variations in the composition and microstructure of the material.

Improved empirical trend models have been developed for pressure vessel steels, to describe the combined effects of copper, nickel, phosphorus, irradiation temperature, and neutron flux and fluence on neutron embrittlement. Typically, steels with a very low copper content show little embrittlement even at relatively high radiation doses. The effect of irradiation exposure at low temperatures (<274°C [525°F]) increases the rate of embrittlement damage. In addition, weld metal is generally more sensitive to neutron embrittlement than base metal. The impurity content, chemistry variability, and different microstructure are responsible for the greater sensitivity of the weld metal. In 2002, the improved trend curve model was approved in a revision to ASTM Standard Guide E900-02, which was later superseded by E900-15.[367]

2.4.2.2 Austenitic Stainless Steels

Until recently, most of the published experimental data on neutron embrittlement of austenitic SSs had been obtained on materials irradiated in high-flux fast reactors.[368–378] In these studies, the embrittlement of the materials has been characterized in terms of tensile properties, Charpy-impact properties, and fracture toughness. The fracture toughness of structural materials is typically characterized by (a) the initiation toughness J_{Ic} and tearing modulus T for materials that fail after substantial plastic deformation (for EPFM analysis) and by (b) the critical stress intensity factor K_{Ic} for materials that fail after little or no deformation (for LEFM analysis). In some studies, the power-law J-R curve parameters, coefficient C and exponent n, are also reported.

The effects of neutron exposure (in dpa) on the fracture toughness of austenitic SSs at 25–427°C (77–842°F) have been investigated for SSs irradiated up to 90 dpa at 90–450°C (194–842°F) in fast reactors.[21,25,26,373–378] As discussed earlier in NRC topical report NUREG/CR-7027,[215] the fast reactor data show substantial decrease in toughness at exposures of 1–10 dpa, and little or no further reduction in toughness beyond 10 dpa. The degradation in fracture properties appear to saturates at a J_{Ic} value of ~30 kJ/m^2 (171 in.-lb/in.^{2}); that is, a K_{Jc} value of 75 MPa m$^{1/2}$ (68.2 ksi in.$^{1/2}$).[215] In addition, the failure mode changes from dimple fracture to channel fracture.

The fracture toughness J_{Ic} for wrought and cast SSs irradiated in LWRs,[19,21–24,26–32,368,379] are shown in Fig. 37. The Westinghouse data for a heat of CASS CF-8 material irradiated to about 6–12 dpa are not included in the figure, because the irradiations were carried out in a fast reactor and the tests were conducted at room temperature. As discussed below, fracture toughness at reactor temperatures is expected to be lower. The fracture toughness data trend for LWR-irradiated materials is similar to the trend for the fast reactor data. Most of the fracture toughness J_{Ic} values for austenitic SSs irradiated in LWRs (288–316°C [550–601°F]) fall within the scatter band of the data obtained on materials irradiated in fast reactors, even though the LWR irradiations were at lower temperatures. However, the extent of embrittlement and the rate of decrease in fracture toughness vary among the different materials. Typically, for the same irradiation conditions, the fracture toughness of thermally aged CASS material is lower than the toughness of HAZ material, and that, in turn, is lower than the fracture toughness of solution-annealed SSs.

The JAPEIC data for Type 304 SS irradiated to 3.0–5.3 dpa at LWR temperatures show very poor fracture toughness. The J_{Ic} values are below the lower-bound curve for the fast reactor data. For the material irradiated to 4.5–5.3 dpa (shown as "+" in Fig. 37), 9 of 10 CT specimens showed no ductile crack extension, and the K_{Ic} values were 52.5–67.5 MPa m$^{1/2}$ (47.7–61.4 ksi in.$^{1/2}$).[22] In Fig. 37, the lowest fracture toughnesses with K_{Ic} or K_{Jc} values in the range

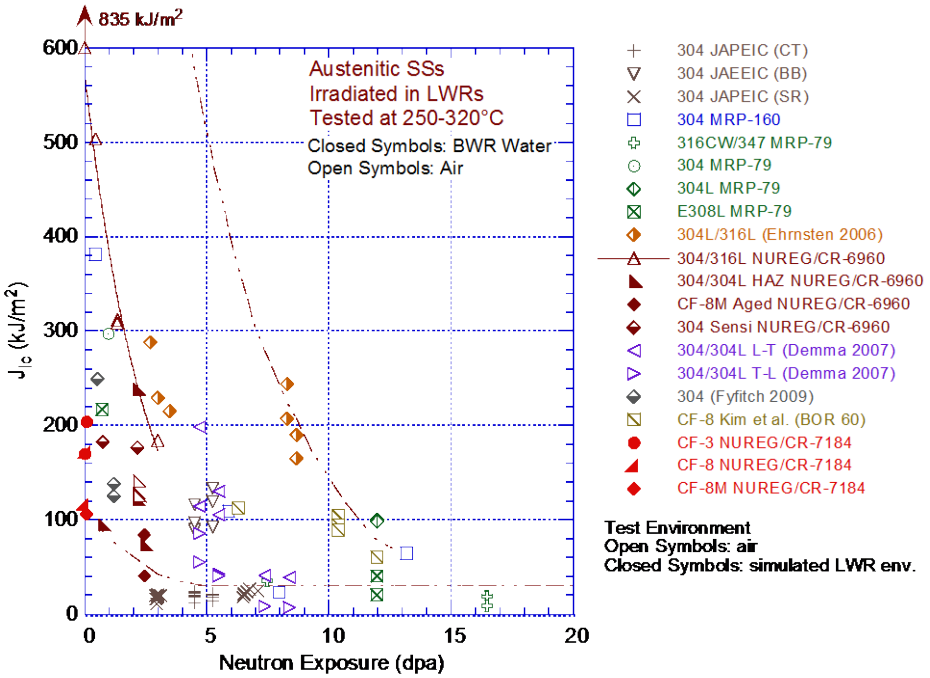

Figure 37. **Change in fracture toughness J_{Ic} as a function of neutron exposure for LWR irradiated austenitic SSs. Dashed lines represent the scatter band for he fast reactor data on SSs irradiated at 350–450°C (662–842°F) (Refs. 19,21–24,26–32,368,379).**

of 36.8–40.3 MPa m$^{1/2}$ (33.5–36.6 ksi in.$^{1/2}$) are for a Type 347 SS irradiated to 16.5 dpa in a PWR[22] and for a Type 304 SS irradiated to 7.4–8.4 dpa in a BWR.[30]

The material's orientation also has a strong effect on fracture toughness. Fracture toughness J-R tests and microstructural and microchemistry characterization have been performed on Types 304 and 304L control-rod and top guide materials irradiated to 4.7–12.0 dpa in a BWR. All materials consistently show lower fracture toughness in the T-L (transverse-longitudinal) orientation than in the L-T orientation (shown as isosceles triangles with their bases to the left or right, respectively, for T-L and L-T orientations).[27] The fracture toughness K_{Ic} values are lower than the limiting value of 55 MPa m$^{1/2}$ (50 ksi in.$^{1/2}$) that has been proposed by industry for flaw tolerance evaluations of irradiated austenitic SSs.[24,27]

The lower fracture toughness along the T-L orientation has been attributed to the presence of stringers consisting of long, narrow γ' particles (2–10 nm, average of 4.4 nm) oriented in the rolling direction. This microstructure results in a long, narrow quasi-cleavage structure parallel to the crack advance, thereby accelerating the crack advance.[27] The γ' phase has been observed at dose levels above 4 dpa in CW Type 316 SS irradiated under the PWR conditions.[380] The low J_{Ic} of this material might be considered a special case of materials containing a high density of particles aligned in the rolling direction.

Fracture Toughness J-R Curve

Fracture toughness J-R curve data have been obtained for Types 304, 304L, and 316L SSs, including weld HAZs, and CF-3, CF-8, and CF-8M CASS materials irradiated in LWRs up to about 14 dpa,[22–32] and irradiated in fast reactors to much higher dose levels. The fracture toughness J-R curve for Type 304 SS irradiated under LWR conditions continues to decrease with increase in neutron dose. The decrease is quite rapid up to about 6 dpa, and the toughness continues to decrease moderately at higher dose levels. The effects of various parameters (e.g., material type and heat treatment; test and irradiation temperatures; neutron energy spectrum; flux, dose) have been discussed in several Argonne publications.[31,32,381]

Test Environment: Nearly all of the existing fracture toughness data have been obtained from tests in air and on specimens that were fatigue precracked at relatively low load ratios (typically 0.1–0.2) in room temperature air. However, in reactor core components, cracks are initiated primarily by SCC and have intergranular morphology, whereas the fatigue precracks in fracture toughness tests are always transgranular). In addition, the corrosion/oxidation reaction could influence fracture toughness. For example, hydrogen generated from the oxidation reaction could diffuse into the material and change the deformation behavior by changing the stacking-fault energy of the material. To investigate potential effects of the reactor coolant environment on the fracture toughness of austenitic SSs and CASS materials, J-R curve tests have been conducted on these materials in a BWR NWC environment[32] and in low-DO, high-purity water or simulated PWR environments.[382] The effect of the reactor coolant environment on the fracture toughness of CASS materials has been discussed earlier.

The results indicate that both NWC BWR and simulated low-DO PWR environments can decrease the fracture toughness of these materials. However, the effect may be insignificant for materials with poor fracture toughness (i.e., J_{Ic} values of <150 kJ/m^2).[31,32,206,382] For example, the fracture toughness J-R curves for irradiated Type 304L SAW HAZ in air and water environments are essentially identical (Fig. 38). However, for a CF-8M material aged for more than 15 years at 350°C (662°F), the J-R curve data for specimens precracked in air at 54°C (129°F) and then tested in a shutdown water chemistry PWR environment at 54°C (129°F) are significantly lower than the data for those specimens tested in air. The specimens precracked in PWR water at 315°C (599°F) and tested in PWR water also show reduced fracture toughness, but the effect is less.[343] The significant decrease in fracture toughness is attributed to the synergism between hydrogen embrittlement and thermal embrittlement. Similarly, J-R curve data for Type 316L GTA welds indicated that the reactor coolant environment could decrease the fracture toughness by up to 40% relative to that in air.[383]

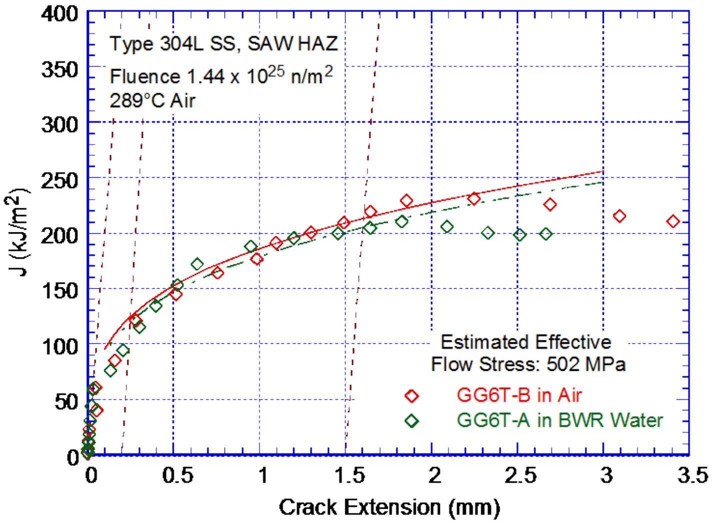

Figure 38.
Fracture toughness J-R curves for irradiated specimens of Type 304L SAW HAZ in air and NWC BWR environment (Ref. 32).

The potential contribution of hydrogen-induced embrittlement has also been observed in the thermal embrittlement study at Argonne. The J-R curves for the two tests on ¼-T CT specimens of thermally aged and irradiated CF-8M steel in NWC BWR water are shown in Fig. 39. Unfortunately, companion tests in air were not conducted on the irradiated material. However, the fracture toughness J-R curve obtained for 1-T CT specimens of unirradiated, thermally aged material are included in the figure. In the two tests in water, large load drops, accompanied by crack extensions of up to 0.5 mm (0.02 in.) in one specimen and 1.0 mm (0.04 in.) in the other, were observed at the onset of these crack extension. Such load drops are not typically observed during tests in air.[326] Thus, although available fracture toughness data in reactor coolant environments are inclusive, the limited data suggest that there could be environmental effects on the fracture toughness of CASS material and austenitic SS welds, at least for materials with moderate or superior fracture toughness. Additional tests on irradiated CASS materials or SS welds in air and water environments are needed to determine the possible effects of LWR coolant environments on their fracture toughness.

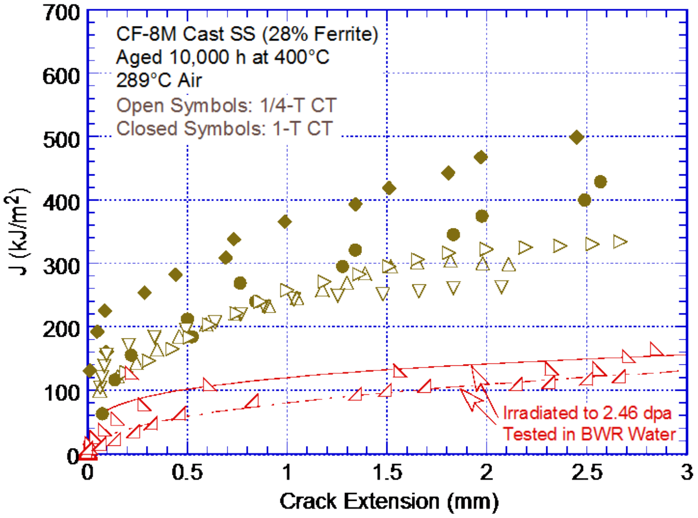

Figure 39.
Fracture toughness J-R curves for thermally aged and irradiated CF-8M steel (Ref. 32).

Lower-Bound Fracture Toughness Curve

In NUREG/CR-7027, the available fracture toughness data on wrought and cast austenitic SSs and associated welds irradiated in fast reactors or LWRs were reviewed and evaluated to define the lower-bound fracture toughness J_{Ic} value or coefficient C of the J-R curve as a function of neutron dose (in dpa).[31,32] The lower-bound curves represent the change in fracture toughness parameters, such as the coefficient C of the power-law J-R curve and the corresponding J_{Ic} value, as a function of neutron dose. The trend curve describes the following information:

(a) The threshold neutron exposure for radiation embrittlement of austenitic SSs and a minimum fracture toughness for these materials irradiated to less than the threshold value,

(b) The saturation neutron exposure and a saturation fracture toughness for materials irradiated to greater than this value, and

(c) The change in fracture toughness between the threshold and saturation neutron exposures.

The change in initiation toughness J_{Ic} of (a) wrought austenitic SSs and (b) CASS materials and weld metals as a function of neutron exposure (dpa) is shown in Fig. 40. The change in the lower-bound J_{Ic} value as a function of the neutron dose (dpa) is given by

$$J_{Ic} = 7.5 + 110 \exp[-0.35(\text{dpa})^{1.4}]. \qquad (35)$$

Note that the JAPEIC data on Type 304 SS only is not bounded by the lower bound curve; the data were obtained on short rod specimens and not the standard fracture toughness CT

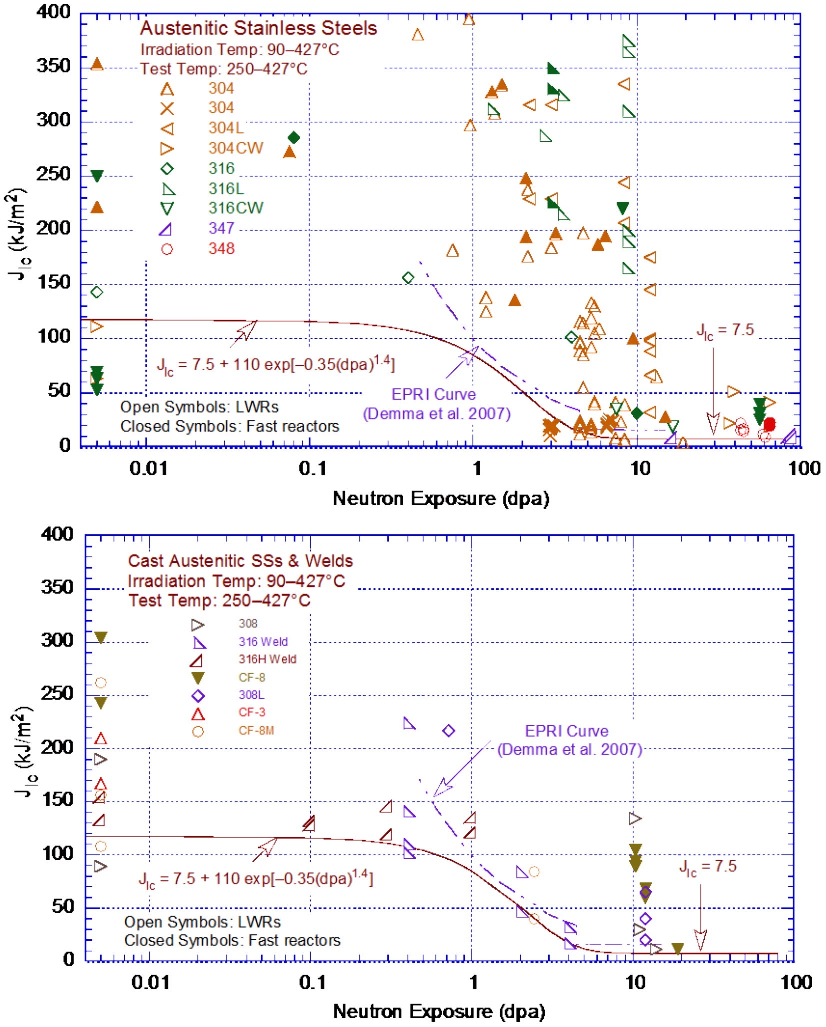

Figure 40. **Change in initiation toughness J_{Ic} of (a) wrought austenitic SSs and (b) CASS materials and weld metals as a function of neutron exposure. The data points plotted at 0.005 dpa are for unirradiated materials (Ref. 32).**

specimens. The lower-bound curve is defined essentially by the austenitic SS weld data. The lower-bound curve represents the following:

(i) Threshold dose of about 0.3 dpa for neutron embrittlement,

(ii) Minimum fracture toughness J_{Ic} of ~116 kJ/m^2 for neutron doses below 0.1 dpa,

(iii) Saturation threshold of about 5–7 dpa beyond which the fracture toughness of these materials appears to saturate,

(iv) Saturation fracture toughness J_{Ic} of 7.5 kJ/m^2 (or K_{Ic} or K_{Jc} of 38 MPa m$^{1/2}$), and

(v) Description of the change in toughness between 0.1 and 10 dpa.

The J_{Ic} value of ~116 kJ/m^2 for neutron doses below the threshold dose is appropriate for thermally aged and unaged CASS materials and SS flux welds. A value that is higher than 116 kJ/m^2 may be considered for the minimum fracture toughness J_{Ic} for wrought austenitic SSs irradiated below the threshold dose for neutron embrittlement. However, appropriate justification for using a higher value should be provided. The description of the change in fracture toughness below the threshold value would also change accordingly. The saturation J_{Ic} value of 7.5 kJ/m^2 does not change; it is the same for wrought and cast SSs and their welds. The K_{Jc} (MPa m$^{1/2}$) values determined from the lower-bound trend curve given by Eq. 35 are comparable to those predicted from the Materials Reliability Program (MRP) lower-bound model proposed for PWRs[28] at 0.3 and 7.0 dpa.

The MRP model bounds all the fracture toughness data from fast reactors, BWRs, and PWRs and is given by the expression

$$K_{Jc} = 180 - 142[1-\exp(-\text{dpa})]. \tag{36}$$

The existing fracture toughness J_{Ic} data at 290–320°C (554–608°F) for CASS materials irradiated under LWR conditions are plotted as a function of neutron dose in Fig. 41.[22,26,28,32,344,369,372,375,383–385]

Note that the fast-reactor irradiated data for a heat of CF-8 material (slashed square symbols) are included in the figure because they have been used for evaluating neutron embrittlement of CASS CF-8 materials in PWRs. Furthermore, the data were obtained at room temperature. Therefore, as shown in Fig. 41, the actual fracture toughness of moderate to high toughness materials is expected to be lower at reactor temperatures. The fracture toughness data obtained at Argonne on neutron irradiated CASS materials in LWR environments and the data obtained earlier on these materials in air are listed in Table 7. Note that the recent data obtained at Argonne were for CASS materials irradiated to a neutron dose of 0.08 dpa. This irradiation level was selected to help understand the combined effects of thermal and neutron embrittlement on SSs with a duplex structure, consisting of both austenite and ferrite phases. It is well-established that at an irradiation dose of about 0.1 dpa, the neutron embrittlement of the ferrite phase is essentially complete, but the embrittlement of the austenite phase occurs at irradiation levels above a threshold value of 0.3 dpa. In addition, data on materials irradiated to less than 0.1 dpa are needed to accurately evaluate the possible effects of the synergism between thermal and neutron embrittlement of CASS materials and their welds.

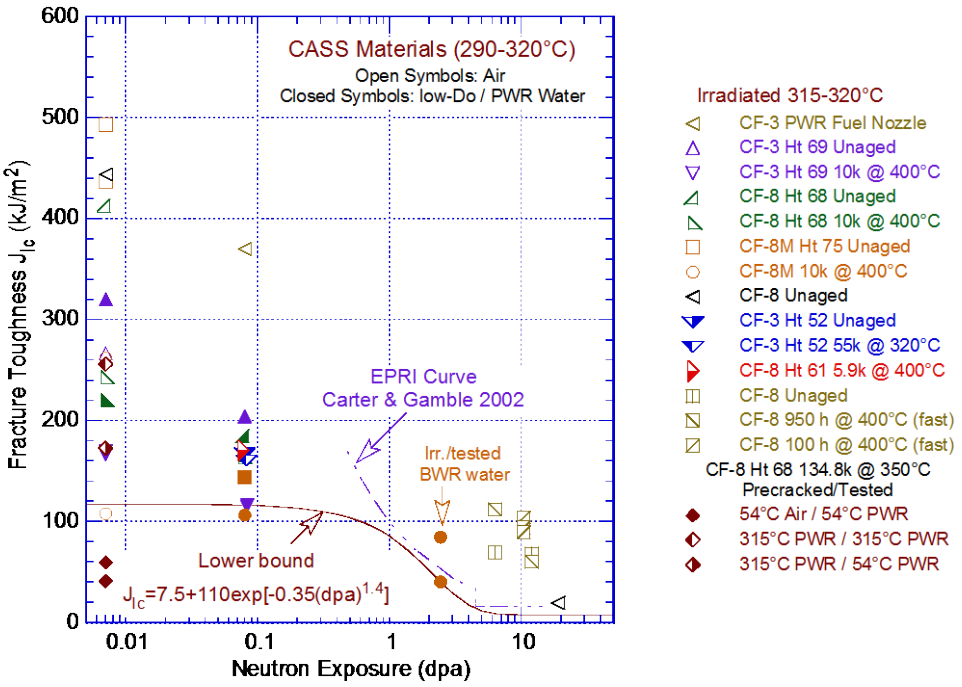

Figure 41. **Plots of fracture toughness J_{Ic} values as a function of neutron dose for CASS materials. Solid line represents the lower-bound J_{Ic} proposed in NUREG/CR-7027. The data points plotted at 0.007 dpa are for unirradiated materials.**

Table 7 **Fracture toughness J-R curve data on irradiated CASS CF-3, CF-8, and CF-8M materials in air and LWR environments.**

Grade	Heat	Material Condition	Unirradiated Material in Air at 290°C (554°F)			Unirradiated Material in Low-DO Water at 320°C (608°F)			Irradiated Material[a] in Low-DO Water at 320°C (608°F)		
			C	n	Jlc (kJ/m^2)	C	n	Jlc (kJ/m^2)	C	n	Jlc (kJ/m^2)
CF-3	69 (21%)	Unaged	756	0.31	700	536	0.68	320	430	0.64	204
CF-3	69 (21%)	Unaged	425	0.54	266	–	–	–	–	–	–
CF-3	69 (21%)	Aged	296	0.51	167	353	0.66	170	362	0.85	116
CF-3	52 (14%)	Unaged	–	–	–	–	–	–	347	0.65	168
CF-3	52 (14%)	Aged	–	–	–	–	–	–	419	0.80	161
CF-8	68 (15%)	Unaged	783	0.27	753	-	-	>500	359	0.57	183
CF-8	68 (15%)	Aged	396	0.51	242	395	0.58	220	372	0.62	171
CF-8	61 (13%)	Aged	–	–	–	–	–	–	406	0.60	205
CF-8M	75 (25%)	Unaged	583	0.45	437	–	–	–	336	0.66	145
CF-8M	75 (25%)	Unaged	600	0.35	493	–	–	–	–	–	–
CF-8M	75 (25%)	Aged	274	0.46	156	–	–	–	259	0.64	106
CF-8M	75 (25%)	Aged	364	0.32	262	–	–	–	–	–	–
CF-8M	75 (25%)	Aged	–	–	–	–	–	–	120[b]	0.24	84
CF-8M	75 (25%)	Aged	–	–	–	–	–	–	80[b]	0.45	40

[a] All specimens were irradiated to a neutron dose of 0.08 dpa at 315°C (599°F)and tested in low-DO high-purity water or simulated PWR water at 320°C (608°F), except for the last two specimens (Heat 75), which were irradiated to 2.46 dpa at 297°C (567°F) and tested at 289°C (552°F) in high-purity water with 400 ppb DO.

[b] Tested at 289°C (552°F) in high-purity water containing 400 ppb DO.

Equations. 35 and 36 predict a saturation fracture toughness K_{Ic} of 38 MPa $m^{1/2}$. For materials irradiated below the threshold dose for irradiation embrittlement, Eq. 35 predicts a minimum K_{Jc} of about 151 MPa $m^{1/2}$, but the MRP (Eq. 36) expression predicts fracture toughness values that for some materials, such as SS weld HAZ, may be higher than the minimum toughness of the materials in the unirradiated condition. The existing data for BWR-irradiated austenitic SSs is not bounded by the disposition curve proposed by EPRI for BWRs. For example, at neutron doses of <0.7 dpa, the J_{Ic} values based on the EPRI curve are higher than the minimum J_{Ic} of some heats of wrought SSs and most thermally aged CASS with >15% ferrite.[326] In addition, the saturation K_{Ic} of 55 MPa $m^{1/2}$ at 4.5 dpa for the EPRI curve is also higher than the value of 38 MPa $m^{1/2}$ previously proposed by MRP for PWRs.[28] The saturation K_{Ic} for the EPRI curve was based on data for which the specimen orientation was unknown. As discussed above, recent data indicate that fracture toughness in the transverse orientation is nearly half of that in the longitudinal orientation.[27] Therefore, the bounding K_{Ic} values above 4.5 dpa are likely to be lower than 55 MPa $m^{1/2}$.

A fracture toughness J-R curve may be used to analyze material behavior for loading beyond J_{Ic}. The J-R curve is expressed in terms of the J integral and crack extension (Δa) by the power law $J = C(\Delta a)^n$. At dose levels below the threshold dose for saturation (i.e., at dose levels less than ~7 dpa), the effect of neutron irradiation on the fracture toughness of austenitic SSs can be represented by a decrease in the coefficient C of the power-law correlation for the J-R curve with neutron dose. The variation of the fracture toughness coefficient C as a function of neutron dose for the data shown in Fig. 41 is plotted in Fig. 42. One curve in the figure represents the disposition curve proposed by EPRI for BWRs,[24] and the other represents a trend curve proposed in NUREG/CR-7027 for coefficient C that bounds the existing data. For neutron

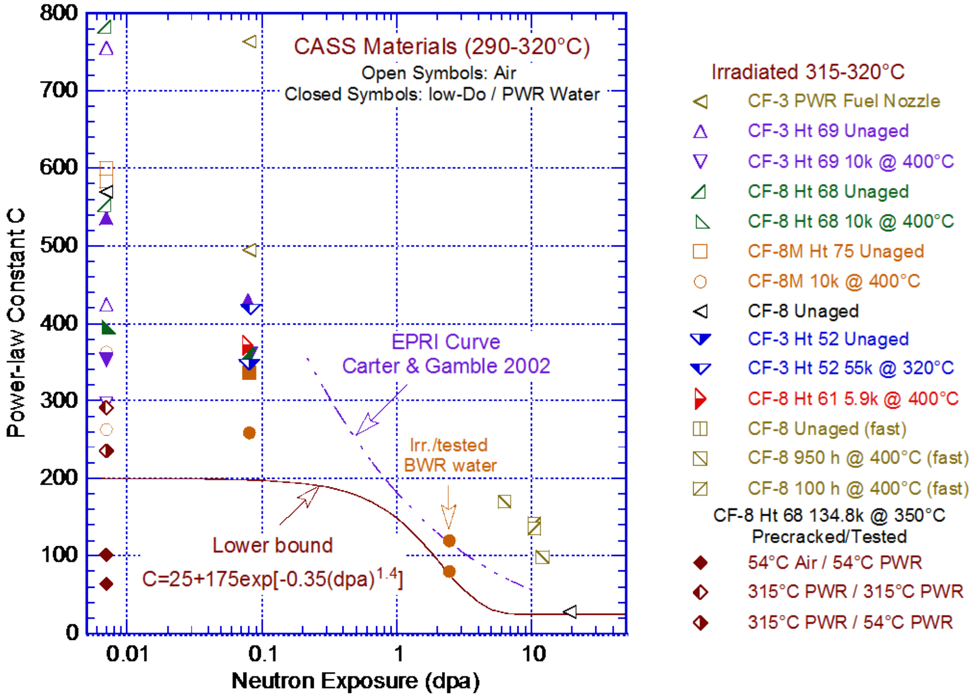

Figure 42. **Coefficient C of the J-R curve as a function of neutron dose for CASS materials. Solid line represents the lower-bound C values proposed in NUREG/CR-7027. The data points plotted at 0.007 dpa are for unirradiated materials.**

doses less than 5 dpa, the existing fracture toughness data are bounded by the following expression for C:

$$C = 25 + 175 \exp[-0.35(\text{dpa})^{1.4}], \qquad (37)$$

and an exponent n equal to 0.37 (i.e., median value of the experimental data). The exponent n of the power-law curve typically ranges from 0.35 to 0.70 for unirradiated materials and 0.16 to 0.65 for irradiated materials. Unlike the behavior seen for thermally aged cast austenitic SSs (in which exponent n typically decreases with a decrease in fracture toughness),[326] no obvious trend of n with fluence is evident. Based on the material and irradiation conditions, a conservative value of 0.3 for exponent n may be used to evaluate the neutron embrittlement of these materials. Equation 37 yields a minimum C value of 192 kJ/m^2 (1,094 in.-lb/in.^{2}) for materials irradiated to less than 0.1 dpa and a minimum C value of ~31 kJ/m^2 (~177 in.-lb/in.^{2}) for materials irradiated to 7 dpa.

For the data shown in Figs. 41 and 42, the J-integral values at a crack extension of 2.5 mm (0.1 in.), $J_{2.5}$, are plotted as a function of neutron dose in Fig. 43. The solid curve in the figure represents the $J_{2.5}$ values that bound the existing experimental data. The curve was obtained by using the power-law J-R curve relationship, with coefficient C determined from Eq. 37 and the median value of 0.37 for exponent n. The lower-bound curve indicates that for CASS materials irradiated up to 0.5 dpa, the predicted $J_{2.5}$ values are above the screening value of 255 kJ/m^2 (1456 in.-lb/in.^{2}).

Note that most of the J-R curve data for neutron irradiated SSs have been obtained on ½-T or ¼-T CT specimens that were about 6-mm (0.24-in.) thick. Therefore, the validity of the fracture

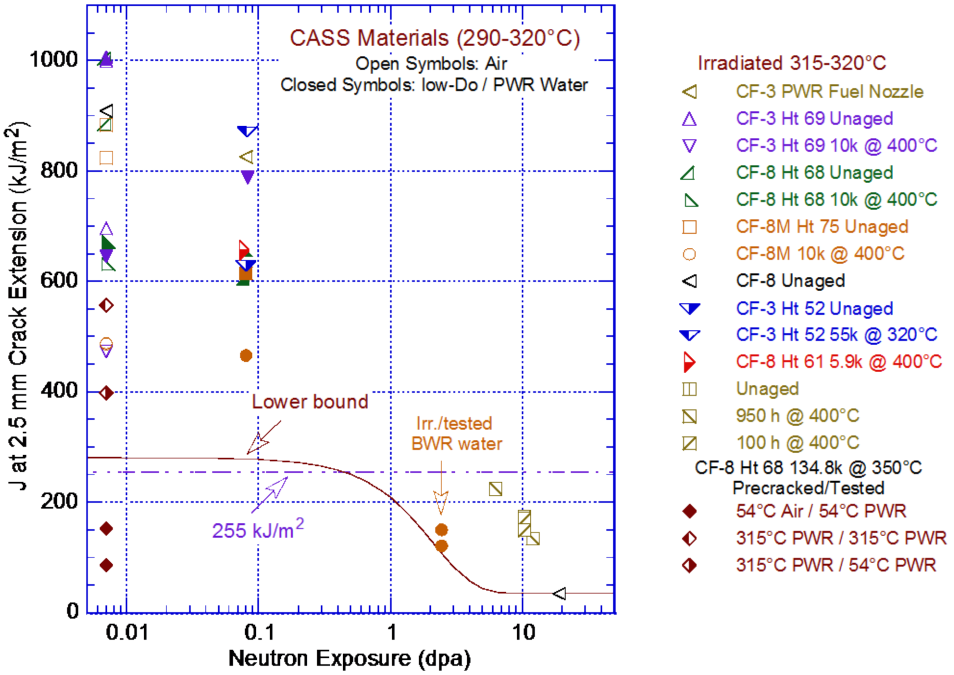

Figure 43. **Fracture toughness $J_{2.5}$ values as a function of neutron dose for CASS materials. Solid line represents the lower-bound $J_{2.5}$ values proposed in NUREG/CR-7027. The data points plotted at 0.007 dpa are for unirradiated materials.**

toughness data using the small CT specimens needs to be assessed. The fracture mechanics approach correlates the behavior of components with that of specimens by using the K parameter. It considers that if the two cracks have the same K, then they have the same strains and stresses in the region near the crack tip. The ASTM specifications for specimen K/size criteria are intended to ensure that the plastic zone is small enough and K is controlling the crack behavior. It has been often argued that since the K/size criterion was developed for materials that show work hardening, it may not be applicable for materials that are irradiated to fluence levels where, on a local level, they do not strain harden and exhibit strain softening. Recent investigations have evaluated the validity of the K/size criterion for irradiated materials by comparing the plastic strain distribution in a ½-T CT specimen estimated from finite element method calculations with the experimentally observed plastic deformation area.[293,294] The plastic zone size was estimated to be 0.2–0.4 mm (0.008–0.016 in.) at K = 30 MPa $m^{1/2}$ [293] The results indicate that for an austenitic SS irradiated to 3×10^{21} n/cm^2, the appropriate K range is at least 30 MPa $m^{1/2}$ for a (5.8-mm [0.23-in.] thick) CT specimen.

Figure 43 shows the results of two tests of CF-8M material thermally aged for 10,000 h at 400°C (752°F) and then irradiated to well above the threshold dose for neutron embrittlement (shown as closed circles). The resulting $J_{2.5}$ values for these two tests are bounded by the proposed lower-bound J-R curve. As discussed above, since only CF-3/CF-8 and, in a few cases, CF-3M CASS materials are used for designs of all BWRs and PWRs, the data for CF-8M represent the worst-case values. Actual values for CF-3/CF-8 materials would be higher. However, there is little or no data on LWR-irradiated CF-3 and CF-8 materials to accurately establish the lower-bound J-R curves for these materials during service in LWRs. The only data for CF-8 material is for fast reactor irradiation. The existing data indicate that for the same neutron dose, the embrittlement of LWR irradiated materials is greater than that of materials irradiated in a fast reactor. In addition, the CF-8 data are on materials irradiated at 325°C (617°F); limited data indicate that the extent of embrittlement is greater under BWR service conditions than PWR service conditions.

2.4.2.3 Methodology for Incorporating Irradiation Effects on CASS Materials including the Combined Effects of Thermal and Neutron Embrittlement

Threshold Neutron Dose for Irradiation Effects: For license renewal, to account for the effects of thermal aging and neutron irradiation embrittlement on the fracture toughness of reactor core internal components, the NRC staff has proposed an AMP.[2] The program does not directly monitor for loss of fracture toughness that is induced by either thermal or neutron irradiation embrittlement. Instead, the impact of a loss of fracture toughness on component integrity is indirectly managed by using visual or volumetric examination techniques to monitor for cracking in the components. If cracking is detected in the components, a flaw tolerance evaluation is performed by using acceptable reduced fracture toughness properties.

The AMP for PWR vessel internals follows the guidance found in EPRI report MRP-227.[386] The AMP states that a loss of fracture toughness due to thermal and/or neutron embrittlement of CASS materials can occur as a result of exposure to neutron fluence of $>10^{19}$ n/cm^2 (E of >1 MeV) (i.e., 0.015 dpa) or if CASS material is more susceptible to thermal embrittlement. A fracture toughness value of 255 kJ/m^2 (1450 in.-lb/in.^{2}) at a crack extension of 2.5 mm (0.1 in.) is used to differentiate between CASS materials that are not susceptible and those that might be susceptible to thermal embrittlement. Based on a recent review and evaluation of the current fracture toughness data of thermally aged CASS materials, a revised version of the screening criteria proposed earlier in NUREG/CR-4513, Rev. 1,[326] is presented in Table. 8.

Table 8. Updated screening criteria for thermal-aging susceptibility of CASS CF-3, CF-8, and CF-8M materials.

Mo Content (wt.%)	Casting Method	Ferrite Content (%)	Susceptibility Determination
High (2.0–3.0)	Static	≤14 (≤11)	Not susceptible
with <10% Ni (≥10% Ni)		>14 (>11)	Potentially susceptible
	Centrifugal	≤19 (≤13)	Not susceptible
		>19 (>13)	Potentially susceptible
Low (0.5 max.)	Static	≤20	Not susceptible
		>20	Potentially susceptible
	Centrifugal	All	Not susceptible

Regarding the neutron dose threshold above which the potential combined effects of thermal and neutron embrittlement are significant and need to be evaluated, the lower-bound curve shown in Fig. 43 indicates that for CASS materials irradiated up to 0.5 dpa, the predicted $J_{2.5}$ values are above the screening value of 255 kJ/m^2 (1,456 in.-lb/in.^{2}). If needed, the lower-bound fracture toughness curves described above can be used to perform a flaw tolerance evaluation. However, note that the fracture toughness of SS weld metals may be significantly lower than this threshold value (see Fig. 40).

Potential Effects of Thermal and Neutron Embrittlement: The embrittlement of the ferrite phase because of neutron irradiation occurs at lower dose levels than does embrittlement of the austenite phase. A shift in the nil-ductility transition (NDT) temperature of up to 150°C (302°F) has been observed in pressure vessel steels irradiated to 0.07–0.15 dpa.[387] Thus, embrittlement of ferrite is expected to occur at 0.05–0.50 dpa, whereas any significant neutron embrittlement of the austenite phase occurs only at above ~0.4 dpa (Fig. 41–43). In recent studies at Argonne, fracture toughness tests have been conducted in LWR environments on unaged and aged heats of CF-3, CF-8, and CF-8M materials that were either in an unirradiated condition or irradiated to a neutron dose of 0.08 dpa at 315°C (599°F) in the Halden reactor. The results are shown in Fig. 44. The ferrite contents of the CF-3, CF-8, and CF-8M materials, determined from Hull's equivalent factors, were 21.0%, 14.9%, and 24.8%, respectively. The results indicate that only the J_{Ic} values are slightly lower for the aged and irradiated materials than those that were only aged or irradiated. The values of coefficient C and $J_{2.5}$ show no effect from combined thermal and neutron embrittlement.

Similarly, the fracture toughness data for two other heats of thermally aged and irradiated CF-8 material (Heats 52 and 61, containing 14% and 13% ferrite, respectively) yield $J_{2.5}$ values that are significantly above 255 kJ/m^2. Therefore, the existing data indicate little or no combined effect from thermal and neutron irradiation. Furthermore, the fracture toughness ($J_{2.5}$) values of aged CASS CF-3 and CF-8 materials irradiated to a neutron dose of less than 0.5 dpa are above the screening value of 255 kJ/m^2 (1456 in.-lb/in.^{2}) proposed by EPRI.[388] Recently, the NRC staff has proposed a threshold value of 0.45 dpa for susceptibility of CASS materials to neutron embrittlement.

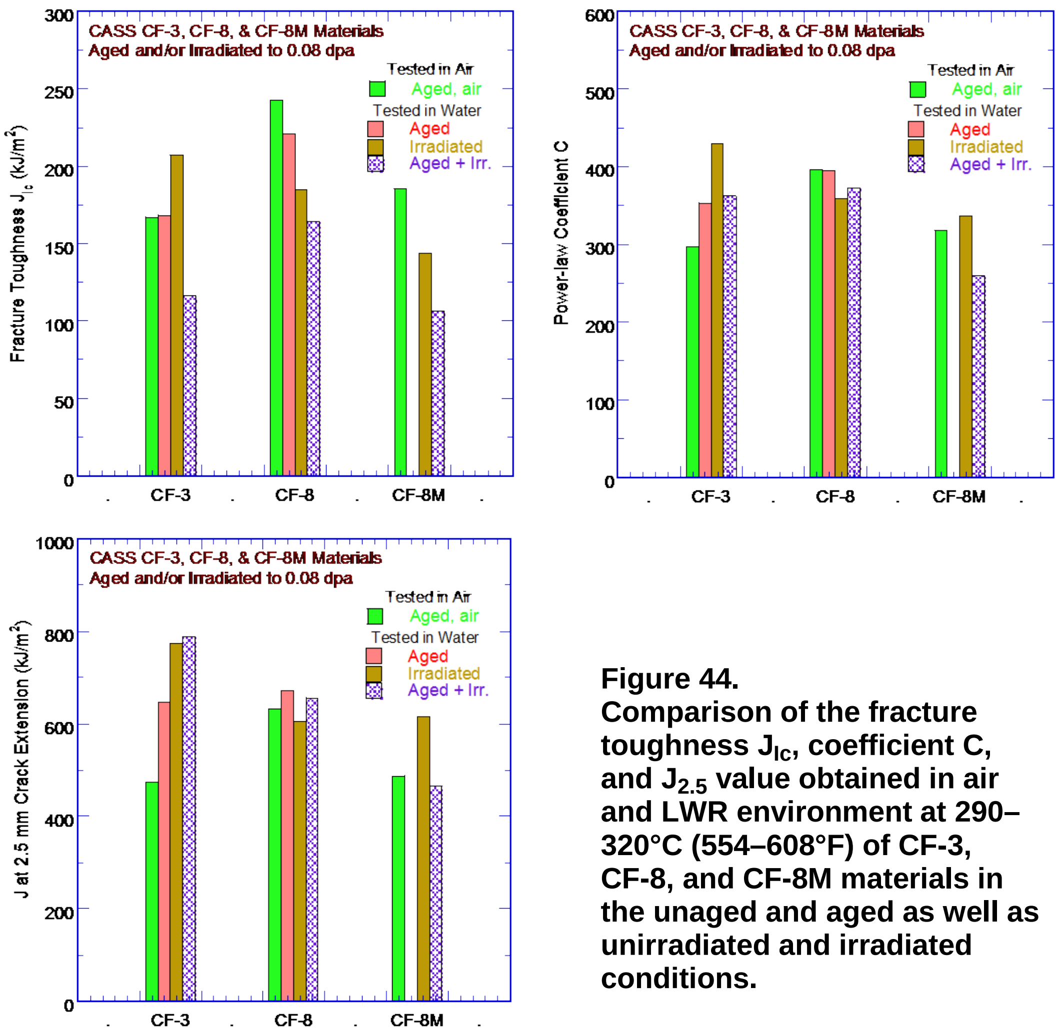

Figure 44.
Comparison of the fracture toughness J_{Ic}, coefficient C, and $J_{2.5}$ value obtained in air and LWR environment at 290–320°C (554–608°F) of CF-3, CF-8, and CF-8M materials in the unaged and aged as well as unirradiated and irradiated conditions.

The existing Charpy-impact, tensile, and fracture toughness data for SMA, SA, and GTA welds have been reviewed and evaluated to characterize the effect of thermal aging on the degradation of fracture properties of austenitic SS welds.[389] The results indicate that the fracture properties of SS welds are strongly dependent on the welding process. In general, GTA welds exhibit higher fracture resistance than SMA or SA welds, and the fracture toughness J-R curves for SA and SMA welds are comparable. Thermal aging of the welds results in moderate decreases in Charpy-impact strength and fracture toughness. The decrease in fracture toughness J-R curve, or $J_{Ic,}$ is relatively small.

The existing fracture toughness data for SS welds indicate that at reactor temperatures, the fracture toughness of GTA/MIG/TIG welds is a factor of about 2.3 higher than that of SA/SMA/MMA welds.[389] Thermal aging decreases the fracture toughness of SS welds by up to 20%. Existing data on potential combined effects of thermal and neutron embrittlement of austenitic SS welds indicate that the coefficient C and exponent n of the fracture toughness J-R curve decrease from 117 kJ/m^2 and 0.45 for welds irradiated less than 0.1 dpa to 25 kJ/m^2 and 0.20 for welds irradiated above 7 dpa. The J_{Ic} decreases from 74 kJ/m^2 to 7.5 kJ/m^2 when the neutron dose increases from <0.1 dpa to >7 dpa. Limited data indicate potential detrimental effects of LWR coolant environments on the fracture toughness of austenitic SS welds.

2.4.3 Fatigue Crack Initiation and Growth

2.4.3.1 Fatigue Crack Initiation in Air

Fatigue crack initiation, including the effects of a LWR coolant environment, has been investigated extensively at Argonne and the results published in several topical reports.[390–397] The existing fatigue ε–N data were evaluated to identify the various material, environmental, and loading parameters that influence fatigue crack initiation, and to establish the effects of key parameters on the fatigue lives of these steels. This report presented a methodology for estimating fatigue lives as a function of material, loading, and environmental parameters, and described the environmental fatigue correction factor, F_{en}, for incorporating the effects of LWR environments into ASME Section III fatigue evaluations.

Deformation and microstructural changes in the surface grains of metals are responsible for fatigue crack initiation. During cyclic straining, the irreversibility of dislocation glide leads to the development of surface roughness. Strain localization in persistent slip bands (PSBs) results in the formation of extrusions and intrusions. With continued cycling, microcracks ultimately form in PSBs or at the edges of slip–band extrusions. At high strain amplitudes, microcracks form in notches that develop at grain, twin, or phase boundaries (e.g., ferrite/pearlite) or by cracking of second–phase particles (e.g., sulfide or oxide inclusions).

Once a microcrack forms, it continues to grow along its primary slip plane or a PSB as a Mode II (shear) crack in Stage I growth (where the orientation of the crack is usually at 45° to the stress axis). At low strain amplitudes, a Stage I crack may extend across several grain diameters before the increasing stress intensity of the crack promotes slip on planes other than the primary slip plane. A dislocation cell structure normally forms at the crack tip. Because slip is no longer confined to planes at 45° to the stress axis, the crack begins to propagate as a Mode I (tensile) crack, normal to the stress axis in Stage II growth. At high strain amplitudes, the stress intensity is quite large and the crack propagates entirely by the Stage II process. Stage II crack propagation continues until the crack reaches an engineering size. The two stages of fatigue crack growth in smooth specimens are shown in Fig. 45.

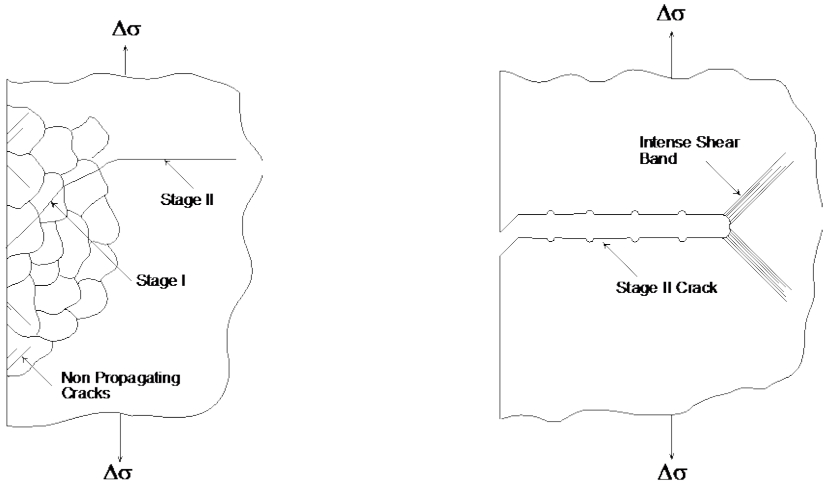

Figure 45. Two stages of fatigue crack growth in smooth test specimens.

In air or mildly corrosive environments, Stage II cracking is characterized by fatigue striations. The process of Stage II fatigue crack growth and formation of fatigue striations[398] is illustrated in Fig. 46. As tensile load is applied, slip bands form at the double notch or “ears” of the crack tip (Fig. 46b). The slip bands widen with further straining, causing blunting of the crack tip (Fig. 46c). Crack surfaces close during compressive loading and slip is reversed, producing ears at the edges of the blunt crack tip (Figs. 46d and 46e). The ears are observed as fatigue striations on the fracture surface. However, there is not necessarily a 1:1 correlation between striation spacing and fatigue cycles. At high strain amplitudes, several striations may be created during one cycle, whereas at low strain amplitudes, one striation may represent several cycles.

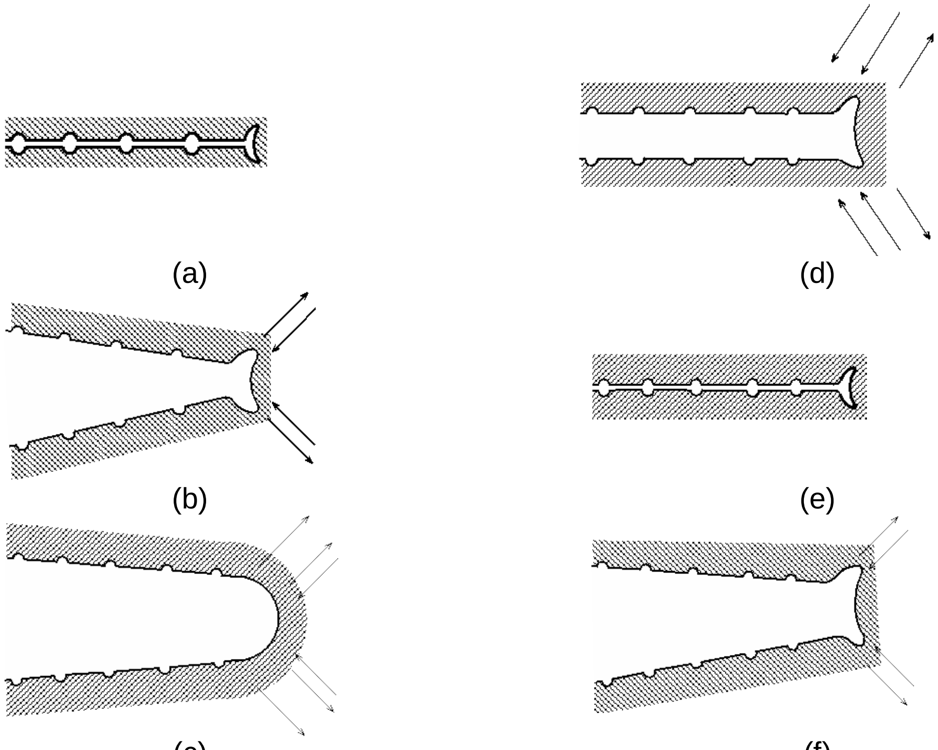

Figure 46. **Schematic illustration of the plastic blunting process of fatigue crack growth in Stage II: (a) zero load; (b) small tensile load; (c) maximum tensile load, widening of slip bands; (d) crack closure, and formation of “ears” at crack tip; (e) maximum compressive load; (f) small tensile load in the subsequent cycle.**

Thus, the formation of surface cracks and their growth as shear and tensile cracks (Stages I and II growth) to an “engineering” size (e.g., a 3-mm-deep) crack constitute the fatigue life of a material, which is represented by the fatigue ε-N curves. Fatigue life is conventionally divided into two stages: initiation, expressed as the number of cycles required to form microcracks on the surface, and propagation, expressed as the number of cycles required to propagate the surface cracks to an engineering size. Thus, the definition of a CUF value of unity conventionally includes both crack initiation and some amount of crack propagation.

An alternative approach considers fatigue life of engineering structures and components to be entirely composed of the growth of short fatigue cracks, i.e., cracks less than “engineering” size.[399,400] It considers that for polycrystalline materials, the time for the formation of surface cracks is negligible. As shown in Fig. 47, during cyclic loading, surface cracks, 5 μm

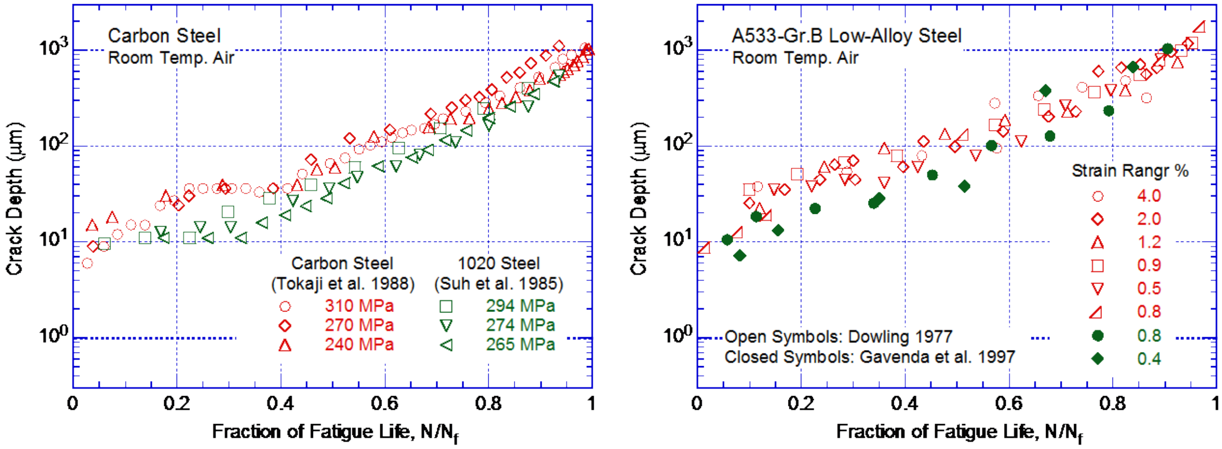

Figure 47. **Crack depth plotted as a function of fractional life for carbon and low–alloy steels tested in air (Refs. 401–404).**

(0.197 mils) or longer, form early in life at surface irregularities either already in existence or produced by slip bands, grain boundaries, second-phase particles, etc.[401–404] Thus, fatigue life may be considered to constitute propagation of cracks from 10 to 3,000 μm long, and fatigue damage in a material may be considered as the current size of the fatigue crack.[400] However, the growth rates of short cracks cannot be predicted accurately from fracture mechanics methodology based on the range of stress intensity factor (ΔK) alone. Under the same ΔK loading, short fatigue cracks (i.e., cracks having lengths comparable to the unit size of the microstructure) grow at a faster rate than longer fatigue cracks.[405] In addition, shorter cracks can grow at ΔK values below those predicted from LEFM because of interactions with microstructural features, effects of mixed mode crack propagation, contributions of crack closure with increasing crack length, and an inadequate characterization of the crack tip stress/strain fields associated with short cracks.

Fatigue cracks greater than a critical size show little or no influence of microstructure and are considered mechanically small cracks.[406] Mechanically small cracks correspond to Stage II (tensile) cracks, which are characterized by striated crack growth, with the fracture surface normal to the direction of maximum principal stress. The growth of mechanically small cracks is characterized in terms of the J-integral range, ΔJ, and CGR data in air and LWR environments. The CGRs estimated from smooth specimen ε-N data show good agreement with CGRs obtained on fracture mechanics CT specimens in air and water environments.[392]

At low stress levels ($\Delta\sigma_1$) (Fig. 48a), the transition from microstructurally small crack (MSC) growth to accelerating crack growth does not occur. This circumstance represents the fatigue limit for a smooth specimen. Although cracks can form below the fatigue limit, they grow to engineering size only at stresses greater than the fatigue limit. Note that the fatigue limit for a material is applicable only for constant loading conditions. Under variable loading conditions, MSCs can grow at high stresses ($\Delta\sigma_3$) (Fig. 48b) to depths larger than the transition crack depth, and then continue to grow at stress levels below the fatigue limit ($\Delta\sigma_1$).

Various criteria are used to define the crack depth for transition from microstructurally to mechanically small cracks.[393] The transition crack depth is a function of applied stress (σ) and the microstructure of the material. For completely reversed fatigue straining, the transition from a MSC to a mechanically small crack for several materials is estimated to be approximately 8 times the unit size of the microstructure;[406] actual values may range from 150 to 250 μm.

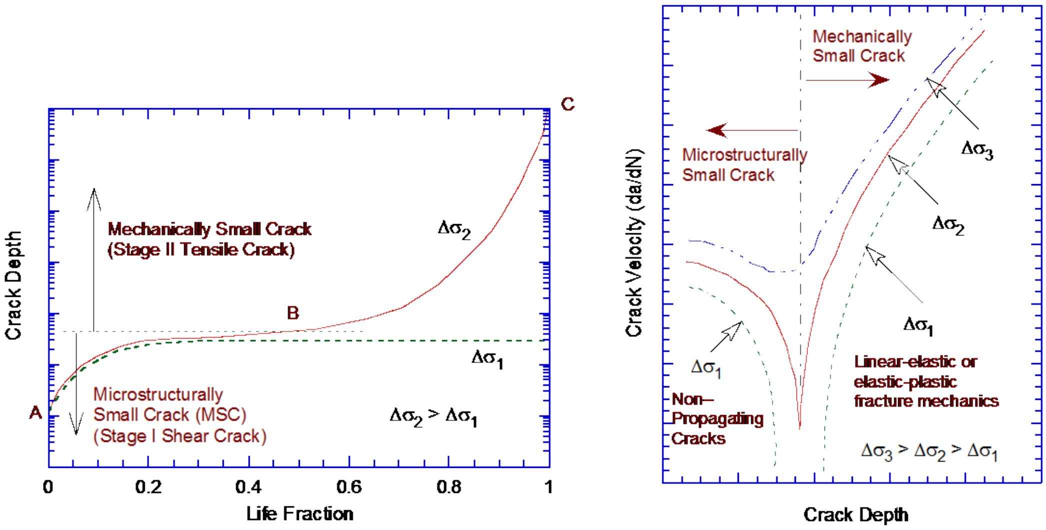

(a) (b)

Figure 48. Schematic illustration of (a) growth of short cracks in smooth specimens as a function of fatigue life fraction, and (b) crack velocity as a function of crack depth.

In the Argonne study, fatigue life is described as the number of cycles of specified strain amplitude that a specimen can sustain before the formation of a 3-mm (0.12-in.)-deep crack (i.e., an “engineering crack”). Thus, fatigue crack initiation is expressed in terms of three parameters: 1) the number of fatigue cycles, 2) the specific strain amplitude, and 3) the 3-mm (0.12-in.) crack size. This is assumed to represent crack initiation in an actual component. Using this definition, a calculated fatigue CUF less than unity provides reasonable assurance that a fatigue crack has not formed in a component, and indicates that the probability of forming a crack in the component is low.

2.4.3.2 Fatigue Crack Initiation in LWR Environments

Carbon Steels and Low-Alloy Steels

Mechanism of Corrosion Fatigue

The environmental enhancement of fatigue crack growth in pressure vessel steels in high-temperature oxygenated water and the effects of sulfur content, loading rate, and flow velocities are well documented.[407–419] Dissolution of MnS inclusions changes the water chemistry near the crack tip, making it more aggressive. This results in enhanced crack growth rates because either (a) the dissolved sulfides decrease the repassivation rate, which increases the amount of metal dissolution for a given oxide rupture rate;[419] or (b) the dissolved sulfide poisons the recombination of hydrogen (H) atoms liberated by corrosion, which enhances H uptake by the steel at the crack tip.

The enhanced CGRs in LWR coolant environments are attributed to either slip oxidation/dissolution[419–423] or hydrogen-induced cracking mechanisms.[424–426] For the slip oxidation/dissolution mechanism, a critical concentration of sulfide (S^{2-}) or hydrosulfide (HS^{-}) ions, which are produced by the dissolution of sulfide inclusions in the steel, is required at the crack tip for environmental effects to occur. The crack tip is supplied with S^{2-} and HS^{-} ions as the advancing crack intersects the sulfide inclusions, and the inclusions dissolve in the high-temperature water environment. Sulfide ions are removed from the crack tip by one or more of the following processes: (a) diffusion due to a concentration gradient, (b) ion transport due to an electrochemical corrosion potential (ECP) gradient, (c) pumping action due to cyclic loading on the crack, and/or (d) fluid flow induced within the crack due to the flow of coolant outside the crack. The morphology, size, and distribution of sulfide inclusions and the probability of advancing the crack to intercept the sulfide inclusions are important parameters affecting growth rates of carbon and low-alloy steels in LWR environments.[413,415–418]

A schematic illustration of the two stages of fatigue crack growth including (a) initiation, and (b) propagation, is shown in Fig. 48. The initiation stage involves growth of MSCs, characterized by decelerating crack growth (Region AB in Fig. 48a). The propagation stage involves growth of “mechanically small cracks,” characterized by accelerating crack growth (Region BC in Fig. 48a). The MSCs correspond to Stage-I cracks and grow along slip planes as shear cracks in the early stage of growth. The growth of the MSCs is very sensitive to microstructure.[401,403–406] The growth rates are markedly decreased by grain boundaries, triple points, and phase boundaries. In ferritic-pearlitic steels, fatigue cracks initiate and propagate preferentially in the ferrite phase that forms as long allotriomorphs at prior austenite phase boundaries.[403,427,428] The ferrite/pearlite phase boundaries act as strong barriers to crack propagation, and growth rates decrease significantly when small cracks grow into the pearlite from the ferrite.[403] Limited data suggest that microstructural effects are more pronounced at negative stress ratios; the compressive component of the applied load plays an important role in the formation of Stage I facets and formation of cracks.[406]

The requirements for a slip dissolution model are that a protective oxide film is thermodynamically stable to ensure that a crack will propagate with a high aspect ratio without degrading into a blunt pit, and that a strain increment occurs to rupture that film and thereby exposes the underlying matrix to the environment (Fig. 49). Once the passive oxide film is ruptured, crack extension is controlled by dissolution of freshly exposed surfaces and by the oxidation characteristics. The effect of the environment increases with decreasing strain rate. The mechanism assumes that environmental effects do not occur during the compressive load cycle because during that period water does not have access to the crack tip. Ford et al.[421,422] proposed that the average environmentally assisted crack growth rate, $\bar{V}_t$ (centimeters/second), is related to the crack tip strain rate, $\dot{\varepsilon}_{ct}$, by the relationship

$$\bar{V}_t = A\left(\dot{\varepsilon}_{ct}\right)^n, \tag{38}$$

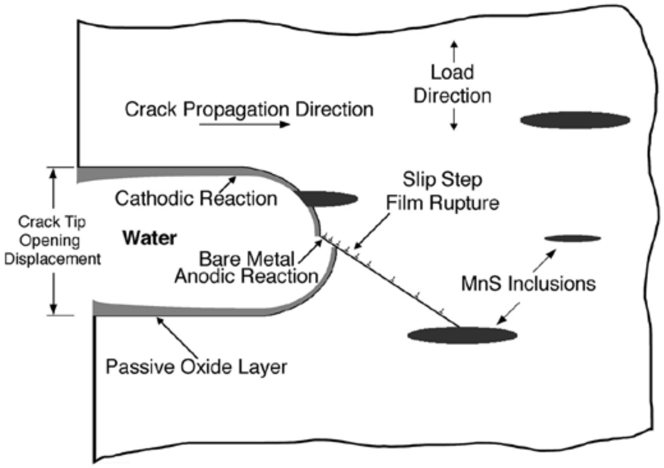

**Figure 49.
Schematic illustration of slip oxidation/dissolution process.**

where the constants A and n depend on the material and environmental conditions at the crack tip. There is a lower limit of crack propagation rate associated either with blunting when the crack tip cannot keep up with the general corrosion rate of the crack sides, or with the fact that a critical level of sulfide ions cannot be maintained at the crack tip. For example, the latter condition may occur when the crack growth rate falls below a critical value such that a high concentration of sulfide ions cannot be maintained at the crack tip. The critical crack growth rate at which this transition occurs depends on the DO level, flow rate, and S content of the steel.

The average critical velocity, $\bar{V}_{in}$ (millimeters/second), for initiation or cessation of environmentally assisted cracking (EAC) was shown to depend on the balance between sulfide supply rate and mass transport away from the crack tip.[408,412] Initiation of EAC requires a critical concentration of sulfide ions at the crack tip, which is supplied with sulfide ions as the advancing crack intersects the sulfide inclusions, and the inclusions dissolve in the high-temperature water.

Hydrogen-induced cracking (Fig. 50) of carbon and low-alloy steels is caused by hydrogen produced by the oxidation reaction at the crack tip that is partly absorbed into the metal; it interacts with MnS inclusions and leads to the formation of cleavage cracks at the inclusion matrix interface. Crack extension occurs by linkage of the cleavage cracks. Other hydrogen-induced fracture processes may also enhance growth rates in LWR environments. According to the decohesion mechanism, significant accumulation of hydrogen at or near the crack tip decreases the cohesive interatomic strength of the lattice.[429] Hydrogen-induced bond rupture ahead of the crack tip links up with the main crack resulting in discontinuous, but enhanced crack growth. Furthermore, adsorbed hydrogen lowers the surface energy of the metal, thus facilitating crack growth at a lower fracture stress level. In addition, hydrogen can cause localized crack tip plasticity by reducing the stress required for dislocation motion.[430] Note that the hydrogen produced at the crack tip by this mechanism is not related to the hydrogen content of the bulk fluid; as a result, hydrogen content of the bulk fluid is not a parameter in the F_{en} expressions.

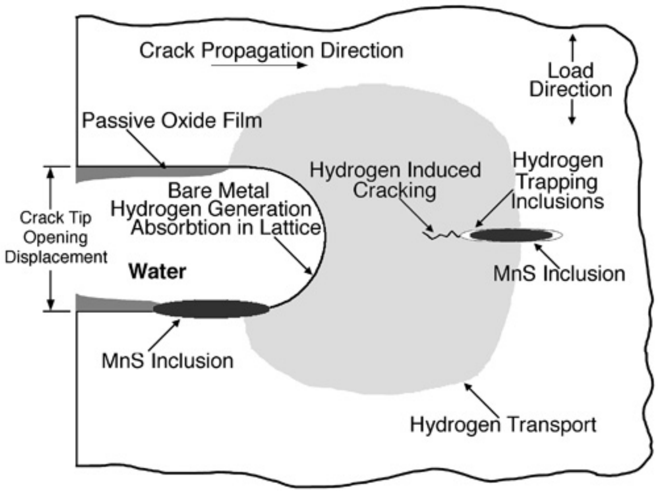

Figure 50.
Schematic illustration of hydrogen-induced cracking of low-alloy steel.

Both the slip-oxidation/dissolution and hydrogen-induced cracking mechanisms are dependent on oxide rupture rates, passivation rates, and liquid diffusion rates. Therefore, it is difficult to differentiate between the two mechanisms or to establish their relative contribution to crack growth rates in LWR environments. However, fatigue crack morphologies in test specimens indicate that both the slip-oxidation/dissolution and hydrogen-induced cracking mechanisms are important for environmental effects of the fatigue lives of carbon and low-alloy steels in LWR environments. A change in fracture appearance from ductile striations in air to brittle facets or cleavage-like fracture in LWR environments lends the greatest support for hydrogen-induced cracking.[417,425,426,431,432]

However, the long-term role of hydrogen on corrosion fatigue and the possible synergistic effects of dynamic strain aging (DSA) are not yet clear for austenitic Types 304 and 316 SSs. The fatigue crack morphologies of carbon and low-alloy steels in a BWR environment also show a strong dependence and change with strain rate. At high strain rates, surface crack morphology is predominantly a zigzag pattern and inclined to the loading axis, whereas entirely straight crack morphology normal to the loading axis is observed at slow strain rates.[432,433] The surface crack morphology in A106 Gr. B carbon steel tested in air and high-DO water at 288°C (550°F) is shown in Fig. 51. In addition, high strain rates lead to a rough fracture surface with the typical fan-like or quasi-cleavage cracking pattern, and slow strain rates result in a flat, nondescript fracture surface.[431,433] The propagation of fatigue cracks in A106 Gr. B carbon steel is shown in Fig. 52. In air, fatigue cracks grow along relatively soft ferrite regions and avoid the hard pearlite regions. In contrast, in a high-DO BWR environment, fatigue cracks appear to grow straight, normal to the stress axis, and through both the soft ferrite and the hard pearlite regions. Such crack growth characteristics are consistent with the slip-oxidation/dissolution mechanism and crack extension by anodic dissolution of the matrix in a corrosive environment.

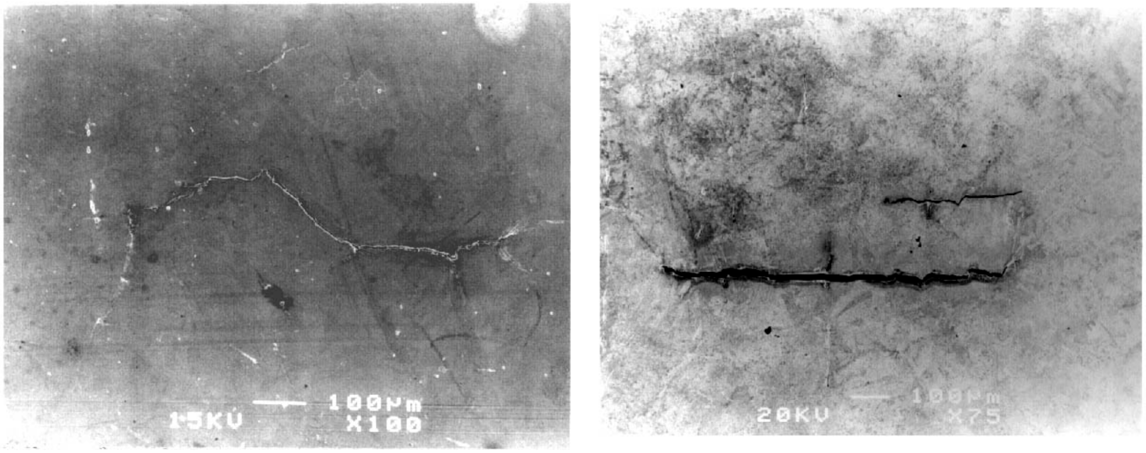

(a) (b)

Figure 51. Fatigue cracks on gauge surfaces of A106 Gr. B carbon steel tested in (a) air and (b) high-DO water at 288°C (550°F) (Ref. 390).

Wu and Katada[431] attributed the change in crack morphology to a change in the corrosion fatigue mechanism from hydrogen-induced cracking to a slip-oxidation/dissolution mechanism with decreasing strain rate. The authors reasoned that, during cyclic loading in high-temperature water, plastic deformation induces slip bands at the crack tip along the maximum shear or preferred slip directions. The extrusion of slip bands may rupture the protective oxide film at the crack tip. The slip bands are the favored path for hydrogen transportation, and the interfaces between the matrix and inclusions or precipitations in the region of maximum hydrostatic tension are the preferred traps for hydrogen. Thus, hydrogen tends to accumulate at these sites and embrittle them. As a result, at high strain rates, fatigue cracking preferentially occurs along the slip bands or preferred slip directions as well as the matrix/inclusions

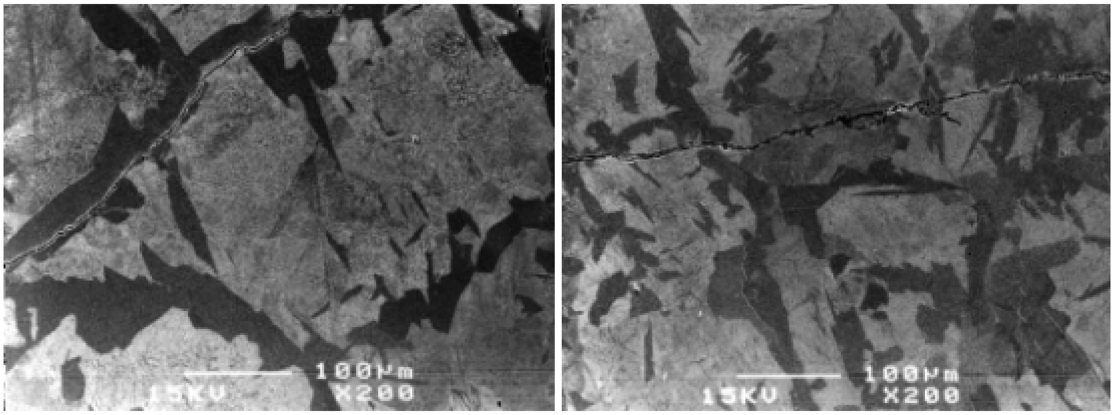

(a) (b)

Figure 52. Fatigue cracks along longitudinal sections of A106 Gr. B carbon steel tested in (a) air and (b) high-DO water at 288°C (550°F) (Ref. 390).

interfaces, which results in macroscopically tortuous fatigue cracks and a rough fracture surface. However, at low strain rates, fatigue crack growth in high-temperature water is controlled by the film-rupture/oxidation-dissolution mechanism, which results in macroscopically straight fatigue cracks and a relatively flat, featureless fracture surface.

Effects of Dynamic Strain Aging

Several studies showed that DSA may play a significant role in the cyclic deformation process of carbon and low-alloy steels in LWR environments.[434–438] DSA occurs in alloys containing solutes that segregate strongly to dislocations resulting in strong interactions between the solute and the stress-strain field of the dislocations, which leads to dislocation pinning (Fig. 53). In carbon and low-alloy steels, DSA occurs due to interstitial elements such as nitrogen and carbon. DSA is sufficiently rapid to occur during fatigue straining and produces a variety of inhomogeneous deformations such as serrated yielding, jerky or serrated flow, etc. These effects depend on temperature and strain rate.

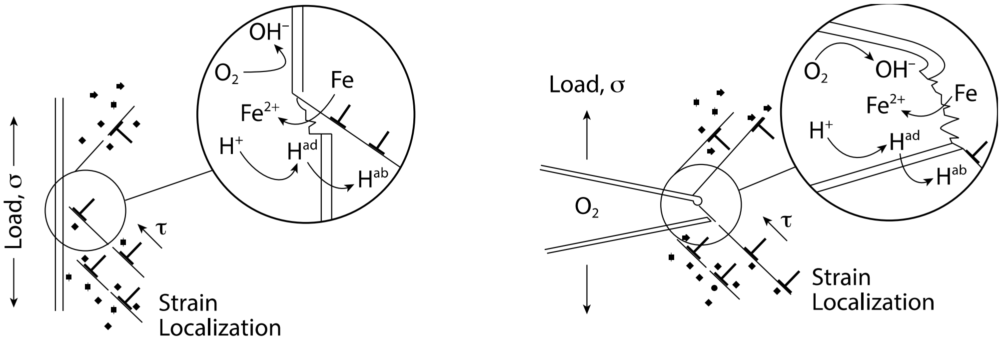

Figure 53. (a) Fatigue crack initiation and (b) crack growth in DSA susceptible low-alloy steel exposed to high-temperature water environment (Ref. 434).

Under certain combinations of temperature and strain rate conditions, DSA may significantly affect the EAC behavior of carbon and low-alloy steels by increasing the yield and tensile strength, the strain hardening exponent, the creep rate, and the crack-tip strain and strain rate.[436] DSA also results in planar deformation, an increase in dislocation density, and inhomogeneous localization of deformation. These factors favor brittle crack extension and rupture of the protective oxide film, thereby enhancing crack advance by either anodic dissolution or hydrogen embrittlement processes. In high-temperature water, the synergistic interactions between EAC and DSA during fatigue straining may be rationalized as follows:[436]

- Hydrogen vacancies produced by the corrosion reaction at the crack tip enter the steel, and hydrogen diffuses to strong trapping sites inside the crack-tip maximum hydrostatic stress region (e.g., MnS inclusions) ahead of the crack tip.

- These sites act as initiation sites for local quasi-cleavage cracking, as well as void formation, and these microcracks link with the main crack.

- In addition, at a given macroscopic strain due to external loads, the microscopic strain in steels that are susceptible to DSA is higher because of strain localization, which leads to higher rates and larger steps of oxide film rupture. As a result, the slip oxidation/ dissolution process enhances fatigue crack initiation or fatigue crack growth rates.

- Such interactions, however, occur only under certain conditions of temperature, strain rate, and DO level in the environment.

In carbon and low-alloys steels, the interaction of nitrogen and dislocations during plastic deformation reduces plasticity, which causes strain localization in the material.[434] Small areas can deform plastically adjacent to areas that might be blocked by nitrogen/dislocation interactions. For a given macroscopic strain, the microscopic strain is higher due to strain localization in steels that are susceptible to DSA. Thus, because of strain localization, stress concentrations at active slip planes lead to higher rates and larger steps of oxide rupture and, simultaneously, to a decreased repassivation rate.[434,435] Consequently, both crack initiation and growth rates may be enhanced in carbon and low-alloy steels. In addition, the effect of hydrogen on fatigue and its interaction with ripple loading and DSA is a potential concern for HWC conditions and needs to be investigated.

Crack Growth Rates in Smooth Fatigue Specimens

Studies on the formation and growth characteristics of short cracks in smooth fatigue specimens in LWR environments indicated that the decrease in fatigue life in LWR environments is caused primarily by the effects of the environment on the growth of MSCs (i.e., cracks less than 200 μm deep) and, to a lesser extent, on the growth of mechanically small cracks.[390,401] Measured crack lengths as a function of fatigue cycles and fraction of fatigue life for smooth cylindrical specimens of A533-Gr. B low-alloy steel in air, simulated PWR environment, and high-DO water are shown in Fig. 54. An example of the growth of a surface crack in A533 Gr. B steel tested in air at room temperature, and the fracture surface and probable crack front for the crack, are shown in Fig. 55. The results indicate that, for this example, three cracks merged to form the final fracture surface. The primary crack initiated near an inclusion and reached a surface length of approximately 100 μm after 3,062 cycles (i.e., approximately 50% of the fatigue life). Two secondary cracks merged with the primary crack after approximately 5,700 and 6,000 cycles. Crack depth was determined by dividing the surface crack length by pi (π).

The crack growth rates corresponding to the data shown in Fig. 54 are plotted as a function of crack depth in Fig. 56. The results indicate that, in LWR environments, the period spent in the growth of MSCs is decreased. At approximately 0.8% strain range, only 30–50 cycles are needed to form a 100-μm crack in high-DO water, whereas approximately 450 cycles are required to form a 100-μm crack in a low-DO PWR environment and more than 3,000 cycles in air. These values correspond to average growth rates of approximately 2.5, 0.22, and

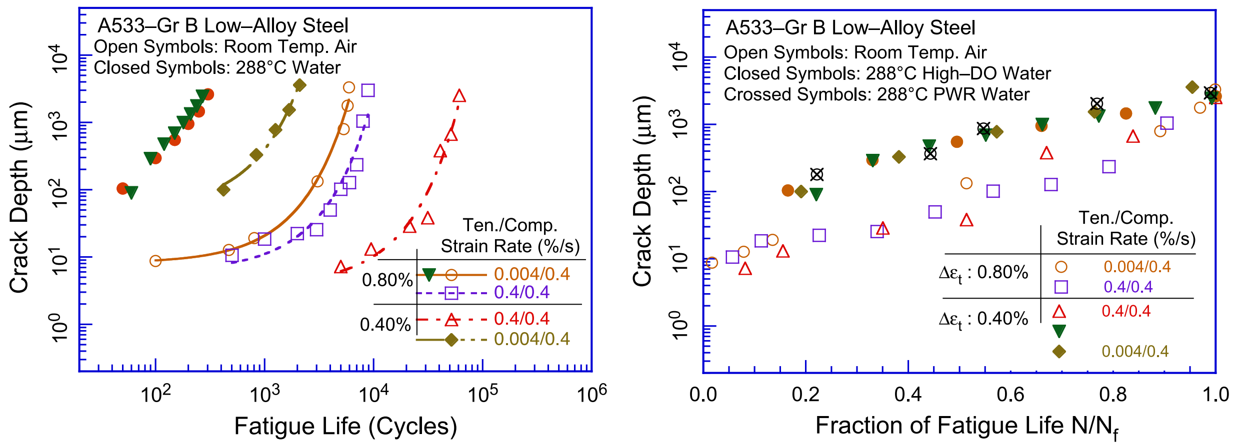

Figure 54. **Depth of largest crack plotted as a function of (a) fatigue cycles and (b) fraction of fatigue life for A533 Gr. B low-alloy steel in air and water environments (Ref. 401).**

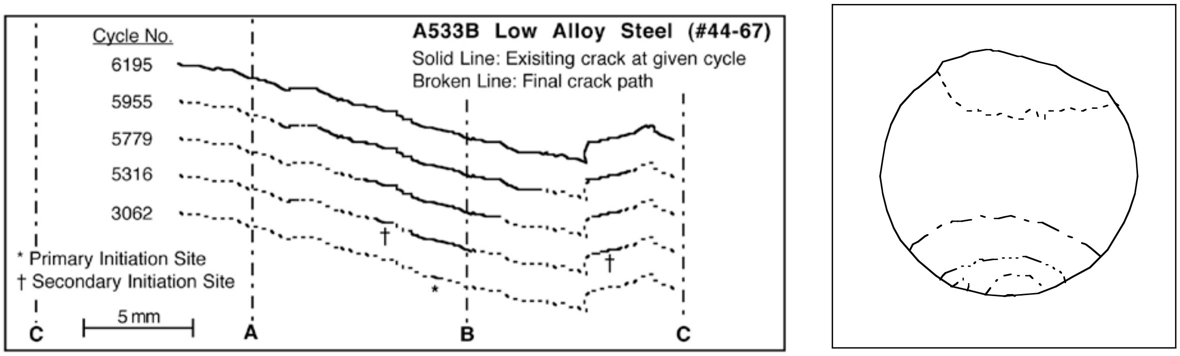

(a)

(b)

Figure 55. **(a) Morphology and length of surface crack after various numbers of cycles for A533 Gr. B steel in air at room temperature, and (b) fracture surface and probable crack front for surface cracks shown in (a) (Ref. 401).**

0.033 µm/cycle in high-DO water, low-DO PWR environment, and air, respectively. The results also indicate that, relative to air, CGRs in high-DO water are nearly two orders of magnitude higher during the initial stages of fatigue life (i.e., for crack sizes less than 100 µm), and are one order of magnitude higher for crack sizes greater than 100 µm.

The surface crack and fracture surface morphologies of the test specimens indicate that, in high-temperature, high-DO water with slow strain rates, the surface cracks appear to grow entirely in Stage II growth as Mode I tensile cracks normal to the stress axis (Figs. 18 and 52). In air and low-DO PWR environments, both Stage I and Stage II growths are observed. Surface cracks grow initially as Mode II (shear) cracks along planes 45° to the stress axis and, when the stress intensities are large enough to promote slip on axes other than the primary slip axis, they grow as Mode I (tensile) cracks normal to the stress axis. In addition, for A106 Gr. B carbon steel, Stage I crack growth in air and low-DO water occurs entirely along the soft ferrite grains, whereas in high-DO water, cracks propagate across both ferrite and pearlite regions. These results are consistent with the slip-oxidation/dissolution mechanism in high-DO water.

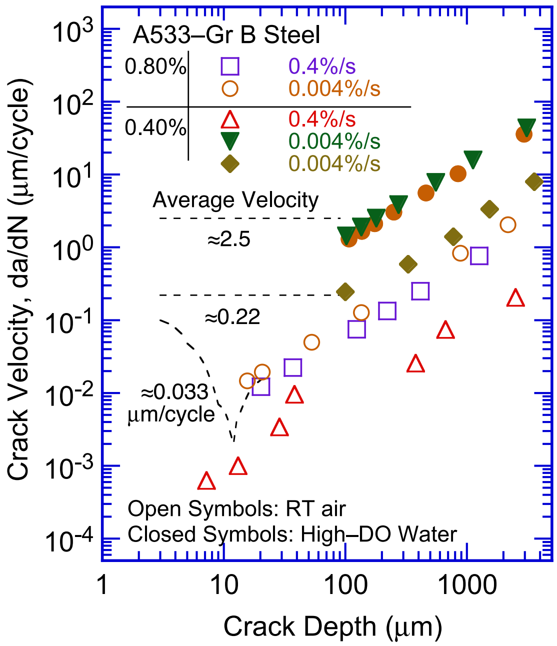

Figure 56.
Crack growth rates plotted as a function of crack depth for A533 Gr. B low-alloy steel tested in air and water environments (Ref. 401).

Austenitic Stainless Steels

Mechanism of Corrosion Fatigue

Austenitic SSs exposed to LWR environments develop an oxide film that consists of two layers: a fine-grained, tightly-adherent, chromium-rich inner layer, and a crystalline, nickel-rich outer layer composed of large and intermediate-sized particles. Photomicrographs of the gauge surface of Type 316NG specimens tested in simulated PWR water and high-DO water are shown in Fig. 57. The inner layer forms by solid-state growth, whereas the crystalline outer layer forms by precipitation or deposition from the solution. A schematic representation of the surface oxide film is shown in Fig. 58.

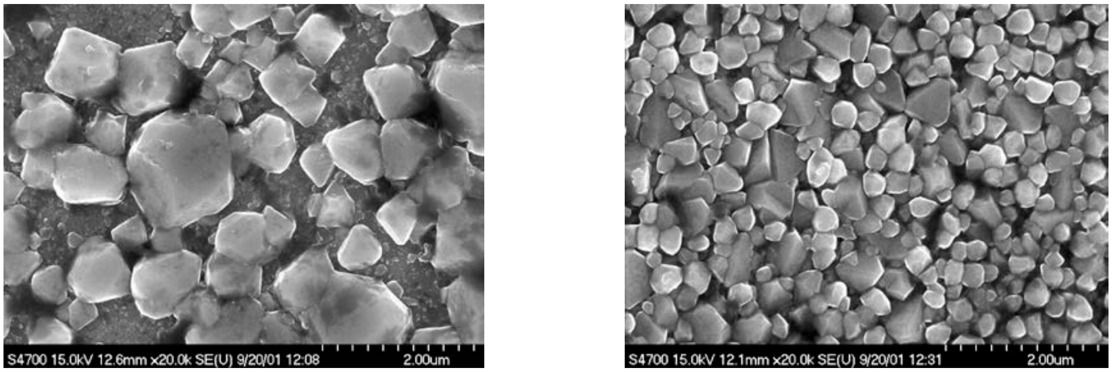

(a) (b)

Figure 57. **Photomicrographs of oxide films that formed on Type 316NG SS in (a) simulated PWR water and (b) high-DO water (Ref. 392).**

Several studies characterized the oxide films that form on austenitic SSs in LWR environments.[439–445] The inner layer consists of chromium-rich spinel ($Ni_xCr_yFe_{3-x-y}O_4$) with a nonstoichiometric composition; the actual composition of spinels varies with environmental

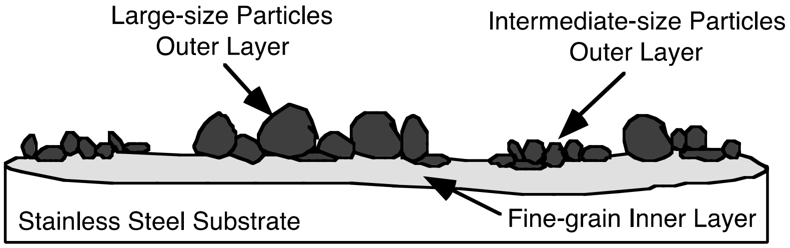

Figure 58. Schematic of the corrosion oxide film formed on austenitic SSs in LWR environments.

conditions. Da Cunha et al.[443] determined that the inner layer that formed on Type 316L SS in a PWR environment at 350°C (662°F) consisted of mixed chromium oxides (Cr_2O_3 + $FeCr_2O_4$) and Fe_3O_4. Nakayama and Oshida[445] characterized the oxide film on SSs exposed to high-DO (8 ppm) water at 300°C (572°F) as chiefly composed of $NiO\cdot(Cr,Fe)_2O_3$ and/or $NiFe_2O_4$, which may be formed by a solid reaction between NiO and $(Cr,Fe)_2O_3$ or α-Fe_2O_3. Kim[439,440] identified the $FeCr_2O_4$ spinel chromite (or $Fe_xCr_{3-x}O_4$), along with $NiFe_2O_4$, in the inner layer formed on Types 304 and 316 SSs exposed at 288°C (550°F) under BWR NWC or HWC conditions. Kim also noted that the inner oxide layer formed in a NWC BWR environment contained a lower concentration of chromium than that formed in a HWC low-DO environment. Such differences were attributed to chromium oxidation in high-DO water.

The structure and composition of the crystalline outer layer vary with the water chemistry. In BWR environments, the large particles in the outer layer are primarily composed of γ–Fe_2O_3 hematite in NWC and Fe_3O_4 magnetite in HWC.[439,440] The intermediate particles in the outer layer are composed of α–Fe_2O_3 in NWC and Fe_3O_4 in HWC. The structure of the outer layer varies when the water chemistry is cycled between NWC and HWC. In PWR environments, the large particles were identified as $Ni_{0.75}Fe_{2.25}O_4$ spinel and the intermediate particles as $Ni_{0.75}Fe_{2.25}O_4$ + Fe_3O_4.[443] The possible effects of minor differences in the surface oxide film on fatigue crack initiation are discussed in the next section.

Effects of Surface Micropits

The reduction of fatigue lives in high-temperature water may be due to the presence of surface micropits. To investigate the effect of surface micropits, fatigue tests were conducted on Type 316NG (Heat P91576) specimens that were pre-exposed to either low-DO or high-DO water and then tested in air or water environments.[392] The results of these tests, as well as data obtained earlier on this heat and Heat D432804 of Type 316NG SS in air and low-DO water at 288°C (550°F), are plotted in Fig. 59. The fatigue lives of specimens preoxidized in high-DO water and then tested in low-DO water were identical to those of specimens tested without preoxidation. Also, fatigue lives of specimens preoxidized at 288°C (550°F) in low-DO water and then tested in air were identical to those of unoxidized specimens (Fig. 59). If micropits reduce fatigue life, the pre-exposed specimens should have shown a decrease in life, and the fatigue limit of these steels should have also been lower in water. These results indicate that surface micropits or minor differences in the composition or structure of the surface oxide film had little or no effect on the formation of fatigue cracks.

Fatigue Crack Initiation

Both the slip oxidation/dissolution and the hydrogen-induced cracking mechanisms depend on the rates of oxide rupture, passivation, and liquid diffusion. Therefore, it is difficult to differentiate between the two processes or to establish their relative contribution to fatigue

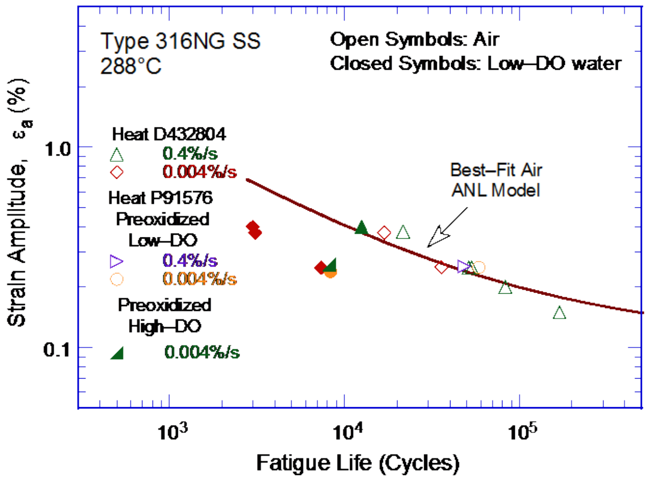

Figure 59. Effects of environment on formation of fatigue cracks in Type 316NG SS in air and low-DO water at 288°C (550°F). Preoxidized specimens were exposed for 10 days at 288°C (550°F) in water that contained either less than 5 ppb DO and approximately 23 cm^3/kg dissolved H_2 or approximately 500 ppb DO and no dissolved H_2 (Ref. 392).

cracking in LWR environments. However, for austenitic SSs, lower fatigue lives in low-DO water versus high-DO water are difficult to reconcile in terms of the slip oxidation/dissolution mechanism, which assumes that crack growth rates increase with increasing DO in the water. Metallographic examination of fatigue test specimens suggests that hydrogen-induced cracking may have played an important role in environmentally assisted reduction in fatigue lives of austenitic SSs.[395] For example, hydrogen can cause localized crack tip plasticity by reducing the stress required for dislocation motion, which leads to higher rates and larger steps of oxide film rupture. Thus, fatigue lives may be decreased, not because of increased growth rates, but because of increased film rupture frequency.

A detailed metallographic evaluation of austenitic SS fatigue test specimens performed to characterize the crack and fracture morphology indicate similar fatigue crack surface morphology to that observed for carbon and low-alloy steels.[395] In an air environment, fatigue cracks were more likely to be oblique, approaching 45° with respect to the tensile axis. By contrast, the cracks that formed in either BWR or PWR environments tended to be perpendicular to the tensile axis. In air, the fracture mode for crack initiation (i.e., crack depths up to 200 μm) and crack propagation (i.e., crack depths greater than 200 μm) was TG, leaving behind relatively smooth surfaces. With an increasing degree of sensitization, cleavage-like, or stepped, TG fracture and ridge structures were observed on the surfaces.

In simulated NWC BWR environments, the initial crack appeared IG under all heat treatment conditions, implying a weakening of the grain boundaries. The extent of IG fracture increased with the degree of sensitization. For crack depths beyond 200 μm, the initial IG fracture mode transformed into TG mode with cleavage-like features. In simulated PWR environments, however, fatigue cracks initiated and propagated in a TG mode irrespective of the degree of sensitization. Prominent features of the fracture surfaces included highly angular, cleavage-like fracture facets that exhibited well-defined “river” patterns.[395] Intergranular facets were rarely observed; they were found mostly in the more heavily sensitized alloys.

The characterization of surface cracks and fracture morphology in austenitic SSs suggests that, in LWR environments, although film rupture was apparent, the formation and growth of fatigue cracks were primarily caused by hydrogen-induced cracking.

Effects of Dynamic Strain Aging

DSA was observed in austenitic SSs in air at strain rates below 0.3 %/s and temperatures in the range of 300–600°C (572–1112°F); the peak effects occurred at 500–600°C (932–1112°F).[446] The fatigue life of a heat of Type 316LN SS at low strain rates was greater at 600°C (1112°F) than at 500°C (932°F). Typically, at temperatures above 400°C (752°F) the fatigue life of austenitic SSs decreased with an increase in temperature or a decrease in strain rate.[447] DSA increased the dislocation density at slow strain rates, which enhanced the degree of inhomogeneity of deformation during fatigue loading.

DSA was also observed in Type 304L SS under LWR operating conditions. At 0.4 %/s strain rate, the fatigue life and fatigue limit in air were higher at 300°C (572°F) than at 150°C (302°F) (due to secondary strain hardening at 300°C [572°F]).[448] A similar behavior was observed for this heat of SS in PWR water. At 0.4 %/s, fatigue life decreased in PWR water relative to that in air at 150°C (302°F), but not at 300°C (572°F). This difference was identified as secondary hardening at 300°C (572°F), which was not observed at 150°C (302°F). The secondary hardening at 300°C (572°F) may be due to DSA, although the temperature was relatively low.

Crack Growth Rates in Smooth Specimens

Studies on the formation and growth characteristics of short cracks in smooth fatigue specimens of austenitic SSs in LWR environments indicated that, although the growth rates of mechanically small cracks were greater in water than in air, the decrease in fatigue lives was caused essentially by environmental effects on the growth of MSCs.[449] The growth of the largest crack in austenitic SSs as a function of fatigue cycles, in air and water environments, is shown in Fig. 60. The data of Orbtlik et al.[450] for Type 316L SS in air at 25°C (77°F) and approximately 0.2% strain range were used to estimate the crack growth in air. Similar studies on carbon and low-alloy steels indicate[401,402–404] that the fatigue crack size at various life fractions was independent of strain range, strain rate, and temperature; thus, the depth of the largest crack at various life fractions was approximately the same at strain ranges of 0.75% and 0.2%. The curve for the test in air at 0.75% (dashed line in Fig. 39) was calculated from the best-fit equation of the experimental data for Type 316L SS at 0.2% strain range; the estimated crack lengths at 0.75% strain range show very good agreement with the measured values. The results show that, at the same number of cycles, the crack length was longer in low-DO (PWR)

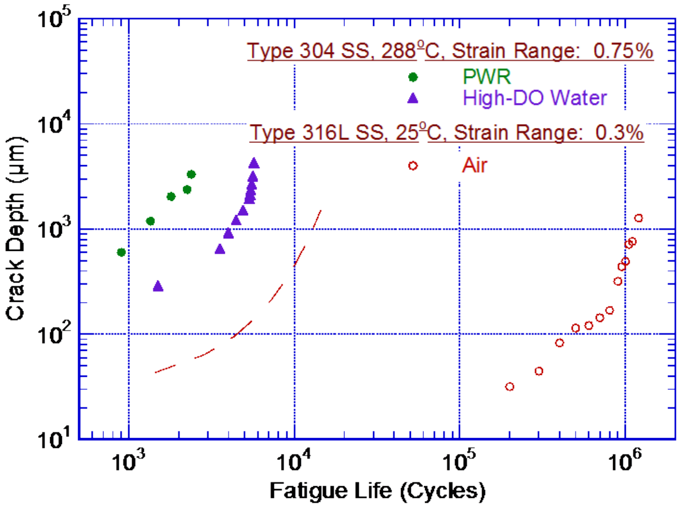

Figure 60.
Depth of largest crack plotted as a function of fatigue cycles for austenitic SSs in air and water (Refs. 392,449,450).

water than in air, e.g., after 1,500 cycles, the crack length in air, high-DO (BWR) water, and PWR water was approximately 40, 300, and 1,100 μm, respectively. The growth of cracks during the initiation stage, i.e., growth of MSCs, was enhanced in water; the fatigue cycles needed to form a 500-μm crack were a factor of approximately 12 lower in low-DO water than in air. Figure 60 shows that the number of cycles required to produce a 500-μm crack is 800, 3,000, and 9,000 in low-DO (PWR) water, high-DO (BWR) water, and air environments, respectively; thus, the number of cycles was more than a factor of 10 lower in low-DO water than in air.

The CGRs during the propagation stage, i.e., growth of mechanically small cracks, in air and water environments are plotted as a function of crack length in Fig. 8; they were calculated from the best fit of the data in Fig. 60. The CGRs in high-DO water for the specimen with a 24-h soak period (closed diamonds in Fig. 61) were determined from measurements of fatigue striations. The CGRs were a factor of 2–6 higher in water than in air. Growth rates in PWR water or high-DO water with a 24-h soak period were higher than in high-DO water with a 120-h soak period. At a crack length of ~1,000 μm, the CGRs in air, high-DO water, and low-DO water were 0.30, 0.64, and 1.05 μm/cycle, respectively. For the 0.75% strain range and 0.004%/s strain rate, these values corresponded to growth rates of approximately 1.6 × 10^{-9} m/s (6.3 × 10^{-8} in./s), 3.4 × 10^{-9} m/s (1.3 × 10^{-7} in./s), and 5.6 × 10^{-9} m/s (2.2 × 10^{-7} in./s) in air, high-DO water, and low-DO water, respectively. Thus, growth rates were a factor of 3.5 greater in low-DO water than in air.

2.4.3.3 Fatigue Crack Growth Rates

The existing fatigue crack growth (da/dN) data obtained on CT specimens of wrought and cast SSs in LWR environments were compiled by Shack and Kassner.[451] The results indicated significant enhancement of CGRs in high-DO water; at CGRs of less than 10^{-10} m/s (4 × 10^{-9} in./s) in air, the rates in BWR NWC conditions exceeded the air curve in Section III of the ASME Code by a factor of approximately 20–30. The CGRs determined from fatigue ε-N tests showed good agreement with the data obtained on CT specimens.

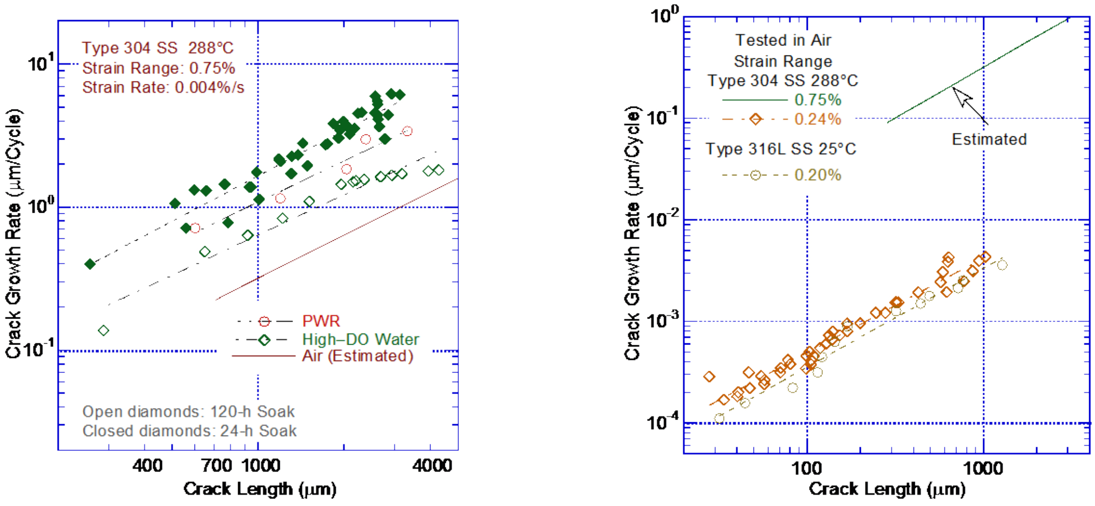

(a) (b)

Figure 61. **Crack growth rates plotted as a function of crack length for austenitic SSs in (a) water and (b) air environments (Refs. 392,449,450).**

Under cyclic loading, the time-based CGR, da/dt (m/s), in an environment can be expressed as the superposition of the rate in air and the rates due to corrosion fatigue and SCC, given as

$$(da/dt)_{env} = (da/dt)_{air} + (da/dt)_{cf} + (da/dt)_{scc}. \tag{39}$$

The CGR_{air} has been determined from the correlation developed by James and Jones:[452]

$$(da/dt)_{air} = C_{SS}\ S(R)\ \Delta K^{3.3}/t_r, \tag{40}$$

where t_r is the rise time (seconds) of the loading waveform, R is the load ratio (K_{min}/K_{max}), ΔK is the stress intensity factor range ($K_{max} - K_{min}$) in MPa $m^{1/2}$, and the function S(R) is expressed in terms of the load ratio R:

$$\begin{aligned} S(R) &= 1.0 && R < 0 \\ S(R) &= 1.0 + 1.8R && 0 < R < 0.79 \\ S(R) &= -43.35 + 57.97R && 0.79 < R < 1.0. \end{aligned} \tag{41}$$

In Eq. 40, C_{SS} is expressed in terms of a third-order polynomial with temperature T (°C):[452]

$$C_{SS} = 1.9142 \times 10^{-12} + 6.7911 \times 10^{-15}\ T - 1.6638 \times 10^{-17}\ T^2 + 3.9616 \times 10^{-20}\ T^3 \tag{42}$$

Shack and Kassner[451] have investigated the effects of LWR coolant environments on fatigue CGR of nonirradiated austenitic SSs. In the absence of any significant contribution of SCC to growth rate, the CGRs in water with ≈0.2 ppm DO were best represented by the expression

$$(da/dt)_{env} = (da/dt)_{air} + 4.5 \times 10^{-5}\ (da/dt_{air})^{0.5}, \tag{43}$$

and in water with ≈8 ppm DO by the expression

$$(da/dt)_{env} = (da/dt)_{air} + 1.5 \times 10^{-4}\ (da/dt_{air})^{0.5}. \tag{44}$$

In Eq. 39, the CGRs are represented by the correlation given in NUREG-0313, Rev. 2,[215] for nonirradiated materials:

$$(da/dt)_{env} = A_1(K)^{2.161}, \tag{45}$$

where the magnitude of the constant A_1 depends on the water chemistry and composition and microstructure of the material. An A_1 value of 2.1×10^{-13} has been proposed for sensitized SS in water containing 8 ppm DO. For water containing 0.2 ppm DO, the CGR is taken as one-third that of the value for 8 ppm DO (i.e., A_1 is 7.0×10^{-14}). The CGRs for irradiated SSs are represented by a value that is six times that of the NUREG-0313 value for nonirradiated material (i.e., A_1 is 1.26×10^{-12}). The SCC contribution may not be significant for nonirradiated materials in low-potential HWC BWR or PWR environments. The austenitic SS CGR disposition curve proposed by EPRI[418] for use in NWC BWR core environments is expressed as

$$(da/dt)_{env} = A_2(K)^{2.5}, \tag{46}$$

where the constant A_2 is 4.564×10^{-13} in a NWC BWR environment and 1.512×10^{-13} in a HWC BWR environment.

An example of enhancement fatigue CGR in high- and low-DO environments relative to those in air for solution-annealed Types 304 and 316 SSs irradiated up to 3 dpa is shown in Fig. 62. In these figures, the data points that lie along the diagonal represent predominantly mechanical fatigue, and those that lie close to the model curve indicate environmentally enhanced crack growth. Austenitic SS irradiated to 0.45 dpa shows little environmental enhancement of CGRs in high-DO water. The curves in the figures are based on the superposition model (Eq. 39). For cyclic loading using either a triangular or a slow/fast sawtooth waveform, $(da/dt)_{SCC}$ is determined by considering the contribution of SCC during the slow rise time of the cycle; an equivalent K is computed to determine the contribution of SCC.

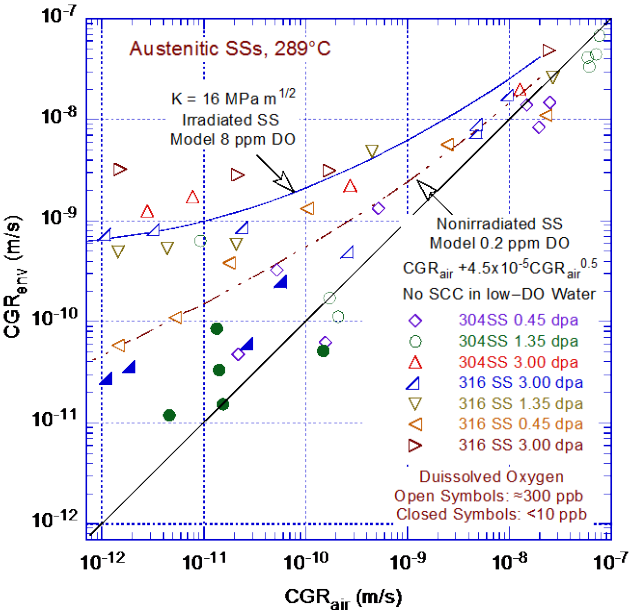

Figure 62.
Fatigue CGRs for irradiated austenitic SSs at 289°C (552°F) in high-purity water (Refs. 37).

The results for austenitic SSs irradiated to 1.35 or 3.0 dpa indicate significant enhancement of the CGRs in high-DO water under cyclic loading with long rise times. For austenitic SSs irradiated to 0.75–3.0 dpa, the fatigue CGRs in water with ≈ 300 ppb DO may be represented by superposition of the SCC growth rates expressed as six times the NUREG-0313 curve and by the Shack/Kassner corrosion fatigue model for nonirradiated SSs in high-purity water with 8 ppm DO.[451] For continuous cyclic loading, decreasing the DO level has a beneficial effect on the CGRs of irradiated SSs; for example, decreasing the DO from ≈300 ppb DO to <30 ppb DO lowers the CGR by a factor of 25 (closed symbols in Fig. 62). At 289°C (552°F), the fatigue CGRs for irradiated austenitic SSs in water with <30 ppb DO are lower than those predicted by the Shack/Kassner model for nonirradiated austenitic SSs in high-purity water with 0.2 ppm DO; there is no contribution of SCC in low-DO water.

Fatigue Crack Growth Reference Curves

Recently,[453] reference fatigue crack growth curves (da/dN) for unirradiated austenitic SSs in PWR environments have been proposed in ASME Section XI Code Case N-809[454] for application of flaw evaluation applications. Separate curves are proposed for Type 304/316 and Type 304L/316L wrought SSs, associated welds (Type 309 and 309), and cast equivalents (CF-8/CF-8M and CF-3/CF-3M). The reference curves explicitly contain the effects of temperature, loading rate, mean stress, and cyclic stress range on fatigue CGRs.

The basic model was developed by Mills.[455] The experimental database used in the analysis came from various research and industry sources including Bettis Labs (U.S.), Rolls Royce (UK), Japan, France, and GE/Sweden. Other data from Argonne and EPRI that were not used in analysis were used to validate the model, and to justify extending the correlation to similar materials such as Type 316L and its cast equivalent and associated welds. The details of the reference fatigue crack growth model for austenitic SSs are as follows.

(a) The fatigue CGR, *da*/*dN*, of the material is characterized in terms of the range of the applied stress intensity factor, ΔK, given by the expression

$$da/dN = C_0 \Delta K^n \tag{47}$$

where

C_0 = scaling parameter that accounts for the effect of loading rate and environment on fatigue CGR

n = slope of the log (da/dN) versus log (ΔK) curve; n and C_0 are parameters dependent on the material and environmental conditions

(b) The fatigue CGR of the material is affected by R ratio (K_{min}/K_{max}), loading rate, and environmental conditions. These variables are accounted for in the definition of C_0 as defined below:

$$C_0 = C S_T S_R S_{ENV} \tag{48}$$

where

C = nominal fatigue CGR constant

S_{ENV} = parameter defining the environmental effects on fatigue CGR

S_R = parameter defining the effect of *R* ratio on fatigue CGR

S_T = parameter defining the effect of temperature on fatigue CGR

These parameters are based on crack growth data obtained from specimens of the same material specification and product form, or suitable alternative. Material variability, environment, test frequency, mean stress, and other variables that affect the data are considered.

(c) The reference fatigue CGR curves are plotted as normalized da/dN versus ΔK where

$$\left.\frac{da}{dN}\right|_{Normalized} = \frac{da/dN}{S_T S_R S_{ENV}} \tag{49}$$

Reference Curves for Wrought Austenitic Stainless Steels

(a) Fatigue CGR of wrought austenitic SSs and associated weld metals in PWR environments can be characterized in terms of the range of the applied stress intensity factor, ΔK, as defined by Eq. 47. The fatigue CGR depends on temperature, R ratio, and environment as defined below.

(b) The parameter S_{ENV} depends on loading rise time for the variation in loading during a transient. The loading rise time, T_R, is the period in seconds for which the stress is increasing during a stress cycle. The loading rise time, which excludes hold times and time periods for which the stress is decreasing during the cycle, includes the time periods from minimum stress to steady state and from steady state to maximum stress. Hold times include periods in which the change in stress does not exceed 1.92 kPa/s (1 ksi/h).

(c) Reference fatigue CGR curves of wrought austenitic SSs and associated weld metals exposed to PWR environments are given in normalized form in accordance with Eq. 49.

(1) For Type 304 and Type 316 SSs and associated weld metals (SI units),

$C = 9.10 \times 10^{-6}$ for $\Delta K \geq \Delta K_{th}$

$C = 0$ for $\Delta K < \Delta K_{th}$

$n = 2.25$

$S_R = 1.0$ for $R < 0$

$S_R = 1 + \exp(8.02(R - 0.748))$ for $0 \leq R < 1.0$

$S_T = \exp(-2516/T_K)$ for 150°C (302°F) $\leq T \leq$ 343°C (649°F)

$S_T = 3.39 \times 10^5 \exp[(-2516/T_K) - 0.0301$ for 20°C (68°F) $\leq T \leq$ 150°C (302°F)

$$S_{ENV} = T_R^{0.3}$$

where

da/dN = fatigue CGR, mm/cycle

ΔK = stress intensity factor range, (MPa√m)

$T_K = T + 273.15$, k

T = metal temperature, °C

T_R = loading rise time, s

$\Delta K_{th} = 1.10$ (MPa√m)

When $T_R < 1$ sec, set $T_R = 1$ s.

(2) For Type 304L and Type 316L stainless steels and associated weld metals (SI units),

$C = 1.39 \times 10^{-5}$ for $\Delta K \geq \Delta K_{th}$

$C = 0$ for $\Delta K < \Delta K_{th}$

$n = 2.25$

$S_R = 1.0$ for $R < 0$ and $0 \leq R \leq 0.7$

$S_R = 1 + 1.5(R - 0.7)$ for $0.7 < R \leq 1.0$

$S_T = \exp(-2516/T_K)$ for 150°C (302°F) $\leq T \leq$ 343°C (649°F)

$S_T = 3.39 \times 10^5 \exp[(-2516/T_K) - 0.0301$ for 20°C (68°F) $\le T \le$ 150°C (302°F)

$S_{ENV} = T_R^{0.3}$

where

da/dN = fatigue CGR, mm/cycle

ΔK = stress intensity factor range, (MPa√m)

$T_K = T + 273.15$, k

T = metal temperature, °C

T_R = loading rise time, sec

$\Delta K_{th} = 1.10$ (MPa√m)

When $T_R < 1$ sec, set $T_R = 1$ sec.

(3) A loading rise-time-independent reference curve for the materials covered above under items (1) and (2) may be used by defining S_{ENV} equal to 20 in Eq. 49 for all transient conditions.

Reference Curves for Cast Austenitic Stainless Steels

Fatigue CGR of CASS materials in PWR environments can be characterized in terms of the range of the applied stress intensity factor, Δ*K*, as defined by Eq. 47. The fatigue CGR is affected by temperature, *R* ratio, and environment. The reference curves for wrought SS may be used for the cast grades.

3 SEISMIC LOAD EFFECTS

3.1 Material Performance

The SSCs in an NPP are required to dissipate a considerable amount of energy in an earthquake event. These SSCs are typically designed to absorb this energy through local elastic deformation and, in more severe seismic events, plastic deformation within the ductility limits of the affected material. For many years, it was generally held that loading rate was not a significant variable in the response of a large structure to earthquakes.[456] However, more recent events with very high ground-motion velocities, such as the 1994 Northridge and 1995 Kobe earthquakes (maximum recorded horizontal ground velocities of 177 and 176 cm/s, respectively) have convinced most researchers that the loading rate effects are important and, in particular, a possible explanation for the unexpectedly poor behavior of large steel structures during these events.[457–459]

Strain rate effects during earthquakes are important for several reasons. First, as discussed below, the imposed strain rate affects the tensile properties of most structural alloys; increasing strain rate generally produces a corresponding increase in the yield and tensile strengths and a decrease in ductility. However, this increase in strength is not as beneficial as one might think, because under seismic loading conditions, the maximum strain, ε, is typically achieved when the strain rate is zero (i.e., $d\varepsilon/dt = 0$ when ε is a maximum). More importantly, the fracture toughness of these same materials generally decreases with increasing strain rate, and because most structural components (and almost all weldments) inevitably contain flaws, this property more than tensile strength controls the behavior of these materials under dynamic loading conditions.

A number of attempts have been made to define the strain rate imposed on structural materials during an earthquake. Chang and Lee[460] estimated that strain rates between 10^{-6} and 10^{-1} s^{-1} might be experienced by steel building frames during earthquake ground motions. Similarly, Uang and Bondad[461] and Nakashima et al.[462] placed an upper limit of 10^{-1} s^{-1} on the strain rate anticipated during an earthquake. However, Antaki[463] estimated that for pipelines subject to plastic loading during seismic events, strain rates as high as 8 s^{-1} were possible. Wiesner and MacGillivray[464] state that typical loading rates under earthquake conditions lie in the range of 0.1 to 10 s^{-1}. Similarly, Gioncu[459] has calculated anticipated strain rates on structural components as high as 2.5 s^{-1} for a single-degree-of-freedom structural system and 10 s^{-1} for a multiple-degree-of-freedom system, and he identifies imposed strain rates of 0.1 to 10 s^{-1} to be typical of strong earthquakes.

As shown in Fig. 2(b), a seismic load is reversing dynamic load about a normal (or mean) operating load. In some incidences, the latter may include some other off-normal or accident load condition. Both the frequency and magnitude of the seismic load vary during a seismic event and include up to a few hundred cycles. Therefore, the cyclic deformation behavior of structural materials used in the construction of the reactor coolant pressure boundary components is reviewed first. Typically, the structural materials include A106 Gr. B and A333 Gr. 6 ferritic steels; A508 Cl. 3, A533 Gr. B, and A302 Gr. B low-alloy steels; and low- and high-carbon grades of Type 304 and 316 SSs, as well as nuclear-grade Type 316NG SS, and their associated weld metals.

3.1.1 Cyclic Deformation Behavior

3.1.1.1 Cyclic Stress-Strain Curves

Ferritic Steels

The existing fatigue strain versus life (ε–N) data indicate that in the temperature range of dynamic strain aging (200–370°C [392–698°F]), some heats of carbon and low-alloy steels are sensitive to strain rate even in an inert environment; with decreasing strain rate, the fatigue life may be either unaffected,[390] decrease for some heats,[465] or increase for others.[466] In the Argonne study,[390] at 288°C (550°F), a decrease in strain rate by 2 orders of magnitude has little or no effect on fatigue lives of A106 Gr. B and A533 Gr. B steel whereas fatigue lives of A302 Gr. B steel in radial orientation decreased by a factor of ≈5. A decrease in life with decreasing strain rate was also observed for the A333 Gr. 6 CS. Inhomogeneous plastic deformation can result in localized plastic strains; this localization retards blunting of propagating cracks that is usually expected when plastic deformation occurs and can result in higher crack growth rates.[467] The increases in fatigue life have been attributed to retardation of crack growth rates due to crack branching and suppression of plastic zone. Formation of cracks is easy in the presence of dynamic strain aging.[466]

The cyclic stress-strain response of carbon and low-alloy steels varies with steel type, temperature, and strain rate. In general, these steels show initial cyclic hardening, followed by cyclic softening or a saturation stage at all strain rates. At high strain amplitudes, a secondary hardening stage is observed prior to fracture. The carbon steels, with a pearlite and ferrite structure and low yield stress, exhibit significant initial hardening. The low-alloy steels, which consist of tempered ferrite and a bainitic structure, have a relatively high yield stress, and show little or no initial hardening, may exhibit cyclic softening during cyclic straining. For both steels, maximum stress increases with increases in applied strain and decreases with increases in temperature. However, in the temperature range of dynamic strain aging (200–370°C [392–698°F]), these steels exhibit enhanced cyclic hardening, a secondary hardening stage, and negative strain rate sensitivity.[465,466] The temperature range and extent of dynamic strain aging vary with composition and structure. Under conditions of dynamic strain aging, cyclic-stress increases with decreases in strain rate.

The effect of strain rate and temperature on the cyclic stress response of A106 Gr. B, A333 Gr. 6, A533 Gr. B, and A302 Gr. B steels is shown in Fig. 63. For both carbon and low-alloy steels, cyclic stresses are higher at 288°C (550°F) than at room temperature. At 288°C (550°F), all steels exhibit greater cyclic and secondary hardening because of dynamic strain aging. The extent of hardening increases as applied strain rate decreases. The cyclic stress-versus-strain curves for carbon and low-alloy steels at 288°C (550°F) are shown in Fig. 64; cyclic stress corresponds to the value at half-life. At 288°C (550°F), the stress-strain curve for carbon steels can be represented with the equation

$$\Delta\varepsilon_t = \frac{\Delta\sigma}{1965} + \left(\frac{\Delta\sigma}{C}\right)^{7.74}, \qquad (50)$$

where the constant C is expressed as

$$C = 1080 - 50.9\mathrm{Log}\left(\dot{\varepsilon}\right); \qquad (51)$$

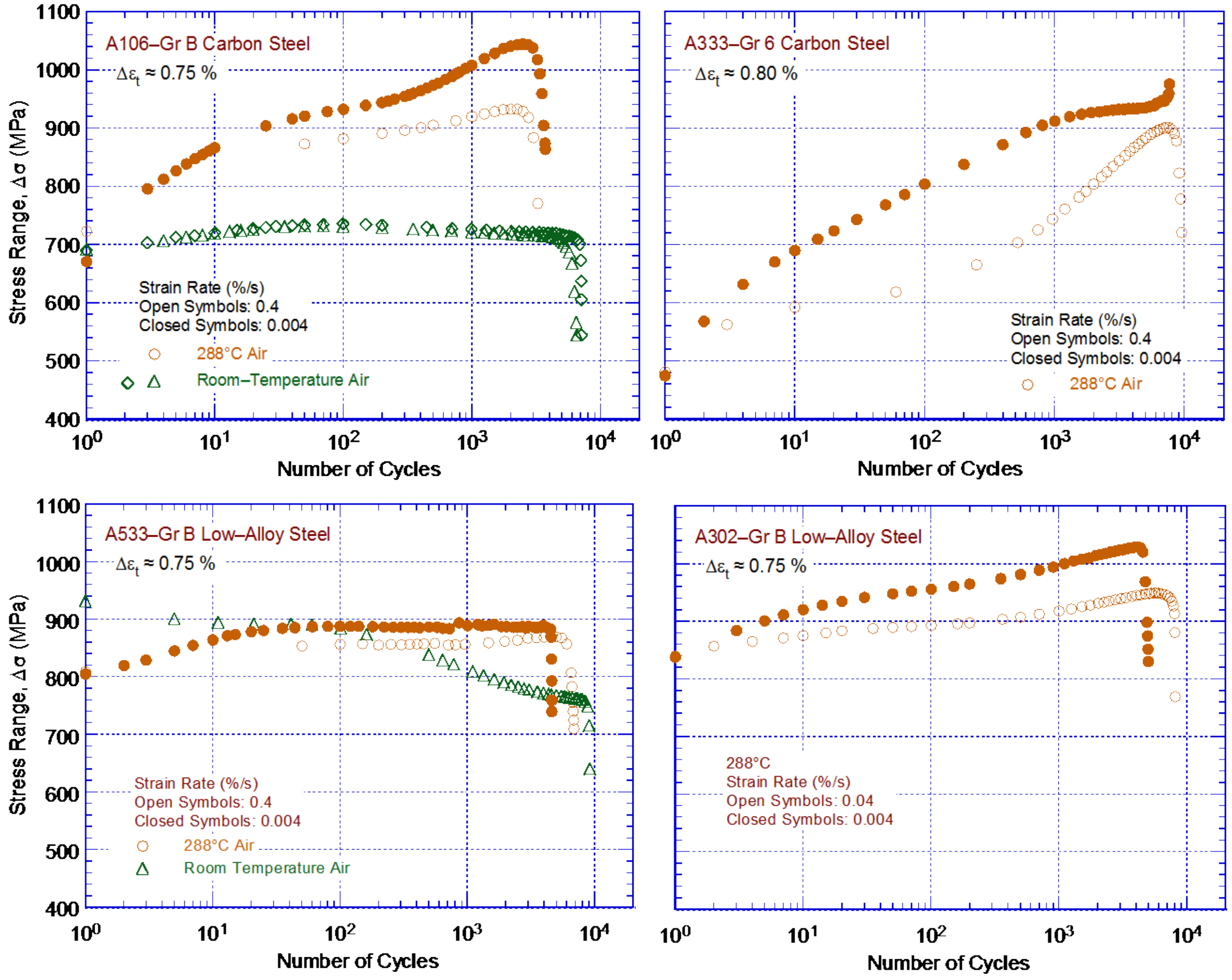

Figure 63. Effect of strain rate and temperature on cyclic stress of carbon and low-alloy steels (Ref. 390).

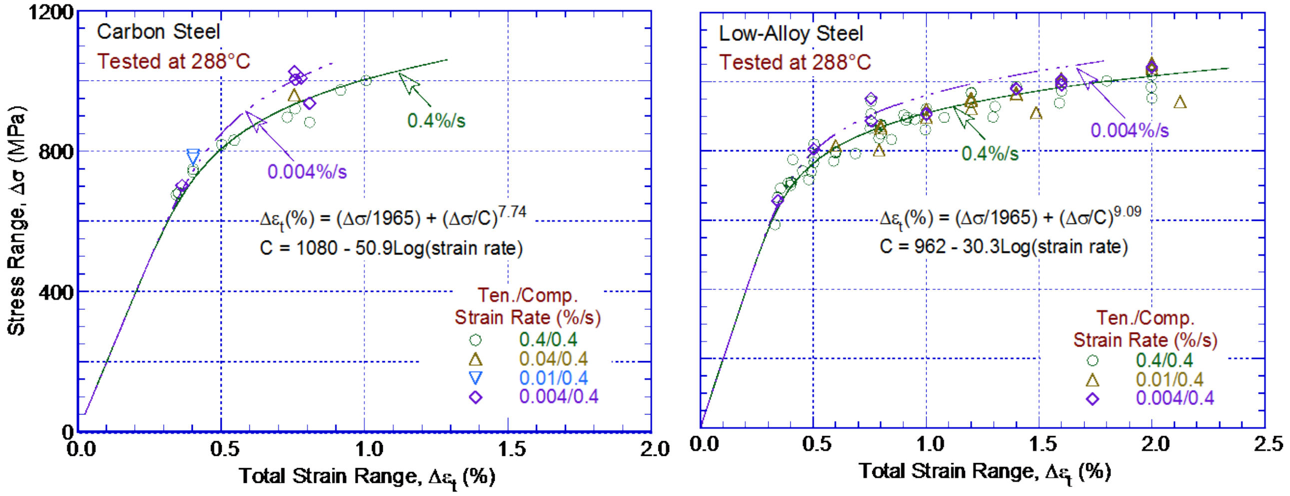

Figure 64. Cyclic stress-strain curve for carbon and low-alloy steels at 288°C (550°F) in air (Ref. 390).

and for low-alloy steels, with the equation

$$\Delta\varepsilon_t = \frac{\Delta\sigma}{1965} + \left(\frac{\Delta\sigma}{D}\right)^{9.09}, \tag{52}$$

where the constant D is expressed as

$$D = 962 - 30.3\mathrm{Log}\left(\dot{\varepsilon}\right), \tag{53}$$

where $\Delta\sigma$ is the cyclic stress range (MPa) and $\dot{\varepsilon}$ is applied total strain rate (%/s). The cyclic stress response is lower at room temperature than at 288°C (550°F).

Wrought Austenitic Stainless Steels

The existing fatigue ε–N data indicate that, in air, the fatigue life of typical austenitic SS reactor structural materials (e.g., Types 304L, 304, 316, 316L, and 316NG SS) is independent of temperature in the range from room temperature to 427°C (801°F).[447] In addition, although the effect of strain rate on fatigue life has been observed at 400–430°C (752–806°F), variation in strain rate in the range 0.4–0.008%/s has no effect on the fatigue lives of these materials at temperatures up to 400°C (752°F).[391,392,447,468] The fatigue ε–N behavior of cast austenitic SSs (CASS materials), such as grades CF-3, CF-8, and CF-8M, is similar to that of wrought austenitic SSs.[391,392]

During cyclic straining, austenitic SSs exhibit rapid hardening during the first 50–100 cycles; the extent of hardening increases with increasing strain amplitude and decreasing temperature and strain rate.[469–471] The cyclic strain hardening behaviors of Types 304 and 316NG SS tested in air at room temperature and 288°C (550°F) are shown in Fig. 65. The initial hardening is followed by softening and a saturation stage at 288°C (550°F), and by continuous softening at room temperature. For both Types 304 and 316NG SS, cyclic hardening at 288°C (550°F) is greater at low strain rates (i.e., cyclic stresses are higher at 0.004%/s than at 0.4%/s).

The cyclic stress-versus-strain curves for Types 304, 316, and 316NG SS at room temperature and 288°C (550°F) are shown in Fig. 66; cyclic stress corresponds to the value at half-life and at a strain rate of 0.4%/s. For the various steels, cyclic stresses increase in magnitude in the following order: Types 316NG, 304, and 316. At room temperature, the strain amplitude, ε_a (%), for Type 316 SS can be expressed in terms of the cyclic stress amplitude σ_a (MPa) by the equation

$$\varepsilon_a = \frac{\sigma_a}{1950} + \left(\frac{\sigma_a}{588.5}\right)^{1.94}; \tag{54}$$

for Type 304 SS, by

$$\varepsilon_a = \frac{\sigma_a}{1950} + \left(\frac{\sigma_a}{503.2}\right)^{2.19}; \tag{55}$$

for Type 316NG SS, by

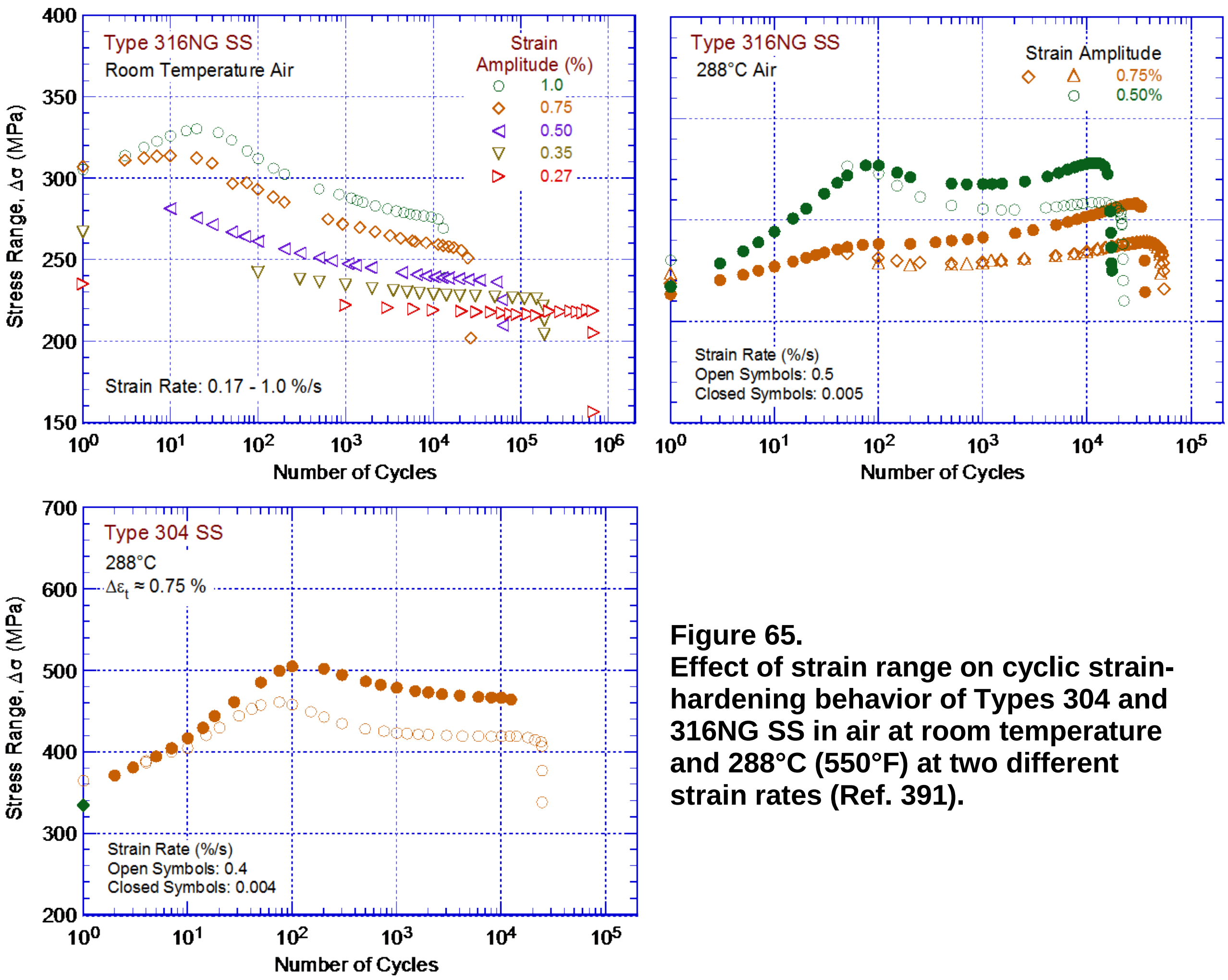

Figure 65.
Effect of strain range on cyclic strain-hardening behavior of Types 304 and 316NG SS in air at room temperature and 288°C (550°F) at two different strain rates (Ref. 391).

$$\varepsilon_a = \frac{\sigma_a}{1950} + \left(\frac{\sigma_a}{447.0}\right)^{2.59}. \qquad (56)$$

At 288–430°C (550–806°F), the cyclic stress versus strain curve for Type 316 SS can be expressed by

$$\varepsilon_a = \frac{\sigma_a}{1760} + \left(\frac{\sigma_a}{496.8}\right)^{2.19}; \qquad (57)$$

for Type 304 SS, by

$$\varepsilon_a = \frac{\sigma_a}{1760} + \left(\frac{\sigma_a}{373.9}\right)^{2.31}; \qquad (58)$$

for Type 316NG SS, by

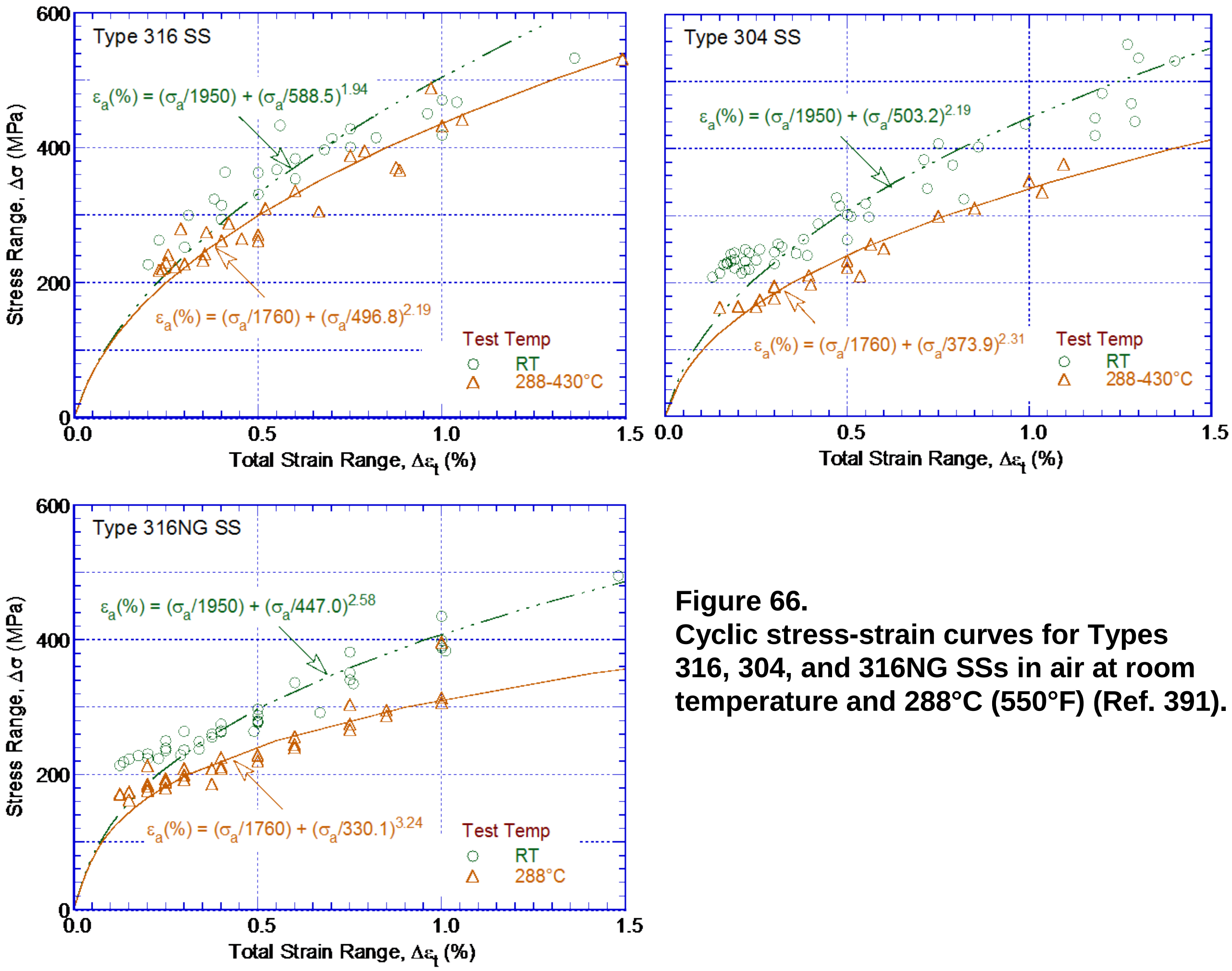

Figure 66.
Cyclic stress-strain curves for Types 316, 304, and 316NG SSs in air at room temperature and 288°C (550°F) (Ref. 391).

$$\varepsilon_a = \frac{\sigma_a}{1760} + \left(\frac{\sigma_a}{330.1}\right)^{3.24}. \qquad (59)$$

CASS Materials

Available fatigue S-N data[391,472–474] indicate that, in air, the fatigue lives of CF-3, CF-8, and CF-8M CASS materials are similar to those of wrought austenitic SSs. It is well known that the Charpy impact and fracture toughness properties of CASS materials decrease significantly after thermal aging at temperatures between 300 and 450°C (572 and 842°F).[310,326] The cyclic-hardening behavior of two heats of unaged and aged CASS CF-8M material is shown in Fig. 67. The results indicate that the cyclic strain-hardening behavior is also influenced by thermal aging. At 288°C (550°F), cyclic stresses of CASS materials aged for 10,000 h at 400°C (752°F) are higher than for unaged material or wrought SSs. In addition, strain rate effects on cyclic stress are greater for aged than for unaged steel (i.e., cyclic stresses increase significantly with decreasing strain rate). However, existing data are inadequate to establish unequivocally the effect of thermal aging on the fatigue life of these steels. For example, thermal aging for 25,200 h at 465°C (869°F) exerted no effect on the fatigue life of a CF-8M steel in air at 325°C (617°F),[472] whereas, in the present study, aging for 10,000 h at 400°C (752°F) decreased the

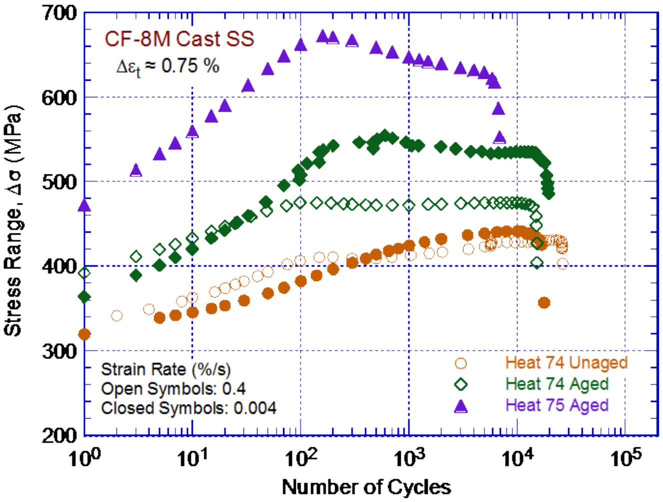

Figure 67.
Effect of strain rate on cyclic-hardening behavior of wrought and cast SSs in air at 288°C (550°F) (Ref. 391).

fatigue life of Heat 74 at 288°C (550°F), particularly in water.[391] These differences are most likely caused by microstructural differences arising from the relatively high temperature of thermal aging (i.e., 465°C [869°F]). Aging at 400°C (752°F) results in spinodal decomposition of the ferrite to form Cr-rich regions that very effectively increase tensile strength, whereas aging at 465°C (869°F) for extended periods results in the formation of Cr-rich α' particles and over-aging.

3.1.1.2 Microstructural Changes

At all strain rates, the cyclic deformation behavior of reactor structural materials typically consists of initial cyclic hardening followed by cyclic softening or a saturation (i.e., steady-state) stage. At high strain amplitudes, a secondary hardening stage is observed prior to fracture. In addition, at 200–370°C (392–698°F), these steels exhibit enhanced cyclic hardening and a secondary hardening stage because of dynamic strain aging. In the temperature regime of dynamic strain aging, the microstructural changes are significantly altered because of the interactions between mobile dislocations and interstitial C or N atoms. Such interactions are strongly dependent on temperature and strain rate.

It is generally believed that surface fatigue cracks nucleate in the regions of localization of plastic strain, known as persistent slip bands (PSBs), which result in the formation of sharp surface slip markings consisting of extrusions and intrusions on the initially flat surface.[475–477] The formation of fatigue cracks is a consequence of the temporary irreversibility of slip activity within the PSBs. Therefore, a detailed knowledge of the evolution of dislocation substructure during cyclic straining is essential for understanding the fundamental mechanisms of surface extrusions/intrusions and fatigue crack initiation.[478]

Plastic deformation in crystalline materials occurs by movement of the line defects or dislocations. There are two basic types of dislocation movement: “glide,” in which the dislocation moves in the surface defined by its line and Burgers vector, and “climb,” in which the dislocation moves out of the glide surface. Slip is the most common manifestation of glide. In crystalline materials, plastic deformation occurs by the movement or sliding of one plane of atoms over another on specific planes, known as slip planes. In other words, plastic deformation occurs by glide or climb of dislocation along specific slip planes. The slip plane is normally the plane with the highest density of atoms, and the direction of slip is the direction in the slip plane in which the atoms are most closely spaced.

At low temperatures at which diffusion is difficult, and in the absence of a non-equilibrium concentration of point defects, the movement of dislocations is restricted entirely to glide.[479] However, at high temperatures, dislocation can move out of its slip plane by climb. When dislocation moves up one atom spacing out of its slip plane, it is called positive climb, and when it moves down one atom spacing, it is called negative climb. Positive climb can occur by either diffusion of vacancies to or a creation of an interstitial at the line of the dislocation. Similarly, a negative climb can occur by an interstitial diffusion to or a creation of vacancy at the line of the dislocation. Thus, these processes require mass transport by diffusion and hence thermal activation. During plastic deformation, slip occurs in several slip systems. Thus, dislocations moving along one slip plane will have to intersect the dislocations moving along other slip planes. Such intersections result in jogs in individual dislocations, creation of vacancies and interstitial multiplication of dislocations, and dislocation tangles, which are all referred to as "forest dislocations." At a sufficiently high stress, movement of jogs leaves behind a trail of vacancies or interstitials, depending on the sign of the dislocation and the direction of motion.

Several studies on microstructural changes in reactor structural materials under cyclic loading have been conducted during the past several decades to define the microstructure at different stages of strain cycling, and to correlate the microstructure to fatigue ε–N data and fatigue damage. For example, previous studies suggest that the saturation stage is associated with the formation of an equilibrium substructure, which does not change with successive cycling. The results of microstructural studies may be briefly summarized as follows.

During the initial, rapid hardening stage, the microstructure consists of clusters or bundles of dislocations, separated by regions free of dislocations.[480] The substructure during the equilibrium stage depends on the applied strain amplitude. At low strain amplitudes, the dislocation bundles produced during the rapid hardening stage shake down into bundles of fragmented dislocations, whereas a cell structure is developed at a high strain range.[481,482] The saturation cell size increases with either a decrease in strain amplitude or an increase in temperature.[483] In the metals studied, the saturation stress is a unique function of the applied strain range, strain rate, and temperature.[484] The saturation stress and the corresponding cell size are related and are independent of the prior strain history.[485] This relationship appears typical of all wavy slip-mode materials.[486] However, as discussed later in this section, this behavior may not be true in all cases; the saturation stress and substructure may not reverse by decreasing the applied strain amplitudes beyond half-life. The evolution of microstructure during cyclic straining of carbon and low-alloy steels and austenitic SSs is discussed below.

Ferritic Steels

The material microstructure generated in annealed iron by cycling at different strain amplitudes was examined at various fractions of fatigue life after the completion of the initial rapid hardening stage. The micrographs of the substructure that developed during cyclic straining at 0.16 and 0,8% strain amplitudes are shown in Figs. 68 and 69, respectively.[487] Although a sharp and well-defined cell structure was generally seen during the later stages, after about 50% of fatigue life, it was not seen during the early stages. The nature of the cell structure and the dislocation arrangements in the cell walls were observed to vary significantly with continued cycling.

At the lower strain amplitude (0.16%), after 10% of fatigue life, the substructure consists of closely spaced bundles of dislocations separated by regions relatively free of dislocations, as seen in Fig. 68a. The bundles consist of tangled dislocation lines associated with dislocation loops and dipoles. A cell structure starts to form after 40% of fatigue life.[487] The existing

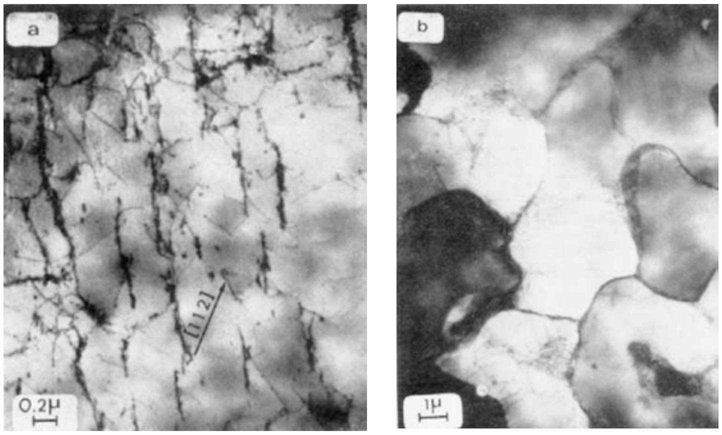

Figure 68. **Dislocation structure of annealed iron cycled at 0.16% strain amplitude to different stages of fatigue life: (a) 10% and (b) 100% (Ref. 487).**

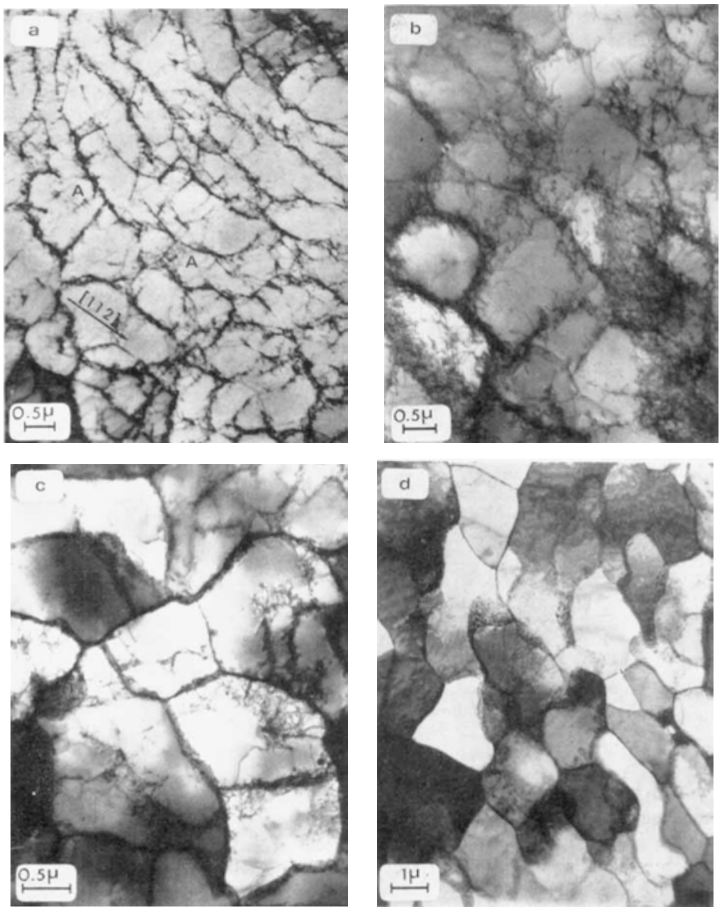

Figure 69. **Dislocation structure of annealed iron cycled at 0.8% strain amplitude to different stages of fatigue life: (a) 3%, (b) 10%, (c) 45%, and (d) 100% (Ref. 487).**

bundles of dislocations break up and the dislocations rearrange into a large-cell structure. Some of the cell walls are composed of dislocation tangles and loops. However, the initial structure consisting of bundles of dislocations can still be seen in some areas. With further cycling, these cells become sharp with no apparent change in the cell size. A well-defined cell structure is observed throughout the specimen. Many low-energy subgrain boundaries made up of cross grids of screw dislocations are also observed. Figure 68b shows a typical substructure produced during the later stages of fatigue life. Although no quantitative measurements were made for the misorientations across the cell walls, the sharp contrasts between neighboring cells indicate the presence of appreciable misorientations between them.

A similar evolution of microstructure is observed during strain cycling at 0.8% strain amplitude. However, a cellular structure forms at an early stage in fatigue life.[487] Figure 69a shows that a semicellular network of dislocations develops at 3% fatigue life. The dislocation walls consist of dislocation tangles with interspersed loops and dipoles. In Fig. 69a, loops appear to be forming from heavily jogged dislocations in the area indicated by A. Since formation of loops is favored at low strain amplitude,[488] the number of loops at 0.8% strain amplitude is smaller than that observed at 0.16%. However, unlike most FCC metals in which dislocation loops are dispersed uniformly throughout the substructure, in the study on Ferrovac E (pure iron), loops were mainly observed in and around the regions of dislocation tangles or cell walls.[487] A more regular cell structure begins to form after 10% of fatigue life (Fig. 69b). No apparent change in the cell size is observed with further cycling, though misorientations develop between groups of cells and the cell walls gradually become sharp and distinct.

The substructure observed after 10 and 50% fatigue life consisted of a cell structure at various degrees of refinement. A homogeneous and well-defined cell structure develops during the later stages of fatigue life. Typical structures observed after 45% of life and after fracture are shown in Figs. 69c and 69d, respectively. Most of the dislocations are present in the cell walls, and the cell size is much smaller than that observed at lower strain amplitude cycling.

The microstructures that developed in A106 Gr. B carbon steel specimens tested at 288°C (550°F), 0.375% strain amplitude, and three different strain rates has also been examined at Argonne.[390] The results indicate that the dislocation structure not only varies with continued cycling at specific strain amplitude but also varies with strain rate. The lower the strain rate, the more mature (i.e., well-established) the dislocation structure. For example, a well-established dislocation structure is not observed at 0.4 %/s strain rate; only diffuse dislocation walls are present. A mature microstructure consisting of dislocation cells, walls, and/or veins with high dislocation density is observed at 0.04 and 0.004 %/s strain rates. The dislocation walls extend across individual cementite plates or particles within a pearlite grain to maintain a consistent crystallographic structure.

The reversibility of the substructure that evolves during cyclic loading has been evaluated.[487] The stress response and microstructure of pure iron specimen cycled at high strain amplitude to 3–45% of its life followed by cycling at low strain amplitude to failure were monitored to investigate the potential effect of the substructure at high strain amplitudes on the subsequent fatigue at low strain amplitudes. The results indicate that the stress response and the microstructure of the material during subsequent fatigue at low strain amplitudes depend on the number of cycles at high strain amplitudes. For example, the cyclic stress response for the specimen that was fatigued at high strain amplitude for 3% of its life and then fatigued at lower strain amplitude was the same as that of a virgin specimen fatigued at the low strain amplitude alone. However, the cyclic stress response for the specimen that was first fatigued for 45% of its life at high strain amplitude was higher than that of a specimen fatigued at the low strain amplitude alone.

The microstructural observations indicate that the reversal of the substructure developed at the high strain amplitude is very slow and continues over the remaining life. A complete reversal of the substructure is not accomplished in the specimen that was fatigued up to 45% of life at high strain amplitude. For that specimen, the substructure is very inhomogeneous and some memory of prior strain cycling is retained even at fracture.

Wrought Austenitic Stainless Steels

A similar evolution of microstructure is also observed during fatigue of austenitic SSs.[489] The cyclic stress versus fatigue cycles response of Type 316NG at room temperature (Fig. 65) consists of a short cyclic hardening stage followed by cyclic softening and ultimately a saturation or stabilized behavior up to failure. Like most other metals, the microstructure of austenitic SSs also changes during cycling straining. At room temperature, the hardening stage lasts less than 1% of life. During this stage, dislocations are arranged essentially in a planar structure. The microstructure is similar to that observed in the as-received condition, except it contains a higher dislocation density and the dislocation interactions are more complex (i.e., more tangled dislocation structure).[489] The microstructure that developed at the end of the hardening stage consists of a uniform distribution of dislocations.

The microstructure observed during the softening stage consists of thick veins or premature walls of dislocations separated by long dislocation-free regions. With continued straining, these thick dislocation veins/walls further developed into better-defined, dense and thin cell walls.[489] In addition, dislocation activity along primary and secondary slip planes may trigger the formation of dislocation walls in different directions, creating a labyrinth structure. The microstructure at mid-life consists of well-defined dislocation walls separated by dislocation-free regions and persistent slip bands. This microstructure represents saturation or steady-state cyclic stress vs. fatigue cycles behavior. The microstructure at end-of-life consists of labyrinth structure and cells. With continued cycling, the cell walls get thinner and the cell size progressively decreases. Overall, the cyclic hardening behavior is associated with an increase in the total dislocation density, and the softening behavior is related to the rearrangement of dislocations into a well-defined cell structure.

3.1.2 Tensile Properties

In general, the tensile strength is increased with increasing strain rate and the strain rate sensitivity increases with temperature. However, there are exceptions for some materials under service and loading conditions where dynamic strain aging (DSA) is likely to occur. The earliest investigations related to strain rate effects on the mechanical properties of metals and alloys date back at least 70 years to the work of Manjoine[490] and Zener and Holloman.[491] Manjoine conducted room-temperature tensile tests on mild steel at 0.00000095–0.03 s^{-1} strain rates. A significant increase in yield stress was observed over the strain rates that are typically associated with strong earthquakes. The yield strength increased from ~270 MPa at 0.1 s^{-1} to 400 MPa at 10 s^{-1}. The corresponding increases in the ultimate tensile strength were lower, from ~410 MPa to 450 MPa. Thus, the yield ratio, defined as the ratio of the yield strength to the ultimate tensile strength, increases with increasing strain rate and the ductility correspondingly decreases.[492–495]

Campbell and Ferguson[496] have observed a similar strain-rate sensitivity for the shear flow stress of mild steel in experiments at temperatures from −78 to 440°C (–108 to 824°F) and strain rates from 0.001 to 0.0004 s^{-1}. The rate sensitivity of the flow stress was found to be a decreasing function of temperature, except at the highest strain rates, at which a large increase in the rate sensitivity was observed, with the flow stress at constant temperature varying approximately linearly with strain rate. The data were interpreted in terms of thermal activation rate theory and the theory of the damping of dislocation motion by phonon viscosity. Qualitatively similar strain-rate sensitivity effects have been observed at room temperature in both torsion and shear loading tests at strain rates up to 3,000 s^{-1} on mild steel, copper, and titanium.[497] The effects of strain rate on the mechanical properties of a number of structural alloys used as pressure boundary materials in NPPs are summarized below.

3.1.2.1 Carbon and Low-Alloy Steels

The yield and ultimate tensile strengths of A508 Cl. 3 and A533 Gr. B ferritic steel generally increase with increasing strain rate, while the ductility decreases or shows little effect. However, limited data suggest a reversal in the yield and tensile strength behavior with strain rate in the region of the normal LWR operating temperatures. For example, at room temperature, the yield and tensile strengths of A508 Cl. 3 steel increase with increasing strain rate, whereas there is little or no change in the elongation and reduction in area. However, at 288°C (550°F), both the ultimate tensile strength and elongation decrease with increasing temperature because of the influence of DSA on deformation and fracture properties.[498] Serrated flow in stress-strain curves was observed between about 140 and 340°C (284 and 644°F) and varied with the strain rate and microstructural condition. The onset temperature of serrated flow for the pearlite-ferrite microstructural condition was lower than that for the as received, tempered martensite condition. The serrated flow range for both microstructural conditions shifted to higher temperatures with increased strain rates. Similar dependence of yield stress on strain rate has also been observed for A533 Gr. B steel.[464] Figure 70 from this work shows yield stress and ultimate tensile strength values determined in round-robin tests over a range of strain rates for 20MnMoNi55 pressure-vessel steel (i.e., A533 Gr. B).

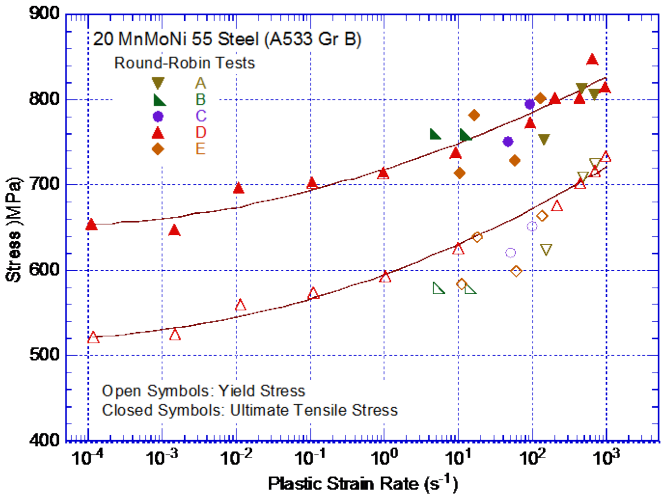

Figure 70.
Results of round-robin tensile tests conducted at various strain rates on 20MnMoNi55 (similar to A533 Gr. B) pressure vessel steel (Ref. 464).

In another study,[499] tensile tests conducted on A508 Cl. 3 steel at 25–400°C (77–752°F) and 0.0000667–0.012 s^{-1} strain rate indicates that the region of DSA is in the temperature range of 250–350°C (482–662°F) at 0.0012 s^{-1} strain rate, 200–300°C (392–572°F) at 0.00012 s^{-1}, and 200–300°C (392–572°F) at 0.0000667 s^{-1}. Serrated stress-strain behavior was observed in these temperature and strain-rate ranges; N played the more important role for DSA than C solute.

The reverse strain rate dependence of tensile flow stress is clearly seen in tensile tests conducted on 20MnMoNi55 (i.e., A533 Gr. B) steel tested at room temperature and 400–600°C (752–1112°F) and strain rates of 0.001–300 s^{-1}.[500] The yield strength and flow stress increase with increasing strain rate at room temperature but the effect is reversed at 400°C (752°F) (Figs. 71 and 72). A similar reversal of strain rate dependence has also been observed in a forged 20MnMoNi55 steel (i.e., A508 Cl. 3) and A533 Gr. B steel at strain rates of 0.0001 and 10 s^{-1}.[501] The results indicate an increase in tensile and yield strengths with increasing strain rate at 25 and 100°C (77 and 212°F) but a reverse effect on tensile strength at 290°C (554°F). The ductility appears to show little effect of strain rate at all three temperatures.

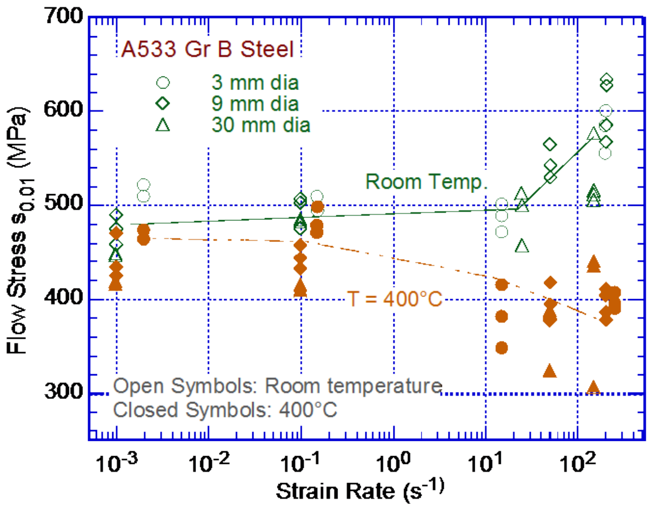

Figure 71.
Variation of yield strength (flow stress at a strain of 0.01) for A533 Gr. B pressure vessel steel with strain rate for three specimen sizes and two temperatures (Ref. 500).

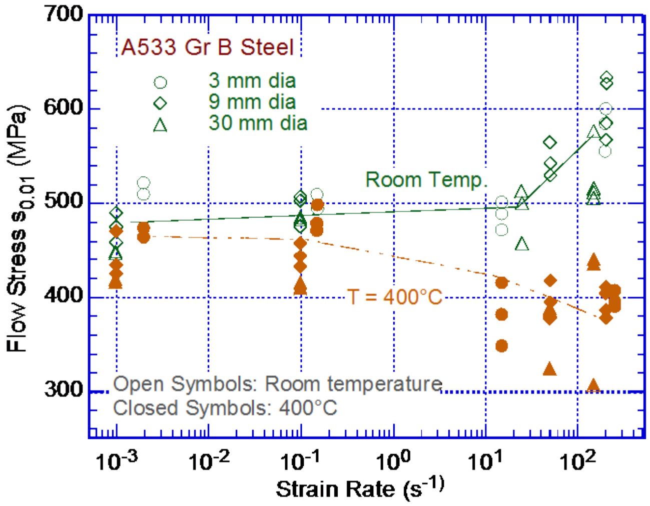

Figure 72.
Variation of ultimate tensile strength of A533 Gr. B pressure vessel steel with strain rate for three specimen sizes and two temperatures (Ref. 500).

3.1.2.2 Wrought Austenitic Stainless Steels

The tensile properties of high- and low-C Type 304 SS have been determined at strain rates from 0.000001 to 1,000 s^{-1} and temperatures from –196 to 1000°C (–321 to 1832°F).[502–511] The results indicate modest increase in yield and flow stress with increasing strain rate, slight decrease in ultimate stress and uniform elongation, and little or no change in the total elongation. At room temperature, the ultimate stress first decreased with increasing strain rate up to 0.1 s^{-1}, and then increased at higher strain rates.[505,506] The variation in yield strength and ultimate tensile strength of Type 304 SS as a function of temperature and strain rate is shown in Fig. 73.[503,509]

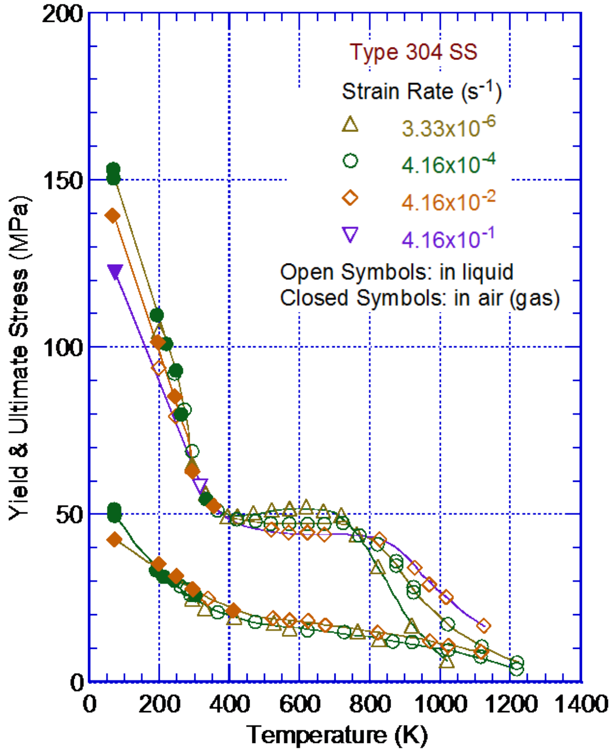

Figure 73.
Temperature and strain-rate dependence of yield strength and ultimate tensile strength for Type 304 SS (Ref. 503).

The deformation behavior of Type 304 SS is controlled by two processes. At low temperatures, the strain-induced transformation of unstable austenite to martensite predominates, and the strain-rate sensitivity is proportional to the transformation rate. At the higher temperatures, slip predominates and the strain-rate sensitivity decreases with increasing strain.[504] Furthermore, the decrease in ultimate tensile strength has been attributed to lesser amount of deformation-induced martensite formation and a greater role of thermal softening due to temperature increase at high strain rates.[508] A similar behavior is also observed for low-C Type 304 SS.[511]

A similar behavior has also been observed for low- and high-C Type 316 SSs.[512–516] Typically, the yield and ultimate tensile strength increase with increasing strain rate and the elongation is decreased slightly. The effect of strain rate on yield strength is much less than on the ultimate strength. For 20% cold-worked material, the yield strength at room temperature in relatively insensitive to strain rate over the range of 0.000033 to 0.033 s^{-1}.[512] Studies on an ultrafine-grained (~2 µm grain size) Type 316 SS in the temperature range of −196 to 950°C (–321 to 1742°F)[513] indicate that the temperature dependence of the yield (0.2% offset) and flow stresses exhibits the following three stages. First, a decrease in stress with increasing temperature up to about 227°C (441°F), followed by a plateau during which the stress is almost independent of temperature up to about 527°C (981°F), and then a continuous drop in stress above 527°C (981°F). The flow stress was observed to increase with increasing strain rate over the range from 0.000044 to 4,400 s^{-1}.

However, there is some indication of a reversal in the strain rate effect on the ultimate tensile strength because of dynamic strain aging at temperatures in the range of 300 to 500°C (572 to 932°F).[514,515] Elongation and reduction of area also appear to increase somewhat with increasing strain rate, though for cold-worked material the opposite effect has been observed. The variation of tensile properties for 17% cold-worked Type 316L SS with temperature for three different strain rates is shown in Fig. 74. The indicated crosshead speeds of 0.2, 2, and 20 mm/min correspond to strain rates of 0.0001, 0.001, and 0.01 s^{-1}, respectively. The strain rate sensitivity in Fig. 74(c) is defined as $d\sigma/d(\ln \dot{\varepsilon})$, where $\dot{\varepsilon}$ is the true strain rate. The dynamic strain hardening stress in Fig. 74(d) is defined as the difference between true ultimate tensile strength and 0.2% yield strength. The temperature regimes in which serrated flow is observed in the stress strain curves for the three different strain rates is indicated by the blue bars in the figures.

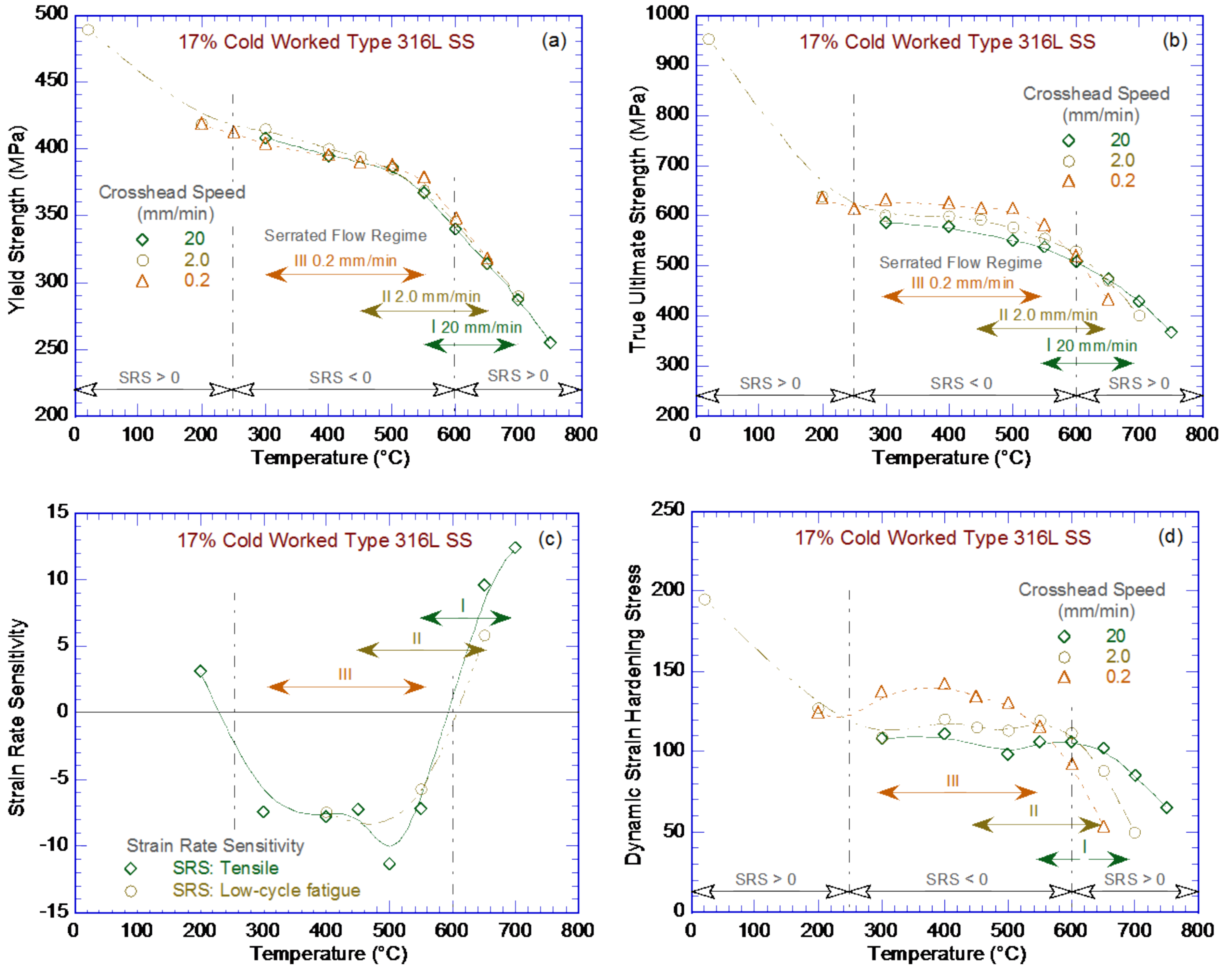

Figure 74. **Variation of tensile properties for 17% cold-worked Type 316L SS with temperature for three different strain rates (Ref. 514).**

However, the reverse strain rate behavior of austenitic SSs may be suppressed by modifying the microstructure and microchemistry of the material. For example, the effects of strain rate sensitivity of Type 316 SS is suppressed by aging the material for 5,000 h at 650°C (1202°F).[516] The serrated flow associated with dynamic strain aging is suppressed apparently because of the precipitation of chromium carbides and the accompanying depletion of chromium and carbon from the grain boundaries, which are preferential sites for dynamic strain aging.

3.1.2.3 Austenitic Stainless Steel Welds

The tensile data for Type 304/308 welds and Type 308 SS weld metal indicate a marked increase in flow stress with increasing strain rate for some welds while others show only moderate increase. In general, the elongation decreases with increasing strain rate for the weld metal. However, most of the data were obtained at temperatures higher than LWR operating temperatures. Tensile tests on Type 308 SS SMA welds[502] at 316–649°C (601–1200°F) and strain rates from 0.00003 to 10 s^{-1} indicate that the tensile properties varies considerably with the weld location (Table 9). In addition, the weld metal has significantly higher yield strength and approximately one-half the ductility of the Type 304 SS base metal, but the ultimate tensile strengths of the two materials were nearly identical. Minor variations in strength and ductility with increasing strain rate are observed over the entire range of test temperatures, but these variations are considered largely within the range of normal data scatter.

Table 9. Tensile properties of Type 308 SS weld metal for various weld locations at 427°C (801°F) and a strain rate of 0.03 s^{-1} (Ref. 502).

Specimen	Stress (MPa)		Elongation (%)		Reduction of
Location	0.2% Yield	Ultimate	Total	Uniform	Area (%)
Near weld surface	292	449	28.8	25.1	52.4
16 mm (0.6 in.) below surface	339	447	20.6	17.1	49.6
25 mm (1 in.) below surface	360	463	22.3	18.8	47.1
Weld center	366	454	19.8	16.7	50.0

Tensile tests at 288°C (550°F) and a range of strain rates on Type 304 SA girth welds[507] exhibit modest increases in the yield and tensile strengths with increasing strain rate (Fig. 75). The welds employed a GTA root pass, followed by two SMA passes, and complete the remaining passes by the SA process using a SFA-5.4 filler metal.

The stress-strain response of Type 304L/308L SS SMA weld joints has also been investigated under compressive loading at strain rates ranging from 0.001 to 7,500 s^{-1}.[517] The test specimens include the weld metal, HAZ, and the original base metal (i.e., composite specimens). The room-temperature stress-strain response (Fig. 76) shows a marked increase of flow stress with increasing strain rate. A similar strain-rate dependence was observed at test temperatures up to 500°C (932°F), though the flow stresses decreased with increasing temperature.[518] Similar tests have been conducted on plasma-arc-welded Type 304L SS joints[519] and GTA-welded joints[520] at room temperature, and the same strain-rate dependence of flow stress is observed.

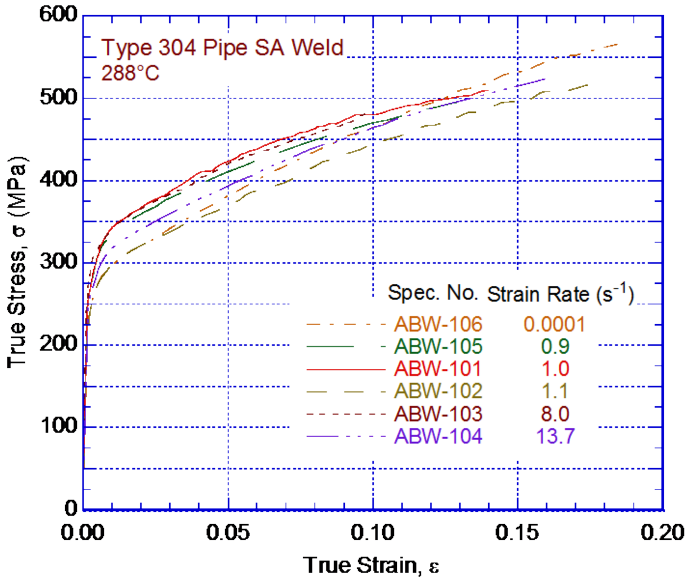

Figure 75.
True stress-true strain curves at 288°C (550°F) for a SA weld in a Type 304 SS pipe at several different strain rates (Ref. 507).

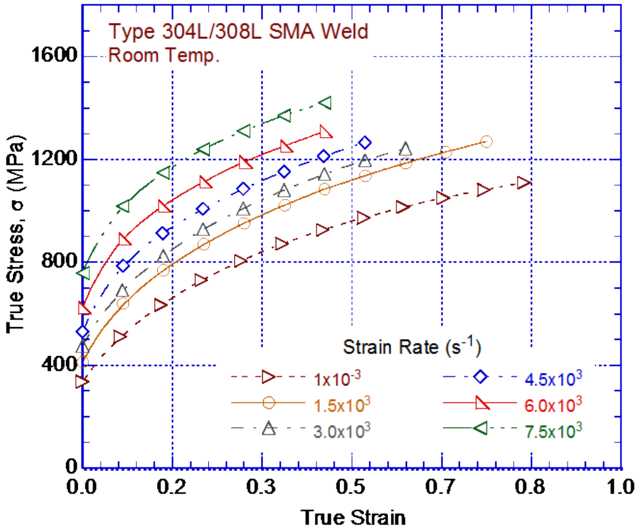

Figure 76.
True stress-true strain curves at room temperature for Type 304L/308L shielded-metal arc weld joints tested at several different strain rates (Ref. 517).

3.1.2.4 Cast Austenitic Stainless Steels

No literature data could be found on the effect of strain rate on the tensile properties of CF-3, CF-8, and CF-8M CASS materials.

3.1.2.5 Nickel Alloys

Most of the tensile properties data on potential strain rate effects on Alloys 600 or 690 have been obtained at very high temperatures (i.e., >500°C [932°F]) or at strain rates that are 2 orders of magnitude higher than those typically observed during a seismic event (i.e., strain rates in the range of 0.1–10 s^{-1}. The tensile properties of annealed and thermally aged Alloy 600 have been determined at temperatures up to 760°C (1400°F) and strain rates up to 1.0 s^{-1}.[521] The results indicate tensile strength and ductility of annealed material are not greatly influenced by strain rate for temperatures up to 538°C (1000°F).

Similarly, the plastic flow behavior of Alloy 690 at room temperature under compressive loading, including impact loading, indicate a modest increase in the compressive flow stress with increasing strain rate in the range of 0.001 to 0.1 s^{-1} and a more dramatic increase at higher strain rates above 1,000 s^{-1}.[522,523] The dramatic increase is attributed to a change in the rate-controlling mechanism from dislocation generation to mechanical twin formation.[523]

3.1.3 Charpy Impact Properties

3.1.3.1 Carbon and Low-Alloy Steels

The tensile data summarized above indicate that, for most of the structural alloys considered, the tensile ductility decreases with increasing strain rate. This behavior raises questions about the possibility of non-ductile behavior of these alloys under the moderately high strain rate loading conditions associated with seismic events. Perhaps the simplest measure of the ductility response of a material under high-loading-rate conditions is provided by Charpy impact test data. Ferritic alloys such as the A508 Cl. 3 and A533 Gr. B structural steels used in nuclear pressure vessel applications undergo a transition from ductile to brittle behavior under impact loading as the temperature is decreased. The associated ductile-to-brittle transition temperature (DBTT) is generally defined as the temperature at which the fracture energy under impact loading falls below 40 J (29.5 ft-lb) for a standard Charpy impact test. The brittle behavior of such materials at temperatures below the DBTT is clearly undesirable for nuclear applications, particularly under seismic loading conditions.

Charpy V-notch impact tests have been conducted on A508 Cl. 3 steel at impact velocities of 5 m/s, 500 µm/s, and 1 µm/s.[524] The results shown in Fig. 77 indicate that the greatest effect of impact velocity is on the upper shelf energy, which increases from ~155 J at a velocity of 1 µm/s to 220 J at 5 m/s. The effect of impact velocity on the DBTT is less clear, with the 40 J DBTT values ranging from approximately −100°C to −75°C (−150°F to −100°F) over this range of velocities. DBTT values in this range are well below anticipated temperatures for an operating or shutdown nuclear power plant. The fracture toughness transition curves data for unirradiated and irradiated A508 Cl. 3 steel (Fig. 78)[525] indicate a DBTT of approximately −40°C (−40°F) for the unirradiated material and 0°C (32°F) for the material irradiated to a fluence of 4.65 × 10^{19} n/cm^2 (>1 MeV). The upper shelf energy for the unirradiated material is noticeably higher.

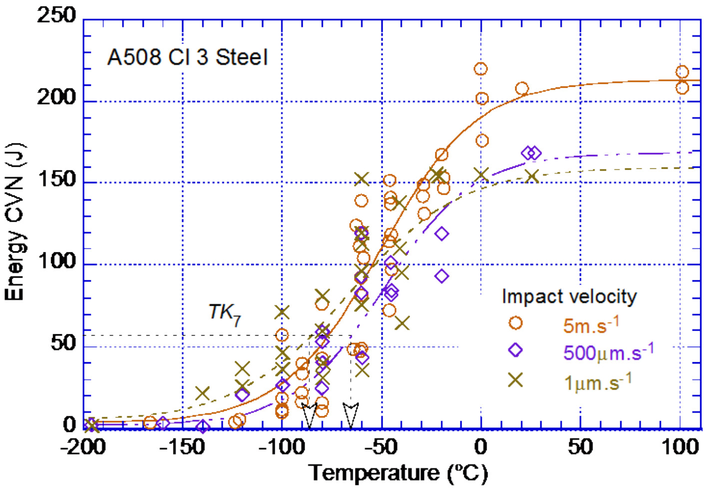

Figure 77.
Charpy V-notch fracture toughness transition curves for A508 Cl. 3 steel tested at three different impact velocities (Ref. 524).

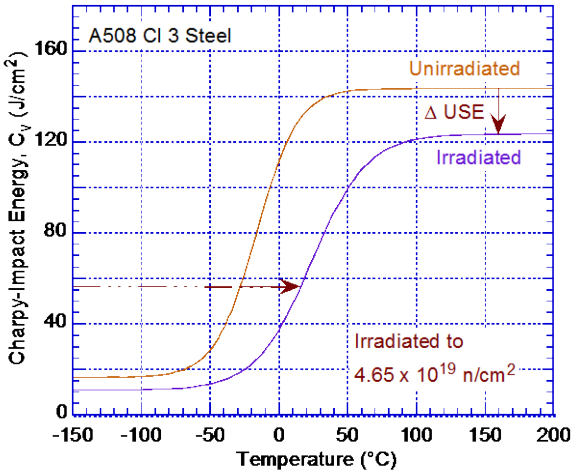

Figure 78.
Charpy V-notch fracture toughness transition curves for A508 Cl. 3 steel in the unirradiated condition and after irradiation to a fluence of 4.65 × 10^{19} n/cm^2 (>1 MeV) (Ref. 525).

The Charpy V-notch and dynamic tear test data for A533 Gr. B steel[526] in the as-received condition and after neutron irradiation to a fluence of 2.8 × 10^{19} n/cm^2 (>1 MeV) at a 288°C (550°F) is shown in (Fig. 79). The results indicate that the DBTT for the unirradiated material is approximately −7°C (20°F) and approximately 104°C (220°F) for the irradiated material. The latter results raise concerns about the susceptibility of this material to brittle fracture in a nuclear plant under cold standby or shutdown conditions. A qualitatively similar behavior is observed for weld-deposited material (Fig. 80); the DBTT increases from approximately −41°C (−42°F) for the unirradiated material to 110°C (230°F) for the material irradiated to a fluence of 2.5 × 1019 n/cm^2.

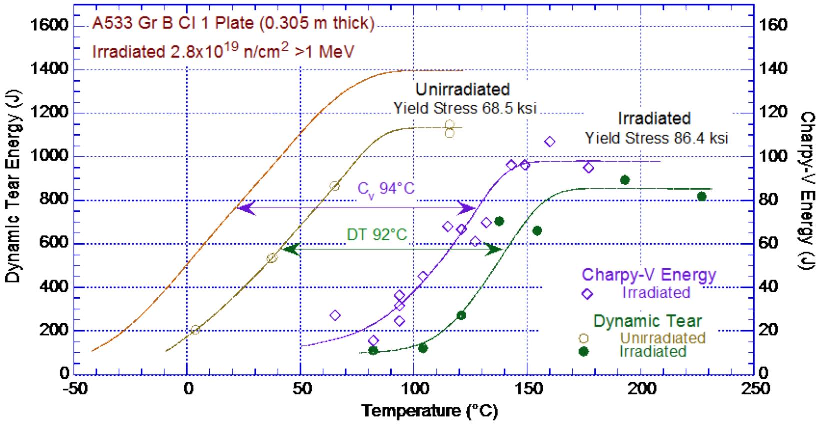

Figure 79. **Charpy-V (Cv) and dynamic tear test data for a 12-in.-thick A533 Gr. B Class 1 steel plate before and after 288°C (550°F) irradiation (Ref. 526).**

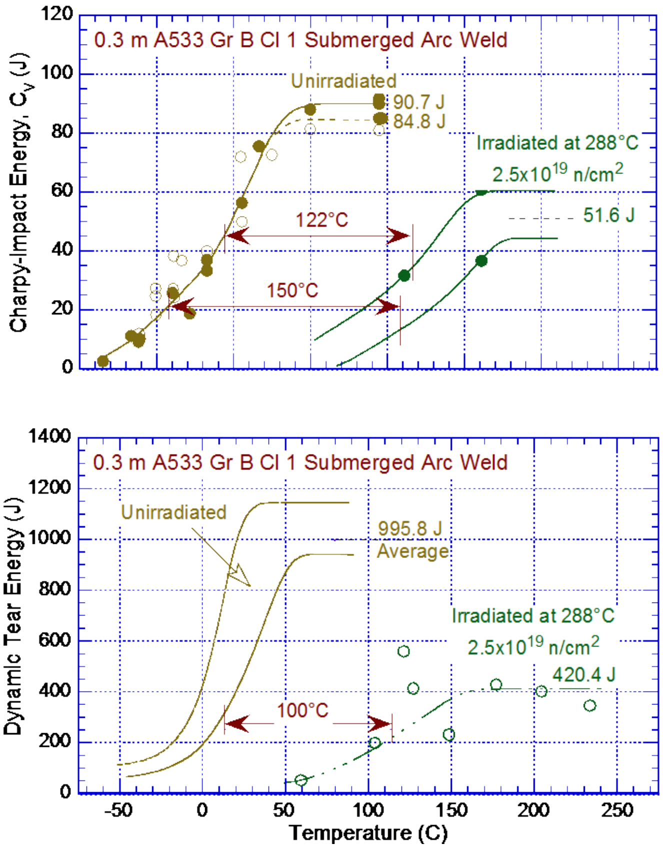

Figure 80.
Charpy-V (Cv) and dynamic tear test data for a 0.3 m-thick A533 Gr. B Cl. 1 SA weld deposit before and after 288°C (550°F) irradiation. Specimens were taken between the quarter- and half-thickness locations with their long dimension perpendicular to the welding direction. (Ref. 526).

Another study reported higher DBTT values for A533 Gr. B steel irradiated at 150°C (302°F) to a fluence of 1.0 × 1019 n/cm^2 (E >1 MeV).[527] The DBTT increased from 88°C (190°F) (unirradiated) to 166°C (331°F) (irradiated) for full-size specimens, from 120 to 203°C (248 to 397°F) for half-size specimens, and from 100 to 170°C (212 to 338°F) for one-third-size specimens. For all these results, note that the strain rate imposed in a standard Charpy V-notch test is considerably higher than that anticipated for seismic loadings.

An international program on the fracture toughness testing of nuclear pressure vessel steels coordinated by the International Atomic Energy Agency (IAEA)[528] investigated the effect of loading rate on the DBTT for A533 Gr. B (Heat JRQ), as shown in Fig. 81. The data for precracked Charpy specimens of various sizes, tested at various loading rates, indicate a steady increase in transition temperature with increasing loading rate. The chain dash curve shown in the figure represents the Wallin model.[529] The temperature dependence of absorbed energy in Charpy impact tests on A508 Cl. 3 and A533 Gr. B pressure vessel steels under dynamic and quasi-static loading conditions is shown in Fig. 82.[501] The results show that the difference between the dynamic and quasi-static DBTT for these two steels is relatively at room temperature or lower temperatures.

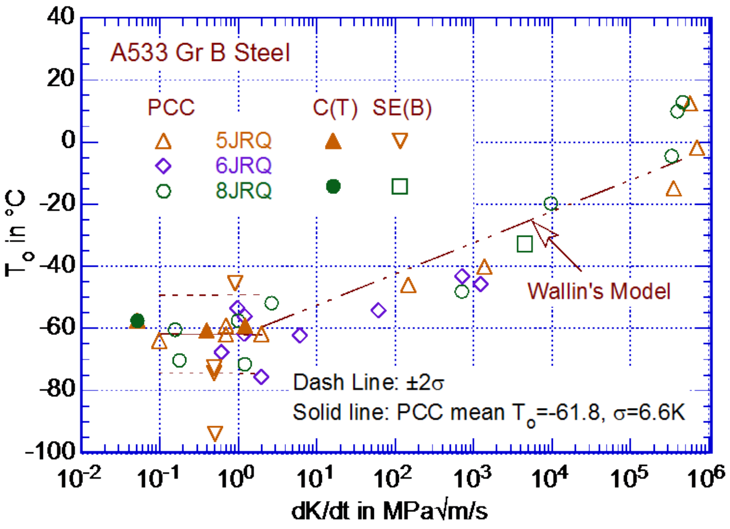

Figure 81.
Effect of loading rate on the DBTT of A533 Gr. B steel (Ref. 528).

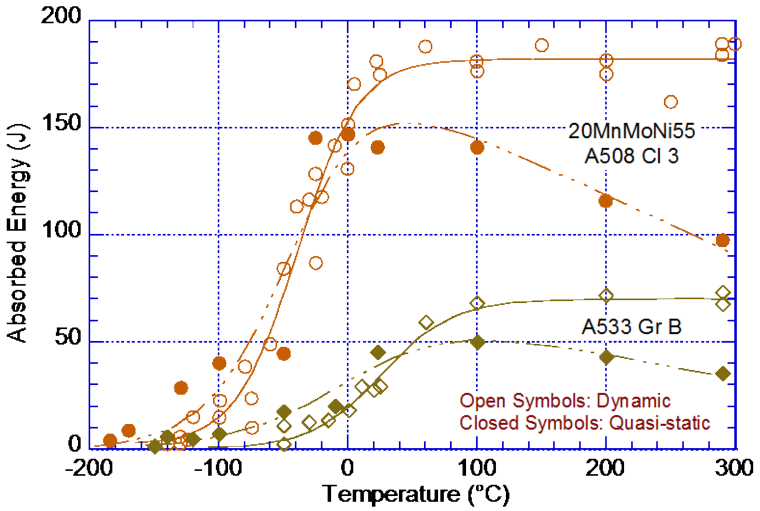

Figure 82. **Effect of loading rate on the ductile-to-brittle Charpy transition curve for A508 Cl. 3 (20MnMoNi55) and A533 Gr. B (JSPS) pressure vessel steels (Ref. 501).**

3.1.3.2 Austenitic Stainless Steels and Nickel Alloys

In general, a well-defined ductile-to-brittle transition is not observed for the austenitic SSs or nickel-base alloys. However, such behavior may be seen in duplex SSs and weldments or in material that has been subject to neutron irradiation. Figure 83 shows the ductile-to-brittle transition behavior of Type 308 SS filler metal in a 12-in. Type 304 SS Schedule 100 pipe weld.[344] The material was tested in the as-received condition and after aging for 7,700 or 10,000 h at 400°C (752°F). The DBTT for these materials is subject to the same loading rate effects as described above for the ferritic pressure vessel steels.

In summary, the Charpy impact data for A508 Cl. 3 and A533 Gr. B pressure vessel steels indicate either little effect or an increase in the DBTT with increasing loading rate. Neutron irradiation clearly increases the DBTT, and Type 308 SS weld filler metal appears to be increasingly susceptible to brittle fracture with elevated-temperature aging.

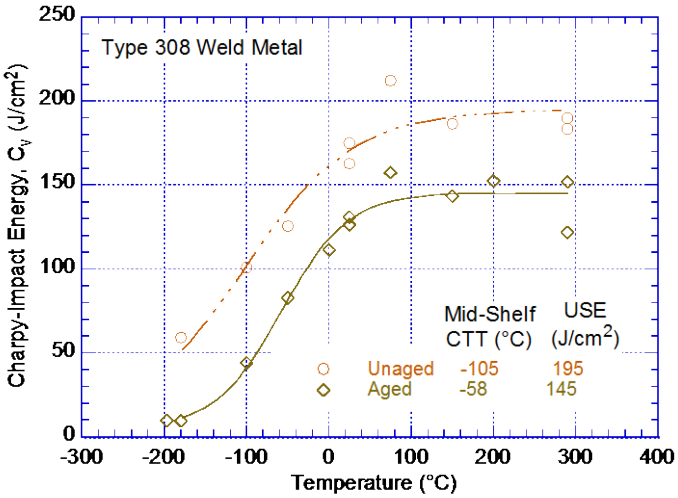

Figure 83.
Effect of thermal aging on the ductile-to-brittle transition temperature for Type 308 SS weld filler metal in the unaged condition and after aging for 7,700 h at 400°C (752°F) (Ref. 344).

3.2 Common Forms of Corrosion

Corrosion affects the crack initiation and propagation behaviors and fatigue life of structural alloys, and this effect is usually deleterious.[530–532] It is well established that the SSs, as well as a number of other metals and alloys, owe their corrosion resistance to the spontaneous formation of a thin adherent protective surface oxide film, as discussed in Section 2.2.1. It follows then that the breakdown or modification of this passive film greatly increases the susceptibility of these metals and alloys to localized corrosion and SCC. One possible cause for film breakdown and consequent loss of passivity is film cracking and rupture due to tensile or cyclic stresses (see Section 2.2.1.4), as may occur during seismic loading; a number of studies have been conducted on passive film breakdown under mechanical loading conditions. Film rupture not only depends on the metal-oxide bond but also the strength, elasticity, and plasticity of the oxide lattice as well as the underlying metal. Unfortunately, studies specifically on oxide film rupture have not been conducted under conditions similar to an LWR environment. Numerous studies have been conducted on SCC under conditions similar to operating reactor environments, but the focus has been on the failure of the underlying metal rather than on the passive oxide film.

3.2.1 General, Pitting, and Crevice Corrosion

Localized pitting and crevice corrosion can produce sites for the initiation of fatigue cracks and stress corrosion cracking, and the presence of a corrosive environment at a crack tip has commonly been shown to accelerate crack growth. On the other hand, the effects of repeated cyclic loadings, as by seismic events, on the corrosion behavior of materials have been much less thoroughly investigated. Seismic cyclic stresses can potentially disrupt protective surface films with the potential to increase the susceptibility of structural alloys to pitting and crack (crevice) formation and thereby accelerate general or localized corrosion. On a micro-scale, these same cyclic stresses can produce localized plastic deformation and residual tensile stresses in the metal substrate that may promote crack initiation and growth either through the process of fatigue or SCC. In addition to the examples discussed in Section 2.2.1.4 and later in this section, residual stresses have been shown to promote pitting in ferritic pipeline steels[138] and in Type 304 austenitic SS.[135] Seismic loadings can also potentially influence the diffusion of corrosion-controlling species, through passive film modification, and the formation of grain boundary precipitates, particularly with respect to the interstitial elements C, N, O, and H.

Most crack propagation models involve the rupture of the oxide film (see Section 2.3), such as at a crack tip, followed by metal dissolution and passivation of the bare metal by the nucleation and growth of an oxide film. This process of oxide rupture and repassivation is cyclical, eventually leading to failure of the metal component. Jivkov[533] has modeled stress corrosion crack nucleation and growth in materials with a passive surface film. His model incorporates three physical processes that affect the surface film, namely, dissolution, passivation, and straining, and he notes that active mechanical loading is an essential prerequisite for continued corrosion cracking. The basic crack growth mechanism is essentially one of localized dissolution at the crack tip, with the imposed stresses exposing new material for the dissolution process and passivation continuously attempting to restore the ruptured film. The cyclic load imposed by a seismic event, even a small one, could provide the necessary stress to rupture a passive film at a crack tip or other location that experiences the imposed shock.

However, rupture of the passive film is not necessary to affect metal corrosion. As shown in Section 2.2.1.4, residual stresses and stresses applied to the underlying metal substrate enhance corrosion. Similarly, one might expect that localized residual stresses and strain hardening from external mechanical loading caused by seismic low-level seismic events could enhance localized passive film modification and/or breakdown and corrosive attack.

One of the conditions necessary for SCC to occur is the presence of tensile stresses, most commonly in the form of residual stresses. Fatigue crack growth is also enhanced by the presence of tensile residual stresses. Thus, to the extent that the plastic deformation associated with seismic loading promotes the creation of tensile residual stresses in structural alloys, these loadings facilitate degradation through corrosion (i.e., SCC) and fatigue crack growth.

Several investigators have alluded to the role of seismic loadings in creating residual stresses. Ikeda and Mahin[534] refer to the “complex distribution of residual stresses” produced by cyclic seismic loadings. Both Andresen et al.[535] and Ahn[536] state that residual stresses produced by seismic-related impact damage are a potential driver for SCC in waste packages used for long-term nuclear waste storage. However, none of these investigators provide direct experimental observations of corrosion or SCC resulting from seismically induced residual stresses. Nonetheless, it is clear that plastic strains produced by any process from seismic activity are likely to result in localized tensile residual stresses that can facilitate corrosion in susceptible materials.

Pitting corrosion itself has been extensively investigated, and several comprehensive reviews exist which may be consulted for details on the commonly accepted views on this topic.[537-540] Hakkarainen[541] provides a limited review of pitting in the presence of microbial corrosion. No specific review or separate consideration in these and other publications explicitly addressed the significance of seismic activity in relation to the kinetics of pitting. As such, the current discussion and assessment are based on relating the processes, factors, and characteristics of pitting, as well as major operational and material conditions in service, to the likely influence of seismic activity in general.

Additional static or dynamic stressing, especially at local stress concentration points created by pitting due to the seismic activity, increases the potential for mechanical damage or disruption of the normally passive oxide films or adsorption layers and the less protective corrosion products in the vicinity of active pits. This disruption will enhance or re-initiate electrochemical reaction rates at such locations, including any emergent second phase particles, grain boundaries, or dislocations which would typically be anodic sites for localized corrosion.

For example, the influence of macro-stresses on pitting was investigated by Chastell et al.[542] on a tempered martensitic SS in aqueous solution containing hydroxide and chloride ions. They reported the pitting susceptibility to be strongly dependent on the surface stress. This dependence was rationalized in terms of the mechanical properties of the corrosion films/products, plastic deformation and high dislocation density, and localized breakdown of protective layers. They also noted that macroscopic plastic deformation has been shown to influence the pitting susceptibility of austenitic and martensitic steels, relating it to the localized breakdown of films followed by anodic dissolution of the unprotected substrate; the latter continuing to occur as a result of the development of a non-re-passivating or non-film-forming condition local to the pit, combined with the effect of stress and plastic deformation on hydrogen solubility. The influence of macro residual stress on the occurrence of pitting preferentially at tensile stress locations and its influence on stress concentration, as well as SCC initiation in pipeline steel, were also confirmed by Van Boven et al.[543] They used a static aqueous test environment simulating a soil condition but without any microbial presence.

While the majority of pitting corrosion investigations in the past have utilized conventional electrochemical methods, their major limitations in measuring the kinetics of heterogeneous and localized electrochemical processes, critical in pitting, have not been fully appreciated or addressed until recently. This limitation also applies to the effect of applied stress on passive materials for pitting sensitivity.[544] Oltra and Vignal[544] used local probe techniques and showed that pitting sensitivity is influenced by the micro-stress gradients and were able to relate it to a mechanical parameter characterizing the scale of the gradient and the average stress within the test area. A more recent investigation on the effect of loading resulting in the peak stress above the material yield strength demonstrated that (1) plastic deformation increases the metastable pitting initiation rate and promotes the growth rate of larger pits, and (2) high stress excursions increase the product of the pit depth and the current density inside the pit, thereby decreasing the threshold potential for stable pitting corrosion.[545]

Similarly, Nickel et al.[546] investigated the effect of strain localization on corrosive attack; their study demonstrated that heterogeneous distribution of microstrains and an increased dislocation density are the controlling microstructural features. Their results showed deformation localizations to impart an enhanced pitting susceptibility, and, regardless of the material condition, dissolution of complete grains was observed to start and stop at primary precipitates predominantly located at the grain boundaries. In this case, however, easier pit initiation was associated with more homogeneous and shallow pit propagation.

The above observations regarding the role of mechanical factors in impacting the pitting propensity has implications for response to seismic activity. The following additional point concerning the role of seismic activity in relation to the pitting corrosion may be noted. In some cases, depending on the wall thickness and loading conditions, an existing pit can lead to cracking at the geometric stress concentration location of the pit base. The initiation and growth of such a crack will be exacerbated by the recurring seismic activity. The location-specific significance and severity of such synergistic damage has not been fully assessed either at the design stage or in the aging degradation management programs. This aspect should be evaluated further for long-term operation, especially where seismic activity may be more frequent and significant.

3.2.2 Flow-Accelerated Corrosion

Wall thinning due to FAC reduces the margin to failure for a component under seismic loadings. In addition, any factor that reduces the stability of the oxide film on carbon and low-alloy steel surfaces will enhance FAC. Based on this assessment, a review of the OBE, mechanistic considerations, and engineering judgment related to the degradation mechanism of FAC, several issues and gaps in understanding the possible impact of seismic activity on FAC are identified.

The EPRI guidelines for managing FAC degradation in NPPs[12] incorporate a “Long-term Strategy” according to which the program focus should be on reducing FAC wear rates without which the number of needed inspections will increase with service time, and even with selective repair and replacement, the likelihood of a consequential leak or rupture may increase with service time. The likely impact of seismic activity, however, even if intermittent, is to enhance the prevailing FAC rates, as discussed below.

Seismic activity, in general, is not limited to an OBE event that is used as a guide for design purposes. In addition to increased or altered loading/deformation of SSCs during such a seismic activity, the fluid flow patterns are expected to be altered and produce different local disturbances. These effects in turn lead to fluid-structure interaction (FSI) and structural vibrations or excitations likely to affect the mechanical integrity of normally formed corrosion products. As such, seismic-related disturbances in flow and FSI may also contribute to enhanced FAC during other events likely to occur below OBE levels.

As noted previously, for a given set of susceptible component materials and water chemistries, FAC is mainly governed by the flow velocity/turbulence affecting the boundary layer (between the fluid and the oxidized surface) and by the solubility limit of the dissolving ions under the prevailing operating conditions at the interface. Near-wall turbulence, shear stress due to flow characteristics, and the local mass transfer coefficient are known to be the significant factors affecting actual FAC rates and not the bulk or section-averaged flow velocities, per se. The resulting action can lead to complete removal or uneven film thickness reduction, locally, where the flow pattern has a sudden change of character near the wall. The flow-induced fluid dynamic forces can destroy protective (oxide) layers, at least locally. Changes in flow characteristics can affect the local concentration of the soluble iron species from its original stabilized level at or near the applicable saturation limit. In addition, the integrity of the boundary layer itself is likely to be impacted by the dynamic loads and/or FSI resulting from the seismic loads and/or flow changes (wall-shear). As the stable boundary layer (next to the component surface) is disturbed, the turbulence increases the oxide dissolution rate, leading, in turn, to reduced oxide thickness and its protective quality.

Thus, flow instabilities leading to (locally) chaotic and highly turbulent flow conditions and increased debris or loose corrosion products are two consequences of the flow pattern disturbances during and following seismic activity, which would alter the FAC kinetics and thereby have an adverse impact on the passive oxide layer and the underlying metal through the enhanced mass transfer factor of the FAC mechanism.

Other points concerning the role of seismic activity in relation to the kinetics of FAC may be noted as follows:

- In the case of two-phase (water-steam) environments, the mass transfer rate, thus the FAC rate, is affected by the (local) steam quality (void fraction) which may change during the sudden change of flow characteristics during/following OBE or sub-OBE events.

- During or following an earthquake event, the plant is likely to operate at lower than normal operating temperatures for longer periods than otherwise. The implication of this is that some FAC locations will be subject to enhanced FAC rates during some time of the operating cycle, relative to the normally expected FAC rate.

- FAC is not of concern, even for carbon steels and low-alloy steels, in the case of a dry steam flow environment. Although the possibility of changing flow conditions (temperature, pressure, and velocity) causing a dry steam environment to become wet cannot be completely excluded, it seems unlikely that such a temporary change would be a significant contributor to the FAC in these locations where normal conditions do not cause any FAC.

- Because of repeated earthquake events over time, the metallurgical and microstructural changes of the underlying carbon steel or low alloy steel are likely to occur due to the high straining rates. As discussed earlier in Section 3.1.1.2, these changes include an increase in vacancies, dislocations, and related structure-deformation interactions. Also, since the operating temperatures associated with the high strain rates are in the range of dynamic strain aging (DSA) in these materials, the likelihood of enhanced diffusion and resulting compositional changes (at or near the metal-oxide interface) exists. FAC kinetics is known to be sensitive to chromium, molybdenum, and copper contents.[547] At present, there is insufficient data or assessment to ascertain the significance, if any, of these expected microstructural and metallurgical changes on the FAC rate.

3.2.3 Microbiologically Induced Corrosion

As with FAC, wall thinning due to MIC reduces the margin to failure for a component under seismic loadings. Likewise, any factor that reduces the stability of the passive film on component surfaces could enhance or be enhanced by MIC. To the extent that the deformations associated with seismic loadings contribute to this destabilization, they have the potential to contribute to this corrosion process.

No specific review or separate consideration was found in the literature that explicitly addresses the significance of seismic activity in relation to the kinetics of MIC. As such, the following discussion and assessment are based on relating the processes, factors, and characteristics of MIC summarized in Section 2.2.3, as well as major operational and material conditions in service, to the likely influence of seismic activity in general.

If sections of piping or other components of water systems that become, or remain, entrapped with stagnant water during or subsequent to a seismic event, or are subject to intermittent shutoff of flows, then the potential for MIC is enhanced in these sections. Identification, elimination, or monitoring of such locations should help as a preventive measure. According to an earlier study concerning MIC in NPPs,[162] the SRB do not appear to be the most prevalent bio-contributors, and conditions of intermittent flow appear to be more damaging than stagnant or low-flow conditions. The latter was attributed to the resulting removal of non-protective (sulfide-rich) films otherwise present under stagnant flow; also noted was the accelerated (or re-initiated) MIC of ferrous alloys after removal of tubercles. In both these cases, the cause of enhanced MIC was attributed to the intermittent exposure of the underlying (degraded) areas until the film structure is re-established.

One of the environmental stressors during a seismic activity of sufficient magnitude is the agitation of an otherwise stagnant flow condition. Wen et al.[548] confirmed that a mild flow agitation enhanced the cell growth and MIC in the case of SRB-influenced MIC of carbon steel, probably because the cells benefited from enhanced nutrient distribution and mass transfer of corrosion products; this observation also was contrary to the conventional belief that a stagnant fluid condition is more damaging to MIC. The results of Beyenal and Lewandowski[141] also confirm that the production rate of hydrogen sulfide increased with the flow rate at low flow rates (below about 4 feet per minute), while the production rate of hydrogen sulfide was limited by the metabolic activity in the biofilm itself above that limit. While the stagnation of water is generally associated with the propensity for MIC, it has been recognized that the intermittent flow condition is also detrimental, if not more so.[145] This aspect of flow condition is expected to be influenced by the seismic activity and any related plant shutdowns in two ways: (1) by adding times of intermittent or changing flow conditions and (2) by a likely increase in the duration of no flow.

Another environmental stressor during seismic activity is related to the induced vibrations that can affect the bacterial growth kinetics. For example, under the controlled conditions of an experimental setup, a vibrational acceleration-induced increase in the bacterial growth rate was observed.[549]

In some cases of MIC, the formation of tubercles has been noted, which provides some measure of protection to the anaerobic conditions required for the SRBs, even when the nominal (bulk) water is oxygenated. The resulting iron removal from underneath the biofilms contributes to the growth of tubercles. If the tubercles are damaged or removed, without the removal of iron-oxidizing microbes, under any mechanical action, such as due to external loading or scrubbing, then the fresh metal exposed to the bulk water can re-initiate an accelerated corrosion rate and damage.[145]

The structure and nature of biofilm act to support localized areas of electrochemical (corrosion) cells, which are also separated from the anodic areas typically under the active parts of the biofilm. In this case, if anions such as chloride are present or carried into the MIC regions due to upset conditions (either in the operation or in the fluid flow content), then these will enhance the rate or re-initiation of local corrosion, including pitting. Unlike the metal oxide films that are stable and reach a steady state in a given environment, the microbial films are dynamic and subject to environmental stressors leading to changes due to the influence of metabolic and cell growth response. Such changes can cause short-term local fluctuations in the electrochemistry at the biofilm interface, potentially initiating or enhancing the rate of localized corrosion under the film sites.

Furthermore, the corrosion product films underneath the microbial colonies are different from the usual abiotic oxide films, in part due to the local chemical environment under which the products are generated (e.g., iron sulfide). These are generally not as protective of the metal as the abiotic products; also, the stability and strength of these corrosion products are inferior. Thus, the oxide film is likely to be readily disrupted under seismic loading conditions of energetic waves and/or enhanced local straining. In addition, likely delay in re-formation of these films will maintain the higher corrosion rate under the new local chemistry conditions with an exposed fresh metallic surface under the biofilm control.

MIC susceptibility is also influenced by external (abiotic) factors near the biofilm and alloy interface, such as the material microstructure,[159,550–556] grain boundary and surface chemistry,[557] and alloying elements.[157,558] Also, the significance of mechanical stress and deformed/distorted crystal lattice structures in influencing the interaction of corrosion products, such as the iron-sulfide layer, with the biofilm activity was noted in the experimental simulation of SRB-induced biocorrosion,[559] and in relation to the residual stress and cold work conditions.[560]

Some of these external factors will be impacted by the seismic activity on an intermittent but repetitive basis. In general, the enhancement or potential for preferential susceptibility to MIC because of these factors seems to be related to the preference of biofilm development and stability at apparently anodic sites. It is known that the formation rate and cell distribution of biofilms are influenced by both the chemical and electrochemical characteristics of the metal substratum.[558] In turn, the reactions within the biofilms can control the type and kinetics of the resulting MIC.

The near-surface microstructure and surface roughness,[561,562] or material surface characteristics in general,[551] have been found to influence the initiation (or preferential location) and kinetics of the MIC. This influence may be a result of the scale of heterogeneity being of the same order as the scale of microbes or biofilm thickness, and the likely variation or role of surface free energy. Grain boundaries and weld regions (microchemistry and roughness at surface) appear to provide a significant driving force for preferential attraction and growth kinetics of MIC, as locally anodic sites/areas, which would indicate that processes contributing to the changes in roughness, chemistry, and structure of surfaces at the micro scale (i.e., micro-heterogeneities) can change the re-initiation and growth kinetics of MIC.[557,563]

Other points concerning the role of seismic activity in relation to the kinetics of MIC may be noted as:

- During an earthquake event, although the (protective) oxide-to-metal interface may not be completely destroyed (in locations of prior roughened surface areas), it is to be expected that the mechanical integrity of the oxide, as well as that of the less protective biotic corrosion products under the biofilm areas, will be adversely impacted due to added energy/load transfer under seismic activity.

- As a result of repeated earthquake events over time, the metallurgical and microstructural changes of the underlying structural steels are likely to occur due to the high straining rates. These changes include increase in vacancies, dislocations, and related structure-deformation interactions. Also, since the operating temperatures associated with the high strain rates are in the range of DSA in these materials, the likelihood of enhanced diffusion and resulting compositional changes (at or near the MIC interfaces) exists. At present, there is insufficient data or assessment to ascertain the significance, if any, of these expected microstructural and metallurgical changes on the MIC rate.

- The combined effect of aging of the existing biofilms and loadings during seismic activity may be not likely sufficient to cause complete detachment from the substrata, but may be sufficient to cause shedding of weaker parts of the biofilm matrix. This would potentially lead to quick re-growth replacing the weaker parts with a stronger biofilm.

- Actual biological response of the microorganisms to seismic activity, in particular their metabolic response, is not known whether this is to increase or decrease the rate of production of species participating in electrochemical (anodic or cathodic) and chemical reactions at the active sites.

3.3 Stress Corrosion Cracking

From the phenomenological and mechanistic considerations of the forms of SCC (IGSCC, TGSCC, and PWSCC) discussed in Section 2, as well as from a general overview of the related literature, it is clear that several factors and their interactions are responsible for all of these SCC types. These factors were broadly categorized as environmental (water chemistry, ionic conductivity, electrochemical corrosion potential, and temperature), material (microstructure, composition, hardening, and cold work condition), and mechanical (stress, strain, and strain rate) factors. Their interactions are reflected in the repassivation, interface (or corrosion film) damage, microcracking, and deformation/dislocation processes, mostly acting locally near or ahead of the damage or crack front. As such, it is useful to relate the potential impact of seismic activity with reference to these factors and interactions, as discussed below, even though the detail mechanism(s) by which any form of SCC damage develops has not been clearly confirmed or universally accepted. Furthermore, to facilitate the linkage between seismic actions and the kinetics of SCC, several of the observations and mechanistic considerations are briefly discussed first with reference to the underlying phenomena (or effects). These considerations are generally applicable to all forms of SCC of primary interest to the LWR applications.

The overall mechanistic basis for SCC that involves the film-rupture (in the broader sense of the disrupting or damaging impact of mechanical loading on the protective interface) can be briefly illustrated by the schematic representation shown in Fig 84. The surface film is considered a brittle oxide that grows preferentially along grain boundaries creating a locally weak region, which fails under stress, thus advancing the SCC front. In Fig. 85, stress is considered to cause a local deformation with dislocation interactions (slip) rupturing the otherwise protective corrosion film.

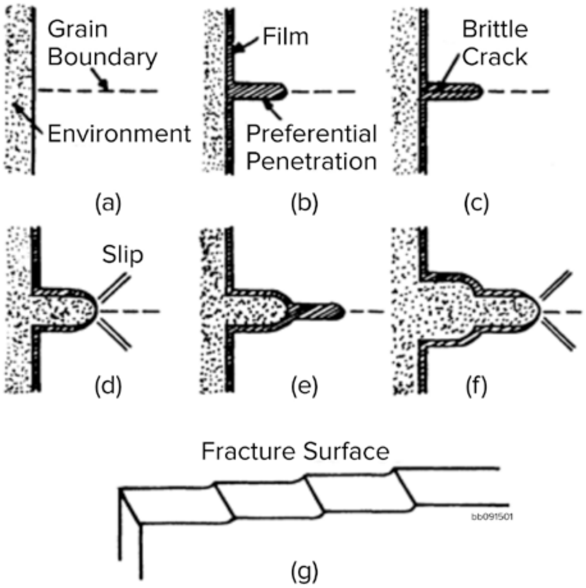

Figure 84.
Schematic representation of film-rupture mechanism for the stress-assisted IGSCC (Ref. 564). Reprinted with permission from NACE International.

3.3.1 Effects of Interactions between Material, Environment, and Mechanics on SCC

Corrosion, by definition, involves oxidation (in the electrochemical sense). Its extreme localization leads to the development and growth of a fine but limited network of cracks (along grain boundaries or along specific crystallographic planes), which is necessary for SCC. This localization is driven primarily by mechanical factors (stress, strain rate) and microstructural effects. In the case of nominally ductile alloys in LWR service, the main effects are related to the anodic dissolution response with a possible modifying role played by the related hydrogen evolution. As a result, the significant effects are mostly related to the local deformation and diffusion processes as affected by the stress and corrosion at the operating temperatures.

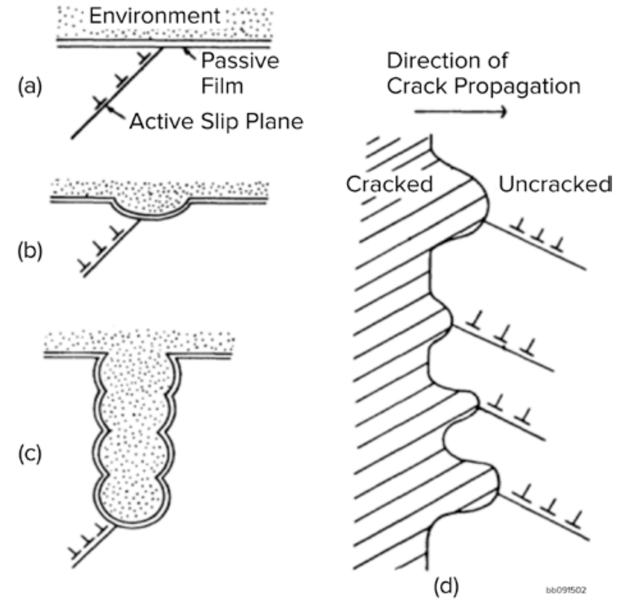

Figure 85.
Schematic representation of film-rupture mechanism for the slip-dissolution model of SCC (Ref. 564). Reprinted with permission from NACE International.

These processes are thermally driven, and the gradients in stress, temperature, and compositional concentrations including vacancies and dislocations play a role at the local level (near the environmental interface of the SCC). These effects are broadly considered below as: creep, DSA, strain localization, and hydrogen.

Since internal oxidation and slip-based deformation are often invoked as basic or alternate steps in SCC, it is of interest to note a few observations from a recent study of detail high-resolution microstructural examinations, as reviewed in light of various mechanisms:[565] "Austenitic SSs and Ni alloys have the same crystal structure and exhibit similar mechanical properties. However, the oxidation behavior is different. Alloy 600, for example, exhibits only very shallow surface oxides, about one order of magnitude thinner than Type 304 SS. However, grain boundaries in Alloy 600 will oxidize to a much greater depth. Since observed CGRs at PWR conditions are similar, either initial IG oxidation rates are similar or IG oxidation does not play a crucial role. Fracture surfaces are observed to have a step-like structure, suggesting that some nanoplasticity has occurred as the crack advances. The step patterns on the fracture surfaces suggest that slip plays a role in the formation of the crack. It is possible that slip leads to crack advance or it could be responsible for crack opening. Alternate slip could lead to both (crack advance and crack opening) at the same time." These pertinent observations seem to emphasize the role of local plasticity in the initiation and growth of SCC process in the LWR material-environment systems of interest.

3.3.1.1 Creep Effects

The well-known work that established the susceptibility of Alloy 600 to IGSCC in high-purity water – before the material saw its large-scale adoption in nuclear reactor systems – has been attributed to Coriou et al.,[566] who were also the first to suggest that creep (strain rate) plays a significant role in the SCC of this material-environment system. Prior to that work, the classical summary by Logan[567] established the significance of creep in relation to SCC, in general. Subsequent works[568,569] and a summary for the LWR-specific IGSCC and PWSCC[570] also confirm this role of creep deformation and resulting strain rates in causing and maintaining the slow growth phenomenon of SCC. It also implies that at the microstructural level, provided sufficient level of stress is present, the diffusion (of vacancies and interstitials) and dislocation processes have a major impact on the SCC kinetics (e.g., Refs. 571 and 572). These processes can also be affected by the type of loading due to seismic activity of interest to this work.

The role of vacancy generation (as a result of anodic dissolution and essential cation migration), its interaction with the motion of dislocations and interstitials, and the resulting local plasticity (creep) seem to fit well with the expected corrosion-deformation interaction responsible for the SCC.[573] This has been well summarized, for example, by Jones[574] and by the selective dissolution-vacancy-creep (SDVC) model.[575] The SDVC model is based on the idea that the formation of vacancies contributes to crack growth via their accumulation in the near-surface layers and subsequent general diffusion, which causes significant changes in the defect distribution and local microstructure. Vacancies interact with crack tip dislocations and, together with applied external loads, lead to passive film breakdown at the crack tip with repeated selective dissolution, vacancy generation, deformation cycles. As such, the SDVC model complements the strain-based rupture of the film with that due to the possible accumulation of vacancies in the (local) near-surface layers and subsequent (diffusion-based) processes in the metal ahead of the SCC damage.

3.3.1.2 DSA Effects

Dynamic strain aging is essentially a form of repeated interaction of dislocations with interstitials (typically, nitrogen and carbon under LWR temperatures) that results in incremental changes in stress-strain or inelastic straining. This repeated action takes place in a range of temperatures and strain rates dependent on the material composition, and it can be expected to occur within a local region, for example, in the vicinity of a crack. In principle, the conditions for DSA need not be globally present for its manifestation. This phenomenon has also been called jerky flow,[576] serrated yielding/flow,[577,578] and the Portevin-LeChatelier effect,[579,580] which accompanies an enhancement in the rate of dislocation multiplication and dislocation motion, thereby also affecting the strain hardening response. As such, the phenomenon contributes to the local and non-homogeneous deformation that is known to increase the SCC susceptibility. The DSA phenomenon has also been observed in austenitic SSs,[577] in addition to the Ni alloys[578–580] and Alloy 600.[576] These observations on the jerky flow and solute interactions in Alloy 600 and Ni-base materials resulting in significant effects on the strain rate and flow strength response were also noted as a consideration in relation to the PWSCC assessment.[581]

Recent observations on DSA and its effect on mechanical properties of Alloys 600 and 690 were reported by a study on the related interstitials diffusion.[582] Their interpretation of the likely impact of DSA observations on the SCC response was also based on the creep and strain localization (deformational aspects) due to the dislocation-interstitials interaction in which the environmental action at the crack-tip was thought of as interfering or opposing the local DSA effects. This increased the SCC kinetics by enhancing the strain rate and strain localization at the crack tip. Consequently, the role of vacancies, dislocations, and their (local) interaction with the interstitials appears to be central in relating the tendency for DSA with the SCC kinetics. Specific assessment of the effect of carbon interstitials on PWSCC of Alloy 600[583] also attributed its relation to DSA and creep resistance due to the interaction of carbon with mobile dislocations (and subsequent pinning of dislocations), noting similar observations in other alloy systems as well.

3.3.1.3 Localized Straining and Hardening Effects

One of the characteristics of SCC, noted earlier at the start of Section 3.1, is the action of localizing the damage so that a sharp crack front is created and maintained during the SCC process. This has been emphasized more recently in terms of the so-called localization of straining, in reference to microscopic observations, which is essentially a form of locally intense heterogeneity (or inhomogeneity) of deformation. This heterogeneity itself is a result of the interaction between the corrosion (anodic dissolution) and vacancy/dislocation and diffusion processes, as implicated in other effects discussed in this section, in which external loading acts as the driving force with possible enhancement due to corrosion-generated hydrogen (see Section 3.1.4).

This characteristic of the strain localization effect is applicable not only to the IGSCC of austenitic alloys but also to the TGSCC.[584,585] It was noted[584] that the role of the environment is to reduce the activation energy for dislocation motion and localize the slip pattern. Figure 86 illustrates the underlying mechanistic principles.[584] In addition, as discussed in Section 3.1.4, the hydrogen effects and local stacking fault energy (SFE) changes help concentrate the strain localization that enhances the SCC kinetics, emphasizing again the role of dislocation motion and diffusion.

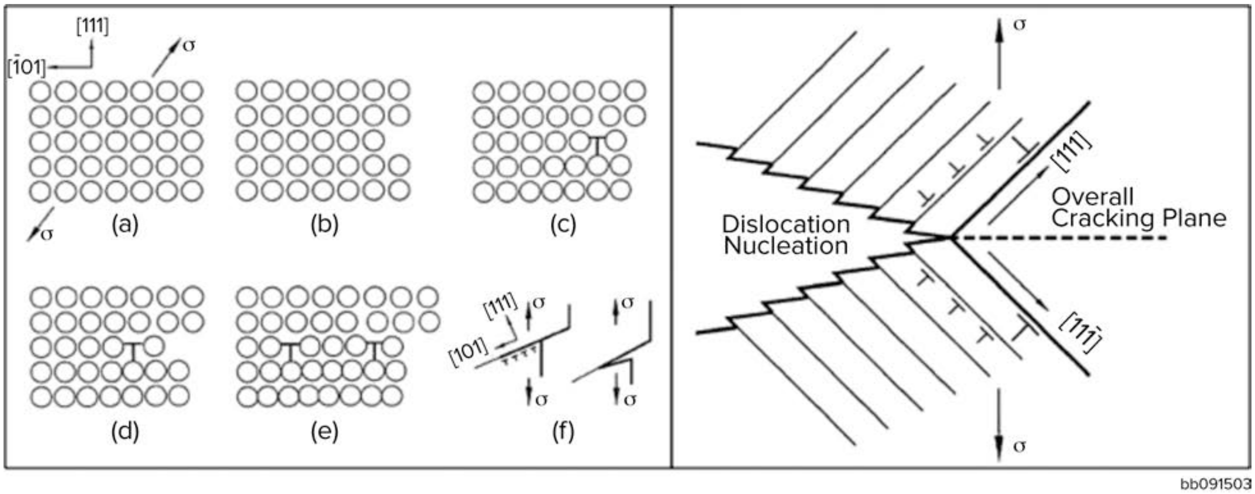

Figure 86. (Left) Schematic of proposed environment-induced dislocation emission: (a) perfect lattice, (b) vacancy generation due to anodic dissolution, (c) generation of a dislocation and out-of-surface displacement by one interatomic distance, (d) and (e) formation of planar dislocation arrangement, and (f) crack nucleation by opening of a dislocation pileup in a slip band. (Right) Schematic of proposed multiple-dislocation nucleation and fracture surface characteristics produced during crack propagation (Ref. 565). Reprinted with permission from NACE International.

In addition, it is of interest to note that even in the case of TGSCC, in which microcracking proceeds (and precedes) as a micro-cleavage through the grains, higher dislocation densities and the (coplanar) mode of deformation seem to be determining factors. Their presence at or near the crack front that can be significantly different than in the bulk remote from the environmental interface suggests the localization is influenced by the environment.[586] A recent analytical study[587] illustrates the importance of slip (plastic strain) localization, preceding the essential microcracking events, indicating its role in the progression of locally enhanced kinetics and manifestation of the SCC process.

Similar focus on the role of localized deformation where grain boundaries play a key role in resolving the matrix strain was the subject of a review[588] that dealt more specifically with IGSCC, with or without effects of irradiation, of austenitic alloys in high-temperature water. It was noted that (a) grain boundaries may either transmit strain to an adjacent grain, absorb dislocations that result in mobile grain boundary dislocations and cause grain boundary sliding, or absorb sessile dislocations increasing the stress on grain boundaries; (b) strain localization can exacerbate or amplify these processes through strain heterogeneity due to the SFE effect or from irradiation-produced obstacles to dislocation motion; and (c) the principal effect of grain boundary strain on cracking is through the rupture of the oxide film due to the intense localized deformation in the boundary. Grain boundary deformation can induce IGSCC through any of the principal mechanisms of cracking. The heterogeneity of strain was also the likely common factor between IGSCC and irradiation-assisted SCC. In the latter, irradiation-induced obstacles result in intense deformation bands terminating at grain boundaries, which may be considered to be an extreme case of the effect of SFE in unirradiated materials.

More recent work[589] focused on characterizing the deformation behavior of austenitic SSs in LWR applications extended the role of deformation to the case of strain heterogeneity due to surface cold work with implications for IGSCC crack initiation. It was pointed out that, from a deformation standpoint, (a) the corrosion-produced vacancies likely interact with dislocations, enhancing dislocation mobility to produce increased creep rates locally, and (b) the corrosion-enhanced plasticity in conjunction with the localized planar slip was likely responsible for crack initiation in aqueous environments when such initiation was absent in the inert (argon) environment. It was also concluded that (a) the commercial SSs with low SFE showed significant strain heterogeneity, sensitive to both temperature and strain rate, and to the degree of prior cold work; (b) the SCC response was correlated with deformation microstructures exhibiting planar slip- and deformation-induced martensite as well as micro twins, all of which accelerate the rate of strain hardening while also promoting strain localization at a granular scale; and (c) strain heterogeneity promotes strain localization, which in turn promotes crack initiation.

3.3.1.4 Hydrogen Effects

In the case of LWR environments, hydrogen is present in the form of aqueous (dissociated hydronium) ions, dissolved gas, and in atomic or molecular form generated as part of the cathodic reaction at the metal-environment interface or crack fronts. From the point of view of loading effects that are significant in the case of seismic activity, hydrogen adsorption and its passage into the corrosion film interface and the material ahead of the crack front are expected to be important. The resulting effects are also related to the localized deformation/creep, film properties, and interactions with the diffusion and dislocation processes discussed above. These aspects of the role of hydrogen are illustrated in Fig. 87. The significance of these effects to SCC in relation to the potential loading due to seismic activity is briefly summarized below.

The synergistic effects of absorbed hydrogen and crack-tip deformation have been considered in the mechanistic models of hydrogen-enhanced local plasticity (HELP)[231] and in the corrosion-enhanced plasticity model (CEPM) of SCC in austenitic SSs,[223] also accounting for the strain localization at/near a crack tip. These effects have a direct linkage to the above-noted Portevin-LeChatelier effect and DSA that emphasize the role of dynamic interaction between solute atoms diffusion and glissile dislocations.[590–592] Furthermore, the mode of deformation and cross-slip/slip planarity in FCC alloys, which are influenced by the SFE and enhance slip/strain localization,[593,594] are likely related to the reduction of SFE due to hydrogen. Generally, the

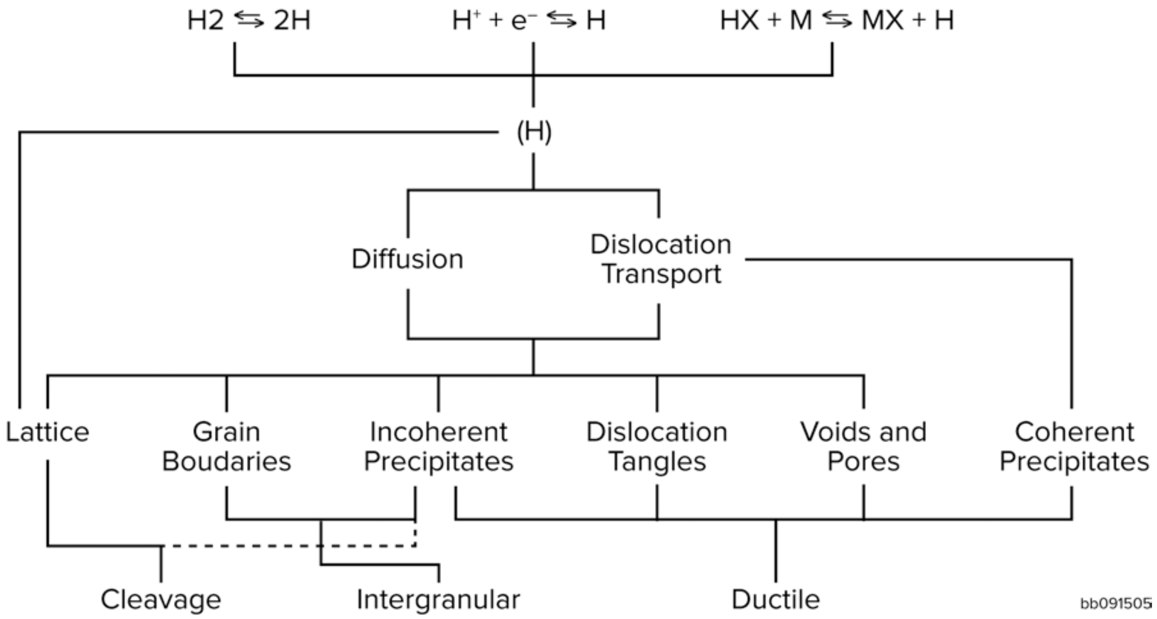

Figure 87. Summary of hydrogen processes and effects on microstructural elements in the case of environmentally assisted cracking in aqueous corrosion, following Ref. 598.

slow straining and localized deformation have been implicated even when hydrogen influence may be involved in environmentally assisted cracking.[595–597] The hydrogen effects fall in the category of enhancing the kinetics of SCC rather than altering the basic mechanism to something like the classical hydrogen embrittlement.

Note also that the local deformation and flow stress response in nickel-base materials are influenced by the addition of hydrogen, with the interaction of interstitial carbon, by its effect on the dislocation motion/barriers (rather than its interaction with the lattice).[599] As reviewed under the localized straining effects, the assessment by Meletis[586] indicates that the primary role of hydrogen in the case of TGSCC also is likely related to its effect on the localized plasticity and altered dislocation behavior close to the environmental interface at the damage front. In addition, the so-called low-temperature crack propagation in several nickel-base alloys in hydrogenated water[600] has been considered to involve hydrogen-enhanced localized (micro) cracking. The similar effect of hydrogen was suggested by the work on SCC of nickel-base alloys in high-temperature PWR environments,[601,602] where local corrosion provides sufficient hydrogen.

One of the main differences between the IGSCC in BWR (oxygenated) water conditions and the PWSCC in PWR (hydrogenated) water conditions was noted to be due to the likely role of hydrogen in influencing the same underlying mechanism.[603] In particular, it was noted that the excess hydrogen may enhance the local deformation and make the role of mechanical (creep) process more prominent in PWSCC than in IGSCC. A recent review[604] also considered the role of hydrogen in conjunction with the material creep deformation and dislocation interactions in the case of PWSCC of both Alloy 600 and Alloy 690.

3.3.2 Potential Seismic Impacts on SCC

Seismic activity refers to all levels or intensities of earthquakes in general and not just the SSE or OBE levels, which are often used as a guide for design purposes. The sub-OBE levels also produce significant loads on structures and resulting changes in stress-strain response of components; these aspects were discussed in more detail in TLR1.[‡‡] In addition to increased or altered loading/deformation of SSCs during such a seismic activity, the material microstructure is also altered. The TLR1 reviewed the primary impact of such activity on the microstructural effects related to the processes of diffusion of interstitials and vacancies and dislocation motion. The more specific aspects of these major factors in relation to various forms of SCC were reviewed above. In view of these reviews and observations, the following points are noted to further elaborate the potential impact of seismic activity on SCC.

It is the stability and passivity offered by the dynamic material-environment interface (generally an oxide film) at the active (crack) front that governs the SCC kinetics in LWR systems. The stability here refers to both the mechanical and (electro)-chemical stability. The former is impacted more significantly because of the changing load levels and rates during and subsequent to a seismic event. This impact is related primarily to the local deformation and disruption of microstructural elements such as the carbide-matrix and dislocation-solute interactions. Higher or changing stress conditions enhance the viscous and non-viscous (elastic-plastic) strain rates. Even if one considers the stress-temperature regime dominated by the typical primary creep response, the changing loads can re-initiate the primary creep; also, any increased kinetics of active material damage – such as due to the interaction of the environment and its interface with the material as discussed earlier in this section – will enhance local straining as well. These enhancements are expected to adversely impact the overall SCC damage evolution over time depending on the cumulative intensity of seismic activity at a given plant location.

While the linear-elastic fracture mechanics parameter K, the applied stress intensity, has been generally used in empirical descriptions of the crack growth kinetics of IGSCC, it is well recognized that the mechanical parameter governing the kinetics is related to the rate of deformation at or close to the crack tip. This deformation rate is affected by the local creep that, in turn, is also affected by the crack size and the rate of crack growth. This synergistic role of the corrosion-deformation interaction at the local level is influenced by the dislocation dynamics and diffusion, especially of vacancies and hydrogen, also discussed in this section. These two processes are likely to be impacted by the response of material to seismic activity, especially over periods following seismic events as these involve time dependencies, as well as during the slower parts of the seismic waves. In addition, elastic stresses have on the other hand been reported to increase the defect content in passive films[605,606] as well.

The specific effects of localized straining, DSA, creep deformation, and hydrogen, as discussed above regarding their influence on SCC kinetics, are all impacted by seismic activity. While such mechanistic considerations strongly suggest the resulting enhancement in SCC kinetics due to the seismic response, the current data and assessments do not provide enough bases to know the extent of such enhanced kinetics. This is a knowledge gap that needs to be addressed with critical testing and integrated modeling that accounts for the corrosion-deformation interaction at least semi-empirically so that reasonable sensitivity analysis can be

---

[‡‡] "Technical Letter Report on Literature Review and Assessment of Potential Seismic Effects on Ongoing Material Degradation – Tensile Strength, Fracture Toughness and Physical Properties," by Omesh Chopra, Dwight Diercks, David Ma, and Bruce Biwer, Nuclear Regulatory Commission, Washington DC, June 2015.

performed to assess the significance of these varied effects as they relate to the seismic response.

Furthermore, strain rate effects during earthquakes are important for several reasons. The imposed strain rate affects tensile properties of most structural alloys; increasing strain rate generally produces an increase in the yield and tensile strengths and a decrease in ductility. The other impact of seismic activity is related to the relatively higher strain rates due to high-frequency or high-loading-rate parts of seismic waves. Thus, the material is subjected to higher strain hardening that is known to have generally adverse influence on SCC kinetics. It is also to be expected that the sudden mechanical loads demanding the fast and greater straining of the material matrix would lead to a greater number of microcracking instances, especially within the grain boundaries and/or precipitate interfaces, thus weakening SCC resistance.

Intermittent high strain rate loads during an earthquake event are expected to increase material hardening, especially its isotropic component, raising the overall stress-strain flow curve. This has implications for changing the subsequent residual stress levels, typically expected to increase in absolute magnitude. That is, at locations under displacement or strain control, the new level of sustainable residual stress (tensile or compressive) is expected to be higher and to remain so (unless the material softens again, which may be rare). The other effect of high strain-rate deformation under seismic events is that of cumulative increase in the stored energy, similar to that under continued cold working of the material. This stored energy, along with the above noted effect on residual stress, is expected to increase the stress corrosion cracking susceptibility.[607,608]

In addition to the sustained strain rate effects, the seismic activity is characterized by a “ripple load” effect: essentially the load changes are not large enough to be considered as fatigue damaging cycles but as a superposition enhancing the SCC kinetics through its impact on induced add-on straining that contributes to the film rupture or interface disruption. This effect of ripple loading on SCC kinetics is well known and, indeed, commonly used in laboratory testing to either generate such a cracking or to perform an accelerated simulation of SCC growth.

In the case of EAC, including SCC, of low-alloy steels, the flow rate plays a significant role by flushing out the local water environments and bringing in more active water chemistry along with dissolution of exposed manganese sulfides that is known to enhance the local corrosion rate and re-initiate the cracking process. Since the local flow rates and turbulence are likely to be increased for some duration because of any significant seismic activity, the overall kinetics of SCC of these materials is expected to increase.

3.3.3 Gaps and Further Work

Although SCC in general, and loading effects on SCC kinetics in particular, have been extensively investigated in the past, there was no specific review or separate consideration available in the open literature that explicitly addressed the significance of seismic activity in SCC. As such, the following discussion and assessment are based on relating the processes, factors, and plausible mechanistic considerations, as reviewed in this report, to the likely influence of seismic activity as deemed applicable to various forms of SCC. Based on this review and engineering judgment related to the SCC phenomena, several issues and gaps in understanding the possible impact of seismic activity on SCC are identified.

As a general observation, it may be noted that material (active) degradation due to SCC is not addressed at the design stage, which makes the (non)consideration of seismic activity in SCC somewhat similar to that of the role of unanticipated transients in fatigue damage.

What is the impact of seismic-type loads on the character of the protective (oxide) interface – such as due to the enhanced action of point defects and/or diffusion within the interface or its formation during the seismic event? Note that for SCC to occur, the normally protective interface is invariably in the range of electrochemical parameters that make it marginally unstable.

Is there beneficial impact of low levels and rates of loading during parts of seismic events, especially in the initiation or short crack regime, e.g., due to stress relaxation or reduction of initial (residual) stress level? This would need to be examined against the material microstructural changes due to enhanced diffusion and dislocation motion. Therefore, the cumulative effect of elastic strain cycling on material microstructure and the resulting effect on fracture properties of reactor structural materials need to be evaluated.

It would be useful to map out typical straining patterns applied to a critical set of components during a seismic event and test the behavior of passive films as well as the relative change in SCC kinetics. In addition, the significance and extent of DSA-related diffusion and deformation effects in relation to SCC may need to be clarified or ascertained.

An effective way to provide an assessment of some of the major effects discussed above is to further evaluate the mechanical properties data for the impact of seismic loading cycles on strength and hardening characteristics – useful in its own way but also an easier way to assess via correlation the SCC susceptibility or kinetics impact. This is because of the previously demonstrated strong correlation between microstructural changes and mechanical properties of significance to SCC and between these properties and SCC kinetics, with or without cold-work effects,[607,608] and with or without irradiation effects.[609]

Additionally, it would be useful to perform critical testing and develop integrated modeling that accounts for the corrosion-deformation interaction at least semi-empirically so that reasonable sensitivity analysis can be undertaken to assess the SCC significance of varied effects noted in this report as they relate to the seismic response.

3.4 Material Embrittlement and Fatigue Cracking

3.4.1 Thermal and Neutron Embrittlement

The fracture toughness of a material, as expressed by the critical stress intensity factor K_c (or, more specifically, K_{Ic} for mode I loading) provides a more quantitative means of measuring its resistance to brittle fracture than the DBTT. For ductile materials, the J-integral value, which is related to the energy release rate during crack extension, can instead be determined at the onset of stable crack extension to obtain the parameter J_{Ic} (or K_J) as a measure of the material's resistance to ductile crack initiation ("crack initiation toughness"). Another parameter that is commonly measured for ductile materials is the "ductile crack growth resistance," which is the J value during stable crack growth and is commonly reported as a function of crack extension "a," in what is often referred to as the fracture toughness or J-R (J-integral/crack resistance) curve. Sometimes the slope of the J-R curve, dJ/da, is also reported as a function of crack extension.

Fracture toughness depends on loading rate for many materials, including most structural alloys, and increases with increasing loading rate, as illustrated in Fig. 88. Here, the linear elastic critical stress intensity factor for fracture, K_c, or alternatively, the J-integral critical stress intensity factor K_J, is schematically plotted as a function of temperature for three loading rates. For brittle behavior at temperature T_1, increasing the loading rate leads to a reduction in fracture toughness for most steels. For ductile behavior at temperature T_3, the initiation toughness increases for most steels with increasing loading rate. In the transition region at temperature T_2, increasing loading rate can lead to an increase in toughness if ductile behavior prevails, but a loading-rate-induced change in fracture mode is possible, leading to marked reduction of toughness at a given temperature.[610]

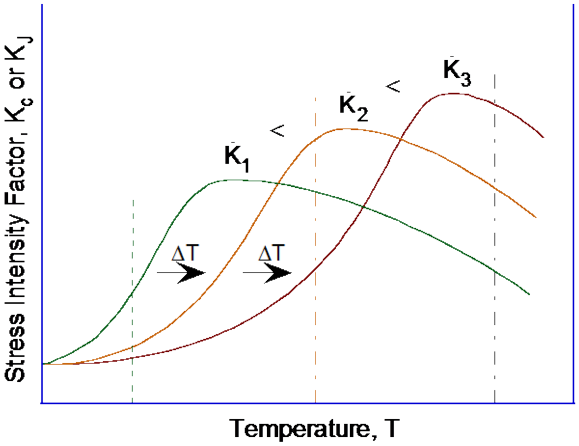

Figure 88.
General effect of loading rate on fracture toughness of most structural alloys (Ref. 610).

3.4.1.1 *Carbon and Low-Alloy Steels*

Studies on the fracture toughness of A508 Cl. 3 pressure vessel steel[611] indicate that the fracture toughness-versus-temperature curves (and the DBTT) shift to higher temperatures with increasing strain or loading rate. This behavior results from an elevation of the flow stress with increasing strain rate. However, the data exhibit a considerable degree of scatter, and the scatter tends to increase with increasing temperature. The crack initiation toughness (J_{Ic}) of A508 Cl. 3 steel at 25–380°C (77–716°F) and loading displacement rates of 0.08, 0.5, and 3.0 mm/min are shown in Fig 89.[498] At room temperature and 380°C (716°F), J_{Ic} increased with increasing strain rate, but at reactor operating temperatures, the lowest loading rate resulted in the highest value of J_{Ic}. The fracture toughness J_{Ic} is decreased by about 30–40% at reactor operating temperatures. These behaviors were attributed to a DSA effect.

The dependence of crack initiation fracture toughness on temperature for A533 Gr. B steel[612] at three different strain rates is shown in Fig. 90. At reactor operating temperatures, the dependence of strain rate on crack initiation fracture toughness appears to be mixed. The results are qualitatively similar to that for A508 Cl. 3 steel shown in Fig. 89.

In summary, the fracture toughness behaviors of A508 Cl. 3 and A533 Gr. B steels follow the behavior shown schematically in Fig. 88. However, a decrease in J_{Ic} with increasing strain rate has been observed by some researchers in the temperature range of interest for LWR applications (Figs. 89).

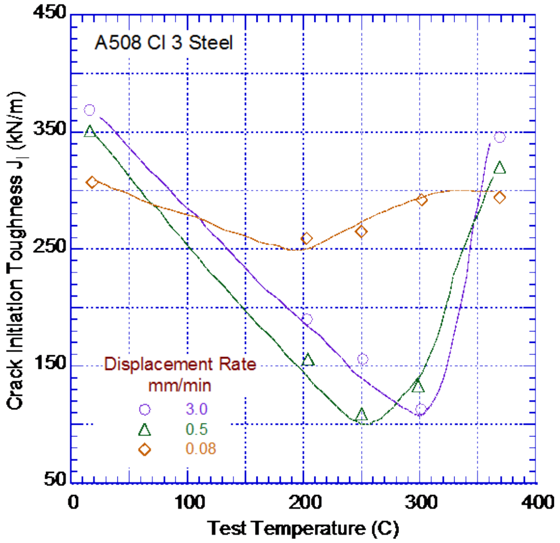

Figure 89.
Dependence of crack initiation toughness J_{Ic} on loading displacement rate and temperature for A508 Cl. 3 pressure vessel steel (Ref. 498).

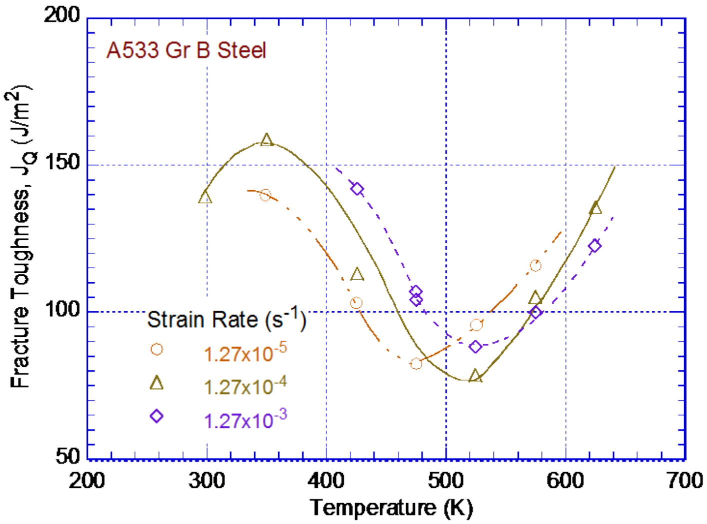

Figure 90.
Effect of temperature and strain rate on the crack initiation fracture toughness (here designated J_q) of A533 Gr. B pressure vessel steel (Ref. 612).

3.4.1.2 Types 304 and 316 Stainless Steels and Their Welds

Similar to the ferritic steels, loading rate also affects the fracture toughness of the austenitic SSs. The results of fracture toughness tests on Type 304 SS and associated welds, under both quasi-static loading conditions and dynamic loading conditions at loading rates comparable to those associated with high-amplitude seismic events, indicate an increase in fracture toughness with the higher loading rate.[613] However, the J values for the welds are appreciably lower than for the Type 304 SS base metal.

The effects of simulated BWR primary coolant on the fracture toughness of sensitized Type 304 SS have also been investigated at 98 and 288°C (208 and 550°F).[614] The tests were conducted in water containing 0.2 and 8 ppm dissolved oxygen at displacement rates of 0.5, 0.01, and 0.001 mm/min (0.02, 0.0004, and 0.00004 in./min). The results indicate that the fracture toughness J increases with increasing displacement rate and with decreasing dissolved oxygen.

In a review of the fracture toughness behaviors of Types 304 and 316 SSs and their welds, Mills compiled data from several investigators on the effect strain rate on fracture toughness properties.[21] The result is shown in Fig. 91, in which the J_{Ic} and dJ/da values are summarized for these materials under static, semi-dynamic, and dynamic loading conditions. The semi-dynamic displacement rates correspond to ~600 mm/min, or crack initiation times of <0.5 s. In no case does increasing the loading rate exert a detrimental effect on fracture toughness properties, and, in most instances, the effect is slightly or even significantly (for one heat of Type 304 SS at 288°C [550°F]) beneficial.

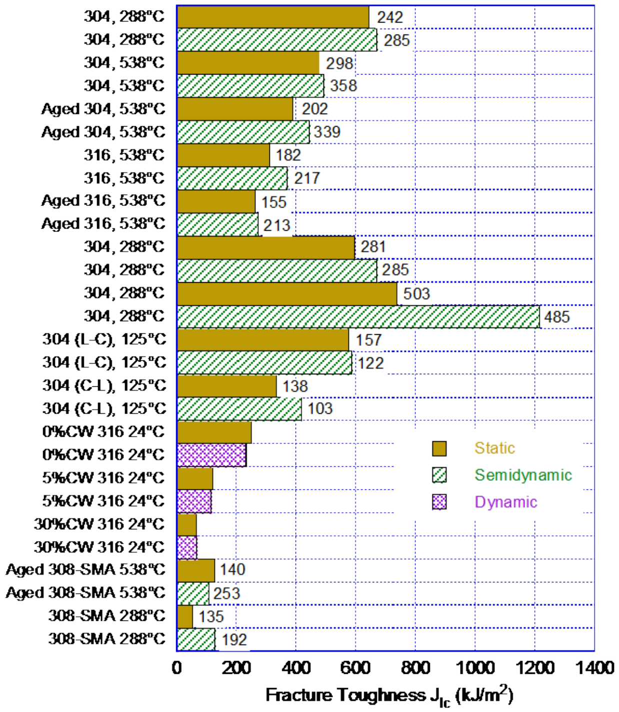

Figure 91.
Effect of strain rate on J_{Ic} and dJ/da (values of the latter parameter are given next to each bar in MPa) for Types 304 and 316 SSs and Type 308 SS weld metal under various conditions (Ref. 21).

In summary, the fracture toughness data for Types 304 and 316 SSs generally indicate a beneficial effect of increasing loading rate on the crack resistance behavior of Types 304 and 316 SSs. However, the variability in the data indicates that the loading conditions of interest must be well defined before these results can be reliably applied to a specific loading situation.

3.4.1.3 Cast Austenitic Stainless Steels

The limited data in the literature on the effect of loading rate on the fracture toughness properties of CASS materials are somewhat inconsistent. Based on a comparison of the energy values measured with Charpy impact toughness tests and slow loading three-point bending tests, Devillers-Guerville et al.[615] concluded that the influence of loading rate on these parameters for CF-8M CASS materials is negligible. They attribute this to the large amount of austenitic phase, the fracture behavior of which they state to be insensitive to strain rate. McConnell et al.[616] conducted fracture toughness tests on a high ferrite CF-3 material in the as-cast and aged conditions at three loading rates at room temperature and 300°C (572°F). The slowest loading rate was a quasi-static rate typical of J-integral testing. The second rate was approximately three orders of magnitude faster, and the highest rate was about one additional order of magnitude faster. For the as-cast material, they observed no significant variation in fracture toughness behavior with increasing strain rate either at room temperature or 300°C (572°F). However, for the room-temperature tests on aged material, increasing the loading rate resulted in an increase in J_c and a decrease in the slope, dJ/da, of the J-R curve.

Anzai et al.[617] likewise conducted fracture toughness tests on CF-3M material containing about 16% ferrite. The specimens were first aged for 1,000 h at 500°C (932°F) to produce embrittlement and then tested at 0°C (32°F). They found that increasing the loading rate reduced the J value for crack initiation (J_c) and the slope of the J-R curve to about 18% of their values for quasi-static loading conditions (Fig. 92). Thus, they agree with McConnell et al.[616] that the slope of the J-R curve is decreased at faster loading rates, but the disagree about the effect on J_c values.

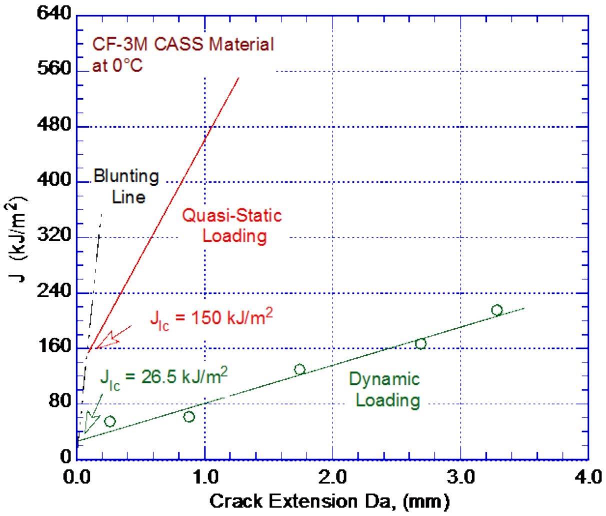

Figure 92.
Effect of loading rate on the J-R curve at 0°C (32°F) for thermally aged CF-3M CASS materials (Ref. 617).

However, there is little or no data related to loading rate effects on the fracture toughness of CASS materials or austenitic SS welds, thermally aged for extended periods at 300–370°C (572–698°F). The possible decrease in fracture toughness of such materials under dynamic loading conditions at temperatures between room temperature and 100°C (212°F) needs to be evaluated.

A recent study on low-temperature crack propagation for CASS CF-8 (Argonne Heat 68) material in PWR environments investigated the potential synergy between thermal and hydrogen embrittlement associated with decomposition of the ferrite at reactor temperatures.[574] The material was aged for 138,000 h (15.8 y) at 350°C (662°F); measured ferrite content was 23%. Fracture toughness tests were conducted on 1-T CT specimens in air and PWR shutdown water chemistry (SWC) at 54°C (129°F). The results are shown in Fig. 93.[618] The specimens were either fatigue precracked in air at 54°C (129°F) or fatigue-plus-SCC precracked in PWR water at 315°C (599°F). Note that one specimen that was precracked in PWR water at 315°C (599°F) was inadvertently tested at an elevated temperature of 315°C (599°F) in PWR primary water chemistry. The updated lower-bound J-R curve developed at Argonne for CF-8 material containing 15–25% ferrite and tested at room temperature is also shown in the figure for comparison.[618]

The results indicate that at 54°C (129°F), the J-R curve data in air are bounded, with additional margin, by the updated lower-bound J-R curve. However, the J-R curve data for specimens precracked in air at 54°C (129°F) and then tested in PWR (SWC) at 54°C (129°F) are significantly below the lower-bound curve. These results show an apparent large effect of the coolant environment on fracture toughness. All material and test conditions are identical for the two sets of duplicate tests except that one was tested in air and the other in water. The specimens that were precracked in PWR water at 315°C (599°F) and then tested in PWR water at 54°C (129°F) or 315°C (599°F) also show reduced fracture toughness relative to that in air,

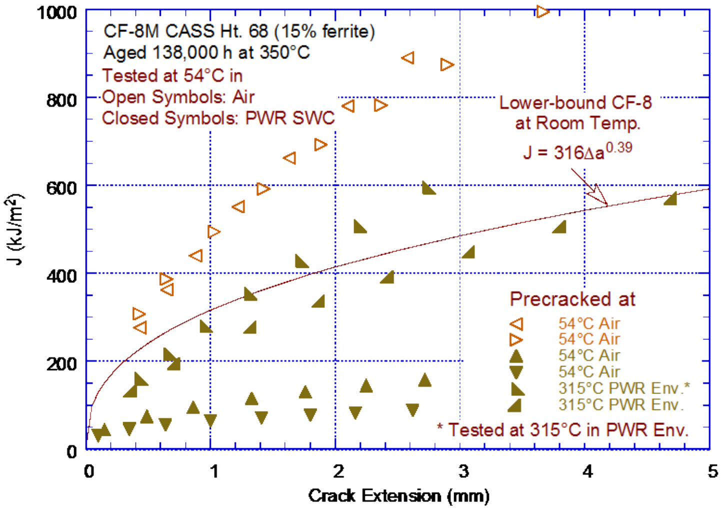

Figure 93. **Fracture toughness J-R curve data for thermally aged Heat 68 of CF-8M plate at 54°C (129°F). The curve represents the lower bound curve at room temperature for static-cast CF-8 material (Ref. 618).**

but the difference is less. The J-R curve data for the specimen that was cooled down from 315°C (599°F) and tested at 54°C (129°F) SWC are only marginally below the lower-bound J-R curve, and the data for the specimen that was precracked and tested at 315°C (599°F) PWR primary water chemistry are slightly above the lower-bound curve.

The reason for the drastic reduction in fracture toughness in PWR SWC at 54°C (129°F) relative to that in air at 54°C (129°F) is not clear. Additional fracture toughness tests on thermally aged CASS CF-3 and CF-8 materials in air and LWR environments should be conducted to better understand the combined effects of hydrogen embrittlement and thermal embrittlement in LWR environments.

3.4.1.4 Nickel Alloys

The ductile J-R crack resistance behaviors of Alloy 600 and its EN82H weld at 54°C to 338°C (129°F to 640°F) in air and hydrogenated water[619] exhibit excellent toughness in both environments at the higher temperatures. However, a dramatic degradation in toughness occurs in water at temperatures below 149°C (300°F), an effect attributed to hydrogen-induced intergranular cracking. Figure 94 shows the J-R curves for Alloy 600 for both environments. All results except for the dashed curve were obtained under quasi-static loading conditions (displacement rate = 0.05 mm/h [0.002 in./h]). The dashed curve was obtained at a loading rate of 300 mm/h (12 in./h). An increase in fracture toughness with increased loading rate is apparent.

Similar ductile J-R crack resistance behavior of Alloy 690 and its EN52 weld was seen in air and hydrogenated water at 24 to 338°C (75 to 640°F).[620] Both alloys exhibit excellent fracture toughness in air and in water at temperatures greater than 93°C (199°F). However, both experience a dramatic loss of toughness in 54°C (129°F) water. The effect of loading rate was investigated for Alloy 690 in a 54°C (129°F) water environment, with displacement rates ranging from 0.005 to 305 mm/h (0.0002 to 12 in./h). The results are shown in Fig. 95. The data for displacement rates in the range of 0.005 to 15 mm/h (0.0002 to 0.6 in./h) fall roughly on the same curve. However, increasing the displacement rate further to 305 mm/h (12 in./h) produces a dramatic increase in the fracture toughness, and the J-R curve falls very near the curve for

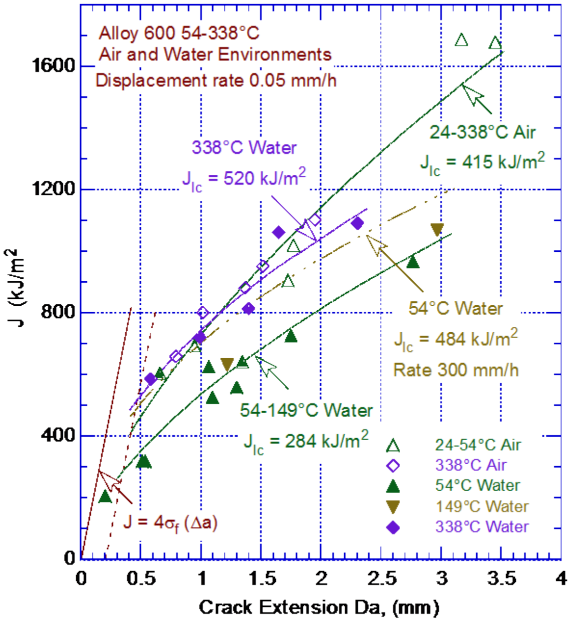

Figure 94.
J-R curves for Alloy 600 in air and water at temperatures of 54 to 338°C (129 to 640°F). All data were obtained under quasi-static loading conditions (displacement rate = 0.05 mm/h [0.002 in./h]) except for the dashed curve, which represents results obtained at 300 mm/h (12 in./h) (Ref. 619).

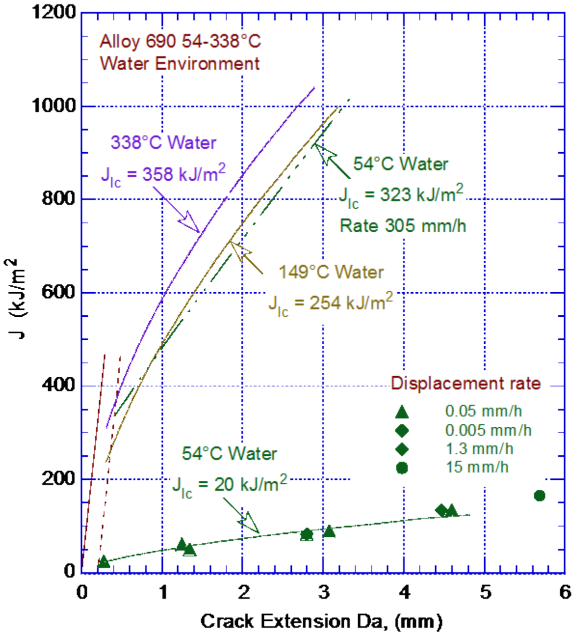

Figure 95.
J-R curves for Alloy 690 in a water environment at a temperature of 54°C (129°F) and displacement rates of 0.005 to 305 mm/h (0.0002 to 12 in./h). The J-R curves at 149 and 338°C (300 and 640°F) obtained under quasi-static conditions are shown for comparison (Ref. 620).

149°C (300°F) water. A similar, though somewhat less dramatic, effect of displacement rate for the EN52 welds was also observed.

As discussed earlier for CF-8 CASS material aged for nearly 16 y at 350°C (662°F), a significant reduction in fracture toughness occurs at 54°C (129°F) in an LWR environment relative to that in air. The large decrease in fracture toughness in LWR SWC has been attributed to potential synergy between thermal embrittlement and hydrogen embrittlement associated with the decomposition of ferrite at reactor temperatures. In addition, similar studies on austenitic SS welds with relatively high ferrite content have not been conducted. The potential effect of reduced fracture toughness (or allowable flaw size) of nickel alloys, aged CASS materials, and austenitic SS welds in LWR SWC on the seismic design of reactor safety-related components have not been performed. Such evaluations need to be evaluated.

3.4.2 Fatigue Crack Growth Rates

The original design of reactor structures and components is based on the mechanical properties of the as-fabricated material. It does not consider the aging degradation of the properties during service and does not consider loading rate effects. Furthermore, because fatigue cycles below OBE are excluded from the fatigue analyses, the potential effect of sudden, repeated below-OBE loading on reactor component design is not considered. Potential effects of low-level seismic loading on fatigue CGRs include the following: (a) the effect of sudden, high-strain loading (i.e., the first loading cycle) on tensile yield and ultimate tensile strength of LWR structural materials, (b) changes in the material microstructure during LWR service, and (c) effect of high-frequency (>1 Hz), high R (≥0.9) and small ΔK (≤5 MPa m$^{1/2}$) or ripple loading on CGRs. These three potential effects of low-level seismic loading are discussed below.

3.4.2.1 Microstructural Changes during Seismic Loading

The reversibility of the substructure that evolves during cyclic loading has been evaluated.[487] The stress response and microstructure of pure iron specimen cycled at high strain amplitude to 3–45% of its life followed by cycling at low strain amplitude to failure were monitored to investigate the potential effect of the nature of the substructure at high strain amplitudes on the subsequent fatigue at low strain amplitudes. The results indicate that the stress response and the microstructure of the material during subsequent fatigue at low strain amplitudes depend on the number of cycles at high strain amplitudes. For example, the cyclic stress response for the specimen that was fatigued at high strain amplitude for 3% of its life and then fatigued at lower strain amplitude was the same as that of a virgin specimen fatigued at the low strain amplitude alone. However, the cyclic stress response for the specimen that was first fatigued for 45% of its life at high strain amplitude was higher than that of a specimen fatigued at the low strain amplitude alone.

The microstructural observations indicate that the reversal of the substructure developed at the high strain amplitude is very slow and continues over the remaining life. A complete reversal of the substructure is not accomplished in the specimen that was fatigued up to 45% of life at high strain amplitude. For that specimen, the substructure is very inhomogeneous and some memory of prior strain cycling is retained even at fracture. Since repeated and sudden below-OBE loading involves high-cycle, elastic-strain cycling of structural materials, which generally generates point defects (i.e., vacancies and interstitials), it is likely to have a strong effect on dislocation motion and therefore the material microstructure, particularly at reactor operating temperatures. Thus, below-OBE seismic loading is also likely to influence growth of existing flaws (i.e., enhance fatigue CGRs). Therefore, the effect of low-level seismic loading on fatigue CGR needs to be evaluated.

3.4.2.2 Effect of High Frequency Ripple Loading

Based on the applied loading conditions, three types of EAC can occur in low-alloy steels in LWR environments:[437,621,551]

(i) Corrosion fatigue which occurs under cyclic loading such as thermal fatigue or thermal stratification,

(ii) SCC which occurs under static loading observed during steady-state power operation, and

(iii) Strain-induced corrosion cracking, which occurs under slow monotonically rising of very low-cycle fatigue such as reactor startup and shutdown.

The existing operating experience with carbon and low-alloy steel primary pressure boundary components in LWRs is generally good worldwide. However, a few incidences of EAC have occurred in low-alloy steel piping, particularly in BWRs. EAC has been observed in wrought material, weld filler metal, and weld HAZ material. Fracture morphology is typically transgranular. The affected components include the steam and feedwater piping, the condensate systems, and pressure vessel feedwater nozzles in BWRs, and the secondary system feedwater piping/tanks and heat exchanges, and steam generator girth welds and feedwater nozzles in PWRs.[551]

The effect of HWC (< -200 mV_{SHE}) and NWC (50–150 mV_{SHE}) on crack growth of low-alloy steel and associated welds has been investigated by Seifert and Ritter[551] under SCC and corrosion fatigue conditions. The tests were conducted on Type SA 508 Cl 2 and 3 steels and associated weld metal and HAZ material. The SA 508 Cl 2 steel had a combination of bainitic/ferritic-pearlite structure whereas the SA 508 Cl 3 steel had a complete bainitic structure. The SCC growth rates were obtained under constant load ($R = 1$) with periodic partial unloading or a ripple loading ($R = 0.95$) in BWR NWC and HWC environments at intermediate temperatures of 180–270°C (356–518°F), where DSA is known to occur in reactor pressure vessel materials. Corrosion fatigue tests were conducted at low frequencies (≤0.01 Hz) and $\Delta K > 5$ MPa $m^{1/2}$ or at frequencies of 0.01–10 Hz, $R \geq 0.9$, and $\Delta K \leq 5$ MPa $m^{1/2}$.

The results are shown in Figs. 96 and 97. The EAC behavior of these steels varied primarily because of the differences in their susceptibility to DSA, the material composition (particularly S content), and yield strength. The susceptibility to DSA was monitored by the relative change in material ductility measured in tensile tests at 250°C (482°F), when the strain rate was decreased from 0.1 to 0.001 %/s. The loss of ductility under the temperature and strain-rate conditions for DSA is caused by negative strain rate sensitivity and localized plastic deformation.

The results confirmed the beneficial effect of HWC (< -200 mV_{SHE}) on SCC and corrosion fatigue CGRs; the CGRs under both loading conditions decreased more than an order of magnitude in HWC relative to NWC conditions. The results also showed that the SCC growth rates under transient free steady-state BWR power operation conditions (i.e., 274–288°C [525–550°F]) for these steels are <0.6 mm/y at stress intensity factors up to 60 MPa $m^{1/2}$.[551] However, as shown in Figs. 96 and 97, depending on a combination of a few critical parameters, SCC growth rates >3 mm/y are observed in low-alloy steels under BWR NWC conditions. For example, the SCC CGRs under periodic partial-unloading or ripple-loading conditions are significantly higher than the BWRVIP-60 disposition curves. Under ripple loading, significantly high CGRs are observed even at relatively low stress intensities of 30 MPa $m^{1/2}$. As seen in Fig. 96, the SCC growth rates in low-alloy steels that showed significant susceptibility to DSA because of a higher C and N content are above the BWRVIP-60 disposition line 1 even at intermediate temperatures.

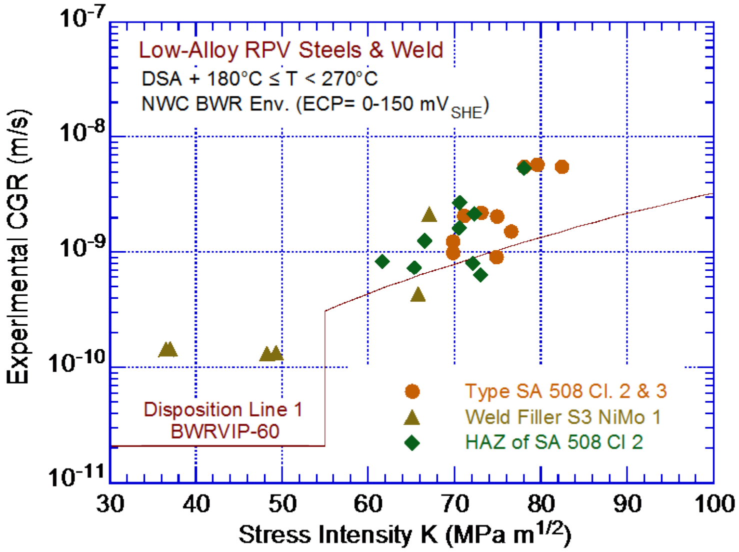

Figure 96.
Constant load tests under simulated BWR/NWC conditions with SCC CGR above the BWRVIP-60 disposition line 1 for stationary BWRVIP operation (Ref. 622).

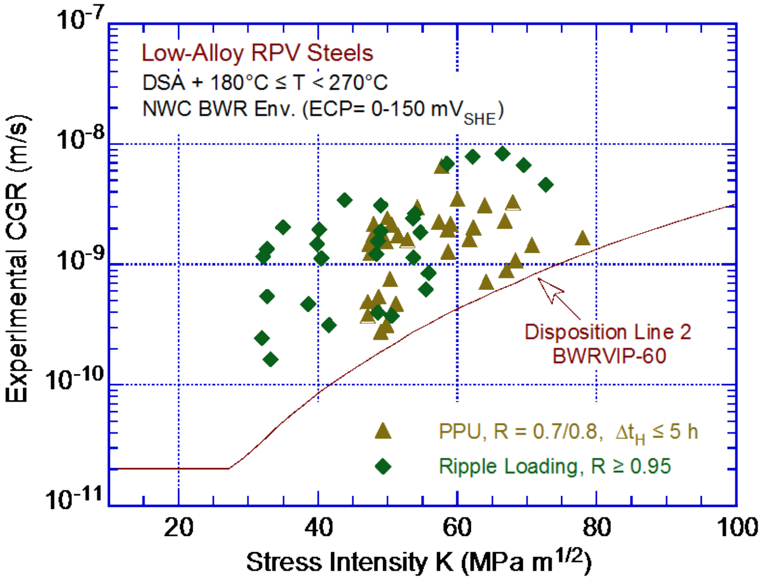

Figure 97.
Tests under simulated BWR/NWC conditions with SCC CGR above the BWRVIP-60 disposition line 2 for water chemistry and load transients (Ref. 622).

These results indicate that under a combination of environmental and loading conditions, even a ripple loading can enhance SCC or corrosion fatigue CGRs of low-alloy steels at reactor intermediate temperatures or operating temperatures. Therefore, the cumulative effect of below-OBE seismic loading on the SCC growth rates of low-alloy reactor pressure vessel and piping steels needs to be evaluated.

4 SUMMARY

All structures, systems, and components in NPPs are subjected to aging degradation during reactor operation because of chemical and mechanical effects and interactions with the service environment. The objective of this program is to evaluate the potential cumulative effects of repeated and sudden, below the design basis earthquake (DBE) loading on progressing degradation of NPP structural materials. The program addresses knowledge gaps in a fundamental manner, considering the mechanical response of degraded material to establish their basic properties under various stages of degradation, and determines whether repeated below-DBE events could adversely affect ongoing material and component degradation. These aging degradation mechanisms include various forms of corrosion, flow accelerated corrosion (FAC), microbiologically induced corrosion (MIC), reduction in fracture toughness due to thermal and neutron embrittlement, and crack growth rates for various forms of stress corrosion cracking (SCC), intergranular (IG), transgranular (TG), primary water (PW), or irradiation-assisted (IA) SCC, and fatigue crack initiation and growth. The effects of seismic loading on specific aging degradation process are summarized below.

Structural damage to NPPs occurs when the cumulative effects of ground acceleration exceed a certain threshold. The seismic loads on a structure are inertial loads generated by the deformation of the structure as it vibrates, and the seismic forces depend on the distribution of mass and stiffness throughout the structure. Because structures are typically designed to respond inelastically under vibration, the seismic forces also depend on the manner by which plasticity spreads through the structure, and these forces are typically amplified by resonance effects. In addition, the maximum vibratory accelerations of the DBE must take into account the characteristics of the underlying soil material in transmitting the earthquake-induced motions. Finally, damping effects within the structure must be taken into account. The information needed for a seismic design includes (a) design ground response spectra, (b) in-structure response spectra, (c) acceleration time history, and (d) seismic anchor movements.

The requirements for the acceptability of a component design by analysis are described in ASME Section III, Division 1 Subarticle NB-3210, “Design Criteria.” Alternatively, a design by rule approach as described in Subarticle NB/NC-3600 may be used for piping and piping components. The design methods in Section III Subarticle NB, NC, or NG for ASME Class 1, 2, and CS components also require a fatigue analysis as well as a fracture mechanics evaluation to prevent the likelihood of nonductile failure. The ASME Code fatigue analysis considers all transient loads, and, for each load-cycle or load set pair, an individual fatigue usage factor is determined by the ratio of the number of cycles anticipated during the lifetime of the component to the allowable cycles.

Included is a literature review to evaluate the effects of repeated and sudden below-DBE loading on specific degradation mechanisms. The potential effects of repeated and sudden below-DBE loading on these various aging degradation mechanisms are evaluated. The review considers possible scenarios in which seismic shock loading could accelerate degradation in structural materials used for LWR passive component, thereby reducing the available margin and useful life of reactor coolant pressure boundary and safety-related components. What is known about the effects of seismic loading on specific aging degradation processes are summarized in the following sections and provide the basis for the identification of six information gaps:

1. Low-level seismic events can impose higher loading rates on reactor structural materials than typically experienced during normal operation. These off-normal events have the potential to cause accelerated crack initiation through passive film rupture, micro crack generation, and plastic deformation. The extent of the accelerated crack initiation needs to be investigated.

2. The possible impact of (a) current material condition, (b) loading rates associated with typical seismic events and with low-level seismic fatigue cycles (e.g., magnitudes associated with seismic accelerations between 0.01 g and OBE) on reactor component design needs to be investigated for at least two components, one from reactor core internal components and the other from primary pressure boundary piping.

3. The cumulative effect of elastic strain cycling on material microstructure and the resulting effect on fracture properties of reactor structural materials need to be examined.

4. The reason for the reversed strain rate dependence (i.e., decrease in yield and flow stress with increase in strain rate) at 400°C (752°F) and its potential impact on seismic design of safety-related structures and components need to be determined.

5. The possible decrease in fracture toughness of CASS materials and austenitic SS welds thermally aged at 300 to 370°C (572 to 698°F) and tested under dynamic loading conditions at temperatures between room temperature and 100°C (212°F) needs to be investigated.

6. The potential effect of reduced fracture toughness of Alloys 600 and 690, aged CASS CF-3 and CF-8 materials, and austenitic SS welds in LWR SWC on the seismic design of reactor safety-related components needs to be determined.

4.1 Material Performance

4.1.1 Tensile Properties

The yield and ultimate tensile strengths of carbon steels such as A508 Cl. 3 and A533 Gr. B, generally increase with increasing strain rate, while the ductility decreases or shows little effect. However, some data suggest a reversal in the yield and tensile strength behavior with strain rate under normal LWR operating temperatures. For austenitic SSs such as Type 304, 304L, 304N, and 304LN SS, the yield stress and flow stress are generally found to increase with increasing strain rate, the ultimate tensile strength tends to decrease, and the ductility decreases or shows little change. For Type 316L and 316LN, the flow stress increases with increasing strain rate. Elongation and reduction of area appear to increase somewhat with increasing strain rate, though the opposite effect is observed for cold-worked material. The tensile data for Type 304/308 welds and Type 308 SS weld metal show mixed results. Regarding Ni-Cr-Fe alloys, little effect of strain rate on the flow stress and ductility is reported for Alloy 600 at temperatures up to 760°C (1400°F) and marked increase in flow stress with increasing strain rate is seen at higher temperatures. For Alloy 690, an increase in flow stress is observed with increasing strain rate at −100 to 1200°C (–148 to 2192°F), though the magnitude of the effect appears to depend on temperature.

4.1.2 Cyclic Deformation Behavior

In the temperature range of dynamic strain aging (200–370°C [392–698°F]), some heats of carbon and low-alloy steels are sensitive to strain rate. With decreasing strain rate, the fatigue life may be unaffected, decrease for some heats, or increase for others. The cyclic stress-strain response of these steels varies with steel type, temperature, and strain rate. In general, these materials show initial cyclic hardening, followed by cyclic softening or a saturation stage at all strain rates. At high strain amplitudes, a secondary hardening stage is observed prior to fracture.

For the wrought austenitic Type 304 and 316 SSs, the fatigue life is generally independent of strain rate at temperatures up to 400°C (752°F). However, the temperature effect on fatigue life is observed for Ti- and Nb-modified SSs. During cyclic straining, austenitic SSs exhibit rapid hardening during the first 50–100 cycles; the extent of hardening increases with increasing strain amplitude and decreasing temperature and strain rate. The CASS CF-3, CF-3M, CF-8, and CF-8M generally show similar behaviors, though the cyclic-hardening behavior may be influenced by aging. The microstructural effects associated with cyclic loading for both ferritic and austenitic steels were reviewed.

4.1.3 Fracture Behavior

The Charpy impact data for A508 Cl. 3 and A533 Gr. B pressure vessel steels indicate either little effect or an increase in the DBTT with increasing loading rate. An increased loading rate also appears to increase the upper shelf energy somewhat for both steels. The fracture toughness of A508 Cl. 3 and A533 Gr. B steels generally increases with increasing loading rate. However, a decrease in the crack initiation toughness J_{Ic} with increasing strain rate has been observed in few investigations in the temperature range of interest for LWR applications. The J-R curves generally show an increase in cracking resistance with increasing loading rate.

The fracture toughness data for Types 304 and 316 SSs suggest a beneficial effect of increasing loading rate on the crack resistance. The limited data in the literature on the effect of loading rate on the fracture toughness properties of the CASS materials are somewhat inconsistent; as-cast and aged material show different behaviors. Recent work on low-temperature crack propagation for CASS CF-8 material in PWR environments investigated the potential synergy between thermal and hydrogen embrittlement associated with decomposition of the ferrite at reactor temperatures. A large effect of the coolant environment on fracture toughness was observed.

For Alloy 600, a dramatic degradation in fracture toughness was observed in hydrogenated water at temperatures below 149°C (300°F), an effect attributed to hydrogen-induced intergranular cracking. This behavior is similar to that observed for aged CF-8 material in LWR SWC. At higher temperatures in the same environment, the fracture toughness increases with increasing loading rate. A qualitatively similar behavior is observed for Alloy 690.

4.2 Various Forms of Corrosion

4.2.1 General, Pitting, and Crevice Corrosion

Seismic loadings can negatively impact the corrosion resistance of NPP structural alloys in a number of ways. The seismic load could strain or rupture the passive oxide film and strain or crack the underlying metal.

If the passive oxide film is ruptured, it would lead to repassivation of the exposed metal and potentially promote pitting and crevice corrosion. The impacts of strain imposed, without rupture, on the passive film are unclear, but corrosion processes would be altered if ion migration in the passive film is altered.

Strain imposed directly on the structural alloy due to a seismic event could cause plastic deformation. The resulting tensile residual stresses can contribute to fatigue crack growth and SCC. Surface tensile residual stresses enhance general corrosion and can enhance crack initiation through strain-enhanced dissolution and contribute to strain-induced corrosion cracking. Seismic loads strong enough to result in metal crack formation would also rupture the overlying passive film. Crevice corrosion would begin and be susceptible to further SCC, as discussed in Section 4.3.

In addition to aspects of the passive oxide layer itself, the characteristics of pitting and crevice corrosion were reviewed and discussed in relation to the possible impact of seismic activity. In particular, the roles of mechanical factors of stress, deformation, and corrosion product integrity were examined, with more recent work showing a definite relation among these factors when viewed at the local, micro-scale level at which the material degradation seems to proceed.

The current assessment shows that the prediction of pitting frequency and growth over long-term operation is a challenge. At present, there is no systematic or accepted method or model for estimating pitting or crevice depth or their sensitivity to factors known to be responsible. At least a conceptual and physically consistent model for pitting and crevice growth should be developed incorporating as many factors as possible.

The potential effects of below-DBE loading on general metal corrosion, pitting, and crevice corrosion of reactor structural materials have been evaluated. Enhanced degradation might occur based on several different factors:

(i) The strain imposed on a passive film and the underlying metal by low-level seismic loading may cause elastic and plastic deformation (and potential rupture) of both the film and the metal. The results of investigations of similar induced strains in a variety of environments have shown that such strains can affect ion mobility in, and composition of, the passive film that can lead to enhanced corrosion rates. The extent of enhanced corrosion processes due to low-level seismic loading depends on the characteristics of the loading (e.g., intensity and number of cycles) over the time frame of interest as well as the nature of the structural alloy, water chemistry, film composition and structure, pH, and temperature.

(ii) The local water chemistry/electrochemical environment that controls the dominant corrosion processes can vary widely in the vicinity of and within pits and crevices. Such environments can be radically disturbed by intermittent flow and/or increased periods of stagnation (in response to seismic activity) or a change of anodic to cathodic area ratios (due to potential film disruption events).

(iii) General corrosion is magnified in locations such as pits and crevices where additional stress from low-level seismic loads would more readily result in deleterious passive film deformation and rupture.

4.2.2 Flow-Accelerated Corrosion

In summary, one may broadly classify the factors influencing the FAC rate to be hydrodynamic, environmental (chemical), and metallurgical. The primary impact of seismic activity on FAC is expected to be through locally disturbed flow patterns, removal of steady-state water chemistry conditions (near the oxide surface), enhanced thinning of the diffusion boundary layer and oxide layer, and possible damage to the integrity (or protective quality) of the oxide layer. All of these effects would contribute to the enhancement of mass transfer leading to increased FAC rate, at least for the duration, until normal and steady-state conditions are achieved again. However, the extent to which low-level seismic loading would impact the FAC rate is highly uncertain. Not included in this assessment is the fracture response (due low-level seismic enhanced wall thinning) to a future seismic event.

4.2.3 Microbiologically Induced Corrosion

MIC is often associated with a localized form of corrosion, the kinetics of which depend on many factors in addition to those in the case of abiotic corrosion. This fact, plus the micro biological considerations, add to the complexity of assessing, if not understanding, all of the relevant factors and their interactions in MIC; as such, it is well to recognize the greater degree of associated uncertainty.

The current assessment shows that the prediction of MIC growth over long-term operation has been more challenging than most other forms of degradation. At present, there is no systematic or accepted method or model for estimating the extent and rate of damage due to corrosion under biofilms, although there appear to be established thermodynamic principles and kinetic expressions that describe certain microbial activity. One aspect complicating the MIC response in general is the highly localized, spatially heterogeneous nature of the biofilm corrosion environment and its sensitivity to the changes, at micro scales (below about a micron), of microchemistry, microstructure, and surface characteristics of the underlying substrata. The interrelation between these changes and the microbial response under the seismic conditions needs to be investigated and better understood.

Pitting under MIC is seen to be more aggressive than the conventional (abiotic) pitting. The interaction of these mechanisms, particularly the role of biofilms and local stress-deformation in relation to pitting kinetics, add to the complexity of assessing all the necessary influence factors; as such, it is well to recognize the greater degree of associated uncertainty (as noted above, even in the case of abiotic pitting).

4.3 Stress Corrosion Cracking

The effects of repeated and sudden below-SSE loading on the three SCC processes, IGSCC, TGSCC, and PWSCC, have been evaluated. The term SCC represents crack initiation and sub-critical crack growth of susceptible alloys under the influence of a “corrosive” environment and tensile stress. It is a complex process controlled by synergistic interactions among metallurgical, electrochemical, and mechanical parameters. These three conditions are necessary and must occur simultaneously for SCC to occur. These three SCC processes and their characteristics and operating experience have been discussed in this report. The critical parameters important for these processes are identified. Significant results are summarized below.

4.3.1 Intergranular Stress Corrosion Cracking

Under “normal” conditions of stress and environment, several structural alloys have shown susceptibility to IGSCC in BWRs because of the alloy itself or its fabrication history. In BWRs, IGSCC has occurred in austenitic SS and nickel alloys. The initiation of IGSCC occurs when the following three necessary conditions are simultaneously present: (i) a microstructure that is “sensitized” due to thermal sensitization during welding and/or stress-relief heat treatment to produce a chromium-depleted region at the grain boundary; (ii) tensile stress, associated primarily with weld residual stresses; and (iii) an oxidizing environment caused by excess oxygen or hydrogen peroxide species in water due to radiolysis. A brief description of the proposed mechanisms for IGSCC is also presented. The parameters that can be influenced by low-level seismic activity include (a) material microstructure and its metallurgical condition, including cold work; (b) environmental parameters such as reactor coolant ECP and conductivity; and (c) applied stress and associated fatigue damage and changing the rupture frequency of protective oxide film.

4.3.2 Transgranular Stress Corrosion Cracking

TGSCC is not expected to occur under normal operating water chemistry conditions in BWRs and PWRs. However, it can occur even in solution-annealed austenitic SSs, in the absence of material sensitization, if it is subjected to high stress or an oxygenated water environment contaminated with chlorides. Marine environments and large industrial complexes are commonly chloride-contaminated. TGSCC is of particular concern if the material surface is highly cold worked by severe fabrication processes such as grinding. The mechanism for TGSCC is not well established. The various mechanisms that have been proposed are briefly described; these processes primarily depend on the nature of the material deformation behavior ahead of the crack tip.

The parameters that can be influenced by low-level seismic activity include (a) material metallurgical condition, particularly when the surface have been abused by fabrication process; (b) an oxygenated water environment contaminated with chlorides; and (c) high applied stress. Corrosion-enhanced local plasticity, crack tip strain rate, and surface repassivation rate are important parameters that influence the rupture frequency of the protective oxide film. Typically, the fracture surface has a fan-like appearance also referred as a river pattern.

4.3.3 Primary Water Stress Corrosion Cracking

Unlike IGSCC, which occurs in oxygenated water, PWSCC occurs in PWR primary coolant environment with low DO content and low corrosion potentials. It affects Ni alloys and associated weld metals. Only a few cases of PWSCC have been reported for austenitic SSs. The material parameters that have a significant effect on PWSCC are the amount of cold work in the material and, for Ni alloys, the metallurgical structure, particularly the carbide morphology. Most of the proposed mechanisms for PWSCC fall into two categories: (a) evolution of hydrogen at the cathode within a crack and (b) oxidation/dissolution of metal at the crack tip. For Ni alloys, the crack growth rates are maximum at a hydrogen concentration approximately corresponding to the Ni/NiO equilibrium potential.

Regarding the effects of applied stress, Alloy 600 exhibits an identifiable threshold stress for PWSCC, whereas, for austenitic SS components, the surface residual stress due to grinding or other finishing processes play an important role. The PWSCC fracture morphology in mill-annealed Alloy 600 tubes is primarily intergranular. However, in the presence of chlorides, the fracture is transgranular, except for the case of sensitized material.

4.3.4 Irradiation-Assisted Stress Corrosion Cracking

As the name implies, IASCC is literally the irradiation-assisted enhancement of the SCC susceptibility of materials. Neutron irradiation increases the IASCC susceptibility of austenitic SSs by changing the material microstructure due to radiation hardening and material microchemistry due to radiation-induced segregation. The susceptibility of austenitic SSs to IASCC increases with neutron fluence, corrosion potential, and water conductivity. In addition, radiolysis can increase the corrosion potential in BWRs, thereby increasing the susceptibility of SSs to IASCC. The material and environmental parameters that enhance IASCC of austenitic SSs are discussed in detail.

The experimental CGR data show significant variability because of the complexities in the IASCC process and uncertainties in experimental measurements. Therefore, it is not possible to determine the effects of specific parameters on IASCC growth rates. Correlations between SCC growth rates and neutron dose are presented for irradiated austenitic SSs in LWR environments. In view of these assessments, the following points are noted to further illustrate the potential effects of sudden, repeated, below-OBE seismic activity on IASCC.

(i) The mechanical and chemical stability of the oxide film at the crack tip governs the SCC kinetics in LWR systems. The former is impacted more significantly because of the changing load levels and rates during a seismic event. The changing stress conditions enhance the elastic-plastic strain rates at or near the crack tip, which govern the kinetics of crack growth. In addition, the environment-deformation interactions at the crack tip are influenced by the dislocation dynamics and diffusion, especially of vacancies and hydrogen. These processes are likely to affect the material response to seismic activity. However, the existing mechanical property data are inadequate to evaluate the effects of such mechanistic considerations on IASCC growth rates.

(ii) Typically, high strain rates increase material hardening and thereby increase the tensile yield and flow stress. However, this behavior is reversed at 180–270°C (356–518°F). In addition, the residual stress levels are increased at high strain rates. The increased strain hardening behavior also results in increased stored energy. This stored energy, along with the effect on residual stress, is expected to increase the SCC susceptibility of the material. The potential effect of ripple loading on SCC is also discussed.

(iii) In the case of environmentally assisted cracking of low-alloy steels, the flow rate plays a significant role by flushing out the local environment and bringing in a more active water chemistry including sulfides, which enhance the local corrosion rate. Since the local turbulence is likely to be increased during seismic activity, the overall kinetics of the SCC of low-alloy steels is likely to increase. Critical tests are needed to examine the effects of low-level seismic activity on the stability and kinetics of the oxide film.

4.4 Material Embrittlement and Fatigue Cracking

The effects of repeated and sudden below-OBE loading on (a) thermal and neutron embrittlement, (b) fatigue crack initiation and growth, and (c) IASCC susceptibility and CGRs have been evaluated. The critical parameters and loading and environmental conditions important for these degradation processes and their relation to seismic loading are identified. The potential effects of below-DBE seismic loading on material embrittlement and fatigue cracking during LWR service are discussed. The significant results are summarized below.

4.4.1 Thermal and Neutron Embrittlement

At LWR operating temperatures, thermal aging effects are not observed in carbon and low-alloy steels. Similarly, under these conditions, thermal aging effects do not occur in wrought austenitic SSs because they consist of primarily the austenite phase. However, since CASS materials and austenitic SS welds have a duplex structure consisting of both austenite and ferrite phases, they are susceptible to thermal embrittlement of the ferrite. In addition, CASS materials and SS welds used in the reactor core internal components are also susceptible to neutron embrittlement. Therefore, thermal aging and, for some components, neutron irradiation for prolonged periods during reactor services can significantly reduce the fracture toughness of CAS materials and austenitic SS welds such that failure may occur by unstable crack extension at stress levels below yield strength and even with little or no controlled crack extension.

Extensive studies at Argonne have developed a methodology for estimating the degradation of fracture properties of CASS components due to thermal aging under LWR service conditions from material information available in certified material test records. However, the Argonne estimation scheme for thermal embrittlement is not applicable to austenitic SS welds. The methodology also considers the combined effects of thermal and neutron embrittlement as a function of neutron dose. The details of the estimation scheme are presented. The potential effects of the reactor coolant environment on the fracture toughness of CASS materials are also discussed.

The degradation of the fracture toughness of austenitic SS welds during service in LWRs has also been evaluated. The approach used to evaluate thermal and neutron embrittlement of SS welds relies on establishing a lower-bound fracture toughness J-R curve for unaged and aged and non-irradiated and irradiated SS welds. The results indicate that CASS materials with very poor fracture toughness (e.g., SA and SMA welds) are relatively more insensitive to thermal aging than the GTA welds. Existing data on the potential combined effects of thermal and neutron embrittlement of austenitic SS welds indicate that the bounding values of coefficient C and exponent n of the fracture toughness J-R curve are about 117 kJ/m^2 and 0.45, respectively, for welds irradiated less than 0.1 dpa and 25 kJ/m^2 and 0.20 for welds irradiated above 7 dpa.

The evaluation identified the following two potential effects of low-level seismic loading on material aging degradation process.

(i) Limited data indicate that under certain combinations of temperature, strain rate, and environment, the fracture toughness of CASS materials, particularly thermally aged material, is lower at high strain rates than that at the low strain rate typically used in fracture toughness J-R curve tests. Similar data on austenitic SSs welds are not available.

(ii) Significant effects of the reactor coolant environment on the fracture toughness of thermally aged CASS materials or Alloys 600 and 690 have been observed at quasi-static loading rates and relatively low temperatures (e.g., 54°C [129°F]). Additional data on strain rate effects are needed to identify the combination of material, loading, and environmental conditions that may lead to the potential effects of seismic loading on fracture toughness of reactor structural materials.

4.4.2 Fatigue Crack Initiation and Growth

During cyclic loading, surface cracks, 5 μm or longer, form early in life at surface irregularities either already in existence or produced by slip bands, grain boundaries, second-phase particles, etc. Typically, fatigue life may be considered to constitute propagation of cracks from 10 to 3,000 μm long, and fatigue damage in a material may be considered as the current size of the fatigue crack. However, the growth rates of micro-structurally short cracks (i.e., ≤200 μm) cannot be predicted accurately from fracture mechanics methods. The micro-structurally short fatigue cracks grow at a faster rate than longer fatigue cracks. Fatigue cracks greater than the critical size (i.e., >200 μm) show little or no influence of microstructure, and their growth rates can be expressed in terms of the fracture mechanics parameters.

The environmental enhancement of fatigue crack growth in LWR environments and the effects of loading rate, flow velocities, and sulfur content (for carbon and low-alloy steels) are described in the report. The enhanced CGRs in LWR coolant environments are attributed to either slip oxidation/dissolution or hydrogen-induced cracking mechanisms. According to the slip/dissolution model, for carbon and low-alloy steels, dissolution of MnS inclusions changes the water chemistry near the crack tip, making it more aggressive. Hydrogen-induced cracking of materials is caused by hydrogen produced by the oxidation reaction at the crack tip that is partly absorbed into the metal; it interacts with MnS inclusions and leads to the formation of cleavage cracks at the inclusion matrix interface. In addition, DSA can occur in alloys containing solutes that segregate strongly to dislocations, resulting in strong interactions with the stress-strain field of the dislocations. Under certain combinations of temperature and strain rate conditions, DSA may significantly affect the EAC behavior of carbon and low-alloy steels.

For austenitic SSs, existing data suggest that hydrogen–induced cracking plays an important role in environmentally assisted reduction in fatigue lives of austenitic SSs. For example, hydrogen can cause localized crack tip plasticity by reducing the stress required for dislocation motion, which leads to higher rates and larger steps of oxide film rupture. Thus, fatigue lives are decreased because of increased film rupture frequency. The long-term role of hydrogen on corrosion fatigue and the possible synergistic effects of DSA are not yet clear for austenitic SSs. Typically, at temperatures above 400°C (752°F), the fatigue life of austenitic SSs decreased with an increase in temperature or a decrease in strain rate.

The potential effects of below-DBE loading on corrosion fatigue initiation and growth rates in reactor structural materials have been evaluated. The following three material degradation processes are identified.

(i) Under certain temperature and strain rate conditions, carbon and low-alloy steels or austenitic SSs exhibit reversed strain rate dependence. Its potential effect on design of reactor primary pressure boundary and safety-related components needs to be evaluated. Potential effects of strain rate on fracture properties of SS welds also need to be evaluated.

(ii) During fatigue loading, the microstructure of the material is significantly altered because of the interactions between dislocations and interstitial atoms. Since sudden and repeated below-OBE loading generally involves high-cycle, elastic-strain cycling, which is likely to generate point defects that would have a strong effect on dislocation motion and therefore the material microstructure, particularly at reactor operating temperatures. Therefore, low-level seismic loading is likely to influence growth of existing flaws.

(iii) Limited data indicate that under a combination of environment and loading conditions, even a ripple loading can enhance SCC or corrosion fatigue CGRs of reactor structural materials at intermediate temperatures (i.e., 180–270°C [356–518°F]) where DSA is likely to occur. Significant effects on CGRs have been observed in low-alloy steels in NWC or HWC BWR environments. Similar data are not available for austenitic SSs. Therefore, the cumulative effect of low-level seismic loading on the SCC growth rates of structural materials needs to be evaluated.

5 REFERENCES

1. Andresen, P.L., F.P. Ford, K. Gott, R.L. Jones, P.M. Scott, T. Shoji, R.W. Staehle, and R.L. Tapping, "Expert Panel Report on Proactive Materials Degradation Assessment," NUREG/CR-6923, BNL-NUREG-77111-2006, Nuclear Regulatory Commission, Washington, DC, 2007.

2. NRC, "Generic Aging Lessons Learned (GALL) Report," NUREG-1801, Rev. 2, Washington, DC, Dec. 2010.

3. Lian, T., "EPRI Materials Degradation Matrix," Rev. 3, Electric Power Research Institute, Palo Alto, CA, May 2013.

4. Gott, K., "Databases of Operationally Induced Damage," *Proc. 15th Intl. Conf. on Environmental Degradation of Materials in Nuclear Power Systems—Water Reactors*, J. T. Busby, G. Ilevbare, and P.L. Andresen, eds., The Minerals, Metals & Materials Society, Warrendale, PA, pp. 1829–1841, 2011.

5. IAEA (International Atomic Energy Agency), "Assessment and Management of Aging of Major Nuclear Power Plant Components Important to Safety: PWR Vessel Internals," IAEA-TECDOC-1557, Vienna, June 2007.

6. IAEA, "Aging Management for Nuclear Power Plants," Safety Guide No. NS-G-2.12, Safety Standards, Vienna, 2009.

7. IAEA, "Proactive Management of Aging for Nuclear Power Plants," Technical Reports Series No. 62, Vienna, 2009.

8. Jones, D.A., *Principles and Prevention of Corrosion*, Prentice Hall, 2nd ed., 1996.

9. Berg, H.-P., "Corrosion Mechanisms and Their Consequences for Nuclear Power Plants with Light Water Reactors," *Reliability and Risk Analysis: Theory and Applications*, 2 (4), Dec. 2009.

10. Newman, R., "Pitting Corrosion of Metals," *The Electrochemical Society Interface*, 33–38, Spring 2010.

11. Johnson, C.J., "Stagnant Water and Microbiologically Induced Corrosion in Cooling Water Systems," EPRI Report TR-101541, Chapter 12, 1993.

12. EPRI, "Recommendations for an Effective Flow-Accelerated Corrosion Program (NSAC-202L-R4)," EPRI 3002000563, Palo Alto, CA, Nov. 2013.

13. EPRI, "Investigations into Flow-Accelerated Corrosion at Low Temperatures," EPRI Report 1013474, Electric Power Research Institute, Palo Alto, CA, Nov. 2006.

14. Garud, Y.S., "Issues and Advances in the Assessment of Flow Accelerated Corrosion," *Proc. 14th Intl. Conf. on Environmental Degradation of Materials in Nuclear Power Systems—Water Reactors*, American Nuclear Society, Lagrange Park, IL, pp. 962–972, 2009.

15. Chopra, O.K., and G.L. Stevens, "Effects of LWR Coolant Environments on the Fatigue Life of Reactor Materials, Draft Report for Comment," NUREG/CR-6909 Rev 1, ANL-12/60, March 2014.

16. Bruemmer, S.M., et al., "Critical Issue Reviews for the Understanding and Evaluation of Irradiation-Assisted Stress Corrosion Cracking," EPRI TR-107159, Electric Power Research Institute, Palo Alto, CA, 1996.

17. Was, G.S., and P.L. Andresen, "Stress Corrosion Cracking Behavior of Alloys in Aggressive Nuclear Reactor Core Environments," *Corrosion,* 63, 19–45, 2007.

18. Bruemmer, S.M., E.P. Simonen, P.M. Scott, P.L. Andresen, G.S. Was, and J.L. Nelson, "Radiation-Induced Material Changes and Susceptibility to Intergranular Failure of Light-Water-Reactor Core Internals," *J. Nucl. Mater.,* 274, 299–314, 1999.

19. Herrera, M.L., et al., "Evaluation of the Effects of Irradiation on the Fracture Toughness of BWR Internal Components," *Proc. ASME/JSME 4th Intl. Conf. on Nucl. Eng. (ICONE-4)*, Vol. 5, A.S. Rao, R.M. Duffey, and D. Elias, eds., American Society of Mechanical Engineers, New York, pp. 245–251, 1996.

20. Mills, W.J., "Fracture Toughness of Irradiated Stainless Steels Alloys," *Nucl. Technol.*, 82, 290–303, 1988.

21. Mills, W.J., "Fracture Toughness of Type 304 and 316 Stainless Steels and Their Welds," *Intl. Mater. Rev.,* 42, 45–82, 1997.

22. Xu, H., and S. Fyfitch, "Materials Reliability Program: A Review of Radiation Embrittlement for Stainless Steels (MRP-79)," Rev. 1, EPRI Report 1008204, Electric Power Research Institute, Palo Alto, CA, Sept. 2004.

23. Ehrnsten, U., K. Wallin, P. Karjalainen-Roikonen, S. van Dyck, and P. Ould, "Fracture Toughness of Stainless Steels Irradiated to ~9 dpa in Commercial BWRs," *Proc. 6th Intl. Symp. on Contribution of Materials Investigations to Improve the Safety and Performance of LWRs*, Vol. 1, Fontevraud 6, French Nuclear Energy Society, SFEN, Fontevraud Royal Abbey, France, pp. 661–670, Sept. 18–22, 2006.

24. Carter, R.G., and R.M. Gamble, "Assessment of the Fracture Toughness of Irradiated Stainless Steel for BWR Core Shrouds," *Fontevraud 5 Intl. Symp., Contribution of Materials Investigation to the Resolution of Problems Encountered in Pressurized Water Reactors*, Avignon, France, Sept. 25, 2002.

25. O'Donnell, I.J., H. Huthmann, and A.A. Tavassoli, "The Fracture Toughness Behaviour of Austenitic Steels and Weld Metal Including the Effects of Thermal Aging and Irradiation," *Intl. J. Pressure Vessels Piping,* 65 (3), 209–220, 1996.

26. Kim, C., R. Lott, S. Byrne, M. Burke, and G. Gerzen, "Embrittlement of Cast Austenitic Stainless Steel Reactor Internals Components," *Proc. 6th Intl. Symp. on Contribution of Materials Investigations to Improve the Safety and Performance of LWRs*, Vol. 1, Fontevraud 6, French Nuclear Energy Society, SFEN, Fontevraud Royal Abbey, France, Sept. 18–22, 2006.

27. Demma, A., R. Carter, A. Jenssen, T. Torimaru, and R. Gamble, “Fracture Toughness of Highly Irradiated Stainless Steels in Boiling Water Reactors,” *Proc. 13th Intl. Conf. on Environmental Degradation of Materials in Nuclear Power Systems–Water Reactors*, T.R. Allen, P.J. King, and L. Nelson, eds., Canadian Nuclear Society, Toronto, Canada, Paper No. 114, 2007.

28. Fyfitch, S., H. Xu, A. Demma, R. Carter, R. Gamble, and P. Scott, “Fracture Toughness of Irradiated Stainless Steel in Nuclear Power Systems,” *Proc. 14th Intl. Conf. on Environmental Degradation of Materials in Nuclear Power Systems—Water Reactors*, American Nuclear Society, Lagrange Park, IL, 2009.

29. Fyfitch, S., H. Xu, K. Moore, and R. Gurdal, “Materials Reliability Program: PWR Internals Material Aging Degradation Mechanism Screening and Threshold Values (MRP-175),” EPRI Report 1012081, Dec. 2005.

30. EPRI, Materials Reliability Program, “Fracture Toughness Testing of Decommissioned PWR Core Internals Material Samples (MRP-160),” EPRI Report 1012079, Sept. 2005.

31. Chopra, O.K., and A.S. Rao, “A Review of Irradiation Effects on LWR Core Internal Materials - Neutron Embrittlement,” *J. Nucl. Mater.,* 412, 195–208, 2011.

32. Chopra, O.K., “Degradation of LWR Core Internal Materials Due to Neutron Irradiation,” NUREG/CR-7027, Dec. 2010.

33. Andresen, P.L. “Emerging Issues and Fundamental Processes in Environmental Cracking in Hot Water,” *Proc. Research Topical Symposium on Environmental Cracking, Corrosion/07*, NACE, 2007.

34. Edwards, D., E. Simonen, and S. Bruemmer, “Radiation-Induced Segregation Behavior in Austenitic Stainless Steels: Fast Reactor versus Light Water Reactor Irradiations,” *Proc. 13th Intl. Conf. on Environmental Degradation of Materials in Nuclear Power Systems—Water Reactors*, T.R. Allen, P.J. King, and L. Nelson, eds., Canadian Nuclear Society, Toronto, Canada, Paper No. P0139, 2007.

35. Fyfitch, S., H. Xu, P. Scott, L. Fournier, and A. Demma, “Criteria for Initiation of Irradiation-Assisted Stress Corrosion Cracking in Stainless Steels in PWR Systems,” *Proc. 14th Intl. Conf. on Environmental Degradation of Materials in Nuclear Power Systems—Water Reactors*, American Nuclear Society, Lagrange Park, IL, 2009.

36. Jenssen, A., J. Stjarnsater, and R. Pathania, “Crack Growth Rates of Irradiated Commercial Stainless Steels in BWR and PWR Environments,” *Proc. 15th Intl. Conf. on Environmental Degradation of Materials in Nuclear Power Systems—Water Reactors*, J.T. Busby, G. Ilevbare, and P.L. Andresen, eds., The Minerals, Metals & Materials Society, Warrendale, PA, pp. 1229–1240, 2011.

37. Chopra, O.K., and A.S. Rao, “A Review of Irradiation Effects on LWR Core Internal Materials–IASCC Susceptibility and Crack Growth Rates of Austenitic Stainless Steels,” *J. Nucl. Mater.,* 409, 235–256, 2011.

38. NRC, “Domestic Licensing of Production and Utilization Facilities*,” Code of Federal Regulations*, Title 10, Energy, Part 50 (10 CFR Part 50), Washington, DC.

39. NRC, “Appendix A to Part 50, “General Design Criteria for Nuclear Power Plants” (10 CFR Part 50).

40. Office of the *Federal Register*, National Archives and Records Administration, “Appendix A to Part 50, “General Design Criteria for Nuclear Power Plants*”* (10 CFR Part 50), Washington, DC.

41. Campbell, K.W., and Y. Bozorgnia, “A Ground Motion Prediction Equation for the Horizontal Component of Cumulative Absolute Velocity on the PEER-NGA Strong Motion Database,” *Earthquake Spectra*, 26 (3), 635–650, Aug. 2010.

42. EPRI, “A Criterion for Determining Exceedance of the Operating Basis Earthquake,” EPRI NP-5930, Electric Power Research Institute, Palo Alto, CA, 1988.

43. Office of the *Federal Register*, National Archives and Records Administration, “Appendix J to Part 50, “Primary Reactor Containment Leakage Testing for Water-Cooled Power Reactors” (10 CFR Part 50), Washington, DC.

44. ASME, “Section XI. Rules for In-service Inspection of Nuclear Power Plant Components,” The ASME Boiler and Pressure Vessel Code, 2004 edition as approved in 10 CFR 50.55a, ASME Boiler and Pressure Vessel Code, New York, NY.

45. Huang, C.T., W.D. Iwan, K.R. Jaquay, and N.C. Chokshi, “Analytical study of frequency effects on seismic margins,” *Trans. of the 14th Int. Conf. on Structural Mechanics and Reactor Technology (SMiRT 14)*, Lyon, France, Paper K13/5, 1997.

46. Machida, H., “Effect of Dispersion of Seismic Load on Integrity of Nuclear Power Plant Piping,” *Trans. of the 16th Int. Conf. on Structural Mechanics and Reactor Technology (SMiRT 16)*, Washington DC, Paper # 116, 2001.

47. Ranganath, S., “Piping and Fitting Dynamic Reliability Program,” EPRI TR-102792, Volume 1–5, Palo Alto, CA, Oct. 1994.

48. DeGrassi, G., J. Nie, and C. Hofmayer, “Seismic Analysis of Large-Scale Piping Systems for the JNES/NUPEC Ultimate Strength Piping Test Program,” NUREG/CR-6983, 2008.

49. Shao, L.C., A.J. Murphy, N. Chokshi, P-T. Kuo, and T.Y. Chang, “Seismic responses and resistance of age degraded structures and components,” *Nucl. Eng. Des.,* 181, 3–15, 1998.

50. Zhang, T., F.W. Brust, D.J. Shim, G. Wilkowski, J. Nie, and C. Hofmayer, “Analysis of JNES Seismic Tests on Degraded Piping,” NUREG/CR-7015, 2010.

51. NRC, “A Performance-Based Approach to Define the Site-Specific Earthquake Ground Motion,” Regulatory Guide 1.208, Washington, DC, March 2007.

52. Office of the *Federal Register*, National Archives and Records Administration “Appendix S to Part 50, “Earthquake Engineering Criteria for Nuclear Power Plants” (10 CFR Part 50), Washington, DC.

53. Roy, H., S. Sivaprasad, S. Tarafder, and K.K. Ray, “Cyclic fracture behaviour of 304LN stainless steel under load and displacement control modes,” *Fatigue Frac. Eng. Mat. Struct.*, 35 (2), 108–113, 2012.

54. Office of the *Federal Register*, National Archives and Records Administration, “Appendix B to Part 50, “Quality Assurance Criteria for Nuclear Power Plants and Fuel Reprocessing Plants” (10 CFR Part 50), Washington, DC.

55. Office of the *Federal Register*, National Archives and Records Administration, “Codes and Standards” (10 CFR 50.55a), Washington, DC.

56. ASME Code Section III, *Rules for Construction of Nuclear Facility Components, Division 1, Subsection NB, Class 1 Components*, ASM 60E Boiler and Pressure Vessel Code, American Society of Mechanical Engineers, New York, NY.

57. ASME, “Section III, Rules for Construction of Nuclear Facility Components, Division 1, Subsection NB, Class 1 Components,” ASME Boiler and Pressure Vessel Code, American Society of Mechanical Engineers, New York, NY.

58. NRC, “Quality Group Classifications and Standards for Water-, Steam-, and Radioactive-Waste-Containing Components of Nuclear Power Plants,” Regulatory Guide 1.26, Washington, DC.

59. NRC, “Design, Fabrication, and Materials Code Case Acceptability, ASME Section III,” Regulatory Guide 1.84, Washington, DC.

60. NRC, “ASME Code Cases Not Approved for Use,” Regulatory Guide 1.193, Washington, DC.

61. Stevenson, J.D., “Historical International Development of Seismic Design and Analysis of Nuclear Power Plant Structures, Systems, and Components over the Last 60 Years,” OECD Nuclear Energy Agency, Nov. 19, 2010.

62. Lockheed Aircraft Corporation and Holmes & Narver, Inc., “Nuclear Reactors and Earthquakes,” TID-7024 prepared for the U.S. Atomic Energy Commission, Washington, DC, Aug. 1963.

63. Andrews, A., and P. Folger, “Nuclear Power Plant Design and Seismic Safety Consideration,” CRS 7-5700 R41805, Congressional Research Service, Library of Congress, Washington, DC, Jan. 12, 2012.

64. NRC, “Design Response Spectra for Seismic Design of Nuclear Power Plants,” Regulatory Guide 1.60, Rev. 2,Washington, DC, July 2014.

65. NRC, “Seismic Design Classification,” Regulatory Guide 1.29, Washington, DC.

66. NRC, “Damping Values for Seismic Design of Nuclear Power Plants,” Regulatory Guide 1.61, Washington, DC.

67. NRC, “Combining Modal Responses and Spatial Components in Seismic Response Analysis,” Regulatory Guide 1.92, Washington, DC.

68. ASME, “Non-Mandatory Appendix N, ASME Code Section III, Boiler and Pressure Vessel Code, Section III, Division 1, Dynamic Analysis Methods,” New York, NY.

69. Newmark, N.M., and W.J. Hall, “Seismic Design Criteria for Nuclear Reactor Facilities,” *Proc. of Fourth World Conf. on Earthquake Engineering*, Vol. 2, pp. B4-37 to B4-50, Santiago, Chile, Jan. 1969.

70. Clarke, R., “Introduction to IBC Seismic Forces,” University of West Indies, St. Augustine, Sept. 2014. Available at http://richardpclarke.tripod.com/seismicload1.pdf.

71. NIST (National Institute of Standards and Technology), U.S. Department of Commerce, “Soil-Structure Interaction for Building Structures,” GCR 12-917-21, Gaithersburg, MD, Sept. 2012.

72. Veletsos, A.S., and N.M. Newmark, “Effect of Inelastic Behavior on the Response of Simple Systems to Earthquake Motions,” *Proc. Second World Conference on Earthquake Engineering (2WCEE)*, July 11–18, 1960. Available at http://nisee.berkeley.edu/elibrary/getpkg?id=S30595 (accessed Nov. 2014).

73. NRC, Rev. 1, “Damping Values for Seismic Design of Nuclear Power Plants,” Regulatory Guide 1.61, Washington, DC, March 2007.

74. NRC, “Standard Review Plan for the Review of Safety Analysis Reports for Nuclear Power Plants: LWR Edition,” NUREG-0800, Washington, DC, June 1987.

75. NRC, “Identification and Characterization of Seismic Sources and Determination of Safe Shutdown Earthquake Ground Motion,” Regulatory Guide 1.165, Washington, DC, March 1997.

76. Newmark, N.M., J.A. Blume, and K.K. Kapur, “Design Response Spectra for Nuclear Power Plants,” American Society of Civil Engineers (ASCE) Structural Engineering Meeting, San Francisco, April 1973 (ADAMS Accession No. ML13207A044).

77. Newmark, N.M., J.A. Blume, and K.K. Kapur, “Seismic Design Spectra for Nuclear Power Plants,” *Journal Power Div., ASCE*, pp. 287–303, November 1973 (ADAMS Accession No. ML13207A045).

78. Newmark, N.M., Consulting Engineering Services, “A Study of Vertical and Horizontal Earthquake Spectra,” Urbana, IL, USAEC Contract No. AT(49-5)-2667, WASH-1255, April 1973 (ADAMS Accession No. ML13203A235).

79. John A. Blume & Associates, “Recommendations for Shape of Earthquake Response Spectra,” San Francisco, California, USAEC Contract No. AT(49-5)-3011, WASH-1254, San Francisco, CA, Feb. 1973 (ADAMS Accession No. ML13203A236).

80. NRC, “Development of Floor Design Response Spectra for Seismic Design of Floor-Supported Equipment or Components,” Regulatory Guide 1.122, Washington, DC, Feb. 1978.

81. IAEA, “Optimization of Water Chemistry to Ensure Reliable Water Reactor Fuel Performance at High Burnup and in Ageing Plant (FUWAC),” Technical Reports Series No. 128, Vienna, 2011.

82. EPRI, “Pressurized Water Reactor Primary Water Chemistry Guidelines: Revision 7,” Vols. 1 and 2, Palo Alto, CA, 2014.

83. EPRI, “BWRVIP-190 Revision 1: BWR Vessel and Internals Project, Volume 1: BWR Water Chemistry Guidelines - Mandatory, Needed, and Good Practice Guidance,” and Volume 2: “BWR Water Chemistry Guidelines - Technical Basis,” 692, Palo Alto, CA, 2014.

84. Potter, E.C., and G.M.W. Mann, “Oxidation of Mild Steel in High-temperature Aqueous Systems,” in *1st International Congress on Metallic Corrosion*, London, Butterworths, 1961.

85. Broomfield, J.P., J.E. Forrest, D.R. Holmes, and M.I. Manning, “Oxide Growth Mechanisms on Cr Alloy Steels,” EPRI NP-4647, Palo Alto, CA, 1986.

86. Robertson, J., “The Mechanism of High Temperature Aqueous Corrosion of Steel,” *Corros. Sci.*, 29 (11–12), 1275–1291, 1989.

87. Mann, G.M.W., “The Oxidation of Iron Base Alloys Containing Less Than 12% Cr in High Temperature Aqueous Solutions,” pp. 34–47 in *High Temperature High Pressure Electrochemistry in Aqueous Solutions* conference held at The University of Surrey, England, January 7–12, 1973, published by the National Association of Corrosion Engineers.

88. Vreeland, D.C., G.G. Gaul, and W.L. Pearl, “Corrosion of Carbon Steel and Other Steels in Simulated Boiling-Water Reactor Environment: Phase II,” *Corrosion*, 18, 368t–377t, 1962.

89. Francis, J.M., and W.H. Whitlow, “The Morphology of Oxide Film Growth on AISI Type 304 Stainless Steel in High Temperature Water at 300 and 350°C,” *J. Nucl. Mater.*, 20, pp. 1–10, 1966.

90. Nakayama, T., and Y. Oshida, “Identification of the Initial Oxide Films on 18-8 Stainless Steel in High Temperature Water,” *Corrosion*, 24 (10), pp. 336–337, 1968.

91. Warzee, M., C. Sonnen, and P. Berge, “Corrosions of Carbon Steels and Stainless Steels in Pressurized Water at High Temperatures,” Brussels, 1967.

92. Bauch, R., M. Cambini, P. Weisgerber, C. Deasmundis, and C. Plog, “Investigations on Oxide Formed in High-Temperature Water on Austenitic Steel,” *J. Nucl. Mater.*, 92 (2–3), pp. 334–344, 1980.

93. Lister, D.H., R.D. Davidson, and E. McAlpine, “The Mechanism and Kinetics of Corrosion Product Release from Stainless Steel in Lithiated High Temperature Water,” *Corros. Sci.*, 27 (2), pp. 113–140, 1987.

94. Stellwag, B., The Mechanism of Oxide Film Formation on Austenitic Stainless Steels in High Temperature Water, *Corros. Sci.*, 40 (2/3), pp. 337–370, 1998.

95. Kim, Y.-J., “Characterization of the Oxide Film Formed on Type 316 Stainless Steel in 288°C Water in Cyclic Normal and Hydrogen Water Chemistries,” *Corrosion*, 51 (11), pp. 849–860, 1995.

96. Kim, Y.-J., "Analysis of Oxide Film Formed on Type 304 Stainless Steel in 288°C Water Containing Oxygen, Hydrogen, and Hydrogen Peroxide," *Corrosion*, 55 (1), pp. 81–88, 1999.

97. Ziemniak, S.E., and M. Hanson, "Corrosion Behavior of 304 Stainless Steel in High Temperature, Hydrogenated Water," *Corros. Sci*., 44, pp. 2209–2230, 2002.

98. Terachi, T., K. Fujii, and K. Arioka, "Microstructural Characterization of SCC Crack Tip and Oxide Film for SUS 316 Stainless Steel in Simulated PWR Primary Water at 320°C," *J. Nucl. Sci. Technol.*, 42 (2), 225–232, 2005.

99. Cissé, S., L. Laffont, B. Tanguy, M.-C. Lafont, and E. Andrieu, "Effect of Surface Preparation on the Corrosion of Austenitic Stainless Steel 304L in High Temperature Steam and Simulated PWR Primary Water," *Corros. Sci.*, 56, 209–216, 2012.

100. Belo, M.D.C., M. Walls, N.E. Hakiki, J. Corset, E. Piquenard, G. Sagon, and D. Noel, "Composition, Structure and Properties of the Oxide Films Formed on the Stainless Steel 316L in a Primary Type PWR Environment," *Corros. Sci.*, 40 (2–3), 447–463, 1998.

101. Perrin, S., L. Marchetti, C. Duhamel, M. Sennour, and F. Jomard, "Influence of Irradiation on the Oxide Film Formed on 316 L Stainless Steel in PWR Primary Water," *Oxidation of Metals*, 80 (5–6), 623–633, 2013.

102. Yassar, R.S., L. Scudiero, A.S. Alamr, D.F. Bahr, and M.G. Norton, "Microstructure-Mechanical and Chemical Behavior Relationships in Passive Thin Films," *Thin Solid Films*, 518 (10), 2757–2763, 2010.

103. Soulas, R., M. Cheynet, E. Rauch, T. Neisius, L. Legras, C. Domain, and Y. Brechet, "TEM Investigations of the Oxide Layers Formed on a 316L Alloy in Simulated PWR Environment," *J. Mater. Sci.*, 48 (7), 2861–2871, 2013.

104. Hirano, H., N. Aoki, and T. Kurosawa, "The Effect of Dissolved Oxygen and NO3- Anions on the Stress Corrosion Cracking of Type 304 Stainless Steel in Water at 290°C," *Corrosion*, 39 (8), 313–322, 1983.

105. Tapping, R.L., R.D. Davidson, E. McAlpine, and D.H. Lister, "The Composition and Morphology of Oxide Films Formed on Type 304 Stainless Steel in Lithiated High Temperature Water," *Corros. Sci.*, 26 (8), 563–576. 1986.

106. Robertson, J., "The Mechanism of High Temperature Aqueous Corrosion of Stainless Steel," *Corros. Sci.*, 32 (4), 443–465, 1991.

107. Miyazawa, T., T. Terachi, S. Uchida, T. Satoh, T. Tsukada, Y. Satoh, and H. Hosokawa, "Effects of Hydrogen Peroxide on Corrosion of Stainless Steel, (V) Characterization of Oxide Film with Multilateral Surface Analyses," *J. Nucl. Sci. Technol.*, 43 (8), 884–895, 2006.

108. Sandler, Y.L., "Structure of PWR Primary Corrosion Products," *Corrosion*, 35 (5), 205–208, 1979.

109. Schuster, E., K.H. Neeb, W. Ahlfanger, R. Henkelmann, and R.T. Jarnstrom, “Analyses of Primary Side Oxide Layers on Steam Generator Tubes from PWRs and Radiochemical Issues on the Contamination of Primary Circuits,” *J. Nucl. Mater.*, 152 (1), 1–8, 1988.

110. Lozano-Perez, S., D.W. Saxey, T. Yamada, and T. Terachi, “Atom-Probe Tomography Characterization of the Oxidation of Stainless Steel,” *Scripta Mater.*, 62 (11), 855–858, 2010.

111. Dumerval, M., S. Perrin, L. Marchetti, M. Tabarant, F. Jomard, and Y. Wouters, “Hydrogen Absorption Associated with the Corrosion Mechanism of 316L Stainless Steels in Primary Medium of Pressurized Water Reactor (PWR),” *Corros. Sci.*, 85, 251–257, 2014.

112. Sennour, M., L. Marchetti, F. Martin, S. Perrin, R. Molins, and M. Pijolat, “A Detailed TEM and SEM Study of Ni-base Alloys Oxide Scales Formed in Primary Conditions of Pressurized Water Reactor,” *J. Nucl. Mater.*, 402 (2–3), pp. 147–156, 2010.

113. Wang, J.Q., X.H. Li, F. Huang, Z.M. Zhang, J.Z. Wang, and R.W. Staehle, “Comparison of Corrosion Resistance of UNS N06690TT and UNS N08800SN in Simulated Primary Water with Various Concentrations of Dissolved Oxygen,” *Corrosion*, 70 (6), 598–614, 2014.

114. Panter, J., B. Viguier, J.M. Cloué, M. Foucault, P. Combrade, and E. Andrieu, “Influence of Oxide Films on Primary Water Stress Corrosion Cracking Initiation of Alloy 600,” *J. Nucl. Mater.*, 348 (1–2), 213–221, 2006.

115. Marchetti, L., S. Perrin, F. Jambon, and M. Pijolat, “Corrosion of Nickel-Base Alloys in Primary Medium of Pressurized Water Reactors: New Insights on the Oxide Growth Mechanisms and Kinetic Modeling”, *Corros. Sci.*, 102, 24–35, 2016.

116. Carrette, F., M.C. Lafont, G. Chatainier, L. Guinard, and B. Pieraggi, “Analysis and TEM Examination of Corrosion Scales Grown on Alloy 690 Exposed to Pressurized Water at 325^{o}C,” *Surf. Interface Anal.*, 34 (1), 135–138, 2002.

117. Kuang, W., X. Wu, and E.-H. Han, “Influence of Dissolved Oxygen Concentration on the Oxide Film Formed on Alloy 690 in High Temperature Water,” *Corros. Sci.*, 69, 197–204, 2013.

118. Allen, G.C., J.M. Dyke, S.J. Harris, and A. Morris, “A Surface Study of the Oxidation of Type 304L Stainless Steel at 600 K in Air,” *Oxid. Met.*, 29 (5–6), 391–408, 1988.

119. Jambon, F., L. Marchetti, F. Jomard, and J. Chêne, “Characterization of Oxygen and Hydrogen Migration through Oxide Scales Formed on Nickel-Base Alloys in PWR Primary Medium Conditions,” *Solid State Ionics*, 231, 69–73, 2013.

120. Han, Y., J. Mei, Q. Peng, E.-H. Han, and W. Ke, “Effect of Electro-polishing on Corrosion of Alloy 600 in High Temperature Water,” *Corros. Sci.*, 98, 72–80, 2015.

121. Souier, T., and M. Chiesa, “ Effect of Surface Conditions and Strain Hardening on the Passivity Breakdown of 304 Stainless Steel,” *J. Mater. Res.*, 27 (12), 1580–1588, 2012.

122. Alamr, A., D.F. Bahr, and M. Jacroux, “Effects of Alloy and Solution Chemistry on the Fracture of Passive Films on Austenitic Stainless Steel,” *Corros. Sci.*, 48, pp. 925–936, 2006.

123. Navai, F., “Effects of Tensile and Compressive Stresses on the Passive Layers Formed on a Type 302 Stainless Steel in a Normal Sulfuric Acid Bath,” *J. Mater. Sci.*, 30, 1166–1172, 1995.

124. Takeda, Y., M. Bojinov, H. Hanninen, P. Kinnunen, T. Laitinem, K. Makela, T. Saario, K. Sakaguchi, T. Shoji, P. Sirkia, and A. Toivonen, “Comparison of the Electric Properties and ESCA Result of Oxide Films Formed on AISI 316L Steel in Simulated BWR Conditions During SSRT,” *Key Engineering Materials*, Vols. 261–263 (Advances in Fracture and Failure Prevention), pp. 925–930, 2004.

125. Navai, F., and O. Debbouz, “AES Study of Passive Films Formed on a Type 316 Austenitic Stainless-Steels in a Stress Field,” *J. Mater. Sci.*, 34, 1073–1079, 1999.

126. Darowicki, K., J. Orlikowski, and A. Arutunov, “Dynamic Electrochemical Impedance Spectroscopy Measurements of Passive Layer Cracking under Static Tensile Stresses,” *J. Sol. State Electrochem.*, 8 (6), 352–359, 2004.

127. Darowicki, K., J. Orlikowski, and A. Arutunov, and W. Jurczak “The Effect of Strain Rate on the Passive Layer Cracking of 304L Stainless Steel in Chloride Solutions Based on the Differential Analysis of Electrochemical Parameters Obtained by Means of DEIS, *J. Electro-analytical Chem.*, 576, 277–285, 2005.

128. Pan, T., “Corrosion Behavior of a Duplex Stainless Steel under Cyclic Loading: A Scanning Kelvin Probe Force Microscopy (SKPFM) Based Microscopic Study,” *J. Appl. Electrochem.*, 42, 1049–1056, 2012.

129. Xu, L.Y., and Y.F. Cheng, “An Experimental Investigation of Corrosion of X100 Pipeline Steel under Uniaxial Elastic Stress in a Near-Neutral pH Solution,” *Corros. Sci.*, 59, 103–109, 2012.

130. Xu, L.Y., and Y.F. Cheng, “An Experimental Investigation of Corrosion of X100 Pipeline Steel under Plastic Strain in a Neutral pH Solution,” *Corros. Sci.*, 64 145–152, 2012.

131. Wang, Y., W. Zhao, H. Ai, X. Zhou, and T. Zhang, “Effects of Strain on the Corrosion Behavior of X80 Steel,” *Corros. Sci.*, 53 (9), 2761–2766, 2011.

132. Little, B., and J.S. Lee, “Case Histories,” Chapter 8 in *Microbiologically Influenced Corrosion*, pp. 150–216, John Wiley & Sons, Inc., Hoboken, New Jersey, 2007.

133. Naus, D.J., et al., “Summary and Conclusions of a Program Addressing Aging of Nuclear Power Plant Structures,” *Nuclear Engineering and Design*, Vol. 194, No. 1, pp.73–96, 1999.

134. Bowman, C.F., and P.V. Guthrie, Jr., “Corrosion in Carbon Steel Service Water Piping,” in *Codes and Standards for Quality Engineering: PVP-Volume 285*, 1994 ASME PVP Conference, American Society of Mechanical Engineers, New York, NY, 1994.

135. Tawancy, H.M., and L.M. Al-Hadhrami, “Case Study: Pitting and Stress Corrosion Cracking in Heat-Affected Zone of Welded Underground 304 Stainless Steel Pipe,” *J. Mater. Eng. and Perform.*, 21 (8), 1757–1762, 2012.

136. Turnbull, A., “Modeling of the Chemistry and Electrochemistry in Cracks - A Review,” *Corrosion*, 57 (2), pp. 175–189, 2001.

137. Cho, K., and H.W. Pickering, “Demonstration of Crevice Corrosion in Alkaline Solution without Acidification,” *J. Electrochem. Soc*., 137 (10), 3313–3314, 1990.

138. Van Boven, G., W. Chen, and R. Rogge, “The Role of Residual Stress in Neutral pH Stress Corrosion Cracking of Pipeline Steels, Part1: Pitting and Cracking Occurrences,” *Acta Mater.,* 55 (1), 29–42, 2007.

139. Diercks, D.R, W.J. Shack, and J. Muscara, “Overview of Steam Generator Tube Degradation and Integrity Issues,” *Nucl. Eng. and Des.,* 194 (1), 19–30, 1999.

140. Beech, I.B., and C.C. Gaylarde, “Recent Advances in the Study of Biocorrosion - An Overview,” *Revista de Microbiologia*, Vol. 30, pp. 177–190, 1999.

141. Beyenal, H., and Z. Lewandowski, “Mass-Transport Dynamics, Activity, and Structure of Sulfate-Reducing Biofilms,” *AIChE Journal*, Vol. 47, No. 7, pp. 1689–1697, 2001.

142. Usher, K.M., A.H. Kaksonen, and D. Marney, “Critical Review: Microbially Influenced Corrosion of Buried Carbon Steel Pipes,” *International Biodeterioration & Biodegradation*, Vol. 93, No. 3–4, pp. 84–106, Sept. 2014.

143. Gu, J.-D., et al., “Microbiological Corrosion of Metallic Materials,” Chapter 39 in *Uhlig’s Corrosion Handbook,* 3rd ed., R. Winston Revie, ed., John Wiley & Sons, Inc., pp. 549–556, 2011.

144. Videla, H.A., “Microbially Induced Corrosion: an Updated Overview,” *International Biodeterioration & Biodegradation*, Vol. 48, Nos. 1–4, pp. 176–201, 2001.

145. EPRI, “Sourcebook for Microbiologically Influenced Corrosion in Nuclear Power Plants,” EPRI NP-5580, Palo Alto, CA, 1988.

146. Borenstein, S.W., *Microbiologically Influenced Corrosion Handbook*, Woodhead Publishing Ltd, Cambridge, England, 1994.

147. NACE, A, *Practical Manual on Microbiologically Influenced Corrosion, Volume 2*, 2nd ed., J.G. Stoecker II, ed., NACE International, Houston, TX, 2001.

148. Lewandowski, Z., and H. Beyenal, “Mechanisms of Microbially Influenced Corrosion,” *Marine and Industrial Biofouling*, Hans-Curt Flemming et al., eds., Springer Series on Biofilms, Vol. 4, pp. 35–64, Springer-Verlag Berlin Heidelberg, 2009.

149. Enning, D., and J. Garrelfs, “Corrosion of Iron by Sulfate-Reducing Bacteria: New Views of an Old Problem,” *Applied and Environmental Microbiology*, Vol. 80, No. 4, pp. 1226–1236, February 2014.

150. Little, B., and P. Wagner, “An Overview of Microbiologically Influenced Corrosion of Metals and Alloys Used in the Storage of Nuclear Wastes,” *Canadian Journal of Microbiology*, Vol. 42, pp. 367–374, 1996.

151. Lee, W., et al., “Role of Sulfate-reducing Bacteria in Corrosion of Mild Steel: A Review,” *Biofouling: The Journal of Bioadhesion and Biofilm Research*, Vol. 8, No. 3, pp. 165–194, 1995.

152. Bunker, H.J., “Microbiological Anaerobic Corrosion,” *Journal of Chemical Technology and Biotechnology*, Vol. 59, Issue 24, pp. 412–414, 1940.

153. Little, B., and J.S. Lee, “Causative Organisms and Possible Mechanisms,” Chapter 2 in *Microbiologically Influenced Corrosion*, pp. 22–55, John Wiley & Sons, Inc., Hoboken, NJ, 2007.

154. Rao, T.S., and V.R. Nair, “Microbiologically Influenced Stress Corrosion Cracking Failure of Admiralty Brass Condenser Tubes in a Nuclear Power Plant Cooled by Freshwater,” *Corrosion Science*, Vol. 40, No. 11, pp. 1821–1836, 1998.

155. Dexter, S.C., and J.P. LaFontaine, “Effect of Natural Marine Biofilms on Galvanic Corrosion,” *Corrosion*, Vol. 54, No. 11, pp. 851–861, 1998.

156. Robinson, M.J., and P.J. Kilgallon, “Hydrogen Embrittlement of Cathodically Protected High-Strength, Low-Alloy Steels Exposed to Sulfate-Reducing Bacteria,” *Corrosion*, Vol. 50, No. 8, pp. 626–635, 1994.

157. Little, B., and J.S. Lee, “Impact of Alloying Elements to Susceptibility of Microbiologically Influenced Corrosion,” Chapter 6 in *Microbiologically Influenced Corrosion*, pp. 127–146, John Wiley & Sons, Inc., Hoboken, NJ, 2007.

158. Javaherdashti, R., et al., “Microbiologically Assisted Stress Corrosion Cracking of Carbon Steel in Mixed and Pure Cultures of Sulfate Reducing Bacteria,” *International Biodeterioration & Biodegradation*, Vol. 58, No. 1, pp. 27–35, 2006.

159. Antony, P.J., et al., “Corrosion of 2205 Duplex Stainless Steel Weldment in Chloride Medium Containing Sulfate-Reducing Bacteria,” *Metallurgical and Materials Transactions A*, Vol. 39A, No. 11, pp. 2689–2697, 2008.

160. Moradi, M., et al., “De-Alloying of 316 Stainless Steel in the Presence of a Mixture of Metal-Oxidizing Bacteria,” *Corrosion Science*, Vol. 53, No. 12, pp. 4282–4290, 2011.

161. Pope, D.H., “A Study of Microbiologically Influenced Corrosion in Nuclear Power Plants and a Practical Guide for Countermeasures,” EPRI NP-4582, Palo Alto, CA, May 1986.

162. Licina, G.J., and D. Cubicciotti, “Microbial-Induced Corrosion in Nuclear Power Plant Materials,” *JOM - Journal of the Minerals, Metals and Materials Society*, Vol. 41, No. 12, pp. 23–27, Dec. 1989.

163. Brennenstuhl, A.M., et al., “Mechanisms of Underwater Corrosion in Freshwater Cooled Austenitic Alloy Heat Exchanger,” *Corrosion Science,* Vol. 35, Nos. 1–4, pp. 699–711, 1993.

164. Updegraff, D.M., “Microbiological Corrosion of Iron and Steel - A Review,” *Corrosion*, Vol. 11, No. 10, pp. 44–48, 1955.

165. NRC, “Microbiologically Induced Corrosion of Containment Service Water System,” *Information Notice No. 85–30*, U.S. Nuclear Regulatory Commission, Washington, DC, April 19, 1985.

166. NRC, “Service Water System Problems Affecting Safety-related Equipment,” *Generic Letter No. 89–13*, U.S. Nuclear Regulatory Commission, Washington, D.C., July 18, 1989.

167. NRC, “Microbiologically Influenced Corrosion of Emergency Diesel Generator Service Water Piping,” *Information Notice No. 94–79*, U.S. Nuclear Regulatory Commission, Washington, D.C., November 23, 1994.

168. Amerenue, “Proposed Alternative to ASME Section XI Requirements for Replacement of Class 3 Buried Piping in Accordance with 10 CFR 50.55a(a)(3)(i),” *ULNRC-05434, Callaway Nuclear Plant 10 CFR 50.55a Request Number 13R-10*, Aug. 30, 2007 (ADAMS Accession No: ML072550488).

169. Heitmann, H.G., and W. Kastner, “Erosion-Corrosion in Water-Steam Cycles - Causes and Countermeasure,” *VGB Kraftwerkstechnik*, Vol. 62, No. 3, 1982, pp. 180–187.

170. Heitz, E., “Chemo-Mechanical Effects of Flow on Corrosion,” *Corrosion*, Vol. 47, No. 2, 1991, pp. 135–145.

171. Cragnolino, G., C. Czajkowski, and W.J. Shack, “Review of Erosion-Corrosion in Single-Phase Flows,” NUREG/CR-5156, U.S. Nuclear Regulatory Commission, Washington, DC, June 1988.

172. Bouchacourt, M., et al. “The BRT-CICERO Code, an Exhaustive Approach to Predict the Flow Accelerated Corrosion,” in *Contribution of Materials Investigation to the Resolution of Problems Encountered in Pressurized Water Reactors, Vol.2*, pp. 761–768, SFEN, France, 1994.

173. Trevin, S., et al., “Flow Accelerated Corrosion Mitigation at EDF with BRT-CICERO. Feedback of Version 3 and Process of Validation,” in *Fontevraud 7 - Contribution of Materials Investigations to Improve the Safety and Performance of LWRs,* INIS-FR-11-0656, SFEN, France, 2011.

174. EPRI, CHECWORKS™ Steam/Feedwater Application (SFA), Version 4.0, Palo Alto, CA: 2012, 1025251.

175. EPRI, “Flow-Accelerated Corrosion in Power Plants,” EPRI TR-106611-R1, Palo Alto, CA, August 1998.

176. EPRI, “Recommendations for an Effective Flow-Accelerated Corrosion Program (NSAC-202L-R4),” Palo Alto, CA, 2013, 3002000563.

177. Wu, P.C. “Erosion/Corrosion-Induced Pipe Wall Thinning in U. S. Nuclear Power Plants,” *NUREG-1344*, U.S. Nuclear Regulatory Commission, Washington, DC, April 1989.

178. Trevin, S., “Flow Accelerated Corrosion (FAC) in Nuclear Power Plant Components,” *Nuclear Corrosion Science and Engineering*, Woodhead Publishing Limited, Oxford, UK, pp. 186–229, 2012.

179. Garud, Y.S., “Issues and Advances in the Assessment of Flow Accelerated Corrosion,” Paper No. 203160, *Proceedings of the 14th International Conference on Environmental Degradation of Materials in Nuclear Power Systems-Water Reactors*, American Nuclear Society, Lagrange Park, IL, pp. 962–972, 2009.

180. Yoneda, K., et al., “Evaluation of Hydraulic Factors Affecting Flow Accelerated Corrosion and Its Verification with Power Plant Data,” Paper No. PVP2009-77486, *Proceedings of the ASME 2009 Pressure Vessels and Piping Division Conference PVP2009*, July 26–30, Prague, Czech Republic, 2009.

181. Pietralik, J.M., and C.S. Schefski, “Flow and Mass Transfer in Bends Under Flow-Accelerated Corrosion Wall Thinning Conditions,” *Journal of Engineering for Gas Turbines and Power*, Transactions of the ASME, Vol. 133, Jan. 2011.

182. Pietralik, J.M., “The Role of Flow in Flow-Accelerated Corrosion under Nuclear Power Plant Conditions,” *E-Journal of Advanced Maintenance*, Japan Society of Maintenology, Vol. 4, No. 2, 2012, pp. 63–78.

183. Shakouchi, T., et al., “Effects of the Geometry of Flow Passages on Flow Accelerated Corrosion,” *Journal of Fluid Science and Technology*, Bulletin of the JSME, Vol. 9, No. 3, Paper No.14-00148, 2014.

184. KCP&L, “Root Cause Investigation of Pipe Rupture Event at the Iatan Plant, December 15, 2007, Volume 5: Lessons Learned from the Iatan Pipe Rupture Event,” Kansas City Power & Light, Kansas City, MO, 2007.

185. Poulson, B., “Predicting and Preventing Flow Accelerated Corrosion in Nuclear Power Plant,” *International Journal of Nuclear Energy*, Volume 2014, Article ID 423295, Hindawi Publishing Corporation.

186. Ford, F.P., D.F. Taylor, P.L. Andresen, and R.G. Ballinger, “Corrosion Assisted Cracking of Stainless and Low Alloy Steels in LWR Environments,” EPRI Report NP 5064M, Palo Alto, CA, 1987.

187. Ford, F.P., and P.L. Andresen, “Corrosion in Nuclear Systems: Environmentally Assisted Cracking in Light Water Reactors,” in *Corrosion Mechanisms*, eds. P. Marcus and J. Ouder, Markel Dekker, pp. 501–546, 1994.

188. Bush, S.H., and A.D. Chockie, “An Overview of Stress Corrosion in Nuclear Reactors from the 1960s to the 1990s,” SKI Report 96:24, Swedish Nuclear Power Inspectorate, February 1996.

189. Andresen, P.L., “Emerging Issues and Fundamental Processes in Environmental Cracking in Hot Water,” *Corrosion* 64 (5), 439–464, 2008.

190. IAEA, “Stress Corrosion Cracking in Light Water Reactors: Good Practices and Lessons Learned,” Nuclear Energy Series No. NP-T-3.13, IAEA, Vienna, 2011.

191. Ford, F.P., B.M. Gordon, and R.M. Horn, “Intergranular Stress Corrosion Cracking (IGSCC) in Boiling Water Reactors (BWRs),” in *Nuclear Corrosion Science and Engineering*, pp. 548–580, ed. D. Feron, Woodhead Publishing Series in Energy, Woodhead Publishing Ltd., Oxford, 2012.

192. Chopra, O.K., W.K. Soppet, and W.J. Shack, “Effects of Alloy Chemistry, Cold Work, and Water Chemistry on Corrosion Fatigue and Stress Corrosion Cracking of Nickel Alloys and Welds,” NUREG/CR–6721, ANL–01/07, April 2001.

193. Alexandreanu, B., O.K. Chopra, and W.J. Shack, “Crack Growth Rates of Nickel Alloys from the Davis-Besse and V. C. Summer Power Plants in a PWR Environment,” NUREG/CR–6921, ANL–05/55, November 2001.

194. Alley, D., and D. Dunn, “Current NRC Perspective Concerning Primary Water Stress Corrosion Cracking,” *Proc. 15th Intl. Conf. on Environmental Degradation of Materials in Nuclear Power Systems – Water Reactors*, J.T. Busby, G. Ilevbare, and P.L. Andresen, eds., The Minerals, Metals & Materials Society, Warrendale, PA, pp. 14–27, 2011.

195. Efsing, P., B. Forssgren, and J. Lagerstöm, “Stress Corrosion Cracking in Austenitic Stainless Steel in a Typical PWR Environment,” presented at *Fontevraud VI: Contribution of Materials Investigations to Improve the Safety and Performance of LWRs*, Intl. Symposium, 2006.

196. Dunn, D.S., J. Collins, D. Alley, B. Alexandreanu, S.M. Bruemmer, and M.B. Toloczko, “Primary Water Stress Corrosion Cracking Tests and Metallurgical Analyses of Davis-Besse Control Rod Drive Mechanism Nozzle #4,” *Proc. 16th Intl. Symp. on Environmental Degradation of Materials in Nuclear Power Systems – Water Reactors*, August 11-15, Ashville, NC, 2013.

197. Park, J.-H., O.K. Chopra, K. Natesan, and W.J. Shack, “Boric Acid Corrosion of Light Water Reactor Pressure Vessel Materials,” NUREG/CR-6875, ANL-04/08, July 2005.

198. Flanagan, W.F., and B.D. Lichter, “A Mechanism of Transgranular Stress Corrosion Cracking,” *Intl. J of Fracture* 79, 121–135, 1996.

199. Hurley, M.F., C.R. Olson, L.J. Ward, B.J. Jaques, K.A. Johnson, J.K. Gunnerson, and D.P. Butt, “Transgranular Stress Corrosion Cracking (TGSCC) of 304L Austenitic Stainless Steel Pipe Clamps in Direct use Geothermal Water Heating Applications,” *Eng. Failure Analysis,* 33, 336–346, 2013.

200. Spenser, D.T, M.R. Edwards, M.R. Wenman, C. Tsitsios, G.G. Scatigna, and P.R. Chard-Tuckey, “The Initiation and Propagation of Chloride-Induced Transgranular Stress Corrosion Cracking (TGSCC) of 304L Austenitic Stainless Steel under Atmospheric Conditions,” *Corrosion Sc*., 88, 76–88, 2014.

201. Gordon, B.M., and G.M. Gordon, “Corrosion in Boiling Water Reactors,” ASM Handbook, Volume 13, *Corrosion*, p 929, Metal Park, OH, 1987.

202. BWRVIP-190 (EPRI 1016579), *BWR Vessel and Internals Project: BWR Water Chemistry Guidelines—2008 Revision*, October 2008.

203. Ford, F.P., “Overview of Collaborative Research into the Mechanisms of Environmentally Controlled Cracking in the Low Alloy Pressure Vessel Steel/Water System,” *Proc. 2nd Int. Atomic Energy Agency Specialists’ Meeting on Subcritical Crack Growth*, NUREG/CP-0067, MEA–2090, Vol. 2, pp. 3–71, 1986.

204. Hänninen, H., K. Törrönen, and W.H. Cullen, "Comparison of Proposed Cyclic Crack Growth Mechanisms of Low Alloy Steels in LWR Environments," *Proc. 2nd Int. Atomic Energy Agency Specialists' Meeting on Subcritical Crack Growth, NUREG/CP-0067*, MEA–2090, Vol. 2, pp. 73–97, 1986.

205. Ford F.P., "The Crack Tip System and its Relevance to the Prediction of Cracking in Aqueous Environments," *Proc. of 1st Intl. Conf. on Environmentally Assisted Cracking of Metals*, Kohler, WI, October 2-7, pp. 139–165, NACE, Houston, TX, 1988.

206. Macdonald, D.D., and M. Urquidi-Macdonald, "A Coupled Environment Model for Stress Corrosion Cracking in Sensitized Type 304 Stainless Steel in LWR Environments," *Corrosion Science,* 32 (1), 51–81, 1991.

207. Macdonald, D,D., P.C. Lu, M. Urquidi-Macdonald, and T.K. Yeh, "Theoretical Estimation of Crack Growth Rate in Type 304 Stainless Steel in Boiling Water Reactor Coolant Environments," *Corrosion,* 52 (10), 768, October 1996.

208. Ford F.P., "Mechanisms of Environmentally Enhanced Cracking in Ally/Environment Systems Peculiar to the Power Generation Industries," EPRI Report NP-2589, Palo Alto, CA, 1982.

209. Ford, F.P., B.M. Gordon, and R.M. Horn, "Corrosion in Boiling Water Reactors," in *Corrosion: Environment and Industries*, 13C, 341–361, ASM Handbook, ASM International, 2006.

210. Ehrnsten, U., P.A. Aaltonen, P. Nenonen, H.E. Hänninen, C. Jansson, and T.M. Angeleu, "Intergranular Racking of AISI 316NG Stainless Steel in BWR Environments," *Proc. 10th Intl. Conf. on Environmental Degradation of Materials in Nuclear Power Systems – Water Reactors*, NACE, Houston, TX, 2001.

211. IAEA, "Assessment and Management of Aging of Major Nuclear Power Plant Components Important to Safety: BWR Vessel Internals," IAEA-TECDOC-1470, Vienna, 2005.

212. NRC, "Investigation and Evaluation of Stress Corrosion Cracking in Piping of Light Water Reactor Plants," NUREG-0513, Washington, DC, 1979.

213. Solomon, H.D., "Transgranular, Granulated, and Intergranular Stress Corrosion Cracking in AISI 304 SS," *Corrosion,* 40 (9), 493–506, NACE, September 1984.

214. Ford, F.P., "Stress Corrosion Cracking," in *Corrosion Processes*, R.N. Parkin, ed., Applied Science, New York, 1982.

215. Hazelton, W.S., and W.H. Koo, "Technical Report on Material Selection and Processing Guidelines for BWR Coolant Pressure Boundary Piping," NUREG-0313, Rev. 2, U.S. Nuclear Regulatory Commission, Washington, DC, January 25,1988; Supplement 1, February 4, 1992.

216. NRC Generic Letter GL 88-01, "NRC Position on IGSCC in BWR Austenitic Stainless Steel Piping," U.S. Nuclear Regulatory Commission, Washington, DC, 1988.

217. Kain, V., “Corrosion Resistant Materials,” in *Functional Materials – Preparation, Processing, and Applications*, S. Banerjee and A.K. Tyagi, eds., pp. 507–548, Elsevier, 2012.

218. Spencer, D.T., M.R. Edwards, M.R. Wenman, C. Tsitsios, G.G. Scatigno, and P.R. Chard-Tuckey, “The Initiation and Propagation of Chloride-Induced Transgranular Stress-Corrosion Cracking (TGACC) of 304L Austenitic Stainless Steel under Atmospheric Conditions,” *Corrosion Science,* 88, 76–88, 2014.

219. Lichter, B.D., H. Lu, and W.F. Flanagan, “Strain-Enhanced Dissolution: A Model for Transgranular Stress Corrosion Cracking,” *2nd Int. Conf. on Environment Sensitive Cracking and Corrosion Damage*, pp. 271–278, M. Matsumura et al. eds., Nishiki Printing Ltd., Hiroshima, Japan, 2001.

220. Qiao, L., and X. Mao, “Thermodynamic Analysis on the Role of Hydrogen in Anodic Stress Corrosion Cracking,” *Acta Metall. Mater*., 43, 4001–4006, 1995.

221. Magnin, T., and J. Lepinoux, “Metallurgical Aspects of the Brittle SCC in Austenitic Stainless Steels,” *Parkins Symposium*, S.M. Bruemmer et al. eds., 323, TMS, Warrendale, PA, 1992.

222. Lepinoux, J., and T. Magnin, “Stress Corrosion Micro cleavage in a Ductile FCC Alloy,” *Mater. Sci. Eng*., A164, 226, 1993.

223. Magnin, T., A. Chambreuil, and B. Bayle, “The Corrosion-Enhanced Plasticity Model for Stress Corrosion Cracking in Ductile FCC Alloys,” *Acta Mater*., 44 (4), 1457–1470, 1996.

224. Leinonen, H., and H. Hänninen, “Prediction of Stress Corrosion Cracking Susceptibility of Austenitic Stainless Steels in 50% CaCl2 Solution,” *Corrosion-Deformation Interactions (CDI ‘96)*, T. Magnin, ed., Inst. of Metals, 131–139, 1997.

225. Lynch, S.P., “A Commentary on Mechanisms of Environmentally Assisted Cracking,” *Corrosion-Deformation Interactions (CDI ‘96)*, T. Magnin, ed., Inst. of Metals, 206–219, 1997.

226. Lynch, S.P., “Environmentally Assisted Cracking: Overview of Evidence for an Adsorption-Induced Localized Slip Process,” *Acta Metall*., 36 (10), 2639–2662, 1988.

227. Lynch, S.P., “Mechanisms and Kinetics of Environmentally Assisted Cracking: Current Status, Issues, and Suggestions for Future Work,” *Metall. and Mater. Trans*., 44A, 1209–1229, 2013.

228. Brozova, A., and S. Lynch, “Transgranular Stress-Corrosion Cracking in Austenitic Stainless Steels at High Temperatures,” in *Corrosion Issues in Light Water Reactors – Stress Corrosion Cracking*, F. Feron and J.-M. Olive, eds., Woodhead Publishing ltd., Cambridge, England, pp. 149–161, 2007.

229. Birnbaum, H.K., “Mechanism of Hydrogen Related Fracture of Metals,” *Hydrogen Effects on Material Behavior*, N.R. Moody and A.W. Thompson, eds., pp. 639–659, TMS, Warrendale, PA, 1990.

230. Shih, D.S., I.M. Robertson, and H.K. Birnbaum, “Hydrogen Embrittlement of Alpha Titanium: In situ TEM Studies,” *Acta Metall*., 36 (10), 111, 1988.

231. Birnbaum, H.K., and P. Safronis, “Hydrogen Enhanced Localized Plasticity – A Mechanism for Hydrogen Related Fracture,” *Mater. Sci. Eng. A,* A176, 191–202, 1994.

232. Zhu, L.K., Y. Yan, J.X. Li, L.J. Qiao, and A.A. Volinsky, “Stress Corrosion Cracking under Low Stress: Continuous or discontinuous Cracks?,” *Corrosion Sc*., 80, 350–358, 2014.

233. Scott, P.M., “Stress Corrosion Cracking in Pressurized Water Reactors – Interpretation, Modeling, and Remedies,” *Corrosion,* 56, 771–782, 2000.

234. Scott, P.M., “A Overview of Materials Degradation by Stress Corrosion in PWRs,” *Corrosion Issues in Light Water Reactors – Stress Corrosion Cracking*, F. Feron and J.-M. Olive, eds., Woodhead Publishing ltd., Cambridge, England, pp. 3–24, 2007.

235. Gorman, J., S. Hunt, P. Riccardella, and G.A. White, “PWR Reactor Vessel – Alloy 600 Issues,” in *Companion Guide to the ASME Boiler and Pressure Vessel Code*, 3rd edition, Volume 3, Chapter 44, 63–87, 2007.

236. Coriou, H., L. Grall, C. Mahieu, and M. Pelas, “Sensitivity to Stress Corrosion and Intergranular Attack of High-Nickel Austenitic Alloys,” *Corrosion,* 22, 280-290, 1966.

237. Le Calvar, M., and I. De Curieres, “Corrosion Issues in Pressurized Water Reactor Systems,” *Corrosion Science and Engineering*, Part V, pp. 473–547, D. Feron, ed., Woodhead Publishing Series in Energy, Woodhead Publishing Ltd., Oxford, 2012.

238. Cassagne, T. and A. Gelpi, “Crack Growth Rate Measurements on Alloy 600 Steam Generator Tubing in Primary and Hydrogenated AVT Water,” *Proc. 6th Intl. Conf. on Environmental Degradation of Materials in Nuclear Power Systems – Water Reactors*, The Minerals, Metals & Materials Society, Warrendale, PA, p. 679, 1993.

239. Scott, P.M., “Some Possible Mechanism of Intergranular Stress Corrosion Cracking of Alloy 600 in PWR Primary Water,” *Proc. 9th Intl. Conf. on Environmental Degradation of Materials in Nuclear Power Systems – Water Reactors*, The Minerals, Metals & Materials Society, Warrendale, PA, pp. 3–12, 1999.

240. Scott, P.M., and M. LeCalvar, “An Overview of Internal Oxidation as a Possible Explanation of Intergranular Stress Corrosion Cracking of Alloy 600 in PWRs,” *Proc. 6th Intl. Conf. on Environmental Degradation of Materials in Nuclear Power Systems – Water Reactors*, F.P. Ford, S.M. Bruemmer, and G.S. Was, eds., The Minerals, Metals & Materials Society, Warrendale, PA, pp. 657–665, 1993.

241. Gendron, T.S., P.M. Scott, S.M. Bruemmer, L.E. Thomas, “Internal oxidation as mechanism for steam generator tube degradation,” *Proc. of 3rd Int. Steam Generator and Heat Exchanger Conference*, Vol. 2, Canadian Nuclear Society, pp. 389–403, 1998.

242. SIA-PRS-11-037 H BMG, “PWSCC Mechanism,” *Corrosion and Corrosion Control in LWRs*, U.S. Nuclear Regulatory Commission, Washington, DC, 20011.

243. Daret, J., “Initiation of SCC in Alloy 600 Wrought Materials: a Laboratory and Statistical Evaluation,” *Proc. 12th Intl. Conf. on Environmental Degradation of Materials in Nuclear Power Systems – Water Reactors*, The Minerals, Metals & Materials Society, Warrendale, PA, pp. 937–945, 2005.

244. de Curieres, I., and M.C. Meunier, “Stress Corrosion Cracking of Steam Generator Tubes Made of Alloy 600TT: Analysis of Operating Experience,” *Proc. Intl. Conf. Fontevraud* 7, Paper A126-T06, French Nuclear Energy Society, SFEN, Fontevraud Royal Abbey, France, Sept. 26–30, 2010.

245. Saint-Paul, P., and G. Slama, “Steam Generators Materials Degradations,” *Proc. 5th Environmental Degradation of Materials in Nuclear Power Systems*, pp. 39–49, NACE, August 25–29, Monterey, CA, 1991.

246. Harris, J., “PWR Generic Tube Degradation Predictions – US Recirculating Steam Generators with Alloy 600 TT and Alloy 690TT,” EPRI Report 1003589, July 2003.

247. Boudot, R., F. Cattant, C. Pichon, Y. Rouillon, A. Teissier, P. Vidal, A. Gelpi, M. Gregoire, C. Gimond, and T. Tsuk, “Stress Corrosion Cracking of Pressurizer Nozzles in French 1300 MWe Units,” *Fontevraud III*, pp. 155–164, SFEN, Fontevraud Royal Abbey, France, September 12–16, 1994.

248. Bamford, W.H., and N.A. Palm, “Service Experience with Alloy 600 and Associated Welds in Operating PWRs, including Repair Activities and Regulatory and Code Actions,” *Proc. 14th Environmental Degradation of Materials in Nuclear Power Systems*, ANS, August 23–27, Virginia Beach, VA, 2009.

249. NRC Bulletin 2003-2, “Leakage from Reactor Pressure Vessel Lower Head Penetrations and Reactor Coolant Pressure Boundary Integrity,” August 21, 2003.

250. Grimmel, B., “US Plant Experience with Alloy 600 Cracking and Boric Acid Corrosion of Light-Water Reactor Pressure Vessel Materials,” NUREG-1823, U.S. Nuclear Regulatory Commission, Washington, DC, April 2005.

251. Cullen, W.H., and T.S. Mintz, “A Survey of Worldwide Experience with the Cracking Susceptibility of Alloy 600 and Associated Welds, – Review of Alloy 600 Experience – Domestic and Foreign,” Rev. 2, U.S. Nuclear Regulatory Commission, Washington, DC, March 25, 2004.

252. Bamford, W., and J. Hall, “Cracking of Alloy 600 Nozzles and Welds in PWRs: Review of Cracking Events and Repair Service Experience,” *Proc. 12th Intl. Conf. on Environmental Degradation of Materials in Nuclear Power System – Water Reactors*, T.R. Allen, F.J. King, L. Nelson, eds., The Minerals, Metal & Materials Society, Warrendale, PA, 2005.

253. Efsing, P., B. Forssgren, and R. Kilian, “Root Cause Failure Analysis of Defected J-Groove Welds in Steam Generator Drainage Nozzles,” *Proc. 12th Intl. Conf. on Environmental Degradation of Materials in Nuclear Power System – Water Reactors*, Salt Lake City, UT, The Minerals, Metal & Materials Society, Warrendale, PA, 2006.

254. Xu, H., S. Fyfitch, J.W. Hyres, F. Cattant, and A. McIlree, “Laboratory Investigation of the Alloy 600 Bottom Mounted Instrumentation Nozzle Samples and Weld Boat Sample from South Texas Project Unit 1,” *Proc. 12th Intl. Conf. on Environmental Degradation of Materials in Nuclear Power Systems – Water Reactors*, August 14–18, Salt Lake City, UT, TMS, 2005.

255. Pathania, R.S., A.R. McIlree, and J. Hickling, “Overview of Primary Water Cracking of Alloys 182/82 in PWRs,” *Proc. Fontevraud V Intl. Symp. on the Contribution of Materials Investigation to the Resolution of Problems Encountered in Pressurized Water Reactors*,” pp. 13–28, September 23–27, 2002.

256. Amzallag, C., J.M. Boursier, C. Pages, C. Gimond, “Stress Corrosion Life Experience of 182 and 82 Welds in French PWRs,” *Proc. Fontevraud V, Intl. Symp. on the Contribution of Materials Investigation to the Resolution of Problems Encountered in Pressurized Water Reactors*, September 23-27, pp. 69–79, 2002.

257. Efsing, P., G. Embring, B. Forssgren, B. Kroes, and R. Lundstrom, “Failure Analysis of the Ringhals Unit 3 EDM Surfaces Removed from the RPV Outlet Nozzle to Safe End Weld,” *Proc. Fontevraud VI, Contribution of Materials Investigations to Improve the Safety and Performance of LWRs*, pp. 283–290, September 18–22, 2006.

258. Scott, P., M.-C. Meunier, F. Steltzlen, O. Calonne, M. Foucault, P. Combrade, and C. Amzallag, “Comparison of Laboratory and Field Experience of PWSCC in Alloy 182 Weld Metal,” *Proc. 13th Environmental Degradation of Materials in Nuclear Power Systems*, CNS, August 19–23, Whistler, BC, Canada, 2007.

259. Deforge, D., L. Duisabeau, S. Miloudi, Y. Thebault, T. Couvant, F. Vaillant, and E. Laire, “Learning from EdF Investigations on SG Divider Plates and Vessel Head Nozzles. Evidence of Prior Deformation Effect on Stress Corrosion Cracking,” *Contribution of Materials Investigations to Improve the Safety and Performance of LWRs*, paper A117-T04, Avignon, France, September 26–30, 2010.

260. NRC, “Resolution of Generic Safety Issue: Issue 72: Control Rod Drive Guide Tube Short Pin Failures (Rev. 1) (NUREG-0933, Main Report with Supplements 1–33),” Washington, DC, December 2011.

261. Heuzé, A., F. Hédin, and A. Richard, “Nouvelles Broches Pour Guide de Grappes des Chaudières 900 et 1 300 MWe,” *Fontevraud II Contribution of Materials Investigations to Improve the Safety and Performance of LWRs*, pp. 43–52, SFEN, Fontevraud Royal Abbey, France, September 10–14, 1990.

262. NRC Bulletin 2001-01, “Circumferential Cracking of Reactor Pressure Vessel Head Penetration Nozzles,” Washington, DC, August 3, 2001.

263. Boursier, J.M., S. Gallet, Y. Rouilion, and P. Bordes, “Stress Corrosion Cracking of Austenitic Stainless Steels in PWR Primary Water: An Update of Metallurgical Investigations Performed on French Withdrawn Components,” *Fontevraud 5 Intl. Symp., Contribution of Materials Investigation to the Resolution of Problems Encountered in Pressurized Water Reactors*, Avignon, France, Sept. 25, 2002.

264. Ilevbare, G., F. Cattant, and N. Peat, “SCC of Stainless Steel under PER Conditions,” *2010 MRP Intl. Conf. and Exhibition on PWR*, June 27-July 2, Colorado Springs, CO, 2010.

265. Matsubara, M., T. Kobayashi, K. Fujimoto, Y. Nomura, S. Hirano, and N. Chigusa, “Research Programs on SCC of cold-worked Stainless Steels in Japanese PWR NPPs,” *Proc. Intl. Conf. Fontevraud* 7, Paper A099-T03, French Nuclear Energy Society, SFEN, Fontevraud Royal Abbey, France, Sept. 26–30, 2010.

266. Tribouilloy, L., F. Vaillant, J.M. Olive, and M. Puiggali, “Stress Corrosion Cracking on Cold-Worked Austenitic Stainless Steels in PWR Environment,” *Advances in Materials Science,* 7, 61–69, 2007.

267. LeCalvar, M., “French PWR Experience – Is Cold Work Detrimental or Beneficial?” Program on Technology Innovation: Proc. 2007 AECL/COG/EPRI Workshop on Cold Work in Iron- and Nickel-Base Alloys Exposed to High Temperature Water Environments, June 3–8, 2007, Mississauga, ON, Canada, #1016519, 2008.

268. Shoji, T., S. Hirano, and T. Kobayashi, “Effect of Cold Work and Stress on Oxidation and SCC Behavior of Stainless Steels in PWR Primary Water Environments,” *Proc. Intl. Conf. Fontevraud* 7, Paper A103-T03, French Nuclear Energy Society, SFEN, Fontevraud Royal Abbey, France, Sept. 26–30, 2010.

269. Couvant, T., E. Herms, P. Combrade, F. Vaillant, I. de Curieres, J.M. Boursier, O. Raquet, and O. de Bouvier, “ Effect of Chlorides and Sulfates on the EAC of Austenitic Stainless Steel in PWR Environment,” *Proc. 13th Intl. Conf. on Environmental Degradation of Materials in Nuclear Power Systems – Water Reactors*, T.R. Allen, P.J. King, and L. Nelson, eds., Canadian Nuclear Society, Toronto, Canada, 2007.

270. NRC, “Stress Corrosion Cracks in Stagnant, Low Pressure Stainless Piping Containing Boric Acid Solution at PWR’s,” NRC IE Circular, 76-06, November 22, 1976.

271. Pezze, C.M., and I.L.W. Wilson, “Transgranular Stress Corrosion Cracking of 304 Stainless Steel Canopy Seal Welds in PWR Systems,” *Proc. 4th Intl. Symp. on Environmental Degradation of Materials in Nuclear Power Systems-Water Reactors*, NACE, Houston, TX, 1990.

272. Ilevbare, G.O., “Comments on Contribution of Cold Work to SCC of Stainless Steels in a PWR Primary Circuit,” EPRI/AECL Workshop on Cold Work and Its Impact on Components in Light Water Nuclear Reactors, June 4–8, 2007.

273. Garud, Y.S., and G.O. Ilevbare, “An SCC Initiation Model: Effects of Cold-Work in Austenitic Stainless Steels in Light Water Reactor Environments,” *Intl. J. Nuclear Energy Science and Engineering*, Vol. 2 (3), pp. 79–87, 2012.

274. Bruemmer, S.M., L.A. Charlot, and C.H. Henager Jr., “Microstructure and Microdeformation Effects on IGSCC of Alloy 600 Steam Generator Tubing,” *Corrosion,* 44 (11), 782–788, 1988.

275. Andresen, P.L., J. Hickling, A. Ahluwalia and J. Wilson, “Mitigation of PWSCC in Ni-base Alloys by Optimizing H_2,” EPRI Alloy 600 Conference, Atlanta, June 2007.

276. Molander, A., et al., "Comparison of PWSCC Initiation and Crack Growth Data for Alloy 600," Water Chemistry of Nuclear Reactor Systems, International Conference, Berlin, 2008.

277. Amzallag, C., S. Le Hong, C. Pagès, and A. Gelpi, "Stress Corrosion Life Assessment of Alloy 600 Components," *Proc. 9th Intl. Conf. on Environmental Degradation of Materials in Nuclear Power Systems – Water Reactors*, The Minerals, Metals & Materials Society, Warrendale, PA, pp. 243–250, 1999.

278. Scott, P., and C. Benhamou, "An Overview of Recent Observations and Interpretation of IGSCC in Nickel Alloys in PWR Primary Water," *Proc. 10th Intl. Symp. on Environmental Degradation of Materials in Nuclear Power Systems – Water Reactor*, NACE, Houston, TX, 2001.

279. Staehle, R.W., J.A. Gorman, K.D. Stavropoulos, and C.S. Welty, "Application of Statistical Distribution of Characterizing and Predicting Corrosion of tubing in Steam Generators of Pressurized Water Reactors," *Proc. Life Prediction of Corrodible Structures*, R.N. Parkins, NACE Intl., Houston, TX, 2001.

280. Economy, G., R.J. Jacko, and J.A. Begley, "Influence of Hydrogen Partial Pressure on the IGSCC of Alloy 600 Tubing in 360°C Water or 400°C Steam, " *Corrosion*, Paper 92, NACE, Houston, TX, 1987.

281. Richey, E., D. Morton, and R. Atien, "SCC Initiation Testing of Ni-based Alloys in High Temperature Water," *Proc. 13th Intl. Conf. on Environmental Degradation of Materials in Nuclear Power Systems*, NACE-TMS-ANS, August 19-23, Whistler, BC, Canada, 2007.

282. Dozaki, K., D. Akutagawa, N. Nagata, H. Takiguchi, and K. Norring, "Effect of Dissolved Hydrogen Content in PWR Primary Water on PWSCC Initiation Property," *EJAM*, *Japan Society of Maintenology*, 2, 65–76, 2010.

283. Molander, A., "Corrosion Potential Monitoring in Nuclear Power Environments," *Corrosion Issues in Light Water Reactors – Stress Corrosion Cracking*, F. Feron and J.-M. Olive, eds., Woodhead Publishing ltd., Cambridge, England, pp. 25–43, 2007.

284. Sawicki, J.A., and H.A. Allsop, " Evidence of Zinc Ferrite Formation on Carbon Steel in Primary-side Coolant with Added Soluble Zinc," *J. Nucl. Mater.,* 240, 22–26, 1996.

285. Kawamura, H. H. Hirano, S. Shirai, H. Takamatsu, T. Matsunaga, K. Yamaoka, K. Oshinden, and H. Takiguvhi, "Inhibitory Effect of Zinc Addition to High-Temperature Hydrogenated Water on Mill-Annealed and Prefilmed Alloy 600," *Corrosion*, pp. 623–637, 2000.

286. Roumiguière, F., "Field Experience on Zn Injection on PWR Plants with a View to Dose Rate Reduction," *Proc. Intl. Conf. Nuclear Energy for New Europe*, pp. 103.1-103.9, Bled, Slovenia, September 5–8, 2005.

287. Slama, G., "Shot Peening Experience after 5 Years," *Fontevraud II Contribution of Materials Investigations to Improve the Safety and Performance of LWRs*, pp. 352–360, SFEN, Fontevraud Royal Abbey, France, September 10–14, 1990.

288. Andresen, P.L., and M.M. Morra, "Emerging Issues in Environmental Cracking in Hot Water," *Proc. 13th Intl. Conf. on Environmental Degradation of Materials in Nuclear Power Systems – Water Reactors*, T.R. Allen, P.J. King, and L. Nelson, eds., Canadian Nuclear Society, Toronto, Canada, Paper No. P0124, 2007.

289. Andresen, P.L., and F.P. Ford, "Irradiation Assisted Stress Corrosion Cracking: From Modeling and Prediction of Laboratory and In-Core Response to Component Life Prediction," *Corrosion/95*, NACE, Houston TX, Paper No. 419, 1995.

290. Chopra, O.K., B. Alexandreanu, E.E. Gruber, R.S. Daum, and W.J. Shack, "Crack Growth Rates of Irradiated Austenitic Stainless Steel Weld Heat Affected Zone in BWR Environments," NUREG/CR-6891, ANL-04/20, 2006.

291. Andresen, P.L.," Similarity of Cold Work and Radiation Hardening in Enhancing Yield Strength and SCC Growth of Stainless Steels in Hot Water," *Corrosion/02*, NACE, Houston, TX, Paper No. 02509, 2002.

292. Jenssen, A., K. Gott, P. Efsing, and P.O. Andersson, "Crack Growth Behavior of Irradiated Type 304L Stainless Steel in Simulated BWR Environment," in *Proc. 11th Intl. Symp. on Environmental Degradation of Materials in Nuclear Power Systems – Water Reactors*, American Nuclear Society, Lagrange, IL, pp. 1015–1024, 2003.

293. Nakamura, T., M. Koshiishi, T. Torimaru, Y. Kitsunai, K. Takakura, K. Nagata, M. Ando, Y. Ishiyama, and A. Jenssen, "Correlation between IASCC Growth Behavior and Plastic Zone Size of Crack Tip in 3.5 dpa Neutron Irradiated Type 304L SS CT Specimen," *Proc. 13th Intl. Conf. on Environmental Degradation of Materials in Nuclear Power Systems – Water Reactors*, T. R. Allen, P. J. King, and L. Nelson, eds., Paper No. P0030, Canadian Nuclear Society, Toronto, Canada, 2007.

294. Sumiya, R., S. Tanaka, K. Nakata, K, Takakura, M. Ando, T. Torimaru, and Y. Kitsunai, "K Validity Criterion of Neutron Irradiated Type 316L Stainless Steel CT Specimen for SCC Growth Test," *Proc. 13th Intl. Conf. on Environmental Degradation of Materials in Nuclear Power Systems – Water Reactors*, T. R. Allen, P. J. King, and L. Nelson, eds., Paper No. P0072, Canadian Nuclear Society, Toronto, Canada, 2007.

295. Andresen, P.L., and M.M. Morra, "Effect of Rising and Falling K Profiles on SCC Growth Rates in High-Temperature Water," *Trans. ASME,* 129, 488–506, 2007.

296. Karlsen, T.M., M. Espeland, and A. Horvath, "Summary Report on the PWR Crack Growth Rate Investigation, IFA-657," HWR-773, OECD Halden Reactor Project, May 2005.

297. Pathania, R., R. Carter, R. Horn, and P. Andresen, "Crack Growth Rates in Irradiated Stainless Steels in BWR Internals," *Proc. 14th Intl. Conf. on Environmental Degradation of Materials in Nuclear Power Systems – Water Reactors*, American Nuclear Society, Lagrange Park, IL, Paper #203178, 2009.

298. Karlsen, T.M., and A. Horvath, "Final Report on the In-Pile Crack Growth Behavior of Irradiated Compact Tension Specimens in IFA-639," HWR-770, OECD Halden Reactor Project, December 2004.

299. Nakano, J., T.M. Karlsen, and M. Espeland, "Summary Report on the BWR Crack Growth Rate Experiment, IFA-658," HWR-862, OECD Halden Reactor Project, February 2007.

300. Karlsen, T.M., P. Bennett, and N.W. Hogberg, “In-core Crack Growth Rate Studies on Irradiated Austenitic Stainless Steels in BWR and PWR Conditions in the Halden Reactor,” *Proc. 12th Intl. Conf. on Environmental Degradation of Materials in Nuclear Power Systems - Water Reactors*, T. R. Allen, P. J. King, and L. Nelson, eds., Minerals, Metals & Materials Society, Warrendale, PA, pp. 337–348, 2005.

301. Chopra, O.K., E.E. Gruber, and W.J. Shack, “Fracture Toughness and Crack Growth Rates of Irradiated Austenitic Stainless Steels,” NUREG/CR-6826, ANL-03/22, 2003.

302. Chopra, O.K., B. Alexandreanu, E.E. Gruber, and W.J. Shack, “Crack Growth Behavior of Irradiated Austenitic Stainless Steel Weld Heat Affected Zone Material in High-Purity Water at 289°C,” *Proc. 12th Intl. Conf. on Environmental Degradation of Materials in Nuclear Power Systems – Water Reactors*, T. R. Allen, P. J. King, and L. Nelson, eds., Minerals, Metals & Materials Society, Warrendale, PA, pp. 289–298, 2005.

303. Nakano, J., T.M. Karlsen, and M. Espeland, “Summary of Results from the PWR Crack Growth Rate Investigation, IFA-670,” HWR-843, OECD Halden Reactor Project, August 2008.

304. Davis, R.B., and P. Andresen, “Evaluation of Fundamental Linkage among SCC Phenomena,” Cooperative IASCC Research (CIR) Final Report, EPRI 1007378, October 2002.

305. Trautwein, A., and W. Gysell, “Influence of Long Time Aging of CF-8 and CF-8M Cast Steel at Temperatures between 300 and 500°C on the Impact Toughness and the Structure Properties,” in *Spectrum, Technische Mitteilungen aus dem+GF+Konzern,* No. 5 (May 1981); also in *Stainless Steel Castings*, V.G. Behal and A.S. Melilli, eds., STP 756, pp. 165–189, ASTM, Philadelphia, PA, 1982.

306. Landerman, E.I., and W.H. Bamford, “Fracture Toughness and Fatigue Characteristics of Centrifugally Cast Type 316 Stainless Steel Pipe after Simulated Thermal Service Conditions,” in *Ductility and Toughness Considerations in Elevated-Temperature Service*, MPC 8, ASME, pp. 99–127, New York, NY, 1978.

307. Solomon, H.D., and T.M. Devine, Jr., “Duplex Stainless Steels – A Tale of Two Phases,” in *Duplex Stainless Steels*, R.A. Lula, ed., pp. 693–756, ASM, Materials Park, OH, 1983.

308. Hale, G.E., and S.J. Garwood, “The Effect of Aging on the Fracture Behaviour of Cast Stainless Steel and Weldments,” *Mater. Sci. Technol.,* 6, 230–235, 1990.

309. McConnell, P., and J.W. Sheckherd, “Fracture Toughness Characterization of Thermally Embrittled Cast Duplex Stainless Steel,” Report NP-5439, Electric Power Research Institute, Palo Alto, CA, September 1987.

310. Slama, G., P. Petrequin, and T. Mager, “Effect of Aging on Mechanical Properties of Austenitic Stainless Steel Castings and Welds,” presented at *SMIRT Post-Conference Seminar 6, Assuring Structural Integrity of Steel Reactor Pressure Boundary Components*, Monterey, CA, Aug. 29–30, 1983.

311. Meyzaud, Y., P. Ould, P. Balladon, M. Bethmont, and P. Soulat, “Tearing Resistance of Aged Cast Austenitic Stainless Steel,” *Int. Conf. on Thermal Reactor Safety (NUCSAFE 88)*, Avignon, France, October 1988.

312. Balladon, P., J. Heritier, and P. Rabbe, “Influence of Microstructure on the Ductile Rupture Mechanisms of a 316L Steel at Room and Elevated Temperatures,” pp. 496–516, in *Proc. Fracture Mechanics: 14th Symp., Vol. II: Testing and Applications*, ASTM STP 791, American Society for Testing and Materials, Philadelphia, PA, 1983.

313. Bethmont, M., Y. Meyzaud, and P. Soulat, “Properties of Cast Austenitic Materials for Light Water Reactors,” *Int. J. Pres. Ves. & Piping,* 66, 221–229, 1996.

314. Pumphrey, P.H., and K.N. Akhurst, “Aging Kinetics of CF3 Cast Stainless Steel in Temperature Range 300–400°C,” *Mater. Sci. Technol.,* 6, 211–219, 1990.

315. Jayet-Gendrot, S., P. Ould, and T. Meylogan, “Fracture Toughness Assessment of In-Service Aged Primary Circuit Elbows Using Mini-CT Specimens Taken from Outer Skin,” *Nucl. Eng. and Design* 184, 3–11, 1998.

316. Bonnet, S., J. Bourgoin, J. Champredonde, D. Guttmann, and M. Guttmann, “Relationship between Evolution of Mechanical Properties of Various Cast Duplex Stainless Steels and Metallurgical and Aging Parameters: An Outline of Current EDF Programs,” *Mater. Sci. Technol.*, 6, 221–229, 1990.

317. Jayet-Gendrot, S., P. Ould, and P. Balladon, “Effect of Fabrication and Test Parameters on the Fracture Toughness of Aged Cast Duplex Stainless Steels,” *Fontevraud III*, Vol. 1, pp. 90–97, French Nuclear Energy Society, 1994.

318. Massoud, Jean-Paul, C. Boveyron, P. Ould, G. Bezdikian, and H. Churier-Bossenec, “Effect of the Manufacturing Process on the Thermal Aging of PWR Duplex Stainless Steel Components,” paper ICINE-6085, *ASME 6th Intl. Conf. on Nucl. Eng*. (ICONE-6), American Society of Mechanical Engineers, New York, NY, 1998.

319. Le Delliou, P., G. Bezdikian, P. Ould, and N. Safa, “Full-Scale Test on an Aged Cast Duplex Stainless Steel Lateral Connection: Results and Analysis,” PVP2006-IVPVT-11-94005, in *Proc. of 2006 ASME Pressure Vessel and Piping Conf.*, Vancouver, BC, Canada, July 23–27, 2006.

320. Faidy, C., “Flaw Evaluation in Elbows Through French RSEM Code,” PVP2010–25085, in *Proc. of ASME 2010 Pressure Vessel and Piping Division/K-PVP Conf.*, Bellevue, WA, July 18-22, 2010.

321. Mills, W.J., “Fracture Toughness of Aged Stainless Steel Primary Piping and Reactor Vessel Materials,” *J. Pressure Vessel Technol. (Trans ASME),* 109, 440–448, 1987.

322. Grimes, C.I. (U.S. Nuclear Regulatory Commission, License Renewal and Standardization Branch), “License Renewal Issue No. 98-0030, Thermal Aging Embrittlement of Cast Stainless Steel Components,” letter to D.J. Walters (Nuclear Energy Institute), May 19, 2000.

323. Nickell, R.E., and M.A. Rinckel, “Evaluation of Thermal Aging Embrittlement for Cast Austenitic Stainless Steels Components in LWR Reactor Coolant Systems,” EPRI TR-106092, Electric Power Research Institute, Palo Alto, CA, 1997.

324. Chopra, O.K., and A. Sather, “Initial Assessment of the Mechanisms and Significance of Low-Temperature Embrittlement of Cast Stainless Steels in LWR Systems,” NUREG/CR-5385, ANL-89/17, August 1990.

325. Chopra, O.K., and W.J. Shack, “Mechanical Properties of Thermally Aged Cast Stainless Steels from Shippingport Reactor Components,” NUREG/CR-6275, ANL-94/37, April 1995.

326. Chopra, O.K., “Estimation of Fracture Toughness of Cast Stainless Steels during Thermal Aging in LWR Systems,” NUREG/CR-4513, Rev. 1, ANL-93/22, May 1994.

327. Michaud, W.F., P.T. Toben, W.K. Soppet, and O.K. Chopra, “Tensile-Property Characterization of Thermally Aged Cast Stainless Steels,” NUREG/CR-6142, ANL-93/35, February 1994.

328. Tanaka, T., S. Kawaguchi, N. Sakamoto, and K. Koyama, “Thermal Aging of Cast Duplex Stainless Steels,” p. 141–146, in *Proc. Joint ASME/JSME Pressure Vessels and Piping Conf. – Structural Integrity of Pressure Vessels, Piping, and Components*, Honolulu, HI, July 23–27, 1995.

329. Suzuki, I., M. Koyama, S. Kawaguchi, H. Mimaki, M. Akiyama, T. Okuba, Y. Mishima, and T.R. Mager, “Long Term Thermal Aging of Cast Duplex Stainless Steels,” pp. 253–257, *Intl. Conf. on Nucl. Eng. (ICONE-4)*, American Society of Mechanical Engineers, New York, NY, 1996.

330. Hojo, K., I. Muroya, S. Kawaguchi, K. Koyama, and K. Sakai, “Application of the Two-Criteria Approach to the Austenitic Cast Stainless Steel Pipe,” ICONE5-2379, *in Proc. of the 5th Intl. Conf. on Nucl. Eng. (ICONE-5)*, May 26–30, American Society of Mechanical Engineers, New York, NY, 1997.

331. Kawaguchi, S., T. Nagasaki, and K. Koyama, “Prediction Method of Tensile Properties and Fracture Toughness of Thermally Aged Cast Duplex Stainless Steel Piping,” PVP2005-71528, in *Proc. of ASME PVP-2005 ASME Pressure Vessel and Piping Division Conf.,* July 17–21, 2005.

332. Japan Nuclear Energy Safety Organization, *Investigation Report on the Integrity of Thermally-Embrittled Cast Stainless Steel Pipe,* Report JNES-SS-0602, Nuclear Energy System Safety Division, April 2006.

333. Heger, J. J., “885°F Embrittlement of the Ferritic Chromium-Iron Alloys,” *Met. Progress*, p. 55, 1951.

334. Grobner, P.J. “The 885°F (475°C) Embrittlement of Ferritic Stainless Steels,” *Metall. Trans*., 4, 251, 1973.

335. Nichol, T.J., A. Datta, and G. Aggen, “Embrittlement of Ferritic Stainless Steels,” *Metall. Trans*., 11A, 573, 1980.

336. Chung, H.M, and T.R. Leax, “Embrittlement of Laboratory- and Reactor-Aged CF3, CF8, and CF8M Duplex Stainless Steels,” *Mater. Sci. Technol.,* 6, 249–262, 1990.

337. Auger, P., F. Danoix, A. Menand, S. Bonnet, J. Bourgoin, and M. Guttmann, “Atom Probe and Transmission Electron Microscopy Study of Aging of Cast Duplex Stainless Steels,” *Mater. Sci. Technol.,* 6, 301–313, 1990.

338. Vrinat, M., P. Cozar, and Y. Meyzaud, “Precipitated Phases in the Ferrite of Aged Cast Duplex Stainless Steels,” *Scripta Metall.*, 20, 1101–1106, 1986.

339. Joly, P., R. Cozar, and A. Pineau, “Effect of Crystallographic Orientation of Austenite on the Formation of Cleavage Cracks in Ferrite in an Aged Duplex Stainless Steel,” *Scripta Metall.,* 24, 2235–2240, 1990.

340. Sassen, J.M., M.G. Hetherington, T.J. Godfrey, and G.D.W. Smith, “Kinetics of Spinodal Reaction in the Ferrite Phase of a Duplex Stainless Steel,” in *Properties of Stainless Steels in Elevated Temperature Service*, M. Prager, ed., MPC Vol. 26, PVP Vol. 132, ASME, New York, NY, pp. 65–78, 1988.

341. Brown, J.E., A. Cerezo, T.J. Godfrey, M.G. Hetherington, and G.D.W. Smith, “Quantitative Atom Probe Analysis of Spinodal Reaction in Ferrite Phase of Duplex Stainless Steel,” *Mater. Sci. Technol.* 6, 293–300, 1990.

342. Bentley, J., M.K. Miller, S.S. Brenner, and J.A. Spitznagei, “Identification of G-phase in Aged Cast CF-8 Type Stainless Steel,” pp. 328–329, in *Proc. 43rd Electron Microscopy Society of America*, G.W. Bailey, ed., San Francisco Press, 1985.

343. Miller, M.K., and J. Bentley, “Characterization of Fine-Scale Microstructures in Aged Primary Coolant Pipe Steels,” pp. 341–349, in *Environmental Degradation of Materials in Nuclear Power Systems-Water Reactors*, G.J. Theus and J.R. Weeks, eds., The Metallurgical Society, Warrendale, PA, 1988.

344. Gavenda, D.J., W.F. Michaud, T.M. Galvin, W.F. Burke, and O.K. Chopra, “Effects of Thermal Aging on Fracture Toughness and Charpy-Impact Strength of Stainless Steel Pipe Welds,” NUREG/CR-6428, ANL-95-47, U.S. Nuclear Regulatory Commission, Washington, DC, May 1996.

345. Kawaguchi, S., N. Sakamoto, G. Takano, F. Matsuda, Y. Kikuchi, and L. Mraz, “Microstructural Changes and Fracture Behavior of CF8M Duplex Stainless Steel after Long-Term Aging,” *Nucl. Eng. and Design,* 174, 273–285, 1997.

346. Bethmont, M., Y. Meyzaud, and P. Soulat, “Properties of Cast Austenitic Materials for Light Water Reactors,” *Intl. J. Pressure Vessels Piping*, 66, 211-219, 1996.

347. Mills, W.J., “Fracture Toughness of Stainless Steel Welds,” *Fracture Mechanics: Nineteenth Symposium*, STP 969, ASTM, Philadelphia, PA, 330–355, 1988.

348. Leone, G.L., and H.W. Kerr, “Ferrite to Austenite Transformation in Stainless Steels,” *Welding Research Supplement*, pp13-s to 21-s, American Welding Society and Welding Research Council, January 1982.

349. DeLong, W.T., G. Ostrom, and E. Szumachowski, “Measurement and Calculation of Ferrite in Stainless Steel Weld Metals,” *Welding Journal*, 51, (11), Research Supplement, pp. 526s–533s, November 1956.

350. Tsuk, T., M. Hubert, and C. Messager, “Influence of Welding Heat on Residual Ferrite of Deposits of Austenitic Nickel-Chrome Steels,” *Rev. de Metall*., 68, 829–837, December 1971.

351. Hull, F.C., “Delta Ferrite and Martensite Formation in Stainless Steels,” *Welding Journal*, Vol. 52 (5), pp. 193s–203s, Research Supplement, May 1973.

352. Suutala, N., T. Takalo, and T. Moisio, “Relationship Between Solidification and Microstructure in Austenitic and Austenitic-Ferritic Stainless Steel Welds,” *Metall. Trans.*, 10 A, 512–514, 1979.

353. Lippold, J.C., and W.F. Savage, “Solidification of Austenitic Stainless Steel Weldments: Part I-A Proposed Mechanism,” *Welding Journal*, Vol. 59 (12), Research Supplement, pp. 362s–374s, December 1979.

354. David, S.A., “Ferrite Morphology and Variations in Ferrite Content in Austenitic Stainless Steel Welds,” Welding Research Supplement, American Welding Society and Welding Research Council, pp73-s to 71-s, April 1981.

355. Brooks, J.A., J.C. Williams, and A.W. Thompson, “Microstructural Origin of the Skeletal Ferrite Morphology of Austenite Stainless Steel Welds,” *Metall. Trans.,* 14A, 1271–1281, 1983.

356. Olson, D.L., “Prediction of Austenitic Weld Metal Microstructure and Properties,” *Welding Journal* Vol. 59 (12), Research Supplement, pp. 281s-295s, October 1985.

357. Siewert, T.A., C.N. McCowan, and D.L. Olson, “Prediction of Austenitic Weld Metal Microstructure and Properties,” *Welding Journal*, Vol. 59 (12), Research Supplement, pp. 289s–298s, December 1988.

358. Inoue, H., and T. Koseki, *Clarification of Solidification Behaviors in Austenitic Stainless Steels Based on Welding Process*, Nippon Steel Technical Report No. 95, Steel Research Laboratories, Nippon Steel Corporation, January 2007.

359. Abe, H., and Y. Watanabe, “Low-Temperature Aging Characteristics of Type 316L Stainless Steel Welds: Dependence on Solidification Mode,” *Metall. & Metal. Trans*., 39A, 1392–1398, 2008.

360. Davies, G.J., *Solidification and Casting*, App. Sc. Pub. Ltd., 1973.

361. AWS A4.2-74, *Standard Procedures for Calibrating Magnetic Instruments to Measure Delta Ferrite Content of Austenitic Stainless Steel Weld Metal*, American Welding Society, Miami, FL, 1974.

362. ASTM A 800/A 800M, “Standard Practice for Steel Casting, Austenitic Alloy, Estimating Ferrite Content Thereof,” American Society of Testing and Materials, West Conshohocken, PA, 2001.

363. Schoefer, E.A., “A Diagram for Estimation of Ferrite Content in Stainless Steel Castings,” in Appendix to *Mossbauer-Effect Examination of Ferrite in Stainless Steel Welds and Castings*, by L.J. Schwartzgruber et al., *Welding Journal*, Vol. 53, Research Supplement, pp. 10s–12s, 1974.

364. Schaeffler, A.L., “Selection of Austenitic Electrodes for Welding Dissimilar Metals,” *Welding Journal*, Vol. 26, No. 10, pp. 601–620, 1947.

365. DeLong, W.T., “Ferrite in Austenitic Stainless Steel Weld Metal,” *Welding Journal*, 53 (7), Research Supplement, pp. 273s–286s, 1974.

366. NRC, “Radiation Embrittlement of Reactor Vessel Materials,” Regulatory Guide 1.99 Rev. 2, Washington, DC, May 1988.

367. ASTM E900-02, “Standard Guide for Predicting Radiation-Induced Transition Temperature Shift in Reactor Vessel Materials, E706 (IIF),” May 2002, superseded by ASTM E900-15, “Standard Guide for Predicting Radiation-Induced Transition Temperature Shift in Reactor Vessel Materials,” 2015.

368. Dufresne, J., B. Henry, and H. Larsson, “Fracture Toughness of Irradiated AISI 304 and 316L Stainless Steels, Effects of Radiation on Structural Materials,” ASTM STP 683, pp. 511–528, J. A. Sprague and D. Kramer, eds., American Society for Testing and Materials, Philadelphia, PA, 1979.

369. Picker, C., A.L. Stott, and H. Cocks, “Effects of Low-Dose Fast Neutron Irradiation on the Fracture Toughness of Type 316 Stainless Steel and Weld Metal,” in *Proc. Specialists Meeting on Mechanical Properties of Fast Reactor Structural Material*s, Paper IWGFR 49/440-4, Chester, UK, 1983.

370. Huang, F.H., “The Fracture Characterization of Highly Irradiated Type 316 Stainless Steel,” *Int. J. Fracture* 25, 181–193, 1984.

371. Bernard, J., and G. Verzeletti, “Elasto-Plastic Fracture Mechanics Characterization of Type 316H Irradiated Stainless Steel up to 1 dpa,” *Effects of Radiation on Materials: 12th Intl. Symp*., ASTM STP 870, pp. 619-641, F.A. Garner and J.S. Perrin, eds., American Society for Testing and Materials, Philadelphia, PA, 1985.

372. Michel, D.J., and R.A. Grey, “Effects of Irradiation on the Fracture Toughness of FBR Structural Materials,” *J. Nucl. Mater*. 148, 194–203, 1987.

373. De Vries, M.I., “Fatigue Crack Growth and Fracture Toughness Properties of Low Fluence Neutron-Irradiated Type 316 and Type 304 Stainless Steels,” in *Influence of Radiation on Mechanical Properties: 13th Symposium (Part II)*, ASTM STP 956, pp. 174–190, F.A. Garner et al., eds., American Society of Testing and Materials, Philadelphia, PA, 1987.

374. Sindelar, R.L., G.R. Caskey, Jr., J.K. Thomas, J.R. Hawthorne, A.L. Hiser, R.A. Lott, J.A. Begley, and R.P. Shogan, “Mechanical Properties of 1950s Vintage Type 304 Stainless Steel Weldment Components after Low Temperature Neutron Irradiation,” in *16th Intl. Symp. on Effects of Radiation on Materials*, ASTM STP 1175, pp. 714–746, American Society of Testing and Materials, Philadelphia, PA, 1993.

375. Haggag, F.M., W.R. Corwin, and R.K. Nanstad, “Effects of Irradiation on the Fracture Properties of Stainless Steel Weld Overlay Cladding,” *Nucl. Eng. and Design,* 124, 129–141, 1990.

376. Hamilton, M.L., F.H. Huang, W.J.S. Yang, and F.A. Garner, “Mechanical Properties and Fracture Behavior of 20% Cold-Worked 316 Stainless Steel Irradiated to Very High Neutron Exposures,” in *Influence of Radiation in Material, Properties: 13th Intl. Symp.* (Part II), ASTM STP 956, pp. 245–270, American Society of Testing and Materials, Philadelphia, PA, 1987.

377. Little, E.A., “Dynamic J-Integral Toughness and Fractographic Studies of Fast Reactor Irradiated Type 321 Stainless Steel,” in *Effects of Radiation on Material, Properties: 12th Intl. Symp.*, ASTM STP 870, pp. 563–579, American Society of Testing and Materials, Philadelphia, PA, 1985.

378. Haggag, F.J., W.L. Server, W.G. Reuter, and J.M. Beeston, “Effects of Irradiation Fluence and Creep on Fracture Toughness of Type 347/348 Stainless Steels,” ASTM STP 870, pp. 548–6562, American Society of Testing and Materials, Philadelphia, PA, 1985.

379. Frew, B., R. Horn, F. Hua, H. Mehta, and S. Ranganath, “BWRVIP-234: BWR Vessel and Internals Project, Thermal Aging and Neutron Embrittlement Evaluation of Cast Austenitic Stainless Steels for BWR Internals,” Report 1019060, Electric Power Research Institute, Palo Alto, CA, December 2009.

380. Fukuya, K., K. Fuji, H. Nishioka, and Y. Kitsunai, “Evolution of Microstructure and Microchemistry in Cold-worked 316 Stainless Steel under PWR Irradiations,” *J. Nucl. Sci. and Technol.,* 43 (2), 159–173. 2006.

381. Chopra, O.K., “Effects of Thermal Aging and Neutron Irradiation on Crack Growth Rate and Fracture Toughness of Cast Stainless Steels and Austenitic Stainless Steel Welds,” NUREG/CR-7185, ANL-14/10, 2015.

382. Chen, Y., B. Alexandreanu, and K. Natesan, “Crack Growth Rate and Fracture Toughness Tests on Irradiated Cast Stainless Steels,” NUREG/CR-7184, ANL-12/56, June 2015.

383. Lucas, T.R., R.G. Ballinger, H. Hanninen, and T. Saukkonen, “Effect of Thermal Aging on SCC, Material Properties and Fracture Toughness of Stainless Steel Weld Metals,” in the *15th Intl. Conf. on Environmental Degradation of Materials in Nuclear Power Systems – Water Reactors*, pp. 883–900, J.T. Busby, G. Ilevbare, and P.L. Andresen, eds., The Minerals, Metals & Materials Society, Warrendale, PA, 2011.

384. Chen, Y., O.K. Chopra, E.E. Gruber, and W.J. Shack, “Irradiated Assisted Stress Corrosion Cracking of Austenitic Stainless Steels in BWR Environments,” NUREG/CR-7018, ANL-09/17, June 2010.

385. Morra, M., “Program on Technology Innovation: Scoping Study of Low Temperature Crack Propagation for 182 Weld Metal in BWR Environments and for Cast Austenitic Stainless Steel in PWR Environments (Revision 1),” EPRI 1020957, Electric Power Research Institute, Palo Alto, CA, May 2010.

386. MRP-227-A, “Materials Reliability Program: Pressurized Water Reactor Internals Inspection and Evaluation Guidelines,” EPRI Report 1022863, Electric Power Research Institute, Palo Alto, CA, December 23, 2011.

387. Eason, E.D., J.E. Wright, and G.R. Odette, “Improved Embrittlement Correlations for Reactor Pressure Vessels,” NUREG/CR-6551 (MSC 970501), November 1998.

388. Meyer, T., C. Boggess, S. Byrne, R. Schwirian, F. Gift, and R. Gold, “Material Reliability Program: Screening, Categorization, and Ranking of Reactor Internals Components for Westinghouse and Combustion Engineering PWR Design (MRP-191),” EPRI Report 1013234, Electric Power Research Institute, Palo Alto, CA, November 2006.

389. Chopra, O.K., and A.S. Rao, “Methodology for Estimating Thermal and Neutron Embrittlement of Austenitic Stainless Steel Welds during Service in Light Water Reactors,” *J. Pressure Vessel Technol*., 138, 1-16, 2016.

390. Chopra, O.K., and W.J. Shack, “Effects of LWR Coolant Environments on Fatigue Design Curves of Carbon and Low-Alloy Steels,” NUREG/CR-6583, ANL-97/18, March 1998.

391. Chopra, O.K., “Effects of LWR Coolant Environments on Fatigue Design Curves of Austenitic Stainless Steels,” NUREG/CR–5704, ANL–98/31, 1999.

392. Chopra, O.K., “Mechanisms and Estimation of Fatigue Crack Initiation in Austenitic Stainless Steels in LWR Environments,” NUREG/CR–6787, ANL–01/25, August 2002.

393. Chopra, O.K., and W.J. Shack, “Environmental Effects on Fatigue Crack Initiation in Piping and Pressure Vessel Steels,” NUREG/CR–6717, ANL–00/27, May 2001.

394. Chopra, O.K., and W.J. Shack, “Review of the Margins for ASME Code Design Curves – Effects of Surface Roughness and Material Variability,” NUREG/CR–6815, ANL–02/39, Sept. 2003.

395. Chopra, O.K., B. Alexandreanu, and W.J. Shack, “Effect of Material Heat Treatment on Fatigue Crack Initiation in Austenitic Stainless Steels in LWR Environments,” NUREG/CR–6878, ANL–03/35, July 2005.

396. Chopra, O.K., and W.J. Shack, “Effect of LWR Coolant Environments on the Fatigue Life of Reactor Materials – Final Report,” NUREG/CR–6909, ANL–06/08, Feb. 2007.

397. Chopra, O.K., and G.L. Stevens, “Effect of LWR Coolant Environments on the Fatigue Life of Reactor Materials – Draft Report for Comment,” NUREG/CR–6909 Rev. 1, ANL–12/60, March 2014.

398. Laird, C., “The Influence of Metallurgical Structure on the Mechanism of Fatigue Crack Propagation,” in *Fatigue Crack Propagation*, ASTM STP 415, American Society for Testing and Materials, Philadelphia, PA, 131-180, 1967.

399. Miller, K.J., “Initiation and Growth Rates of Short Cracks,” in Fundamentals of Deformation and Fracture, B.A. Bilby, K.J. Miller, and J.R. Willis, eds., Cambridge United Press, 476–500, 1984.

400. Miller, K.J., “Damage in Fatigue: A New Outlook,” in *Pressure Vessels and Piping Codes and Standard: Volume 1 – Current Applications*, PVP Vol. 313–1, K.R. Rao and Y. Asada, eds., American Society of Mechanical Engineers, New York, 191–192, 1995.

401. Gavenda, D.J., P.R. Luebbers, and O.K. Chopra, “Crack Initiation and Crack Growth Behavior of Carbon and Low-Alloy Steels,” Fatigue and Fracture 1, Vol. 350, S. Rahman, K.K. Yoon, S. Bhandari, R. Warke, and J.M. Bloom, eds., American Society of Mechanical Engineers, New York, pp. 243–255, 1997.

402. Suh, C.M., R. Yuuki, and H. Kitagawa, “Fatigue Microcracks in a Low Carbon Steel,” *Fatigue Fract. Eng. Mater. Struct*. 8, 193–203, 1985.

403. Tokaji, K., T. Ogawa, and S. Osako, “The Growth of Microstructurally Small Fatigue Cracks in a Ferritic-Pearlitic Steel, Fatigue Fracture,” *Eng. Mater. Struct*., 11, 331–342, 1988.

404. Dowling, N.E., “Crack Growth During Low-Cycle Fatigue of Smooth Axial Specimens,” in *Cyclic Stress-Strain and Plastic Deformation Aspects of Fatigue Crack Growth*, ASTM STP 637, American Society for Testing and Materials, Philadelphia, PA, 97–121, 1977.

405. Suresh, S., and R.O. Ritchie, “Propagation of Short Fatigue Cracks,” *Int. Metals Reviews,* 29, 445–476, 1984.

406. Tokaji, K., and T. Ogawa, “The Growth of Microstructurally Small Fatigue Cracks in Metals,” in *Short Fatigue Cracks*, ESIS 13, M. J. Miller and E. R. de los Rios, eds., Mechanical Engineering Publication, London, 85–99, 1992.

407. James, L.A., “The Effect of Temperature and Cyclic Frequency Upon Fatigue Crack Growth Behavior of Several Steels in Elevated Temperature Aqueous Environment,” *J. Pressure Vessel Technol*., 116, 122–127, 1994.

408. James, L.A., “The Initiation of Environmentally-Assisted Cracking in Semi-Elliptical Surface Cracks,” in *Pressure Vessel and Piping Codes and Standards*, PVP Vol. 353, T. C. Esselman, ed., American Society of Mechanical Engineers, New York, pp. 125–139, 1997.

409. Bulloch, J.H., “A Review of the Fatigue Crack Extension Behaviour of Ferritic Reactor Pressure Vessels Materials in Pressurized Water Reactor Environments,” *Res. Mech*., 26, 95–172, 1989.

410. Lenz, E., N. Wieling, and H. Munster, “Influence of Variation of Flow Rates and Temperature on the Cyclic Crack Growth Rate under BWR Conditions,” in *Proc. 3rd Int. Symp. on Environmental Degradation of Materials in Nuclear Power Systems – Water Reactors*, G.J. Theus and J.R. Weeks, eds., The Metallurgical Society, Warrendale, PA, pp. 283–288, 1988.

411. James, L.A., G.L. Wire, and W.H. Cullen, “The Effect of Water Flow Rate Upon the Environmentally-Assisted Cracking Response of a Low-Alloy Steel,” *J. Pressure Vessel Technol*., 117 (3), 238–244, 1995.

412. Wire, G.L., and Y.Y. Li, “Initiation of Environmentally–Assisted Cracking in Low–Alloy Steels,” *Fatigue and Fracture* Vol. 1, PVP Vol. 323, H.S. Mehta, ed., American Society of Mechanical Engineers, New York, pp. 269–289, 1996.

413. Van Der Sluys, W.A., and R.H. Emanuelson, “Environmentally Acceleration of Fatigue Crack Growth in Reactor Pressure Vessel Materials,” EPRI Report TR-102796, Electric Power Research Institute, Palo Alto, CA, August 1993.

414. Cullen, W.H., M. Kemppainen, H. Hänninen, and K. Törrönen, “The Effects of Sulfur Chemistry and Flow Rate on Fatigue Crack Growth Rates in LWR Environments,” NUREG/CR–4121, 1985.

415. Van Der Sluys, W.A., and R.H. Emanuelson, “Environmental Acceleration of Fatigue Crack Growth in Reactor Pressure Vessel Materials and Environments,” *Environmentally Assisted Cracking: Science and Engineering*, ASTM STP 1049, W.B. Lisagor, T.W. Crooker, and B.N. Leis, eds., American Society for Testing and Materials, Philadelphia, PA, pp. 117–135, 1990.

416. Atkinson, J.D., and J.E. Forrest, “The Role of MnS Inclusions in the Development of Environmentally Assisted Cracking of Nuclear Reactor Pressure Vessel Steels,” in *Proc. 2nd Int. Atomic Energy Agency Specialists’ Meeting on Subcritical Crack Growth*, NUREG/CP–0067, MEA–2090, Vol. 2, pp. 153–178, April 1986.

417. Atkinson, J.D., J. Yu, and Z.-Y. Chen, “An Analysis of the Effects of Sulfur Content and Potential on Corrosion Fatigue Crack Growth in Reactor Pressure Vessel Steels,” *Corros. Sci*., 38 (5), 755–765, 1996.

418. Auten, T.A., S.Z. Hayden, and R.H. Emanuelson, “Fatigue Crack Growth Rate Studies of Medium Sulfur Low Alloy Steels Tested in High Temperature Water,” *Proc. 6th Int. Symp. on Environmental Degradation of Materials in Nuclear Power Systems – Water Reactors*, R.E. Gold and E.P. Simonen, eds., The Metallurgical Society, Warrendale, PA, pp. 35–40, 1993.

419. Ford, F.P., and P.L. Andresen, “Stress Corrosion Cracking of Low–Alloy Pressure Vessel Steel in 288°C Water,” *Proc. 3rd Int. Atomic Energy Agency Specialists’ Meeting on Subcritical Crack Growth*, NUREG/CP–0112, Vol. 1, pp. 37–56, August 1990.

420. Ford, F.P., “Overview of Collaborative Research into the Mechanisms of Environmentally Controlled Cracking in the Low Alloy Pressure Vessel Steel/Water System,” *Proc. 2nd Int. Atomic Energy Agency Specialists’ Meeting on Subcritical Crack Growth*, NUREG/CP–0067, MEA–2090, Vol. 2, pp. 3–71, April 1986.

421. Ford, F.P., D.F. Taylor, and P.L. Andresen, “Corrosion-Assisted Cracking of Stainless and Low-Alloy Steels in LWR Environments,” EPRI NP-5064S, Electric Power Research Institute, Palo Alto, CA, February 1987.

422. Ford, F.P., S. Ranganath, and D. Weinstein, “Environmentally Assisted Fatigue Crack Initiation in Low-Alloy Steels – A Review of the Literature and the ASME Code Design Requirements,” EPRI Report TR-102765, Electric Power Research Institute, Palo Alto, CA, August 1993.

423. Ford, F.P., “Prediction of Corrosion Fatigue Initiation in Low–Alloy and Carbon Steel/ Water Systems at 288°C,” *Proc. 6th Intl. Symp. on Environmental Degradation of Materials in Nuclear Power Systems – Water Reactors*, R.E. Gold and E.P. Simonen, eds., The Metallurgical Society, Warrendale, PA, pp. 9–17, 1993.

424. Hänninen, H., K. Törrönen, and W.H. Cullen, “Comparison of Proposed Cyclic Crack Growth Mechanisms of Low Alloy Steels in LWR Environments,” in *Proc. 2nd Int. Atomic Energy Agency Specialists’ Meeting on Subcritical Crack Growth*, NUREG/CP–0067, MEA–2090, Vol. 2, pp. 73–97, April 1986.

425. Hänninen, H., K. Törrönen, M. Kempainen, and S. Salonen, “On the Mechanisms of Environment Sensitive Cyclic Crack Growth of Nuclear Reactor Pressure Vessel Steels,” *Corros. Sci*., 23, 663–679, 1983.

426. Törrönen, K., M. Kempainen, and H. Hänninen, “Fractographic Evaluation of Specimens of A533B Pressure Vessel Steel,” EPRI Report NP–3483, Project 1325–7, May 1984.

427. de los Rios, E.R., Z. Tang, and K.J. Miller, “Short Crack Fatigue Behavior in a Medium Carbon Steel,” *Fatigue of Engineering Materials and Structures,* 7, 97–108, 1984.

428. de los Rios, E.R., A. Navarro, and K. Hussain, “Microstructural Variations in Short Fatigue Crack Propagation of a C–Mn Steel,” *Short Fatigue Cracks*, ESIS 13, M.J. Miller and E.R. de los Rios, eds., Mechanical Engineering Publication, London, pp. 115–132, 1992.

429. Oriani, R.A., “A Mechanistic Theory of Hydrogen Embrittlement of Steels,” *Ber. Bunsenges. Phys. Chem*., 76, 848–857, 1972.

430. Beachem, C.D., “A New Model for Hydrogen Assisted Cracking,” *Met. Trans*., 3A (2), 437–451, 1972.

431. Wu, X., and Y. Katada, “Strain-Rate Dependence of Low Cycle Fatigue Behavior in a Simulated BWR Environment,” *Corros. Sci*., 47, 1415–1428, 2005.

432. Wu, X., E. Han, W. Ke, and Y. Katada, “Effects of Loading Factors on Environmental Fatigue Behavior of Low-Alloy Pressure Vessel Steels in Simulated BWR Water,” *Nucl. Eng. Des*., 237, 1452–1459, 2007.

433. Wu, X., and Y. Katada, “Corrosion Fatigue Behavior of Low-Alloy Pressure Vessel Steels in High Temperature Water under Multi-Factor Conditions,” *J. Pressure Vessel Technol. Trans. ASME*, Vol. 126, 466–472, 2004.

434. Devrient, B., A. Roth, K. Kuster, U. Ilg, and M. Widera, “Effect of Dynamic Strain Ageing on the Environmentally Assisted Cracking of Low-Alloy Steels in Oxygenated High-Temperature Water,” *Proc. of the 13th Intl. Conf. on Environmental Degradation of Materials in Nuclear Power Systems*, Whistler, BC, Canada, August 19–23, 2007.

435. Devrient, B., A. Roth, K. Kuster, M. Widera, and U. Ilg, “Influence of Dynamic Strain Ageing on the Crack Growth Rates and Crack Tip Plasticity of Low-Alloy Steels in Oxygenated High-Temperature Water,” *Proc. of the 14th Intl. Conf. on Environmental Degradation of Materials in Nuclear Power Systems*, Virginia Beach, VA, August 23–27, 2009.

436. Hanninen, H., Y. Yagodzinskyy, O. Tarasenko, U. Ehrnsten, and P. Aaltonen, H.-P. Seifert, “Effects of Dynamic Strain Ageing on Environmentally Assisted Cracking of Low-Alloy Pressure Vessel and Piping Steels,” *Proc. of the Tenth Intl. Conf. on Environmental Degradation of Materials in Nuclear Power Systems – Water Reactors*, *The Metallurgical Society*, Warrendale, PA, Paper #0047, Lake Tahoe, NV, August 5–9, 2001.

437. Seifert, H.-P., and S. Ritter, “Strain-Induced Corrosion Cracking Behavior of Low-Alloy Steels under Boiling Water Reactor Conditions,” *J. Nucl. Mater*., 378, 312–326, 2008.

438. Wu, Q.X., and Y. Katada, “Role of Dynamic Strain Aging in Corrosion Fatigue of Low-Alloy Pressure Vessel Steel in High Temperature Water,” *J. Mater. Sci*., 42, 633–639, 2007.

439. Kim, Y.J., “Characterization of the Oxide Film Formed on Type 316 Stainless Steel in 288°C Water in Cyclic Normal and Hydrogen Water Chemistries,” *Corrosion,* 51 (11), 849–860, 1995.

440. Kim, Y.J., “Analysis of Oxide Film Formed on Type 304 Stainless Steel in 288°C Water Containing Oxygen, Hydrogen, and Hydrogen Peroxide,” *Corrosion,* 55 (1), 81–88, 1999.

441. Tapping, R.L., R.D. Davidson, E. McAlpine, and D.H. Lister, “The Composition and Morphology of Oxide Films Formed on Type 304 Stainless Steel in Lithiated High-Temperature Water,” *Corrosion Sci*., 26 (8), 563–576, 1986.

442. Lister, D.H., R.D. Davidson, and E. McAlpine, “The Mechanism and Kinetics of Corrosion Product Release from Stainless Steel in Lithiated High-Temperature Water,” *Corrosion Sci*., 27 (2), 113–140, 1987.

443. Belo, M. Da Cunha, M. Walls, N.E. Hakiki, J. Corset, E. Picquenard, G. Sagon, and D. Neol, “Composition, Structure and Properties of the Oxide Films Formed on the Stainless Steel 316L in a Primary Type PWR Environment,” *Corrosion Sci*., 40 (2/3), 447–463, 1998.

444. Stellwag, B., “The Mechanism of Oxide Film Formation on Austenitic Stainless Steels in High-Temperature Water,” *Corrosion Sci*., 40 (2/3), 337–370, 1998.

445. Nakayama, T., and Y. Oshida, “Identification of the Initial Oxide Films on 18-8 Stainless Steel in High-Temperature Water,” *Corrosion NACE,* 24 (10), 336–337, 1968.

446. Srinivasan, V.S., M. Valsan, R. Sandhya, K. Bhanu Sankara Rao, M.L. Mannan, and D.H. Sastry, “High Temperature Time-Dependent Low Cycle Fatigue Behavior of a Type 316L(N) Stainless Steel,” *Intl. J. Fatigue,* 21, 11–21, 1999.

447. Amzallag, C., P. Rabbe, G. Gallet, and H.-P. Lieurade, “Influence des Conditions de Sollicitation Sur le Comportement en Fatigue Oligocyclique D’aciers Inoxydables Austénitiques,” *Memoires Scientifiques Revue Metallurgie Mars*, pp. 161–173, 1978.

448. Solomon, H.D., C. Amzallag, A.J. Vallee, and R.E. De Lair, “Influence of Mean Stress on the Fatigue Behavior of 304L SS in Air and PWR Water,” *Proc. of the 2005 ASME Pressure Vessels and Piping Conf.*, Denver, CO, paper #PVP2005-71064, 2005.

449. Smith, J.L., and O.K. Chopra, “Crack Initiation in Smooth Fatigue Specimens of Austenitic Stainless Steel in Light Water Reactor Environments,” in *Operations, Applications, and Components – 1999*, PVP Vol. 395, I. T. Kisisel, ed., American Society of Mechanical Engineers, New York, pp. 235–242, 1999.

450. Obrtlik, K., J. Polák, M. Hájek, and A. Vasek, “Short Fatigue Crack Behavior in 316L Stainless Steel,” *Intl. J. Fatigue,* 19, 471–475, 1997.

451. Shack, W.J., and T.F. Kassner, “Review of Environmental Effects on Fatigue Crack Growth of Austenitic Stainless Steels,” NUREG/CR-6176, ANL-94/1, May 1994.

452. James, L.A., and D.P. Jones, “Fatigue Crack Growth Correlation for Austenitic Stainless Steels in Air,” in *Predictive Capabilities in Environmentally Assisted Cracking*, PVP Vol. 99, ASME, pp. 363–414, 1985.

453. Cipolla, R.C., and W.H. Warren, “Technical Basis for Code Case N-809 on Reference Fatigue Crack Growth Curves for Austenitic Stainless Steels in Pressurized Water Reactor Environments,” PVP2015-45884, in *Proc. of 2015 ASME Pressure Vessel and Piping Conf.*, Boston, MA, July 19–23, 2015.

454. ASME BPVC.CC.NC.S2-2015, Case N-809, Reference Fatigue Crack Growth Rate Curves for Austenitic Stainless Steels in Pressurized Water Reactor Environments, Section XII, Division 1, The American Society of Mechanical Engineers, 2 Park Avenue, New York, NY, June 23, 2015.

455. Mills, W.J., “Critical Review of Fatigue Crack Growth Rates for Stainless Steel in Deaerated Water – Parts 1 and 2,” Session 9, EPRI International PWR MRP Materials Reliability Conference and Exhibition, June 28–July 1, 2010.

456. Dinu, F., A. Stratan, and D. Dubina, “Influence of Strain Rate on the Weld Detailing Behaviour in MR Connections,” in *Behaviour of Steel Structures in Seismic Areas: Proceedings of the Fourth International Conference STESSA 2003*, Federico M. Mazzolani, ed., June 9–12, pp. 835–840, Naples, Italy, 2003.

457. Kurobane, Y., K. Ogawa, and C. Veda, “Kobe Earthquake Damage to High-Rise Ashiyama Apartment Buildings: Brittle Tensile Fracture of Box Section Columns,” in *Tubular Structures VII*, I. Farkas and K. Jarmai, eds., Miskolc, pp. 277–284, Balkema, Rotterdam, Netherlands, August 28–30, 1996.

458. Kohzu, I., and K. Suita, “Single or Few Excursions Failure of Steel Structural Joints Due to Impulsive Shocks in the 1995 Hyogoken-Nanbu Earthquake,” *Proc. 11th World Conference on Earthquake Engineering*, Acapulco, Mexico, Paper 412, June 26–28, 1996.

459. Gioncu, V., “Influence of Strain Rate on the Behaviour of Steel Members,” in Behaviour of Steel Structures in Seismic Areas: *Proc. of the Third International Conference STESSA*, Montreal, Canada, Federico M. Mazzolani and Robert Tremblay, eds., pp. 19–26, 2000.

460. Chang, K.-C., and G.C. Lee, “Strain Rate Effect on Structural Steel under Cyclic Loading.” *J. Eng. Mech.*, 113 (9), 1292–1301,1987. Available at http://dx.doi.org/10.1061/(ASCE)0733-9399(1987)113:9(1292).

461. Uang, C.M., and D.M. Bordad, “Dynamic Testing of Full-Scale Steel Moment Connections,” *Proc. 11th World Conference on Earthquake Engineering*, Acapulco, Mexico, Paper 407, June 26–28, 1996.

462. Nakashima, M., K. Suita, K. Morisako, and Y. Marioka, “Tests of Welded Beam-Column Subassemblies I. Global Behaviour, II. Detailed Behaviour,” *J. Struct. Eng.,* 124 (11), 1236–1252, 1998.

463. Antaki, G.A., “Pipeline and Pipeline Engineering,” p. 238, Marcel Dekker, Inc., New York, NY, 2003.

464. Wiessner, C.S., and M. MacGillivray, “Loading Rate Effects on Tensile Properties and Fracture Toughness of Steel,” 1999. Available at http://www.twi-global.com/technical-knowledge/published-papers/loading-rate-effects-on-tensile-properties-and-fracture-toughness-of-steel-april-1999/.

465. Abdel–Raouf, H., A. Plumtree, and T.H. Topper, “Effects of Temperature and Deformation Rate on Cyclic Strength and Fracture of Low–Carbon Steel,” in *Cyclic Stress-Strain Behavior-Analysis, Experimentation, and Failure Prediction*, ASTM STP 519, American Society for Testing and Materials, Philadelphia, pp. 28–57, 1973.

466. Lee, B.H., and I.S. Kim, “Dynamic Strain Aging in the High-Temperature Low-Cycle Fatigue of SA 508 Cl. 3 Forging Steel,” *J. Nucl. Mater*., 226, 216–225, 1995.

467. Terrell, J.B., “Fatigue Life Characterization of Smooth and Notched Piping Steel Specimens in 288°C Air Environments,” NUREG/CR–5013, EM–2232 Materials Engineering Associates, Inc., Lanham, MD, May 1988.

468. Jaske, C.E., and W.J. O’Donnell, “Fatigue Design Criteria for Pressure Vessel Alloys,” *Trans. ASME J. Pressure Vessel Technol.,* 99, 584–592, 1977.

469. Hayashi, M., K. Enomoto, T. Saito, and T. Miyagawa, “Development of Thermal Fatigue Testing with BWR Water Environment and Thermal Fatigue Strength of Austenitic Stainless Steels,” *Nucl. Eng. Des*. 184, 113–122, 1998.

470. Shack, W.J., and W.F. Burke, “Fatigue of Type 316NG SS,” in *Environmentally Assisted Cracking in Light Water Reactors, Semiannual Report*, October 1989–March 1990, NUREG/CR–4667 Vol. 10, ANL–91/5, pp. 3–19, March 1991.

471. Pellissier–Tanon, A., J. L. Bernard, C. Amzallag, and P. Rabbe, “Evaluation of the Resistance of Type 316 Stainless Steel Against Progressive Deformation,” in *Low-Cycle Fatigue and Life Prediction*, ASTM STP 770, C. Amzallag, B.N. Leis, and P. Rabbe, eds., American Society for Testing and Materials, Philadelphia, pp. 69–80, 1982.

472. Kanasaki, H., R. Umehara, H. Mizuta, and T. Suyama, “Fatigue Lives of Stainless Steels in PWR Primary Water,” *Trans. 14th Intl. Conf. on Structural Mechanics in Reactor Technology (SMiRT 14)*, Lyon, France, pp. 473–483, 1997.

473. Tsutsumi, K., H. Kanasaki, T. Umakoshi, T. Nakamura, S. Urata, H. Mizuta, and S. Nomoto, “Fatigue Life Reduction in PWR Water Environment for Stainless Steels,” in *Assessment Methodologies for Preventing Failure: Service Experience and Environmental Considerations*, PVP Vol. 410-2, R. Mohan, ed., American Society of Mechanical Engineers, New York, pp. 23–34, 2000.

474. Chopra, O.K., and J.L. Smith, “Estimation of Fatigue Strain-Life Curves for Austenitic Stainless Steels in Light Water Reactor Environments,” in *Fatigue, Environmental Factors, and New Materials*, PVP Vol. 374, H.S. Mehta, R.W. Swindeman, J.A. Todd, S. Yukawa, M. Zako, W.H. Bamford, M. Higuchi, E. Jones, H. Nickel, and S. Rahman, eds., American Society of Mechanical Engineers, New York, pp. 249–259, 1998.

475. Mughrabi, H., *Dislocations and Properties of Real Material*, Book No. 323, The Inst. of Metals, London, pp. 244–262, 1985.

476. Laird, C., Chapter 27, in *Physical Metallurgy*, 4th ed., R.W. Cahn and P. Haasen, eds., pp. 2293–2397, Elsevier Science, 1996.

477. Polak, J., Cyclic Deformation, Crack Initiation, and Low-Cycle Fatigue, in *Comprehensive Structural Integrity*, Vol. 4.01, I. Milne, R.O. Ritche, and B. Karihallo, eds., Elsevier, Amsterdam, pp. 1–39, 2003.

478. Weidner, A., J. Man, W. Skrotzki, and J. Polak, “Slip Localization and Dislocation Structure at Early Stages of Fatigue Damage in Austenitic Stainless Steel (316L),” *International Conference on Fatigue*, ICF12, Ottawa, 2009.

479. Hull, D., in *Introduction to Dislocations*, Pergamon Press, Oxford, 1965.

480. Basinski, S.J., Z.S. Basinski, and A. Howie, “Early Stages of Fatigue in Copper Single Crstal,” *Phil. Mag.*, 19 (161), 899–924, 1969.

481. Grosskreutz, J.C, “The Mechanisms of Metal Fatigue (I),” *Phys. Stat. Sol.,* 47, 11–31, 1971.

482. McGrath, J.T., and W.J. Bratina, “Dislocation Structures in Fatigued Iron-Carbon Alloys,” *Phil. Mag.* 12 (120), 1293–1305, 1965.

483. Weissmann, S., A. Shrier, and V. Greenhut, “Dislocation Substructure and Extension of Fatigue Life in Metal Crystals,” *Trans. Am. Soc. Metals,* 59, 709, 1966.

484. Feltner, E., and C. Laird, “The Role of Slip Character in Steady State Cyclic Stress Strain Behavior,” *Trans. Metall. Soc. A.I.M.E., 245,* 1372, 1969.

485. Feltner, E., and C. Laird, “Cyclic Stress-Strain Response of F.C.C. Metals and Alloys – I Phenomenological Experiments,” *Acta Metall.,* 15, 1621, 1967.

486. Abdel-Raouf. H., P.P. Benham, and A. Plumtree, “Mechanical Behavior and Substructure of Strain Cycled Iron,” *Can. Met. Q.,* 10, 87, 1971.

487. Chopra, O.K., and C.V.B. Gowda, “Substructural Development during Strain Cycling of Alpha-iron,” *Phil. Mag.,* 30 (3), 583–591, 1974.

488. Segall, R.L., “Lattice Defects in Fatigued Metals,” in *Electron Microscopy and Strength of Crystals*, Interscience, NY, 515, 1963.

489. Pham, M.S., C. Solenthaler, K.G.F. Janssens, and S.R. Holdsworth, “Dislocation Structure Evolution and its Effect on Cyclic Deformation Response of AISI 316L Stainless Steel,” *Mater. Sc. Eng*., 528, 3261–3269, 2011.

490. Manjoine, M.J., “Influence of Strain Rate and Temperature on Yield Stress of Mild Steel,” *J. of Applied Mechanics*, 66 (11), 211–218, 1944.

491. Zener, C., and J. H. Hollomon, “Effect of Strain Rate upon Plastic Flow of Steel,” *J. Appl. Phys.*, 15, 22–32, 1944.

492. Nagaraja Rao, N., M. Lohrmann, and L. Tall, “Effect of strain rate on the yield stress of structural steel,” *ASTM J. Mat.*, 1 (1), Publication No. 293, Fritz Laboratory Reports, Paper 1684, March 1966.

493. Kaneta, K., I. Kohzu, and K. Fujimara, “On the Strength and Ductility of Steel Structural Joints Subjected to High-Speed Monotonic Tensile Loading,” in *8th European Conference on Earthquake Engineering*, Lisbon, September 12–17, 1986.

494. Soroushian, P., and K.B. Choi, “Steel Mechanical Properties at Different Strain Rates, *J. Struct. Eng.*, 113 (11), 863–872, 1987.

495. Kassar, M., and W.W. Wu, “Effect of Strain Rate on Material Properties of Sheet Steels,” *J. Struct. Eng.*, 118 (11), 3136–3150, 1992.

496. Campbell, J.D., and W.G. Ferguson, “The temperature and strain-rate dependence of the shear strength of mild steel,” *Phil. Mag.*, 21 (169), 63–82, 1970.

497. Campbell, J.D., A.M. Eleiche, and M.C. Tsao. “Strength of Metals and Alloys at High Strains and Strain Rates,” in *Fundamental Aspects of Structural Alloy Design*, R.I. Jaffee and B. A. Wilcox, eds., Plenum, NY, pp. 545–561, 1977.

498. Kim, I.S., and S.S. Kang, “Dynamic Strain Aging in SA508-Class 3 Pressure Vessel Steel,” *Int. J. Pres. Vessels Piping*, 62, 123–129, 1995.

499. Xu, S., X.Q. Wu, E.H. Han, and W. Ke, “Effects of dynamic strain aging on mechanical properties of SA508 class 3 reactor pressure vessel steel, *J. Mater. Sci.*, 44 (11), 2882–2889, 2009.

500. Solomos, G., C. Albertini, K. Labibes, V. Pizzinato, and B. Viaccoz, “Strain rate effects in nuclear steels at room and higher temperatures,” *Nucl. Eng. Des.*, 229 (1-2), 139–149, 2004.

501. Chaouadi, R., and J.L. Puzzolante, “Loading Rate Effect on Ductile Crack Resistance of Steels Using Precracked Charpy Specimens,” *Int. J. Pres. Vessels Piping*, 85, 752–761, 2008.

502. Steichen, J.M., and A.L. Ward, “High Strain Rate Tensile Properties of Type 308 SMA Weld Metal,” *Welding Research Supplement*, 130-s to 135-s, April 1975.

503. Iino, Y., “Tensile Properties of Type 304 Stainless Steel in Temperature Range 77 to 1223K and Strain Rate Range 10^{-6} to 10^{-1} s^{-1},” *Bull. Japan Soc. Mech. Eng.*, 29, 355–361, 1986.

504. Huang, G.L., D.K. Matlock, and G. Krauss, “Martensite Formation, Strain Rate Sensitivity, and Deformation Behavior of Type 304 Stainless Steel Sheet,” *Met. Trans. A*, Vol. 20A, pp. 1239–1246, 1989.

505. Iino, Y., J. Svejcar, I. Dlouhý, and M. Forejt, “Effect of strain rate 10^{-4} to 10^{3} s^{-1} on room temperature tensile properties and notched plastic zone of type 304 stainless steel,” in *17th European Conference on Fracture 2008: Multilevel Approach to Fracture of Materials*, Components and Structures, pp. 773–779, 2008.

506. Iino, Y., J. Svejcar, I. Dlouhý, and M. Forejt, “Effect of strain rate 10^{-7} to 10^{-4} s^{-1} on room temperature tensile properties and notched plastic zone of type 304 stainless steel,” in *18th European Conference on Fracture 2010: Fracture of Materiále and Structures from Micro to Macro Scale*, pp. 1–8, 2010.

507. Marschall, C.W., M.P. Landow, G.M. Wilkowski, and A.R. Rosenfield, “Comparison of Static and Dynamic Strength and J-R Curves of Various Piping Materials from the IPIRG-1 Program,” *J. Press. Vessels Piping*, Vol. 62, pp. 49–58, 1995.

508. Kundu, A, and P.C. Chakraborti, “Effect of Strain Rate on Quasistatic Tensile Flow Behaviour of Solution Annealed 304 Austenitic Stainless Steel at Room Temperature,” *J. Mater. Sc.*, 45 (20), 5482–5489, Oct. 2010.

509. Rodriguez-Martinez, J.A., R. Pesci, and A. Rusinek, “Experimental Study on the Martensitic Transformation in AISI 304 Steel Sheets Subjected to Tension under Wide Ranges of Strain Rate at Room Temperature,” *Mater. Sci. Eng.*, 528, 5974–5982, July 2011.

510. Stout, M.G., and P.S. Follansbee, “Strain Rate Sensitivity, Strain Hardening, and Yield Behavior of 304L Stainless Steel,” *J. Eng. Mater. Technol.,* 108 (4), 344–353, Oct. 1986.

511. Lichtenfeld, J., J.A. Vab Tyne, and M.C. Mataya, “Effect of strain rate on stress-strain behavior of alloy 309 and 304L austenitic stainless steel,” *Metall. Mater.*, 37 (1), 147–161, Jan. 2006.

512. Fahr, D., “Analysis of Stress Strain Behavior of Type 316 Stainless Steel,” ORNL-TM-4292, Oak Ridge National Laboratory, November 1973.

513. Varin, R., “The Effects of Temperature and Strain Rate on the Plastic Flow and Ductility of Ultrafine-Grained Type 316 Austenitic Stainless Steel,” *Mat. Sci. Eng.*, 94, 93–107, Oct. 1987.

514. Hong, S-G, and S-B Lee, “The Tensile and Low-Cycle Fatigue Behavior of Cold Worked 316L Stainless Steel: Influence of Dynamic Strain Aging,” *Intl. J. Fatigue*, 26, 899–910, 2004.

515. Choudhary, B.K., “Influence of Strain Rate and Temperature on Tensile Deformation and Fracture Behavior of Type 316L(N) Austenitic Stainless Steel,” *Metall. Mater. Trans.*, 45A, 302–316, 2014.

516. Samuel, K.G., S.L. Manan, and P. Rodriguez, “Effect of Aging on the Strain Rate Sensitivity and Serrated Flow of a Type 316 Stainless Steel at 923 K,” *Scripta Metall. Mater.*, 26, 685–689, 1992.

517. Lee, W-S, and F-T Tzeng, “Mechanical Properties of 304L Stainless Steel SMAW Joints under Dynamic Impact Loading,” *J. Mater. Sci.*, 40, 4839–4847, 2005.

518. Lee, W-S, C-F Lin, and B-T Chen, “Tensile Properties and Microstructural Aspects of 304L Stainless Steel Weldments as a Function of Strain Rate and Temperature,” *Proc. of the Institution of Mechanical Engineers*, Part C, pp. 439–451, May 2005.

519. Lee, W-S, C-F Lin, C-Y Liu, and C-W Cheng, “The Effects of Strain Rate and Welding Current Mode on the Dynamic Impact Behavior of Plasma-Arc Welded 304L Stainless Steel Weldments,” *Met. Trans.*, 35A, 1505–1515, 2004.

520. Lee, W-S, C-F Lin, C-Y Liu, and F-T Tzeng, “Impact Properties of 304L Stainless Steel GTAW Joints Evaluated by High Strain Rate of Compression Test,” *J. Nucl. Mater.*, 335 (3), 335–344, 2004.

521. Steichen, J.M., and A.L. Ward, “Effects of Test Temperature, Strain Rate, and Thermal Exposure on the Tensile Properties of Alloy 600,” HEDL-TME 76-62, UC-79h,p, Hanford Engineering Development Laboratory, Hanford, WA, July 1976.

522. Lee, W-S, and T-N Sun, “Plastic Flow Behavior of Inconel 690 Super Alloy Under Compressive Impact Loading,” *Mat. Trans.*, 45 (7), 2339–2345, 2004.

523. Lee, W-S, C-Y. Liu, and T.N. Sun, “Behavior of Inconel 690 Super Alloy Evaluated by Impact Test,” *J. Mater. Process. Technol.*, 153, 219–225, 2004.

524. Tanguy, B, J. Besson, R. Piques, and A. Pineau, “Ductile to Brittle Transition of an A508 Steel Characterized by Charpy Impact Test. Part-I: Experimental Results,” *Eng. Fract. Mech.*, 72, 49–72, 2005.

525. Bouchet, C., B. Tanguy, J. Besson, and S. Bugat, “Prediction of the Effects of Neutron Irradiation on the Charpy Ductile to Brittle Transition Curve of an A508 Pressure Vessel Steel,” *Comput. Mater. Sci.,* 32, 294–300, 2005.

526. Hawthorne, J.R., “Post-irradiation Dynamic Tear and Charpy-V Performance of 12-in. Thick A533-B Steel Plates and Weld Metal,” *Nucl. Eng. Design*, 17, 116–130, 1971.

527. Schubert, L.E., A.S. Kumar, S.T. Rosinski, and M.L. Hamilton, “Effect of Specimen Size on the Impact Properties of Neutron Irradiated A533B Steel,” *J. Nucl. Mater.*, 225, 231–237, 1995.

528. IAEA, *Master Curve Approach to Monitor Fracture Toughness of Reactor Pressure Vessels in Nuclear Power Plants*, IAEA-TECDOC-1631, International Atomic Energy Agency, Vienna, 2009.

529. Wallin, K., “Effect of Strain Rate on the Fracture Toughness Reference Temperature T0 for Ferritic Steels,” *Recent Advances in Fracture*, The Minerals, Metals & Materials Society, 1997.

530. Gangloff, R.P., “Environmental Cracking-Corrosion Fatigue,” Chapter 26 in *Corrosion Tests and Standards-Application and Interpretation*, 2nd ed., R. Baboian, ed., American Society for Testing and Materials, West Conshohocken, PA, 2004.

531. Schijve, J., “Corrosion Fatigue,” Chapter 16 in *Fatigue of Structures and Materials,* 2nd ed., Springer Science+Business Media, New York, 2009.

532. Milella, P.P., “Corrosion Fatigue,” Chapter 16 in *Fatigue and Corrosion in Metals*, Springer Verlag Italia, Milan, 2013.

533. Jivkov, A.P., “ Strain-induced Passivity Breakdown in Corrosion Crack Initiation,” *Theoretical and Applied Fracture Mechanics*, 42 (1), 43–52, 2004.

534. Ikeda, K., and S. Mahin, S., “Cyclic Response of Steel Braces,” *J. Struct. Eng.*, 112 (2), 342–361, 1986.

535. Andresen, P.L., G.M. Gordon, and S.C. Lu, "The Stress-Corrosion-Cracking Model for High-Level Radioactive-Waste Packages," *J. Minerals., Met., and Mater. Soc. (JOM)*, 57 (1), 27–30, 2005.

536. Ahn, T.M. "Assessing and Modeling the Performance of Nuclear Waste and Associated Packages for Long-Term Storage," Chapter 7 in *Radioactive Waste Management and Contaminated Site Clean-Up: Processes, Technologies, and International Experience*, W.E. Lee, M.I. Ojovan, and C. Jantzen, eds., Woodhead Publishing Ltd., Cambridge, U.K., pp. 273–300, 2013.

537. Frankel, G.S., "Pitting Corrosion of Metals : A Review of the Critical Factors," *J. Electrochem. Soc.*, Vol. 145, No. 6, pp. 2186–2198, 1998.

538. Szklarska-Smialowska, Z., "Review of Literature on Pitting Corrosion Published Since 1960," *Corrosion*, Vol. 27, No. 6, pp. 223–233, 1971.

539. Szklarska-Smialowska, Z., *Pitting and Crevice Corrosion*, NACE International, Houston, TX, 2005.

540. Soltis, J., "Passivity Breakdown, Pit Initiation and Propagation of Pits in Metallic Materials - Review," *Corrosion Science*, Vol. 90, No. 1, pp. 5–22, 2015.

541. Hakkarainen, T.J., "Microbiologically Influenced Corrosion of Stainless Steels - What Is Required for Pitting?" *Materials and Corrosion*, Vol. 54, No. 7, pp. 503–509, 2003.

542. Chastell, D., et al., "The Influence of Stress on the Pitting Susceptibility of a 12%CrMoV Martensitic Stainless Steel," *Corrosion Science*, Vol. 19, No. 5, pp. 335–341, 1979.

543. Van Boven, G., W. Chen, and R. Rogge, "The Role of Residual Stress in Neutral pH Stress Corrosion Cracking of Pipeline Steels. Part 1: Pitting and Cracking Occurrence," *Acta Materialia*, Vol. 55, No. 1, pp. 29–42, 2007.

544. Oltra, R., and V. Vignal, "Recent Advances in Local Probe Techniques in Corrosion Research - Analysis of the Role of Stress on Pitting Sensitivity," *Corrosion Science*, Vol. 49, No. 1, pp. 158–165, 2007.

545. Guan, L., et al., "Effects of Cyclic Stress on the Metastable Pitting Characteristic for 304 Stainless Steel under Potentiostatic Polarization," *Corrosion Science,* http://dx.doi.org/10.1016/j.corsci.2015.01.009, 2015.

546. Nickel, D., et al., "Effect of Strain Localization on Pitting Corrosion of an AlMgSi0.5 Alloy," *Metals*, Vol. 5, pp. 172–191, (doi:10.3390/met5010172), 2015.

547. Cubicciotti, D., "Flow-assisted Corrosion of Steel and the Influence of Cr and Cu Additions," *Journal of Nuclear Materials*, Vol. 152, pp. 259–264, 1988.

548. Wen, J., et al., "Effects of Mass Transfer and Flow Conditions on SRB Corrosion of Mild Steel," CORROSION/NACExpo2006, Paper No. 06666, NACE International, Houston, TX, 2006.

549. Juergensmeyer, E.A., and M.A. Juergensmeyer, “Effect of Vibration on Bacterial Growth and Antibiotic Resistance,” *Summary of Research, NASA Grant NAG2-1512*, May 2001-October 2004, Judson College, IL, October 29, 2004.

550. Ibars, J.R., D.A. Moreno, and C. Ranninger, “MIC of Stainless Steels: A Technical Review on the Influence of Microstructure,” *International Biodeterioration & Biodegradation*, Vol. 29, No. 3–4, pp. 343–355, 1992.

551. Walsh, D., et al., “The Effect of Microstructure on Microbiologically Influenced Corrosion,” *JOM - Journal of the Minerals, Metals and Materials Society*, Vol. 45, No. 9, pp. 22–30, Sept. 1993.

552. Otero, E., J.M. Bastidas, and V. Lopez, “Analysis of a Premature Failure of Welded AISI 316L Stainless Steel Pipes Originated by Microbial Induced Corrosion,” *Materials and Corrosion*, Vol. 48, No. 7, pp. 447–454, 1997.

553. Sreekumari, K.R., K. Nandakumar, and Y. Kikuchi, “Bacterial Attachment to Stainless Steel Welds: Significance of Substratum Microstructure,” *Biofouling: The Journal of Bioadhesion and Biofilm Research*, Vol. 17, No. 4, pp. 303–316, 2001.

554. Sreekumari, K.R., Y. Kikuchi, and K. Nandakumar, “Effect of Metal Microstructure on Bacterial Attachment: A Contributing Factor for Preferential MIC Attack of Welds,” Paper No. 04597, CORROSION/2004: March 21-April 1, New Orleans, NACE International, 2004.

555. George, R.P., et al., “Influence of Surface Characteristics and Microstructure on Adhesion of Bacterial Cells onto a Type 304 Stainless Steel,” *Biofouling: The Journal of Bioadhesion and Biofilm Research*, Vol. 19, No. 1, pp. 1–8, 2003.

556. Antony, P.J., et al., “Role of Microstructure on Corrosion of Duplex Stainless Steel in Presence of Bacterial Activity,” *Corrosion Science*, Vol. 52, No. 4, pp. 1404–1412, 2010.

557. Geesey, G.G., et al., “The Influence of Surface Features on Bacterial Colonization and Subsequent Substratum Chemical Changes of 316L Stainless Steel,” *Corrosion Science*, Vol. 38, No. 1, 73–95, 1996.

558. Wagner, P., and B. Little, “Impact of Alloying on Microbiologically Influenced Corrosion - A Review,” *Materials Performance*, Vol. 32, No. 9, pp. 65–68, 1993.

559. Tributsch, H., J.A. Rojas-Chapana, C.C. Bartels, A. Ennaoui, and W. Hofmann, “Role of Transient Iron Sulfide Films in Microbial Corrosion of Steel,” *Corrosion*, Vol. 54 (3), 216–227, 1998

560. Mor, E.D., E. Traverso, and G. Ventura, “Effects of Rolling Direction and Tensile Stress on the Corrosion of a Naval Carbon Steel in Natural Marine Environments - II: Harbour Anaerobic Sediments,” *British Corrosion Journal*, Vol. 14, No. 2, pp. 103–108, 1979.

561. Percival, S.L., et al., “Physical Factors Influencing Bacterial Fouling of Type 304 and 316 Stainless Steels,” *British Corrosion Journal*, Vol. 33, No. 2, pp. 121–129, 1998.

562. Chen, Y., et al., "Characterizing Pitting Corrosion Caused by a Long-Term Starving Sulfate-Reducing Bacterium Surviving on Carbon Steel and Effects of Surface Roughness," *Corrosion*, Vol. 70, No. 8, 767–780, 2014.

563. Kielemoes, J., F. Hammes, and W. Verstraete, "Measurement of Microbial Colonization of Two Types of Stainless Steel," *Environmental Technology*, Vol. 21, No. 7, pp. 831–843, 2000.

564. Pugh, M.E., "A Post-conference Evaluation of Our Understanding of the Failure Mechanisms," *Proc. of Conf. on Stress Corrosion Cracking and Hydrogen Embrittlement of Iron Base Alloys*," pp. 37–51, R.W. Staehle, J. Hochman, R.D. McCright, and J.E. Slater, eds., NACE-5, Houston, TX, 1977.

565. Lozano-Perez, S., et al., "SCC in PWRs: Learning from a Bottom-Up Approach," *Metall. and Mater. Trans*. E, 1A, 194–210, 2014.

566. Coriou, H., et al., "Influence of Carbon and Nickel Content on Stress Corrosion Cracking of Austenitic Stainless Alloys in Pure or Chlorinated Water at 350°C," *Fundamental Aspects of Stress Corrosion Cracking*, pp. 352–356, R.W. Staehle, A.J. Forty, and D. van Rooyen, eds., NACE, Houston, 1969.

567. Logan, H.L., *The Stress Corrosion Cracking of Metals*, John Wiley & Sons, Inc., New York, 1966.

568. Vermilyea, D.A., "A Theory for the Propagation of Stress Corrosion Cracks in Metals," *J of Electrochemical Soc.*, 119 (4), 405–407, 1972.

569. Parkins, R.N., "1990 Plenary Lecture: Strain Rate Effects in Stress Corrosion Cracking," *Corrosion,* 46 (3), 178–189, 1990.

570. Garud, Y.S., "Significance and Integration of Creep Deformation Modeling in the Quantitative Evaluation of Intergranular SCC at Moderate Temperatures," Paper No. 10.44, *10th Intl. Cong. on Met. Co*r, 2215–2222, Central Electrochemical Research Institute, Karaikudi, India, 1987.

571. Arioka, K., et al., "Cold Work and Temperature Dependence of Stress Corrosion Crack Growth of Austenitic Stainless Steels in Hydrogenated and Oxygenated High-Temperature Water," *Corrosion,* 63 (12), 1114–1123, 2007.

572. Arioka, K., et al., "Dependence of Stress Corrosion Cracking for Cold-Worked Stainless Steel on Temperature and Potential, and Role of Diffusion of Vacancies at Crack Tips," *Corrosion,* 64 (9), 691–706, 2008.

573. Magnin, T., and J.M. Gras (eds.), *Corrosion-Deformation Interactions, CDI'92 Intl. Conf.*, Fontainbleau, France, October 5–7, 1992 — Publisher: Les Editions de Physique Les Ulis, 1993.

574. Jones, D.A., "Localized Surface Plasticity during Stress Corrosion Cracking," *Corrosion,* 52(5), 356–362, 1996.

575. Saario, T., et al., “Selective Dissolution – Vacancy – Creep Model for IGSCC of Alloy 600,” *Proc. 7th Intl. Conf. on Environmental Degradation of Materials in Nuclear Power System – Water Reactors*, 841–851, NACE International, Houston, TX, 1995.

576. Mulford, R.A., and U.F. Kocks, “New Observations on the Mechanisms of Dynamic Strain Aging and Jerky Flow,” *Acta Met*., 27, 1125–1134, 1979.

577. Jenkins, C.F., and G.V. Smith, “Serrated Plastic Flow in Austenitic Stainless Steel,” *Trans. Met. Soc. of AIME,* 245, 2149–2156, 1969.

578. Nakada, Y., and A.S. Keh, “Serrated Flow in Ni-C Alloys,” *Acta Met*., 18, 437–443, 1970.

579. Blakemore, J.S., “The Portevin–Le Chatelier Effect in Hydrogenated Nickel,” *Met. Tr*ans., 1, 145–149, 1970.

580. Blakemore, J.S., “The Portevin–Le Chatelier Effect in Carburized Nickel Alloys,” *Met. Tr*ans., 1, 1281–1285, 1970.

581. Garud, Y.S., “Technical Review on IGSCC of Inconel 600 Tubes – Model Development Needs,” EPRI Project S138-8, EPRI, Palo Alto, CA, November 10, 1982.

582. Hanninen, H., et al., “Dynamic Strain-Aging of Nickel-Base Alloys Inconel 600 and 690,” *Proc. 7th Intl. Conf. on Environmental Degradation of Materials in Nuclear Power System – Water Reactors*, pp. 1423–1430, T.R. Allen, P.J. King, and L. Nelson, eds., The Minerals, Metals & Materials Society, Warrendale, PA, 2005.

583. Hur, D.H., and D.H. Lee, “Effect of Solid Solution Carbon on Stress Corrosion Cracking of Alloy 600 in a Primary Water at 360°C,” *Mat. Sc. & Eng. A,* 603, 129–133, 2014.

584. Lian K., and E.I. Meletis, “Environment-Induced Deformation Localization during Transgranular Stress Corrosion Cracking,” *Corrosion,* 52 (5), 347–355, 1996.

585. Aubert, I., et al., “Modification of Plastic Strain Localization Induced by Hydrogen Absorption,” *Advances in Materials Science,* 8, No. 1 (15), pp. 5–14, 2008.

586. Meletis, E.I., “A Review of Present Mechanisms of Transgranular Stress Corrosion Cracking,” *J Mech. Behaviour of Mat*., 7 (1), 1–14, 1996.

587. Sauzay, M., and K. Vor, “Influence of Plastic Slip Localization on Grain Boundary Stress Fields and Microcrack Nucleation,” *Eng. Frac. Mechanics,* 110, 330–349, 2013.

588. Was, G.S., B. Alexandreanu, and J. Busby, “Localized Deformation Induced IGSCC and IASCC of Austenitic Alloys in High Temperature Water,” *Key Engineering Materials,* 261–263, 885–902, 2004.

589. Karlsen, W., G. Diego, and B. Devrient, “Localized Deformation as a Key Precursor to Initiation of Intergranular Stress Corrosion Cracking of Austenitic Stainless Steels Employedi Nuclear Power Plants,” *J. Nucl. Mater*., 406, 138–151, 2010.

590. Boniszewski, T., and G.C. Smith, “The Influence of Hydrogen on the Plastic Deformation, Ductility and Fracture of Nickel in Tension,” *Acta Metall.*, 11, 165–178, 1963.

591. Wilcox, B.A., and G.C. Smith, “The Poertevin-Le Chatellier Effect in Hydrogen Charged Nickel,” *Acta Metall*., 12, 371–376, 1964.

592. Wilcox, B.A., and G.C. Smith, “Intercrystalline Fracture in Hydrogen-Charged Nickel,” *Acta Metall*., 13, 331–343, 1965.

593. Abraham, D.P., and C.J. Altstetter, “Hydrogen Enhanced Localization of Plasticity in an Austenitic Stainless Steel,” *Metall. and Mat. Trans. A,* 26A, 2859–2878, 1995.

594. Robertson, I.M., “The Effect of Hydrogen on Dislocation Dynamics,” *Eng. Fract. Mechanics,* 64, 649–673, 1999.

595. Scully, J.R., and P.J. Moran, “Influence of Strain on the Environmental Hydrogen Assisted Cracking of a High-Strength Steel in Sodium Chloride Solution,” *Corrosion,* 44, 176–185, 1988.

596. Iyer, R.N., and R.F. Hehemann, “Strain-Rate Effects in Hydrogen Embrittlement of a Ferritic Stainless Steel,” *Environment-induced Cracking of Metals (NACE-10)*, 527–530, R.P. Gangloff and M.B. Ives, eds., NACE, Houston, TX, 1990.

597. Shen, C.H., and P.G. Shewmon, “Mechanism of Hydrogen-Induced Intergranular Stress Corrosion Cracking in Alloy 600,” *Metall. Trans. A,* 21A, 1261–1271, 1990.

598. Thompson, A.W., and I.M. Bernstein, “The Role Of Metallurgical Variables in Hydrogen-Assisted Environmental Fracture,” *Advances in Corrosion Science and Technology*, 53–175, M.G. Fontana et al., eds., Plenum Press, NY, 1980.

599. Eastman, J., et al., “The Effect of Hydrogen on the Solid Solution Strengthening and Softening of Nickel,” *Acta Met*., 30, 1579–1586, 1982.

600. Brown, C.M., and W.J. Mills, “Fracture Toughness, Tensile and Stress Corrosion Cracking Properties of Alloy 600, Alloy 690 and Their Welds in Water,” *Corrosion’96*, Paper 96090, NACE International, Houston, TX, 1996.

601. Symons, D.M., “The Effect of Hydrogen on the Fracture Toughness of Alloy X-750 at Elevated Temperatures,” *J. Nucl. Mater.,* 265, 225–231, 1999.

602. Chêne, J., and A.M. Brass, “Role of Temperature and Strain Rate on the Hydrogen-Induced Intergranular Rupture in Alloy 600,” *Metal. and Mat. Trans. A,* 35A, 457–464, 2004.

603. Garud, Y.S., “Intergranular Stress Corrosion Cracking Damage Model: An Approach and its Development for Alloy 600 in High-Purity Water,” *Corrosion,* 42 (2), 99–105, 1986.

604. Rebak R.B., and Hua F.H., “The Role of Hydrogen and Creep in Intergranular Stress Corrosion Cracking of Alloy 600 and Alloy 690 in PWR Primary Water Environments – A Review,” *Proc. 2nd Intl. Conf. on Environment Induced Cracking of Metals (EICM-2)*, 19–23 September 2004, Banff, Alberta, Canada, 2004.

605. Navai, F., and O. Debbouz, “AES Study of Passive Films Formed on a Type 316 Austenitic-Steels in a Stress Field,” *J. Mat. Sci*., 34, 1073–1079, 1999.

606. Vignal, V., R. Oltra, M. Verneau, and L. Coudreusu, “Influence of an Elastic Stress on the Conductivity of Passive Films,” *Mat. Sci. and Eng*., A303, 173–178, 2001.

607. EPRI, “Stress Corrosion Cracking Initiation Model for Stainless Steel and Nickel Alloys: Effects of Cold Work,” EPRI Report 1019032, Electric Power Research Institute, Palo Alto, CA, 2009.

608. Garud, Y.S., “Technical Review on IGSCC of Inconel 600 Tubes – Model Development Needs,” EPRI Project S138-8, EPRI, Palo Alto, CA, November 10, 1982.

609. Garud, Y.S., and G.O. Ilevbare, “An Engineering Approach to Access IASCC Initiation in Austenitic Stainless Steels of Light Water Reactors,” Paper No. 112, *Proc. 17th Intl. Conf. on Environmental Degradation of Materials in Nuclear Power Systems – Water Reactors*, Canadian Nuclear Society, August 9–12, Ottawa, Canada, 2015.

610. Wiessner, C.S., and M. MacGillivray, “Loading Rate Effects on Tensile Properties and Fracture Toughness of Steel,” 1999. Available at http://www.twi-global.com/technical-knowledge/published-papers/loading-rate-effects-on-tensile-properties-and-fracture-toughness-of-steel-april-1999/.

611. Iwadate, T., M. Kusuhashi, and Y. Tanaka, “Effect of Strain Rate on Small Specimen Fracture Toughness in the Transition Region,” in *Fracture Mechanics: Twenty-Fourth Volume*, ASTM STP 1207, J. Landes, D. McCabe, and J. Boulet, eds., American Society for Testing and Materials, Philadelphia, PA, pp. 325–341, 1994.

612. Jung, Y.H., and K.L. Murty, “Effect of Temperature and Strain Rate on Upper Shelf Fracture Behavior of A533 Class 1 Pressure Vessel Steel,” in *Fracture Mechanics: Nineteenth Symp.*, ASTM STP 969, American Society for Testing and Materials, Philadelphia, 392–401, 1988.

613. Marschall, C.M., M.P. Landow, and G.M. Wilkowski, “Loading Rate Effects on Strength and Fracture Toughness of Pipe Steels Used in Task 1 of the IPIRG Program,” NUREG/CR-6098, BMI-2175, Oct. 1993.

614. Nakajima, N., S. Shima, H. Nakajima, and T. Kondo, “The Fracture Toughness of Sensitized 304 Stainless Steel in Simulated Reactor Water,” *Nucl. Eng. Des.*, 93, 95–106, 1986.

615. Devillers-Guerville, L., J. Besson, and A. Pineau, “Notch Fracture Toughness of a Cast Austenitic Stainless Steel: Modeling of Experimental Scatter and Size Effect,” *Nucl. Eng. Des.*, 168 (1–3), 211–225, 1997.

616. McConnell, P., W. Sheckherd, and D.M. Morris, “Properties of Thermally Embrittled Cast Duplex Stainless Steel.” *J. Mater. Eng.*, 11 (3), 227–236. 1989.

617. Anzai, H., J. Kuniya, and I. Masaoka, “Effect of 475°C Embrittlement on Fracture Resistance of Cast Duplex Stainless Steel, *Trans. Iron Steel Inst. Japan*, 28, 400–405, 1988.

618. Chopra, O.K., “Effects of Thermal Aging and Neutron Irradiation on Crack Growth Rate and Fracture Toughness of Cast Stainless Steels and Austenitic Stainless Steel Welds,” NUREG/CR-7185, ANL-14/10, to be published.

619. Mills, W.J., and C.M. Brown, “Fracture Toughness of Alloy 600 and an EN82H Weld in Air and Water,” *Metall. and Mater. Trans. A*, 32A, 1161–1174, 2001.

620. Brown, C.M., and W.J. Mills, “Fracture Toughness of Alloy 690 and EN52 Welds in Air and Water,” *Metall. and Mater. Trans. A*, 33A, 1725–1735, 2002.

621. Seifert, H.-P., S. Ritter, and J. Heldt, “Strain-Induced Corrosion Cracking of Low-Alloy Reactor Pressure Vessel Steels under BWR Conditions,” *Proc. of the Tenth Intl. Conf. on Environmental Degradation of Materials in Nuclear Power Systems – Water Reactors*, *The Metallurgical Society*, Warrendale, PA, Lake Tahoe, NV, August 5–9, 2001.

622. Seifert, H.-P., and S. Ritter, “Mitigation Effect of Hydrogen Water Chemistry on Stress Corrosion and Low-Frequency Corrosion Fatigue crack Growth in Low-Alloy Steels,” *Proc. of the Twelth Intl. Conf. on Environmental Degradation of Materials in Nuclear Power Systems – Water Reactors*, T.R. Allen, P.J. King, and L. Nelson, eds., The Minerals, Metals & Materials Society, Warrendale, PA, pp. 485–4928, 2005.